Mussel-Inspired Advanced Materials for Biomedical Applications

Jose Daniel Bolaños Cardet

Departamento de Bioquímica y Biología Molecular
Facultad de Medicina

Mussel-Inspired Advanced Materials for Biomedical Applications

Jose Daniel Bolaños Cardet

Ph.D. Thesis

Biochemistry, Molecular Biology and Biomedicine

2025

Directors:

Dr. Salvio Suárez García

Dr. Víctor J. Yuste Mateos

Memoria presentada para aspirar al Grado de Doctor para Jose Daniel Bolaños Cardet.

Jose Daniel Bolaños Cardet

Dr. Salvio Suárez García

Dr. Víctor Yuste José Mateos

Barcelona, 17 de Julio del 2025

Abstract

Catechols are highly versatile molecules, consisting of a benzene ring and two hydroxyl groups, naturally found in plants, food and the human body. Notably present in the byssus of mussels, these molecules exhibit a broad range of interactions with various compounds, enabling adhesion to virtually any surface. Additionally, their ability to participate in oxidation-reduction reactions grants them remarkable properties, such as antioxidant activity. Over the course of the past two decades, the application of catechol-based compounds in materials science has significantly increased, attracting particular interest from researchers in the biomedical field.

In this Thesis, two main catechol-based materials were developed, specifically using amine-based ligands to generate polymers. The first type, coatings, consist of a thin polymeric layer of hundreds of nanometers deposited on different substrates. The second, free-standing membranes, are polymeric thin films with micrometer-scale thicknesses, which can be manually handled and applied to a desired surface after the generation. Despite their structural differences, both materials were synthesized from the same precursors using a straightforward, one-step and environmentally friendly process.

Each of these materials was studied in relation to a specific biomedical application, addressing two major global health challenges: antimicrobial resistance and cancer, both of which are projected to worsen in the coming decades. To address antimicrobial resistance, coatings were applied to woven and non-woven substrates commonly used in healthcare, such as paper, cotton and polypropylene. These coatings demonstrated outstanding antimicrobial properties, effectively eradicating various pathogens associated with nosocomial infections within three hours. Regarding cancer treatment, the obtained membranes were evaluated against a wide range of organ-derived cancer cell lines, with a particular focus on Glioblastoma. The strong cytotoxic activity exhibited by the membranes and their manipulability suggests promising potential for use as a localized post-resection treatment for Glioblastoma.

In both cases, the antimicrobial and cytotoxic properties were driven by the sustained production of reactive oxygen species. This mechanism has been proved to be highly effective in counteracting bacterial resistance to antibiotics, while also exacerbating the already elevated oxidative stress levels in tumor cells, ultimately leading to their death. These findings underscore the transformative potential of catechol-based materials in addressing critical healthcare challenges, paving the way for innovative treatments that could revolutionize medical practices and improve patient outcomes.

Resumen

Los catecoles son moléculas altamente versátiles, formadas por un anillo bencénico y dos grupos hidroxilo, que se encuentran de manera natural en plantas, alimentos y en el cuerpo humano. Presentes de forma destacada en el biso de los mejillones, estas moléculas presentan una gran capacidad de interacción con diversos compuestos, lo que permite su adhesión a prácticamente cualquier superficie. Además, su participación en reacciones redox les confiere propiedades notables, como la actividad antioxidante. En las últimas dos décadas, el uso de compuestos basados en catecoles en ciencia de materiales ha crecido de forma significativa, generando un interés particular en el ámbito biomédico.

En esta Tesis se desarrollaron dos materiales principales basados en catecoles, utilizando ligandos con grupos amino para formar polímeros. El primero, recubrimientos, consiste en capas poliméricas delgadas, de cientos de nanómetros, depositadas sobre distintos sustratos. El segundo, membranas, son películas poliméricas con espesores del orden de micras que pueden manipularse y aplicarse tras su síntesis. Aunque estructuralmente distintos, ambos materiales se sintetizaron a partir de los mismos precursores mediante un proceso simple, de un solo paso y respetuoso con el medio ambiente.

Cada material fue evaluado en una aplicación biomédica concreta, abordando dos desafíos sanitarios globales: la resistencia antimicrobiana y el cáncer, ambos en aumento a nivel mundial. Para combatir la resistencia antimicrobiana, los recubrimientos se aplicaron a sustratos como papel, algodón y polipropileno, comúnmente usados en entornos clínicos. Estos demostraron una excelente actividad antimicrobiana, eliminando diversos patógenos asociados a infecciones nosocomiales en menos de tres horas. Para el tratamiento del cáncer, las membranas fueron probadas frente a múltiples líneas celulares tumorales, con énfasis en el Glioblastoma. Mostraron La alta citotoxicidad mostrada por una de estas membranas, junto con su fácil manipulación, las convierte en candidatas prometedoras como tratamiento localizado tras la resección tumoral.

En ambos casos, las propiedades antimicrobianas y citotóxicas se deben a la producción sostenida de especies reactivas de oxígeno, un mecanismo eficaz frente a bacterias resistentes y capaz de intensificar el estrés oxidativo en células tumorales, llevándolas a la muerte. Estos hallazgos subrayan el potencial transformador de los materiales basados en catecoles para abordar desafíos críticos en el ámbito sanitario, allanando el camino hacia tratamientos innovadores que podrían revolucionar las prácticas médicas y mejorar los resultados para los pacientes.

Resum

Els catecols són molècules altament versàtils, formades per un anell benzènic i dos grups hidroxil, que es troben de manera natural en plantes, aliments i en el cos humà. Presents de manera destacada en el biso dels musclos, aquestes molècules mostren una gran capacitat d'interacció amb diversos compostos, cosa que els permet adherir-se pràcticament a qualsevol superfície. A més, la seva participació en reaccions redox els confereix propietats remarcables, com l'activitat antioxidant. En les darreres dues dècades, l'ús de compostos basats en catecols en la ciència dels materials ha crescut significativament, generant un interès especial en l'àmbit biomèdic.

En aquesta Tesi es van desenvolupar dos materials principals basats en catecols, emprant lligands amb grups amino per formar polímers. El primer, recobriments, consisteix en capes polimèriques fines, de centenars de nanòmetres, dipositades sobre diferents substrats. El segon, membranes, són films polimèrics amb gruixos de l'ordre de micres, que es poden manipular i aplicar després de la seva síntesi. Tot i les seves diferències estructurals, ambdós materials es van sintetitzar a partir dels mateixos precursors mitjançant un procés senzill, d'un sol pas i respectuós amb el medi ambient.

Cada material va ser avaluat en una aplicació biomèdica concreta, abordant dos grans reptes sanitaris globals: la resistència antimicrobiana i el càncer, ambdós en augment a escala mundial. Per combatre la resistència antimicrobiana, els recobriments es van aplicar a substrats com paper, cotó i polipropilè, habitualment emprats en entorns clínics. Aquests van mostrar una excel·lent activitat antimicrobiana, eliminant diversos patògens associats a infeccions nosocomials en menys de tres hores. Per al tractament del càncer, les membranes es van provar davant de múltiples línies cel·lulars tumorals, amb un èmfasi especial en el Glioblastoma. L'elevada citotoxicitat mostrada per una d'aquestes membranes, juntament amb la seva fàcil manipulació, les converteix en candidates prometedores com a tractament localitzat després de la resecció tumoral.

En ambdós casos, les propietats antimicrobianes i citotòxiques es deuen a la producció sostinguda d'espècies reactives d'oxigen, un mecanisme eficaç contra bacteris resistents i capaç d'intensificar l'estrès oxidatiu en cèl·lules tumorals, provocant-ne finalment la mort. Aquests resultats posen de manifest el potencial transformador dels materials basats en catecols per afrontar reptes crítics en l'àmbit de la salut, obrint la porta a tractaments innovadors que podrien revolucionar la pràctica mèdica i millorar els resultats clínics dels pacients.

List of abbreviations

ACTD: actinomycin D

AMR: antimicrobial resistance

AsAc: ascorbic acid

BAFI: bafilomycin

CFU: colony-forming units

CHX: cycloheximide

CNS: central nervous system

DEF: deferoxamine

DMEM: Dulbecco's Modified Eagle's Medium

ECAR: extracellular acidification rate

EDX: X-ray spectroscopy

ERA: erastine

FBS: fetal bovine serum

FER1: ferrostatin-1

FTIR: Fourier-transform Infrared Spectroscopy

GBM: Glioblastoma multiforme

HCQL: hydroxychloroquine

H42: Hoechst33342

ICP-MS: Inductively Coupled Plasma Mass Spectrometry

MRSA: methicillin-resistant *S. aureus*

NAC: n-acetyl-cysteine

NEC1: necrostatin-1

NRF2: nuclear factor erythroid 2

OCR: oxygen consumption rate

OLAP: olaparib

PEI: polyethyleneimine

PBS: phosphate-buffered saline

PDA: polydopamine

PI: propidium iodide

QAS: quaternary ammonium salts

QVD: Q-VD-OPH

RNS: reactive nitrogen species

ROS: reactive oxygen species

RUCA: rucaparib

SEM: Scanning Electron Microscopy

SP-SDS: Single Plate-Serial Dilution Spotting

STAURO: staurosporine

TMZ: temozolomide

UN: United Nations

WHO: World Health Organization

XPS: X-ray Photoelectron Spectroscopy

3MA: 3-methyladenine

List of molecules

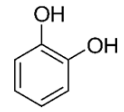

Pyrocatechol
PYRO

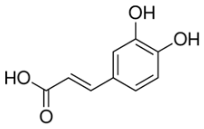

Caffeic Acid
CAFF

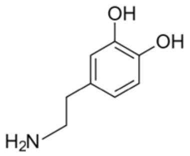

Dopamine
DOPI

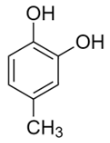

4-Methylcatechol
4MET

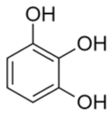

Pyrogallol
GALL

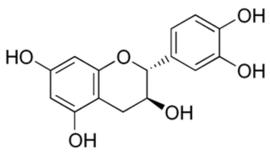

(+)-Catechin
CATH

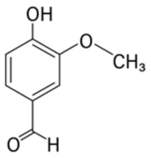

Vanillin

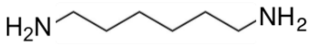

Hexamethylenediamine
HMDA

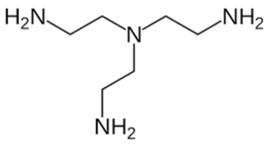

Tris(2-aminoethyl)amine
TRI2

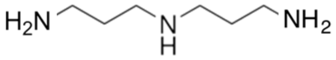

Norspermidine
NORE

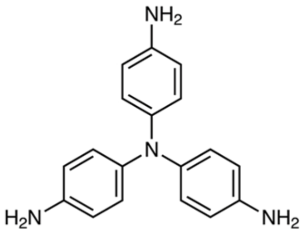

Tris(4-aminophenyl)amine
3PHEN

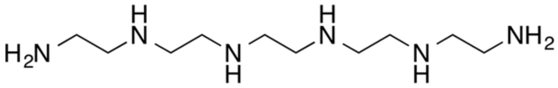

Pentaethylenehexamine
PETH

Table of Contents

Chapter 1 *General introduction* 1

1.1 Catechols 3

1.2 Properties of catechols 5

1.2.1 Adhesion 5

1.2.1.1 Hydrogen bonds 5

1.2.1.2 π-interactions 5

1.2.1.3 Coordination to metals 6

1.2.1.4 Covalent bonds 7

1.2.2 Reduction-oxidation (redox) 7

1.2.3 Conductivity 11

1.2.4 Photoreactivity 11

1.2.5 Biological interactions 12

1.2.5.1 Biocompatibility 12

1.2.5.2 Metabolic effect 13

1.3 Sources of polyphenols in the nature 14

1.3.1 Phenolic compounds in the plant kingdom 14

1.3.1.1 Foods rich in phenolic compounds and their role as antioxidants 14

1.3.1.2 Phenols in plant physiology and defense mechanisms 15

1.3.2 Phenolic compounds in the animal kingdom 16

1.3.3 Industrial processes as source of polyphenols 17

1.4 Catechol-based materials 17

1.4.1 Nanoparticles 18

1.4.2 Hydrogels 18

1.4.3 Bioadhesives 19

1.4.4 Coatings 20

1.4.5 Membranes 20

1.5 Scope of this thesis 22

1.6 References 24

Chapter 2 *Objectives* 33

Chapter 3 *Bioinspired Phenol-Based Coatings Against Antimicrobial Resistance and Environmental Applications* 37

3.1 Introduction 39
  3.1.1 Antimicrobial resistance 39
  3.1.2 Antimicrobial coatings 40
  3.1.3 ROS-mediated bacteria cell death 44
  3.1.4 Scope of this Chapter 46
3.2 Results and Discussion 48
  3.2.1 Coatings on paper, properties and characterization 48
  3.2.2 Antimicrobial activity 57
    3.2.2.1 General screening 57
    3.2.2.2 Determination of the minimum contact-killing time 58
    3.2.2.3 Spectrum of antimicrobial activity 60
  3.2.3 Antimicrobial mechanism 62
  3.2.4 Stability and biocompatibility 67
  3.2.5 Antibacterial activity on different substrates 68
    3.2.5.1 Coating universality 68
    3.2.5.2 Antibacterial activity 69
  3.2.6 Proof-of-concept case: in vitro and ex vivo validation of commercial band-aids 71
  3.2.7 Bioinspired coatings for enhanced filtration 74
    3.2.7.1 Retention of metallic nanoparticles 75
3.3 Conclusions 79
3.4 Future work 79
3.5 Experimental section 80
3.6 References 88

Chapter 4 *Bioinspired Phenol-Based Membrane for Post-Surgical Glioblastoma Treatment* .. 93

4.1 Introduction 95
  4.1.1 Cancer: its importance and impact 95

4.1.2 Glioblastoma multiforme 96
4.1.3 GBM standard of care 96
4.1.4 ROS and their role in cancer 98
4.1.5 Innovative approaches for Glioblastoma 101
4.1.6 Scope of this Chapter 102
4.2 Results and Discussion 103
4.2.1 Synthesis of the catechol-based free-standing membranes 103
4.2.1.1 HMDA 104
4.2.1.2 Post-synthesis manipulation 108
4.2.1.3 Other amines 108
4.2.2 Characterization of the bioinspired polyphenol-HMDA-based membranes 110
4.2.2.1 Physicochemical and morphological characterization 111
4.2.2.2 Cytotoxicity activity screening against Glioblastoma cells 117
4.2.3 CATH-M and its suitability for Glioblastoma post-surgical treatment 119
4.2.3.1 Physiological degradation and stability 120
4.2.3.2 Antibacterial activity 123
4.2.3.3 Ex vivo adhesion and brain conformability of CATH-M 124
4.2.3.4 Cell death spectrum of the CATH-M membrane 125
4.2.3.5 Survivability and viability 130
4.2.3.6 Comparison with standard-of-care treatments 132
4.2.3.7 Similarities in the catechin-stereoisomers-based membranes 132
4.2.3.8 Identification of the cell death subroutine(s) engaged by CATH-M in GBM cells 134
4.2.4 Influence of CATH-M in cell adhesion and migration 138
4.2.4.1 Cell morphology and tumor-like environment 138
4.2.4.2 Cell migration 144
4.2.4.3 Cell adhesion 147
4.2.5 Cell energetic metabolism alterations 149
4.2.5.1 Ultrastructural analysis 149
4.2.5.2 Mitochondrial function 149
4.2.6 ROS production and oxidative damage 153
4.2.6.1 Antioxidant protection and ROS modulation 153
4.2.6.2 ROS capacity and identification 155

4.2.6.3 Lipid peroxidation 157

4.2.7 Storage and stability of the CATH-M activity 157

4.2.7.1 Presence of water.. 158

4.2.7.2 Presence of light and inert atmosphere.. 159

4.2.8 Evaluation of protein profile alteration induced by CATH-M.................... 159

4.2.8.1 Protein arrays... 160

4.2.8.2 Proteomic analysis.. 161

4.3 Conclusions... 164

4.4 Future work... 164

4.5 Experimental section.. 165

4.6. References.. 176

Chapter 5 *General conclusions*.. 183

Chapter 1

General Introduction

1.1 Catechols

Among the huge variety molecules found in nature, polyphenols are a relevant group of compounds characterized by their versatile psychochemical and biological properties.[1] They are composed of one or more benzene rings, each of them usually bearing one or more hydroxyl (-OH) group, which contributes to their functional activity. Based on their structure, most of them can be classified into flavonoids, phenolic acids, catechols, stilbenes, lignans and tannins.[2] Within polyphenols, the most structurally simple are catechols, which base moiety consist of one benzene ring and two hydroxyl groups in ortho-position. The simplest catechol molecule is denominated pyrocatechol (1,2-dihydroxybenzene) (**Figure 1.1**). More complex derivatives generally present additional functional groups in the para-position of the catechol (e.g., dopamine). Interestingly, the pyrocatechol moiety can also be found in more complex polyphenols, such as gallic acid (phenolic acid), catechin (flavonoid) or tannic acid (tannin), reason why these molecules are often considered as "catechol derivatives".

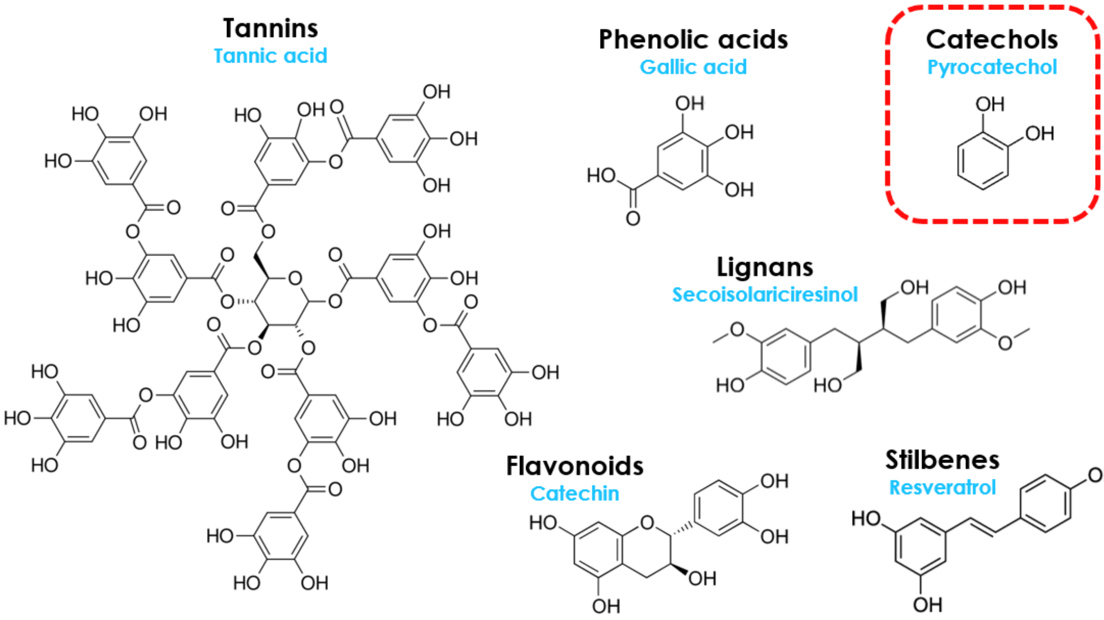

Figure 1.1. Polyphenols structure. Representative examples (blue) of different polyphenolic families (black).

Given their unique structural properties, catechols have been involved in the development of new biomaterials over the last two decades, with a particular focus on healthcare applications such as tissue regeneration and drug delivery.[3] It was the extensive research on mussel adhesion what stablished catechols as an exciting field in research. In 1981, Waite and Tanzer identified that 3,4-dihydroxypheny-l-alanine (or L-DOPA) may play a pivotal role in the effective adhesion of the Mytilus edulis (mussels) byssus to different substrates found in nature.[4] This discovery led to future researches about the proteins responsible of that harsh and wet resistant adhesion to organic, inorganic, and adhesion-resistant surfaces as paraffin and polytetrafluoroethylene (also known as Teflon).[5]

In order to explain the adhesion offered by catechol derivatives, subsequent studies revealed the presence of different mussel foot proteins (Mfps). Waite and colleagues characterized the key proteins involved, determining the molar percentage of L-DOPA in each of them. Specifically, Mfp1, Mfp3 and Mfp5 contained the outstanding amount of 15%, 20% and 30% molar mass of L-DOPA, respectively (**Figure 1.2**).[6,7] Additionally, transcriptomic analysis led to the identification of numerous new Mfps, once again laying the foundation for future research.[8] Besides, the outstanding adhesion properties have been studied in deep using advanced characterization techniques to elucidate the different interactions between catechol moieties and surfaces.[9]

In later works, Messersmith and collaborators elucidated the broad range of substrates capable of interacting with dopamine.[10] Among them, noble metals, oxide surfaces, semiconductors, ceramics, and even synthetic polymers. Besides the interaction with such a diverse surfaces,[11] other outstanding properties of catechols have been studied, such as their redox ability,[12] conductivity,[1] photo reactivity[13] and biocompatibility.[14]

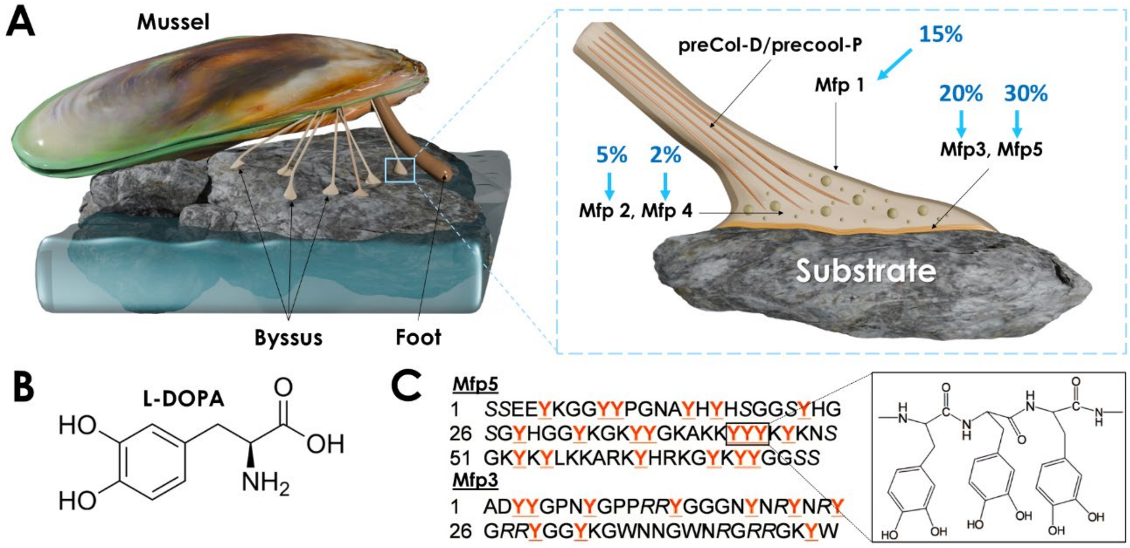

Figure 1.2. Mussel byssus and principal Mfps. Mussel foot secretions of byssal prepolymerized collagens (pre-Col) and mussel foot proteins (Mfps) can self-assemble and solidify to finally create the adhesive plaque, which is in contact with the substrate. **A)** Its core is primarily composed of low-content dopamine Mfps (2 and 4), which function mainly as coatings. In contrast, the interface (shown in green), which directly interacts with the substrate, consists of L-DOPA rich Mfps (3, 5, and 6) that functions as adhesives. In blue, the approximate % in molar mass of **B)** L-Dopa. **C)** Amino acid sequence of the mfp 5 and 3. Inset shows a tyrosine (Y) tripeptide post-translationally modified to L-DOPA. Adapted from [10].

Additionally, multidisciplinary studies in recent decades have elucidated numerous health benefits associated with catechols, including antioxidant, antitumoral, anti-inflammatory and antimicrobial, among others.[3] As a result, catechols—particularly dopamine—have gained an increasing relevance in the field of biomaterials (e.g. hydrogels, bioadhesives, coatings for medical fabrics and nanoparticles for drug delivery, among others), where they are commonly known as "mussel-inspired materials".[15,16,17]

1.2 Properties of catechols

The multifaceted properties of catechols enable them to form an exceptionally versatile group of molecules, a characteristic primarily attributed to their hydroxyl groups and aromatic ring. Among these properties, the most relevant are outlined below.

1.2.1 Adhesion

Despite their simple structure, several publications have confirmed that catechols can interact with virtually any surface.[10,18,19] The Nanostructured Functional Materials (Nanosfun) group, one of the groups involved in this thesis, has extensive experience in the chemistry of catechols. The research group has exploited their versatile adhesion properties, attributed to a surface-adaptable adhesion mechanism. In this context, both covalent (covalent bonding and coordination) and non-covalent (hydrogen bonds and π) interactions contribute to the mechanism (**Figure 1.3**).[11]

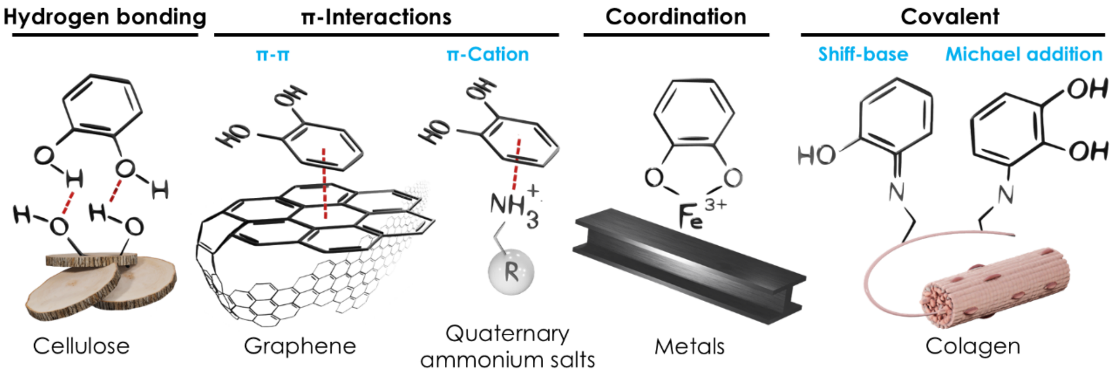

Figure 1.3. Interactions of catechols. Examples of catechols performing, hydrogen bonds, π-π interactions, coordination and covalent bonding.

1.2.1.1 Hydrogen bonds

Attributed to the presence of hydroxyl groups (**Figure 1.3A**), this adhesion mechanism is particularly effective under acidic conditions, becoming weaker and reversible as the pH increases. In such conditions, the hydroxyl groups are oxidized and transformed into quinones, leading to different interaction mechanisms. Furthermore, molecular dynamics simulations have demonstrated that catechols can displace water molecules from surfaces, what explains their strong adhesion even under wet conditions.[20] This behavior has been extensively demonstrated in a wide variety of surfaces, generally by coating with polydopamine (PDA) and analyzing the resulting water contact angle on the pristine (higher) and coated (lower) surfaces.[21,22,23]

1.2.1.2 π-interactions

π-π interactions occur when two aromatic rings align in a favorable orientation, allowing their electron clouds to overlap (**Figure 1.3B**). For instance, our research group successfully coated carbon nanotubes using alkylated catechols in non-polar solvents. As a result, the nanotubes became highly insoluble due to the hydrophobicity of the alkyl chains.[24] Additionally, positively charged cations can interact with the electron-rich π-system of an aromatic ring, forming cation-π interaction. Both π-π and cation-π play a crucial role in the binding, recognition, and function of catecholamine neurotransmitters within the central nervous system. For instance, the interaction between acetylcholine and the acetylcholine-binding protein (**Figure 1.4A**),[25] or between epinephrine and the β_2 adrenergic receptors (**Figure 1.4B**).[26]

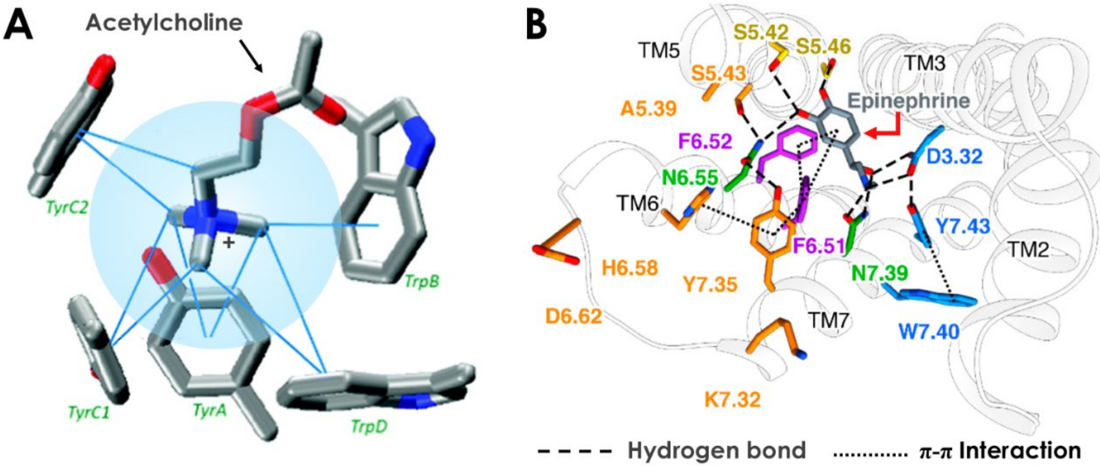

Figure 1.4. π-interactions between molecules and receptors. A) 3D representation of the quaternary ammonium of the acetylcholine being surrounded by the aromatic residues of the acetylcholine-binding protein. Blue lines represent plausible cation-π interactions. **B)** Key interactions between the β_2 adrenergic receptor and the endogenous ligand epinephrine. Adapted from [25] and [26], respectively.

1.2.1.3 Coordination to metals

The interactions between metal ions and catechols are mainly mediated by coordination bonds. The hydroxyl groups of catechols can form bidentate or monodentate coordination bonds with different metal ions (**Figure 1.3C**). These interactions are mostly described for titanium oxide, a metal widely used for its relevant applications (e.g., prosthesis). For instance, Li and collaborators studied the coordination process with rutile-titanium oxide, determining that isolated catechols tend to form a bidentate bond with the ring perpendicularly to the surface.[27] These catechols can then diffuse through the surface, become monodentate, rotate and exchange protons with surrounding oxygen atoms. Furthermore, other researchers have confirmed this theory with different metallic surfaces (e.g., zinc oxide), and catechol derivatives (e.g., caffeic acid), identifying bidentate bonds as the most probable.[28] In general, catechols are exceptional metallic-ions chelators and play a fundamental role in biology. For instance, among the different siderophores (metal scavenger) found in nature, enterobactin is one of the strongest. It is characterized by three catechol groups converging at a single point, allowing a simultaneous coordination with Fe^{3+} ions (**Figure 1.5A**).[29]

1.2.1.4 Covalent bonds

Covalent interactions of catechols were demonstrated by Messersmith and collaborators, who functionalized an AFM tip with a single L-DOPA molecule and observed strong bonding to an amine-modified surface.[4] These kind of interactions can occur through Schiff base or Michael-type addition (**Figure 1.3D**). In recent years, a specific research line in Nanosfun research group has focused on developing catechol-amine-based materials, leveraging covalent interactions such as the copolymerization of hexamethylenediamine and pyrocatechol (**Figure 1.5B**).[30] This approach has been thoroughly optimized in this Thesis for the development of novel catechol- and polyphenol-based materials.

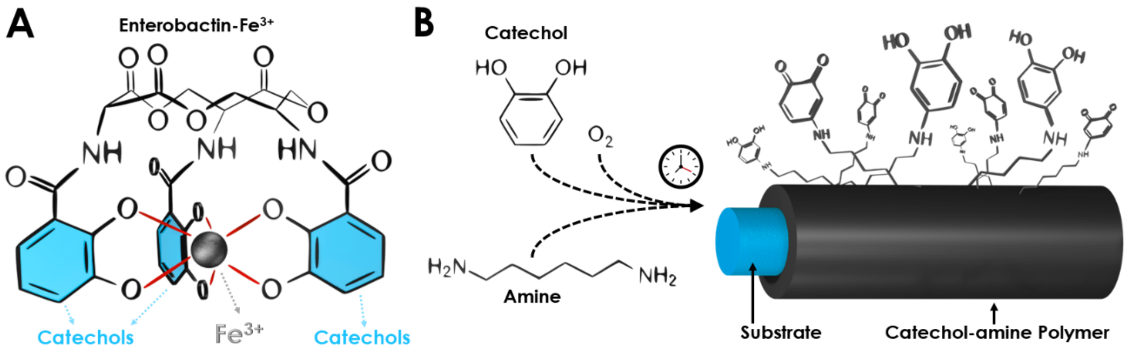

Figure 1.5. Coordination and covalent bonding examples of catechols. A) The siderophore enterobactin chelating a Fe^{+3} ion through three catechol groups simultaneously. **B)** Schematic representation of the copolymerization between pyrocatechol and hexamethylenediamine through covalent bonding. Adapted from [30].

1.2.2 Reduction-oxidation (redox)

Polyphenols, including single phenols like pyrocatechol, exhibit redox properties that enable them to function as both oxidants and reducers depending on the surrounding conditions. These properties are often referred to as antioxidant (prioritizing the oxidation of catechols before other molecules) and reactive oxygen species (ROS) generation capacity, respectively.

The self-oxidation of the catechol group can mainly occur at neutral to basic pH. During this process, molecular oxygen oxidizes the hydroxyl group, generating a superoxide anion and converting the catechol into a semiquinone and then a quinone (**Figure 1.6**). During this process, the catechol loses two electrons. The produced superoxides can further transform into hydrogen peroxide in the presence of protons, generating molecular oxygen.[12,31] Nevertheless, this process can be reversed if two electrons are donated to the quinone by reducing agents like nicotinamide adenine dinucleotide (NADH). This polyphenol property is often referred to as redox cycling.

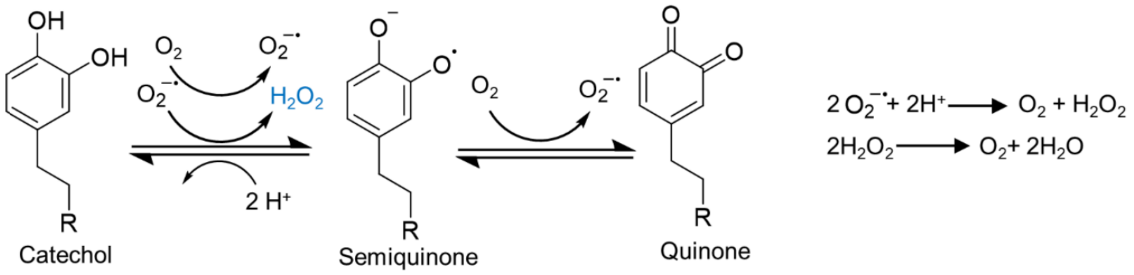

Figure 1.6. Scheme of the self-oxidation of catechol.[31]

The antioxidant activity of phenols can be attributed to their ability to donate hydrogens to free radicals (hydrogen-atom-transfer), such as peroxyl or hydroxyl radicals, forming a phenoxyl radical.[1] Moreover, catechols can also perform a single-electron-transfer with ROS radicals (for instance converting $OH\cdot$ to OH^-) in order to stabilize them, leaving the catechol in cationic state (**Figure 1.7**).[13,32] In both cases, these cations and radical states of the catechol are relatively stabilized due to resonance with the remaining hydroxyl groups and the benzene ring/s.

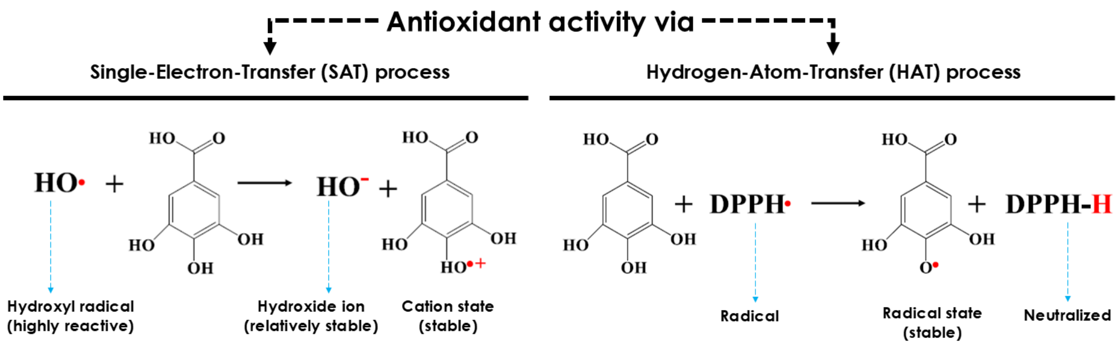

Figure 1.7. Catechols antioxidant activity towards radicals. Catechols can act as antioxidants through two distinct mechanisms. In the first, single-electron transfer (SET), the catechol donates an electron to a radical ($OH\cdot$), converting it into a more stable hydroxide ion (OH^-). In the second mechanism, the catechol donates a hydrogen atom to a radical, such as DPPH (a commonly used commercial radical), effectively neutralizing it. In both cases, the resulting cationic or radical form of the catechol is stabilized by resonance and the influence of the neighboring hydroxyl groups. Edited from [32].

The catechol/polyphenol structure and the environmental conditions, such as pH, solvent polarity or the presence of metals can influence their redox activity. For instance, under acidic conditions, catechols tend to remain neutral or protonated. On the contrary, under basic conditions they are often deprotonated, leading to the formation of semiquinones and quinones.[33]

The redox activity can be modulated by the addition of different molecules. For example, the presence of metal ions plays a considerable role in the redox regulation of catechols and polyphenols. These compounds act as antioxidants through metal chelation.[34,35] As previously explained, catechol moieties can interact with metal ions such as Fe^{2+} through coordination bonding. Fe^{2+} ions, known for their reactivity, can catalyze the Fenton reaction, resulting in the production of reactive oxygen species. Despite pk_a values of the most acidic phenolic hydrogen in these molecules (usually ranging between 7 to 10), catechols and gallol moieties can be easily deprotonated at physiological pH in the presence of iron, forming very stable complexes. These ligands strongly stabilize Fe^{3+} over Fe^{2+}, leading to the rapid oxidation of Fe^{2+} to Fe^{3+} (self-oxidation) in the presence of oxygen (**Figure 1.8A**).[34] Conversely, when catechol or gallol binds to Fe^{3+}, it can reduce Fe^{3+} to Fe^{2+} while self-oxidizing into a semiquinone (**Figure 1.8B**). At low pH, this semiquinone can be protonated, forming a neutral ligand that can bind to an additional Fe^{3+}, stabilizing it into a quinone and reducing the metal ion to Fe^{2+} (**Figure 1.8C**). At higher pH, the formation of bis- and tris-polyphenol complexes (two or three catechols coordinated to a single iron) inhibits the reduction of Fe^{3+} (**Figure 1.8D**).[13,35]

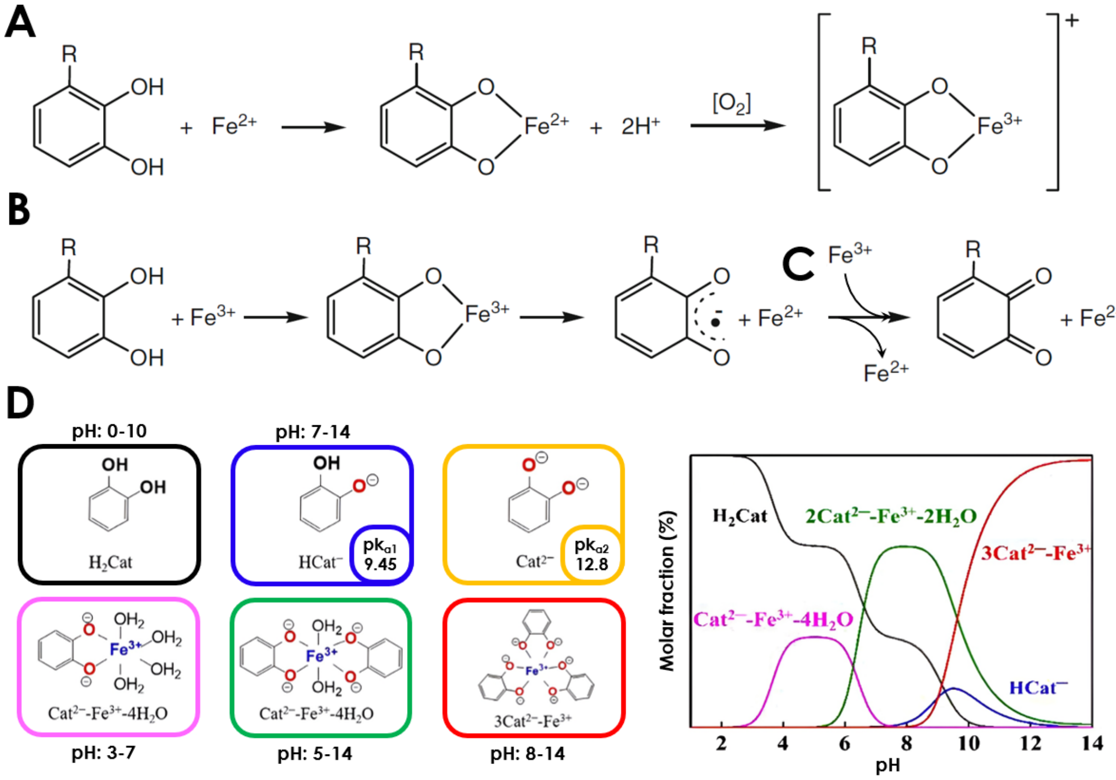

Figure 1.8. Redox behavior of catechol in the presence of iron ions. A) Self-oxidation of catechol in the presence of Fe^{2+} and oxygen (antioxidant behavior inside the cells). **B)** Self-oxidation of catechol to a semiquinone in the presence of Fe^{3+}, reducing it into Fe^{2+}, followed by a **C)** second oxidation to a quinone and the reduction of another Fe^{3+} to Fe^{2+}. Adapted from [34]. **D)** Distribution of relative molar fractions of different dissociation and complexation forms between catechol and Fe^{3+} in base of the pH. Despite pk_{a1} values of catechol being approximately 9.5, in the presence of iron, catechol can undergo deprotonation at low pH. Adapted from [35].

The presence of Fe^{2+} within the cell, which is a predominantly reductive environment, can induce the generation of ROS through the Fenton and Haber-Weiss reactions. This process transforms relatively stable peroxide into highly reactive hydroxyl radicals. Therefore, the chelation of Fe^{2+} by polyphenols can explain their antioxidant role in biological systems (**Figure 1.8A and 1.9**).

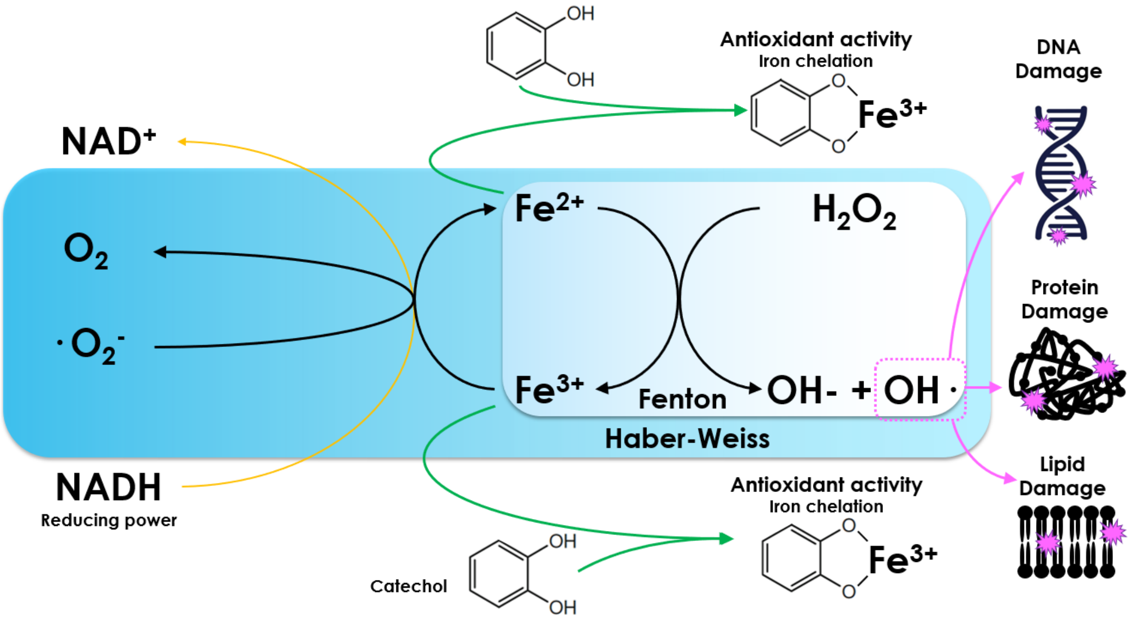

Figure 1.9. Fenton and Haber-Weiss reactions coupled with catechols. Fenton reaction transforms H_2O_2 into highly reactive hydroxyl radicals through the oxidation of Fe^{2+} to Fe^{3+}. The Haber-Weiss can complement this process by reducing Fe^{3+} back to Fe^{2+} (which is then used by Fenton). Additionally, intracellular reducing agents, such as NADH, can reduce Fe^{3+} to Fe^{2+}. Catechols play a protective role by chelating Fe^{3+}, however, their ability to chelate Fe^{2+} is particularly important, as it prevents its participation in the Fenton reaction. This is crucial, since hydroxyl radicals are extremely damaging for cell components, including DNA, proteins and lipids.

The antioxidant capacity of polyphenols is a key factor in their biological role. This capacity is significantly influenced by the structure of the molecule, particularly the number and position of hydroxyl groups in their aromatic rings. The catechol moiety can delocalize the resulting radical and stabilize the molecule. For instance, a comparison of different flavonoids showed that those with a pyrocatechol group in the C ring (such as quercetin or luteolin) significantly improved the antioxidant activity related to iron, being much higher than when this group was present in the ring A (as in baicilein) (**Figure 1.10A**). This observation highlights the critical role of the moieties present in the C ring in determining the antioxidant efficacy of these compounds.[36]

Interestingly, a different study examined how the presence of pyrocatechol or gallol moieties in catechols and flavonoids influences their antioxidant capacity, specifically in the presence of iron and peroxide.[37] The study measured the pK_a values of the most acidic phenolic hydrogen in each molecule and observed that values were correlated with the lowest iron-mediated DNA damage. This suggests a predictive model of antioxidant activity based on the ability to bind iron. Additionally, molecules containing a pyrocatechol ring exhibited lower pK_a value and greater DNA protection compared to those based with gallol rings, thereby confirming that gallol groups provide stronger antioxidant protection than catechol groups (**Figure 1.10B**). This is strongly supported by the case of epigallocatechin gallate, a complex flavonoid featuring two gallol rings.[37]

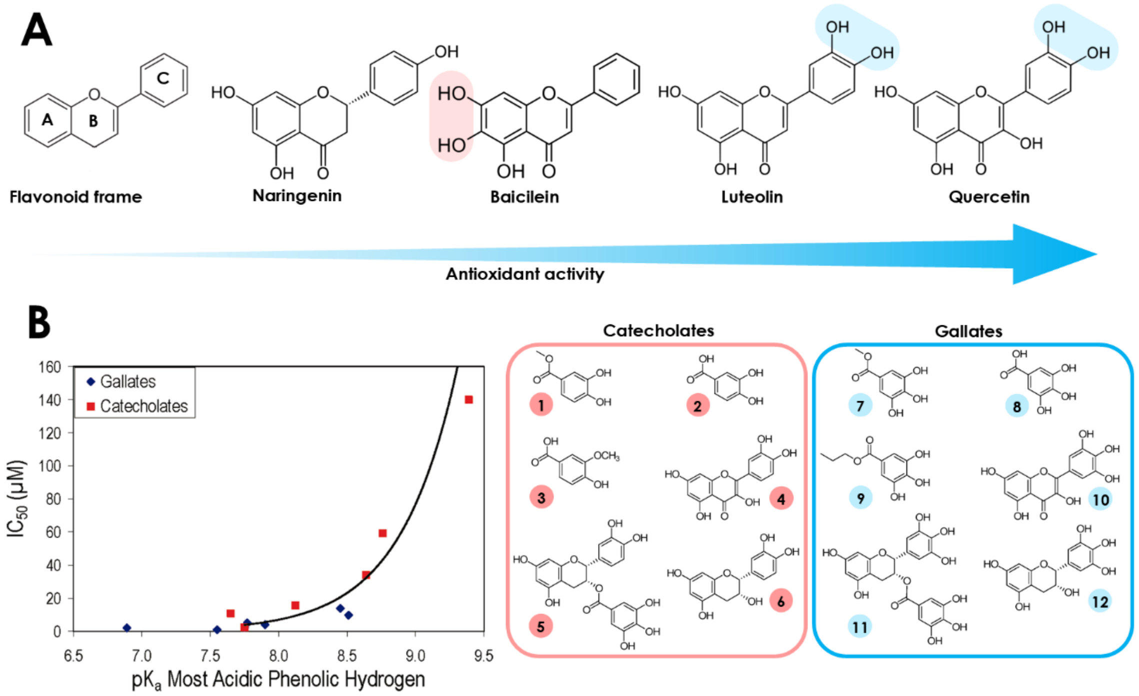

Figure 1.10. Antioxidant activity of polyphenols in base of their structure. A) Fe^{3+}-mediated antioxidant activity in flavonoids is reduced when two hydroxyl groups are located in the A ring, whereas it is enhanced when these hydroxyl groups are positioned in the C ring. **B)** Polyphenols containing a gallol moiety (in blue) exhibit a lower pKa value compared to those with a catechol moiety (in red), indicating that the former are generally better antioxidants. Methyl 3,4-dihydroxybenzoate (1), protocatechuic acid (2), vanillic acid (3), quercetin (4), (-)-epicatechin-3-gallate (5), (-)-epicatechin (6), methyl 3,4,5-trihydroxybenzoate (7), gallic acid (8), *n*-propyl gallate (9), myricetin (10), (-)-epigallocatechin-3-gallate (11), (-)-epigallocatechin (12). Adapted from [37].

1.2.3 Conductivity

The unique properties of polyphenols extend beyond their antioxidant capabilities. Their structural features, particularly electron delocalization, contribute to fascinating applications in material science. Electron delocalization is a distinctive property of the benzene ring, which can also be found in materials like graphene, known for their excellent conductivity. For catechols and other polyphenols, this property is predominantly observed during the stabilization of the molecule under phenolate or o-semiquinones states, enabled by electron resonance between the hydroxyl groups and the benzene ring (**Figure 1.11A**). This property can be leveraged in polyphenol-based materials focused in developing conductive polymers.[1] For instance, our group recently obtained conductive thin films based on hexahydroxytriphenylene, an aromatic molecule with three catechol rings (**Figure 1.11B**).[38]

1.2.4 Photoreactivity

Catechols and polyphenols are known for their significant photoreactivity properties, which play a crucial role in both biological and material applications. These phenolic compounds exhibit intense absorption in the ultraviolet region of the spectrum. For instance, phenols and flavonoids show spectral maxima in the range of 250-290 nm and 250-350 nm, respectively. Additionally, certain colored polyphenols, such as anthocyanins and betacyanins, can absorb in the visible range, with characteristic bands at 475-560 nm and 535-545 nm, respectively. Interestingly, the complexation of these molecules with specific metal ions (e.g., Mg^{2+}, Fe^{3+}) through coordination mechanisms can create specific colors, such as blue.[13] This interaction highlights the versatility and functional potential of catechols and polyphenols in various applications, such as the case of dopamine-curcumin nanoparticles for photodynamic therapy.[39]

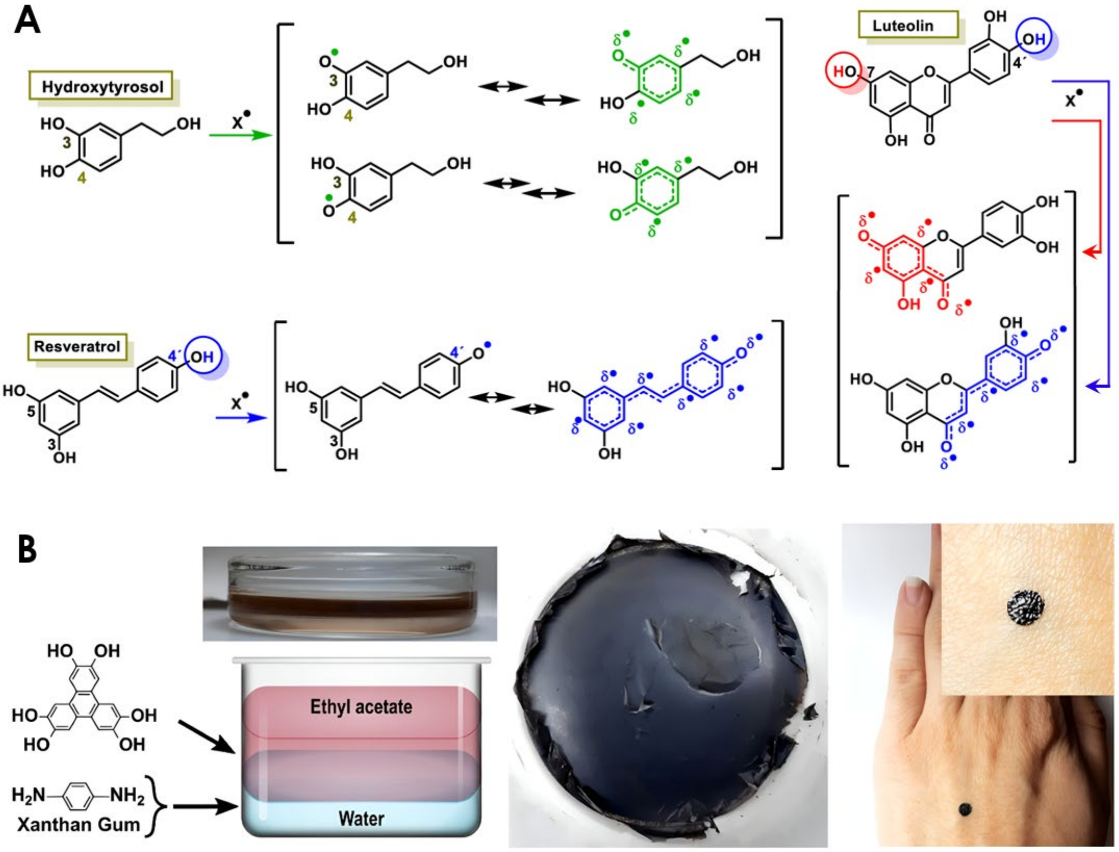

Figure 1.11. Polyphenols and their conductivity. A) The electron delocalization capacity of polyphenols positions them as promising candidates for the development of novel materials in sensor technologies. **B)** An illustrative example of this is the fabrication of conductive thin films composed of hexahydroxytriphenylene and xanthan gum for wearable electronic applications on the skin. Adapted from [1] and [38], respectively.

1.2.5 Biological interactions

Phenolic moieties play a crucial role at the biointerface due to their distinctive structural properties and reactivity, significantly impacting surface biocompatibility. Furthermore, the involvement of polyphenols in metabolic processes underscores their importance in studying their effects on health and their use in the design of bioinspired materials.[1,3]

1.2.5.1 Biocompatibility

In addition to the remarkable properties of catechols, their biocompatibility has awakened special interest due to its relevance in biomedical applications. For instance, the functionalization of materials with dopamine enhances the cell adhesion due to multiple interactions and improved surface hydrophilicity (**Figure 1.12A**).[40] Furthermore, the incorporation of peptides, proteins, growth factors, or antibodies into polyphenol coatings can significantly improve cell-surface interactions.[14] Moreover, these coatings also contribute to reduce immune responses, such as platelet adhesion to surfaces like titanium, thereby improving hemocompatibility.[41]

Worth to mention that catechols are structurally similar to biological metabolites (such as dopamine or melanin),[42] making them compatible with enzymatic and cellular processes.

1.2.5.2 Metabolic effect

Polyphenols can interact directly as inhibitor of oxidases when binding them, as well as inducing antioxidant enzymes, providing secondary ROS protection mechanisms alongside metal coordination.[13] Moreover, the oxidation of catechols into quinones, can induce the NRF2 factor, which strongly upregulates the oxidative stress protection pathway. Notably, studies have shown that keratinocytes can upregulate NRF2 when exposed to melanin-based polymers (**Figure 1.12B**).[43] Besides their pro/antioxidant influence, dietary polyphenols are able to inhibit the activity of alfa-amylase and alfa-glucosidase (which convert starch into glucose). Other examples of polyphenol-mediated inhibitions are the NF-kB transcription factor (related with various physiological and pathological processes), the PI3K (cell growth, proliferation and survival) and the downregulation of BCL-2 protein family (related with the apoptosis).[1]

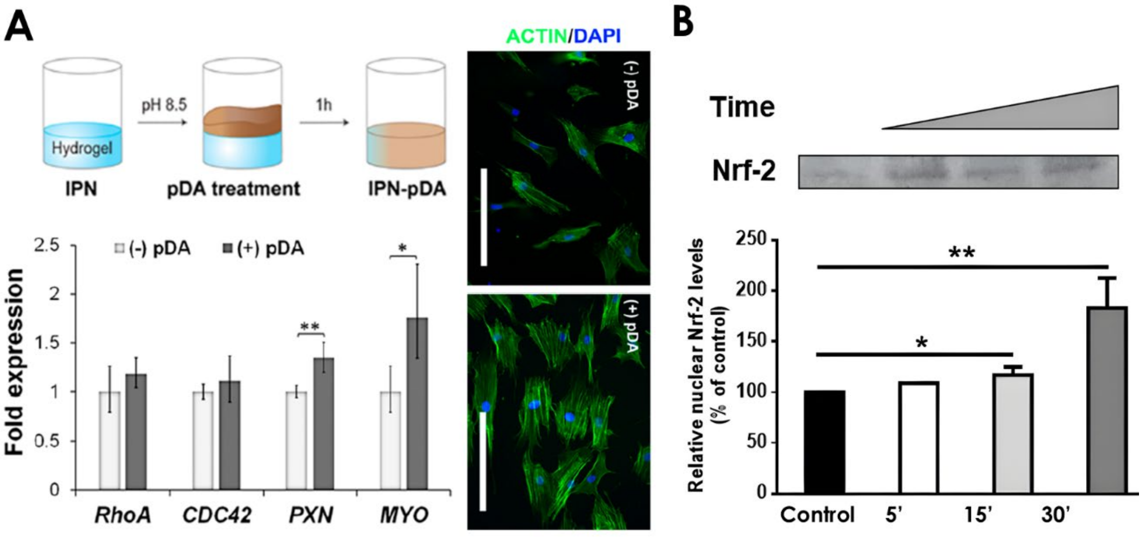

Figure 1.12. Influence of catechols in cell adhesion and metabolism regulation. A) Increased expression of proteins associated with cytoskeletal dynamics and adhesion in cells cultured on a dopamine-coated substrate, evidenced by a stronger fluorescent signal from actin fibers. **B)** Time-dependent increase in NRF2 expression in keratinocytes following the exposure to a melanin-based polymer. Adapted from [40] and [43], respectively.

As discussed in the following section, the widespread sources of phenolic-compounds in nature—particularly in our diet—provides additional indirect evidence of their biocompatibility, as humans are constantly exposed to them and benefit from their antioxidant properties.

1.3 Sources of polyphenols in the nature

Phenols are organic compounds naturally produced by microorganisms, animals and especially in plants.[44] They play a crucial role in ecosystems by contributing to key biochemical functions, enhancing resilience, and supporting ecological processes.

1.3.1 Phenolic compounds in the plant kingdom

In the plant kingdom, these compounds are vital for plant growth, defense, and adaptation, in addition to their importance as dietary sources for humans.

1.3.1.1 Foods rich in phenolic compounds and their role as antioxidants

Among various food sources, plant-based foods are particularly rich in phenolic compounds. Among the different subclasses of polyphenols, phenolic acids (such as chlorogenic, ferulic and caffeic acid) and flavonoids (such as quercetin, catechins and anthocyanins) are the primary sources in our diet (**Figure 1.13**). The foods with the highest content include a wide variety of fruits (e.g., berries, apples), nuts (e.g., almonds, hazelnuts), cereals (e.g., oat, wheat), spices (e.g., cinnamon, turmeric) and especially tea and coffee. [2,45,46]

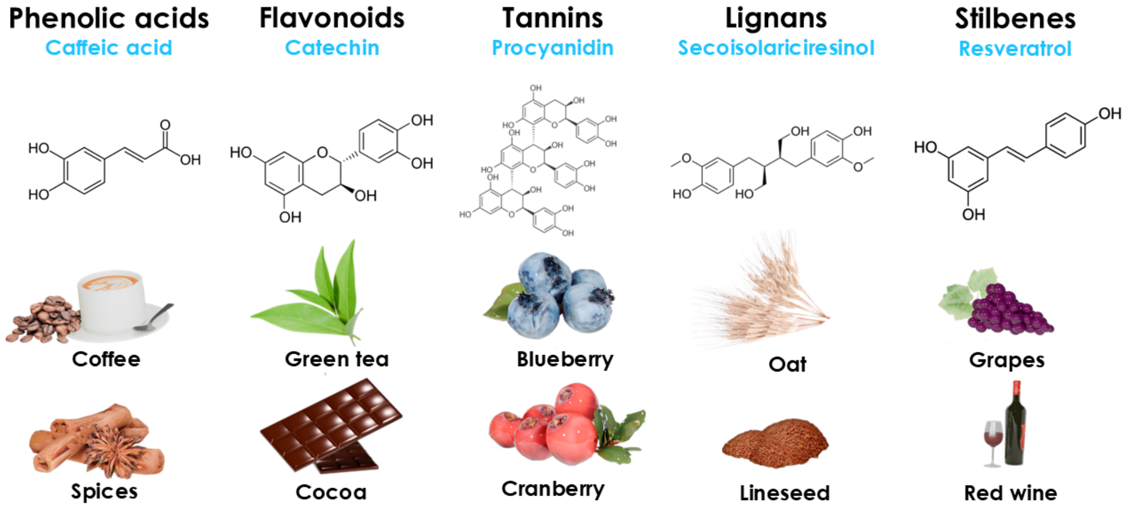

Figure 1.13. Sources of different dietary polyphenols in base on their classification.

Several clinical trials have highlighted the benefits of polyphenol-rich supplements in humans, particularly their role as antioxidants. For instance, healthy participants with a poor plant-based diet showed an increase in oxidative and inflammatory biomarkers related to cardiovascular diseases.[47] Similarly, in another study with post-operative hysterectomy patients, a relief in the symptoms and considerable reduction in oxidative stress markers, linked to an increased antioxidant capacity, was achieved.[48] The supplementation of these molecules has been demonstrated to be beneficial even for both physical and mental health, confirming their importance in the human diet.[49]

Another indirect benefit of a polyphenol-rich diet is the enhancement of beneficial gut microbiota, inducing for instance an increase in Lactobacillus levels.[50] Moreover, a positive correlation between the dietary intake of certain aliments and the phenolic composition of breast milk has been observed, especially between tea and epicatechin, coffee and caffeic acid, and legumes and daidzein.[51]

1.3.1.2 Phenols in plant physiology and defense mechanisms

Phenols comprise a diverse group of secondary metabolites that are essential for plant physiology, supporting growth and development. The biosynthesis of most of these molecules is initiated by the aminoacid phenylalanine, which enters the phenylpropanoid pathway and leads to more complex molecules.[52,53] For instance, lignins confer structural integrity, particularly in vascular tissues, and flavonoids play an important role in plant development, maintaining the apical-basal axis (cytokine-auxin) and enhancing metal absorption.[54,55] Anthocyanins, found in flowers and mature fruits, are crucial for enhancing pollination.[56]

However, phenolic compounds in plants are primarily recognized as a key factor in response mechanisms to stresses. Counteracting both biotic factors, such as herbivory and pathogens attack, as well as abiotic challenges, like adverse environmental conditions is fundamental for plant survival due to their sessile nature (**Figure 1.14**). For instance, lignin accumulation confers

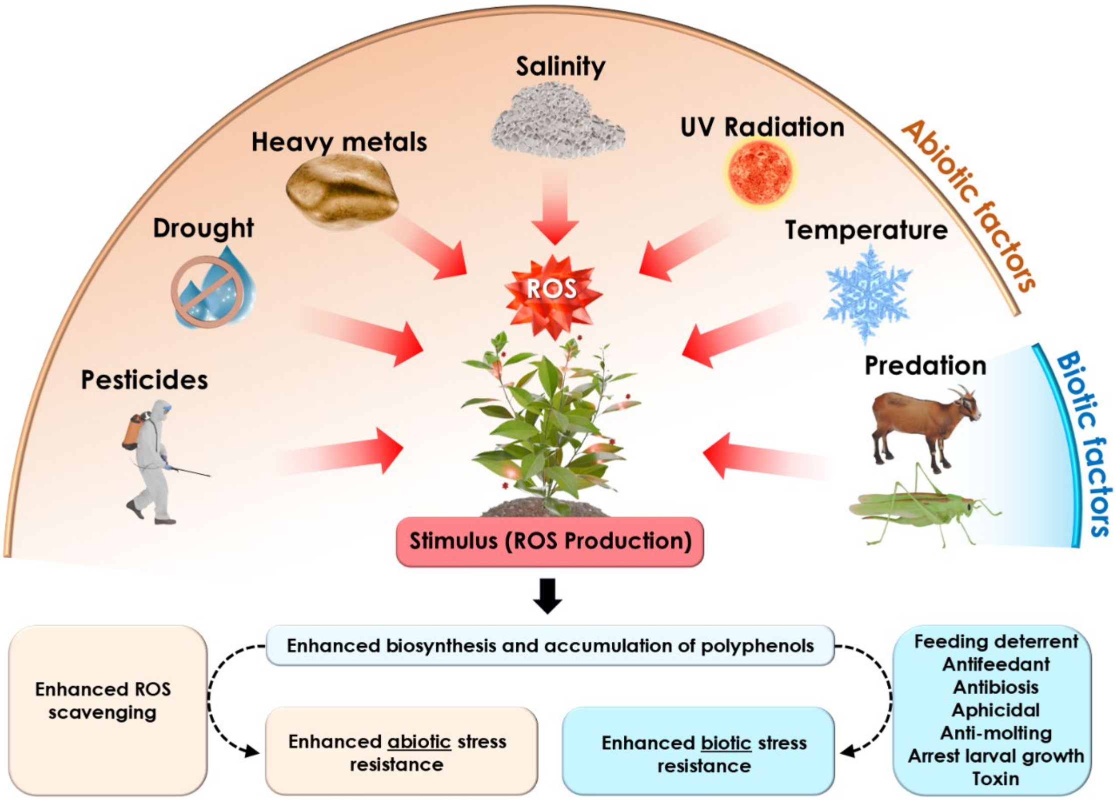

Figure 1.14. Plant response toward biotic and abiotic stresses. Schematic representation of various stress sources in plants, whose exposure induces ROS production. This stimulus enhances the polyphenol biosynthesis, strengthening resistance to abiotic stress (as ROS scavengers) and biotic stress (as antifeedants and toxins). Adapted from [53].

drought and salinity tolerance due to its natural hydrophobicity,[57] in addition to pathogenic resistance.[56] Similarly, the antioxidant properties of flavonoids can mitigate stress produced by various factors (e.g., salinity, UV exposure, drought and pathogens, among others), counteracting the generated ROS.[52,58,59] Salicylic acid can act as a phytohormone, triggering the systemic acquired defense of the plant once activated.[60] Additionally, other molecules like coumarins, tannins and anthocyanins discourage herbivores and insects due to their toxicity and bitter taste rather than conferring metabolic protection.[53,56,60]

1.3.2 Phenolic compounds in the animal kingdom

Despite phenolic compounds are predominantly found in plants, there are specific forms exclusively synthetized in animals. Unlike plants, these polyphenols tend to have a similar structure, usually made of resembling monomers. The most representative examples include dopamine, melanin and DOPA-derived compounds (**Figure 1.15**).[43,61]

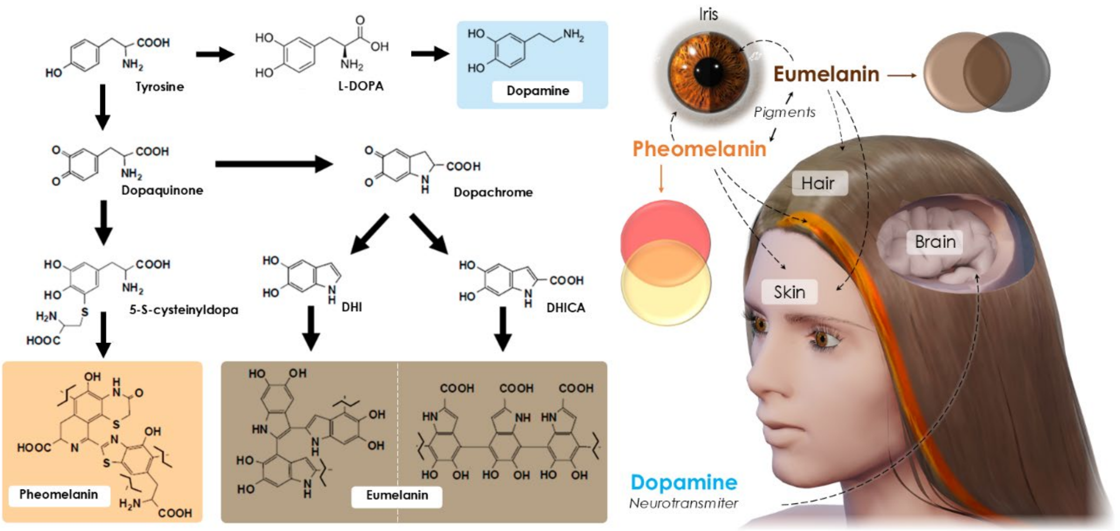

Figure 1.15. Simplified biosynthesis pathways leading to dopamine, eumelanin and pheomelanin. Adapted from [43].

Dopamine is an essential neurotransmitter used in signaling within the nervous system of vertebrates and as a precursor of the hormones noradrenaline and adrenaline.[62] Melanin also plays a significant role in biological functions, functioning both as pigmentation and UV protection for DNA. Particularly, eumelanin and pheomelanin confer colors from brown to black and reddish to yellowish colors, respectively.[42] Similarly, DOPA (3,4-dihydroxyphenylalanine) plays a fundamental role in marine bivalves, such as mussels, being the key component of the byssal threads, which enable their adhesion under harsh and wet conditions.[63] Also, DOPA levels have been correlated with antioxidant activity.[64] Furthermore, polyphenols also have other mechanical and structural roles. For example, in insects, molecules like N-acetyldopamine and N-β-alanyldopamine play key roles in the sclerotization or hardening of the cuticle.[65,66]

1.3.3 Industrial processes as source of polyphenols

A wide range of polyphenols can be obtained from industrial processes, either as desirable end products during fermentation or as by-products/waste in other processes. For example, in the winemaking industry, desired phenolic-compounds like catechins and phenolic acids are obtained.[67] On the contrary many industries generate polyphenol-rich residues as byproducts, which can be recovered, purified and used for different applications. For instance, the black liquor (ligning extract) obtained during the paper manufacturing can be converted to phenol-rich oil through thermal processes.[68] In agriculture, husks, brans and germs from cereals like rice can be processed to obtain these phenol rich-extracts (**Figure 1.16**),[69] similar to the process used for olive mill wastewater.[70]

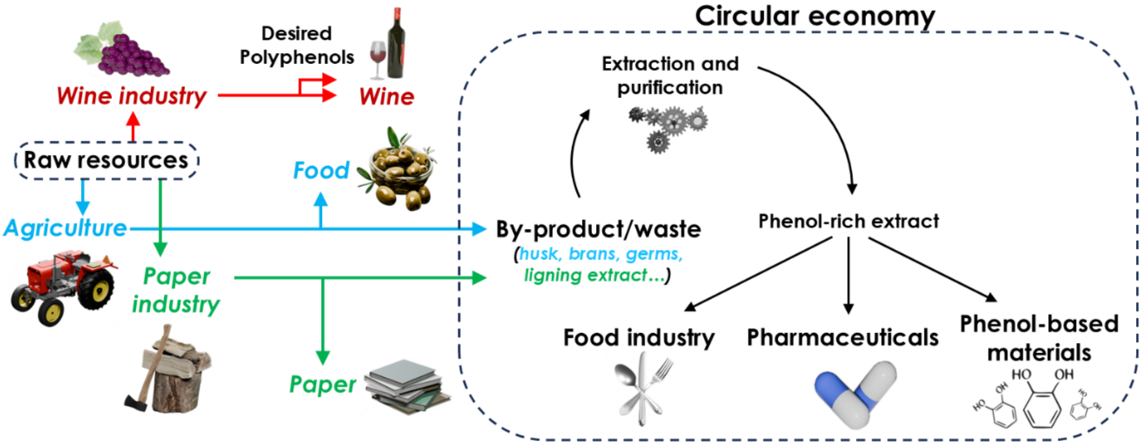

Figure 1.16. Examples of the polyphenols as desired or by-products in the industry and their circular economy.

Although the optimization of these techniques remains a work in progress, the extraction of purified phenolic compounds from byproducts represents a valuable advancement towards a circular economy.[71] These compounds hold significant potential for diverse applications, including the food industry, pharmaceuticals, and, in our case, the development of polyphenol-based materials.

1.4 Catechol-based materials

In the past decade, the previously described outstanding and versatile properties of catechols have attracted significant attention from materials science researchers, being a promising component in the development of new materials to tackle complex challenges. The use of catechols and polyphenol-based compounds has essentially led to the development of materials with improved adhesion, performance, durability, biocompatibility and versatility for further functionalization. Due to these exceptional features, which are crucial in biomedical applications, there has been growing interest in the development of materials to address unmet clinical needs. Among these catechol-based materials, particular attention is given to nanoparticles, hydrogels, bioadhesives, coatings and membranes (**Figure 1.17**). The latest advances on these materials are discussed in this section.

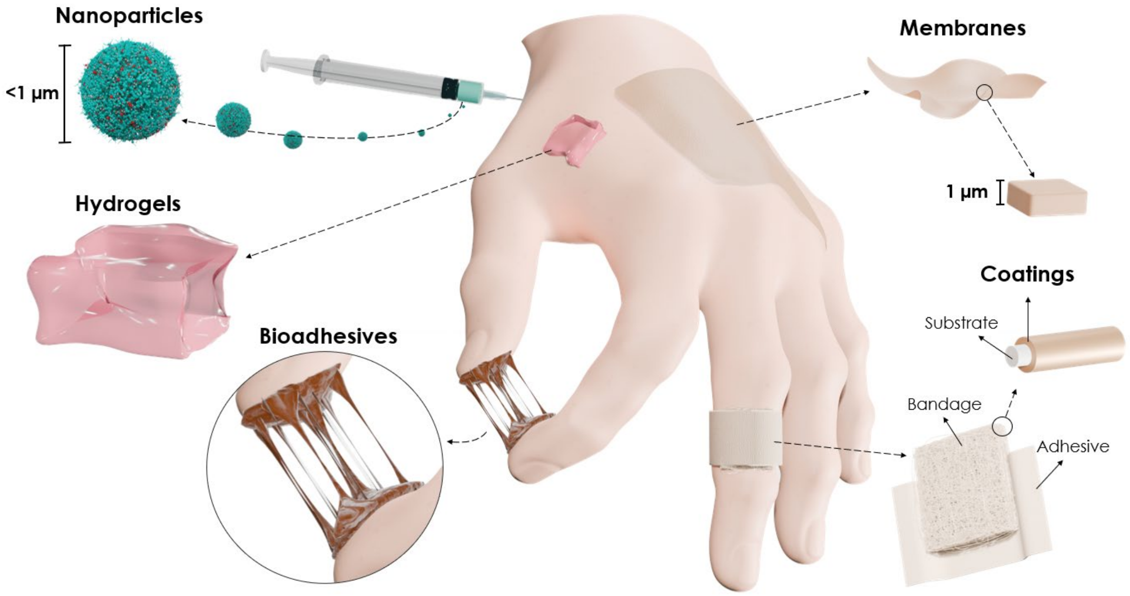

Figure 1.17. Catechol-based materials. Schematic representation of different types of materials that can be synthetized using catechols for biomedical applications, highlighting the nanoparticles, hydrogels, bioadhesives, coatings and membranes.

1.4.1 Nanoparticles

One of the most studied approaches for nanoparticle formation has been based on the inherent ability of dopamine to self-polymerize. The resulting PDA-based nanoparticles can be further functionalized to endow them with additional properties.[72] Moreover, the ability of catechol moieties to establish coordination bonding with metals has allowed for the formation of a family of nanoparticles called metal-phenolic network particles or nanoscale coordination polymers.[73] The inclusion of metal ions such as Fe^{3+} and Cu^{2+} has enabled the design of systems with different uses, such as contrast agents.[74] This ability has also been used by our research group for different applications, such as the delivery of active drugs for cancer, including platinum (IV) (**Figure 1.18A**) [75,76,77] and ruthenium complexes,[78] the local delivery of dopamine for Parkinson disease,[79] or even for imaging.[80]

1.4.2 Hydrogels

Hydrogels are 3D networks of crosslinked hydrophilic polymers. In the case of biological applications, they are designed to mimic the extracellular matrix of soft tissues. Their permeable structure, water content, composition and functional activity can be finely tuned, making them highly promising for biomedical applications.[81]

Catechol moieties and polyphenols can endow hydrogels with enhanced properties such as improved hydrophilicity, adhesion in wet conditions, biocompatibility and ability to interact with a broad range of molecules, allowing for further functionalization. Therefore, catechol-based hydrogels have been used for regenerative medicine, tissue engineering, sustained drug release, antimicrobial activity and tissue adhesion, among other applications.[82] Among polyphenols, dopamine is the most commonly chosen molecule for synthesizing hydrogels (**Figure 1.18B**).[83,84] Nevertheless, other polyphenols such as epigallocatechin gallate (a flavonoid) and tannic acid (a tannin), have also been used in the synthesis of hydrogels.[85]

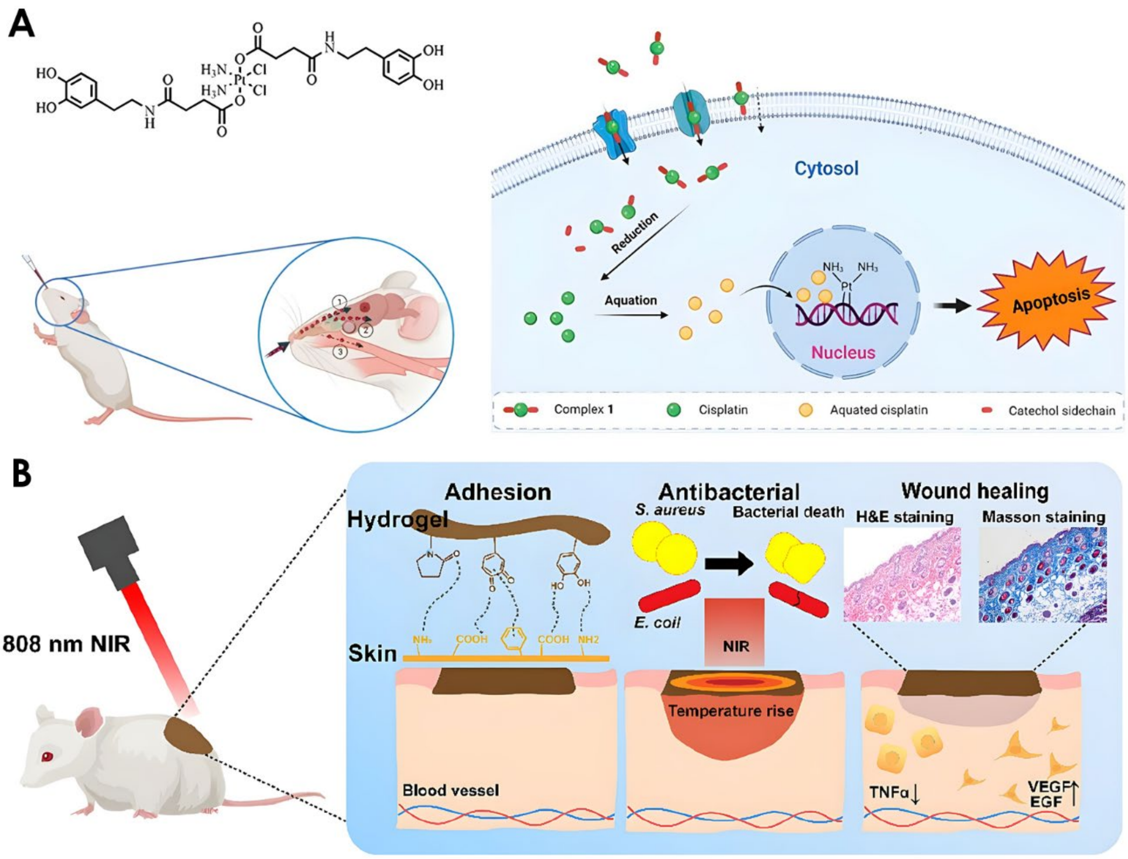

Figure 1.18. Catechol-based nanoparticles and hydrogels. A) Representation of intranasal administration of dopamine-cisplatin complex nanoparticles for cancer treatment, triggering apoptosis in the cells that uptake them. **B)** Scheme of the application of a dopamine-based hydrogel, activating antibacterial properties in response to temperature rise and enhancing wound healing. Adapted from [75] and [84], respectively.

1.4.3 Bioadhesives

Bioadhesives can function as surgical glue, keeping the tissues attached until completely healed, as well as being a sealant to prevent bleeding or fluid leakage. This suture-free method can fasten the healing process and provide improved aesthetic outcome.[86] Unlike hydrogels, bioadhesives require a lower water retention in order to achieve better cohesion between their polymeric network (e.g., fibrin, collagen, albumin, chitosan, polyethylene glycol) and adhesion towards the surfaces. When functionalized with dopamine or other polyphenols, these bioadhesives can significantly improve hydrogen bonding, hydrophilicity and wet adhesion.[87]

Dopamine-based bioadhesives have shown promising results as bone adhesives (**Figure 1.19A**) [88] and, especially, as hemostatic sealants, allowing for pre-shaping [89] or direct application to wounds, [90] similar to other polyphenols, like tannic acid.[91]

1.4.4 Coatings

The remarkable adhesive properties of catechols (allowing them to adhere virtually any surface) have inspired researchers to develop a variety of coatings for different applications in materials science, such as antibacterial, antifouling, hydrophilicity modulation and biocompatibility, among others.[92] Dopamine is the most widely used catechol in coatings, and has been extensively studied for nearly two decades as PDA deposited on different surfaces.[10] Among several applications, dopamine-based coatings have been primarily used to obtain antimicrobial wound dressings (**Figure 1.19B**),[93] the fabrication of biosensors,[94] enhancement of the hemocompatibility of medical devices, like catheters,[95] or the osteointegration of implants. [96]In addition, other catechols, such as caffeic acid, have also been employed to enhance the osteointegration when copolymerized with other molecules on titanium implants.[97]

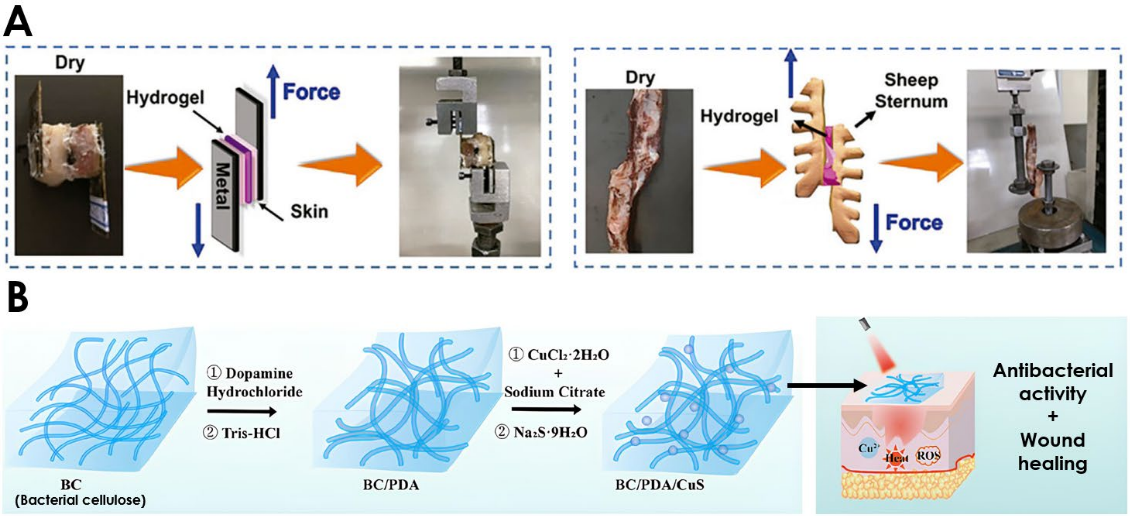

Figure 1.19. Catechol-based bioadhesives and coatings. A) *In vitro* adhesive strength evaluation of a dopamine-based adhesives in contact with skin and bone tissue. **B)** Schematic representation of a PDA/CuS coating on bacterial cellulose for an accelerated wound healing thanks to its antibacterial activity. Adapted from [[88]] and [[93]], respectively.

1.4.5 Membranes

Catechol-based materials can also be obtained as free-standing films or membranes. Unlike coatings (which are directly generated on a given substrate, from which cannot be detached once formed), membranes are obtained without the presence of a support and can be later manipulated, offering a significant advantage for biomedical applications. For the formation of these membranes, catechols are typically co-diluted with amine-rich molecules in the same solution, forming a crosslinked polymer. This mixture allows for the establishment of strong bonds in the air-liquid or liquid-liquid interphase, resulting in a floating free-standing membrane.

In the literature, there are few examples describing the ability to develop a free-standing film using a variety of molecules for the crosslinking with catechols. Yang and colleagues utilized dopamine as the catechol source (to form PDA) and polyethyleneimine (PEI) for crosslinking, successfully obtaining a free-standing film at the air/water interface with Janus faces (**Figure 1.210A**).[98] In the same line, Hong *et al.* used also polydopamine and PEI for the development of membranes under similar conditions (**Figure 1.20B**).[99]

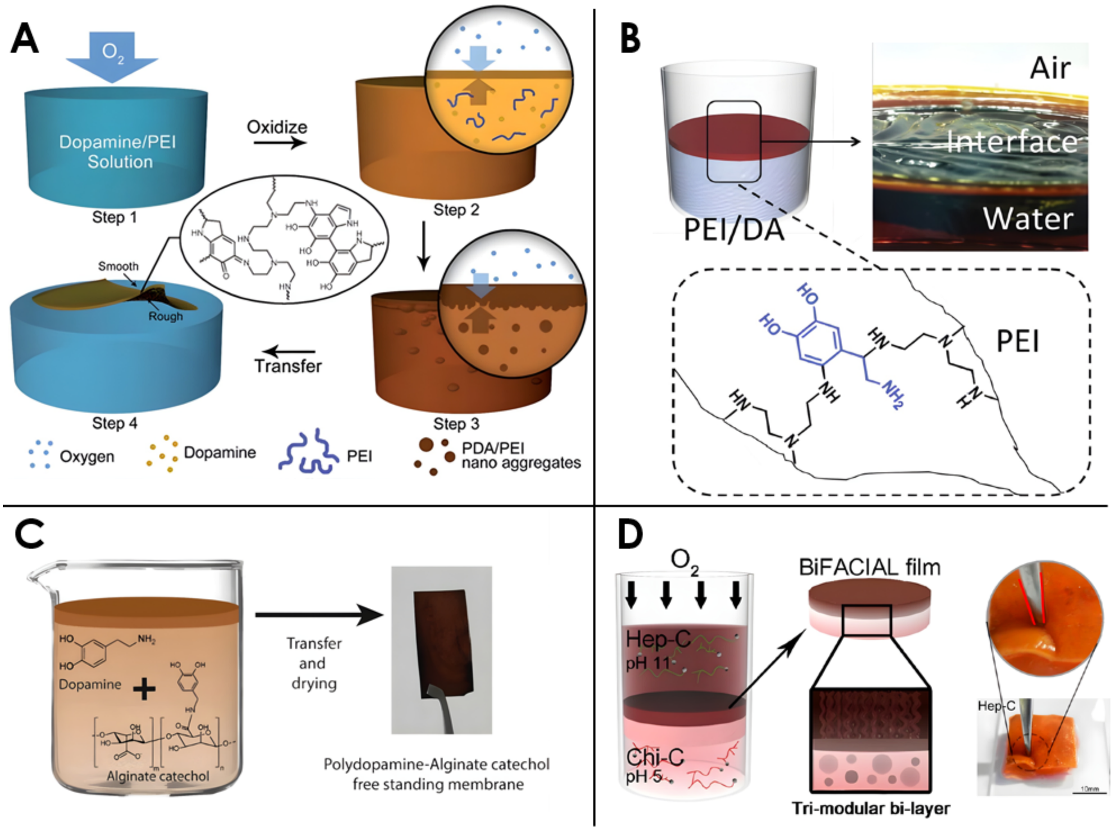

Figure 1.20. Catechol-based membranes. Schematic representation of the synthesis and composition of dopamine-based membranes using as crosslinker **A-B)** polyethyleneimine (PEI), **C)** alginate or **D)** chitosan and heparin. Adapted from [98], [99], [100] and [101], respectively.

Other studies have managed to develop free-standing membranes using different materials for crosslinking. For instance, a film with PDA and pyrocatechol-enriched alginate was formed in the air/water interface after 24 h (**Figure 1.20C**).[100] Other membranes have also been obtained in the liquid-liquid interface using solutions of heparin-dopamine and chitosan-dopamine (**Figure 1.20D**). However, given that the resulting structure achieved a thickness on the millimeter scale, it cannot be classified as a thin film.[101] More complex methodologies, such as layer-by-layer assembly (which requires a substrate that is later released), have been used to obtain these membranes by mixing enriched-dopamine polyacrylic acid, polyvinylpyrrolidone and dopamine. Nevertheless, despite offering a high degree of control over subsequent modifications, this approach required multiple steps, components and specific conditions.[102]

It is worth to mention that all these examples are based on dopamine, which has the ability to self-polymerize under oxidizing conditions. The fragility and weakness of the obtained PDA films can be are improved by incorporating molecules such as PEI, chitosan, alginate or xanthan gum, which provide crosslinking and robustness to the system. Notably, some of these molecules can form *in situ* substrates on their owns, thereby reducing the reliance on catechols and shifting their role from a central component to a more auxiliary function in the material synthesis.[103,104] Additionally, since this strategy is only limited to dopamine, it is necessary to find new mechanisms and strategies in order to obtain free-standing films from other catechol derivatives. This challenge has been addressed throughout the execution of this Thesis.

1.5 Scope of this thesis

During this first Chapter, a comprehensive introduction to catechols, their properties, sources and applications has been discussed. This information underscores the relevance and utility of catechols and polyphenolic compounds in various fields, particularly in medicine and materials science. Notably, it emphasizes the crucial role of these molecules in the development of biomaterials for health applications, demonstrating their potential at the intersection of these disciplines. This thesis aimed to face the main challenges previously described, by the collaboration between the **Nanostructured Functional Materials** research group at the Catalan Institute of nanoscience and Nanotechnology (ICN2) and the **Cell Death, Senescence and Survival** research group at the Neuroscience Institute (INc-UAB). The convergence of their knowledge and expertise in materials and medicine has been fundamental for the development and shaping of this multidisciplinary Thesis.

As thoroughly explained in the previous sections, polyphenols—particularly catechols—exhibit a versatile redox ability, which has been widely exploited in different catechol-based materials. Among the numerous promising applications of these biomaterials, this Thesis has been focused on two key areas of notable relevance: **antimicrobial resistance** (Chapter 3) and **cancer treatment** (Chapter 4).

Interestingly, both research areas are closely related, not in their final application, but due to their catechol-amine based approach, features and mechanism of action. This parallel development throughout the Thesis enhanced data acquisition, optimized methodologies, strengthened evidences and reinforced the final conclusions. The overall structure of this Thesis and the interrelation within its Chapters is described in **Figure 1.21**.

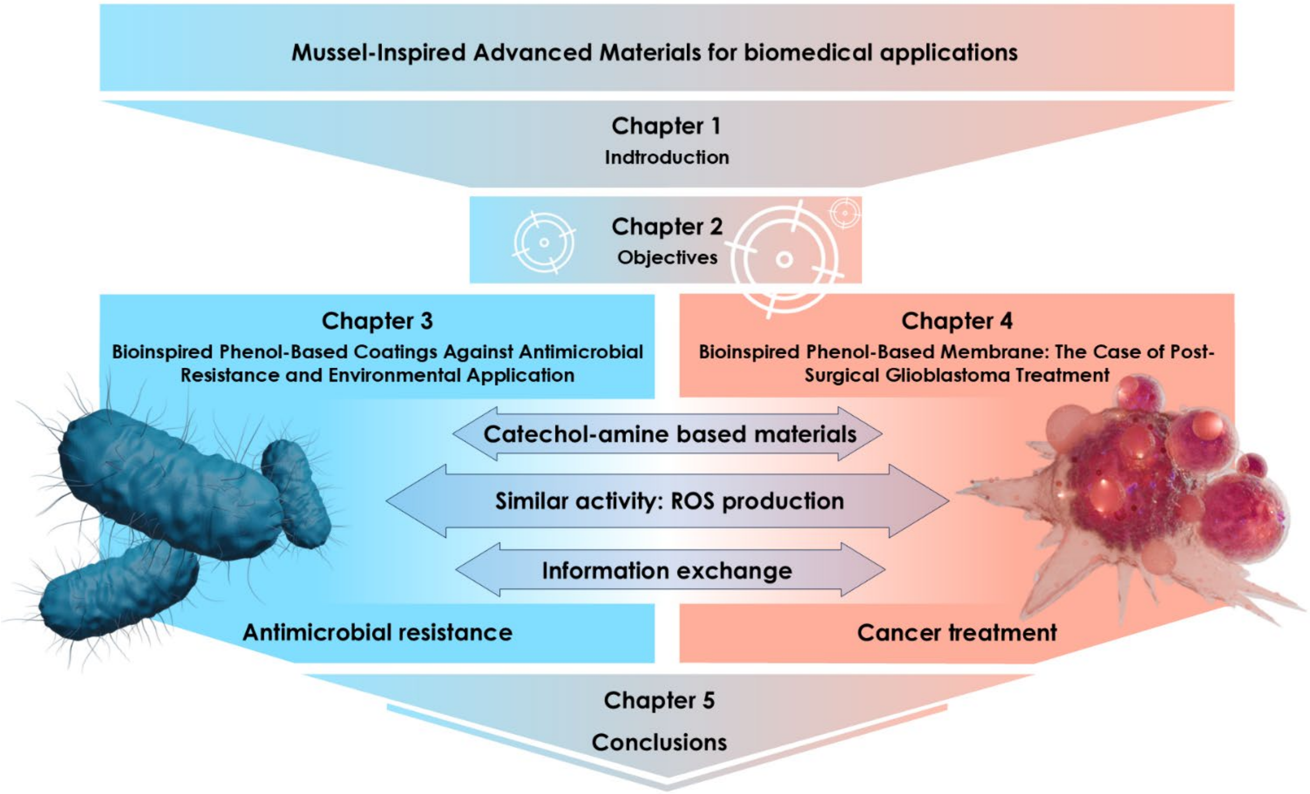

Figure 1.21. Overall structure of this thesis. Both Chapter 3 and 4, while exploring different applications and approaches, shares the same material composition and a similar activity based on ROS production. This consistency facilitated the exchange of information between chapters, thus reinforcing the overall cohesion of the thesis.

1.6 References

[1] Curieses, C. M..; Pérez, J. M.; Andrés, C.; Plou, F. J.; Pérez-Lebeña, E. *Processes* **2023**, *11*, 2771. https://doi.org/10.3390/pr11092771

[2] Li, W.; Chen, H.; Xu, B.; Wang, Y.; Zhang, C.; Cao, Y.; Xing, X. *Journal Of Future Foods* **2023**, *3*, 289-305. https://doi.org/10.1016/j.jfutfo.2023.03.001

[3] Barros, N. R.; Chen, Y.; Hosseini, V.; Wang, W.; Nasiri, R.; Mahmoodi, M.; Yalcintas, E. P.; Haghniaz, R.; Mecwan, M. M.; Karamikamkar, S.; Dai, W.; Sarabi, S. A.; Falcone, N.; Young, P.; Zhu, Y.; Sun, W.; Zhang, S.; Lee, J.; Lee, K.; et. al. *Biomaterials Science* **2021**, *9*, 6653-6672. https://doi.org/10.1039/d1bm01126j

[4] Waite, J. H.; Tanzer, M. L. *Science* **1981**, *212*, 1038-1040. https://doi.org/10.1126/science.212.4498.1038

[5] Young, G. A; Crisp, D.J. *Applied Science Publishers* **1982**, 19–39

[6] Lin, Q.; Gourdon, D.; Sun, C.; Holten-Andersen, N.; Anderson, T. H.; Waite, J. H.; Israelachvili, J. N. *Proceedings Of The National Academy Of Sciences* **2007**, *104*, 3782-3786. https://doi.org/10.1073/pnas.0607852104

[7] Balkenende, D. W.; Winkler, S. M.; Messersmith, P. B. *European Polymer Journal* **2019**, *116*, 134-143. https://doi.org/10.1016/j.eurpolymj.2019.03.059

[8] DeMartini, D. G.; Errico, J. M.; Sjoestroem, S.; Fenster, A.; Waite, J. H. *Journal Of The Royal Society Interface* **2017**, *14,* 0151. https://doi.org/10.1098/rsif.2017.0151

[9] Lee, H.; Scherer, N. F.; Messersmith, P. B. *Proceedings Of The National Academy Of Sciences* **2006**, *103*, 12999-13003. https://doi.org/10.1073/pnas.0605552103

[10] Lee, H.; Dellatore, S. M.; Miller, W. M.; Messersmith, P. B. *Science* **2007**, *318*, 426-430. https://doi.org/10.1126/science.1147241

[11] Saiz-Poseu, J.; Mancebo-Aracil, J.; Nador, F.; Busqué, F.; Ruiz-Molina, D. *Angewandte Chemie* **2018**, *131*, 706-725. https://doi.org/10.1002/ange.201801063

[12] Pinnataip, R.; Lee, B. P. *ACS Omega* **2021**, *6*, 5113-5118. https://doi.org/10.1021/acsomega.1c00006

[13] Belščak-Cvitanović, A.; Durgo, K.; Huđek, A.; Bačun-Družina, V.; Komes, D. *Polyphenols: Properties, Recovery, and Applications* **2018**, 3-44. https://doi.org/10.1016/b978-0-12-813572-3.00001-4

[14] Zhang, X.; Li, Z.; Yang, P.; Duan, G.; Liu, X.; Gu, Z.; Li, Y. *Materials Horizons* **2020**, *8*, 145-167. https://doi.org/10.1039/d0mh01317j

[15] Zhang, W.; Wang, R.; Sun, Z.; Zhu, X.; Zhao, Q.; Zhang, T.; Cholewinski, A.; Yang, F.; Zhao, B.; Pinnaratip, R.; Forooshani, P. K.; Lee, B. P. *Chemical Society Reviews* **2020**, *49*, 433-464. https://doi.org/10.1039/c9cs00285e

[16] Singh, I.; Dhawan, G.; Gupta, S.; Kumar, P. *Frontiers In Microbiology* **2021**, *11*, 607099. https://doi.org/10.3389/fmicb.2020.607099

[17] Kumar, N.; Goel, N. *Biotechnology Reports* **2019**, *24*, e00370. https://doi.org/10.1016/j.btre.2019.e00370

[18] Ryu, J.; Ku, S. H.; Lee, H.; Park, C. B. *Advanced Functional Materials* **2010**, *20*, 2132-2139. https://doi.org/10.1002/adfm.200902347

[19] Tsai, W.; Chen, W.; Chien, H.; Kuo, W.; Wang, M. *Acta Biomaterialia* **2011**, *7*, 4187-4194. https://doi.org/10.1016/j.actbio.2011.07.024

[20] Mian, S. A.; Yang, L.; Saha, L. C.; Ahmed, E.; Ajmal, M.; Ganz, E. *Langmuir* **2014**, *30*, 6906-6914. https://doi.org/10.1021/la500800f

[21] Lee, S. J.; Lee, D.; Yoon, T. R.; Kim, H. K.; Jo, H. H.; Park, J. S.; Lee, J. H.; Kim, W. D.; Kwon, I. K.; Park, S. A. *Acta Biomaterialia* **2016**, *40*, 182-191. https://doi.org/10.1016/j.actbio.2016.02.006

[22] Yang, H.; Liao, K.; Huang, H.; Wu, Q.; Wan, L.; Xu, Z. *Journal Of Materials Chemistry A* **2014**, *2*, 10225-10230. https://doi.org/10.1039/c4ta00143e

[23] Huang, L.; Zhao, S.; Wang, Z.; Wu, J.; Wang, J.; Wang, S. *Journal Of Membrane Science* **2015**, *499*, 269-281. https://doi.org/10.1016/j.memsci.2015.10.055

[24] Saiz-Poseu, J.; Sedó, J.; García, B.; Benaiges, C.; Parella, T.; Alibés, R.; Hernando, J.; Busqué, F.; Ruiz-Molina, D. *Advanced Materials* **2013**, *25*, 2066-2070. https://doi.org/10.1002/adma.201204383

[25] Davis, M. R.; Dougherty, D. A. *Physical Chemistry Chemical Physics* **2015**, 17, 29262-29270. https://doi.org/10.1039/c5cp04668h

[26] Wu, Y.; Zeng, L.; Zhao, S. *Biomolecules* **2021**, *11*, 936. https://doi.org/10.3390/biom11070936

[27] Li, S.; Chu, L.; Gong, X.; Diebold, U. *Science* **2010**, *328*, 882-884. https://doi.org/10.1126/science.1188328

[28] Zhang, T.; Wojtal, P.; Rubel, O.; Zhitomirsky, I. *RSC Advances* **2015**, *5*, 106877-106885. https://doi.org/10.1039/c5ra21511k

[29] Sedó, J.; Saiz-Poseu, J.; Busqué, F.; Ruiz-Molina, D. *Advanced Materials* **2012**, *25*, 653-701. https://doi.org/10.1002/adma.201202343

[30] Suárez-García, S.; Sedó, J.; Saiz-Poseu, J.; Ruiz-Molina, D. *Biomimetics* **2017**, *2*, 22. https://doi.org/10.3390/biomimetics2040022

[31] Forooshani, P. K.; Pinnaratip, R.; Polega, E.; Tyo, A. G.; Pearson, E.; Liu, B.; Folayan, T.; Pan, L.; Rajachar, R. M.; Heldt, C. L.; Lee, B. P. *Chemistry Of Materials* **2020**, *32*, 8182-8194. https://doi.org/10.1021/acs.chemmater.0c01551

[32] Theofanous, A.; Deligiannakis, Y.; Louloudi, M. *Langmuir* **2024**, *40*, 26412-26424. https://doi.org/10.1021/acs.langmuir.4c02760

[33] Salomäki, M.; Marttila, L.; Kivelä, H.; Ouvinen, T.; Lukkari, J. *The Journal Of Physical Chemistry B* **2018**, *122*, 6314-6327. https://doi.org/10.1021/acs.jpcb.8b02304

[34] Perron, N. R.; Brumaghim, J. L. *Cell Biochemistry And Biophysics* **2009**, *53*, 75-100. https://doi.org/10.1007/s12013-009-9043-x

[35] An, Z.; Sun, J.; Mei, Q.; Wei, B.; Li, M.; Xie, J.; He, M.; Wang, Q. *Journal Of Environmental Sciences* **2021**, *115*, 392-402. https://doi.org/10.1016/j.jes.2021.08.011

[36] Cheng, I. F.; Breen, K. *BioMetals* **2000**, *13*, 77-83. https://doi.org/10.1023/a:1009229429250

[37] Perron, N. R.; Hodges, J. N.; Jenkins, M.; Brumaghim, J. L. *Inorganic Chemistry* **2008**, *47*, 6153-6161. https://doi.org/10.1021/ic7022727

[38] Contreras-Pereda, N.; Suárez-García, S.; Pfattner, R.; Ruiz-Molina, D. *Materials Today Chemistry* **2023**, *35*, 101855. https://doi.org/10.1016/j.mtchem.2023.101855

[39] Su, R.; Yan, H.; Li, P.; Zhang, B.; Zhang, Y.; Su, W. *Photodiagnosis And Photodynamic Therapy* **2021**, *35*, 102417. https://doi.org/10.1016/j.pdpdt.2021.102417

[40] Pacelli, S.; Paolicelli, P.; Petralito, S.; Subham, S.; Gilmore, D.; Varani, G.; Yang, G.; Lin, D.; Casadei, M. A.; Paul, A. *ACS Applied Bio Materials* **2020**, *3*, 945-951. https://doi.org/10.1021/acsabm.9b00989

[41] Hu, Y.; Zhou, H.; Liu, T.; Yang, M.; Zhang, Q.; Pan, C.; Lin, J. *Frontiers In Bioengineering And Biotechnology* **2022**, *10*, 884258. https://doi.org/10.3389/fbioe.2022.884258

[42] Solano, F. *New Journal Of Science* **2014**, 1-28. https://doi.org/10.1155/2014/498276

[43] Liberti, D.; Alfieri, M. L.; Monti, D. M.; Panzella, L.; Napolitano, A. *Antioxidants* **2020**, *9*, 270. https://doi.org/10.3390/antiox9040270

[44] Di Lorenzo, C.; Colombo, F.; Biella, S.; Stockley, C.; Restani, P. *Nutrients* **2021**, *13*, 273. https://doi.org/10.3390/nu13010273

[45] Coletro, H. N.; Bressan, J.; Diniz, A. P.; Hermsdorff, H. H. M.; Pimenta, A. M.; Meireles, A. L.; De Deus Mendonça, R.; Carraro, J. C. C. *International Journal Of Food Sciences And Nutrition* **2023**, *74*, 338-349. https://doi.org/10.1080/09637486.2023.2190058

[46] Carnauba, R. A.; Hassimotto, N. M. A.; Lajolo, F. M. *British Journal Of Nutrition* **2020**, *126*, 441-448. https://doi.org/10.1017/s0007114520004237

[47] Arcusa, R.; Carrillo, J. Á.; Xandri-Martínez, R.; Cerdá, B.; Villaño, D.; Marhuenda, J.; Zafrilla, M. P. *Molecules* **2021**, *26*, 3604. https://doi.org/10.3390/molecules26123604

[48] Ferianec, V.; Fülöp, M.; Ježovičová, M.; Radošinská, J.; Husseinová, M.; Feriancová, M.; Radošinská, D.; Barančík, M.; Muchová, J.; Högger, P.; Ďuračková, Z. *Nutrients* **2020**, *12*, 913. https://doi.org/10.3390/nu12040913

[49] Romain, C.; Chung, L. H.; Marín-Cascales, E.; Rubio-Arias, J. A.; Gaillet, S.; Laurent, C.; Morillas-Ruiz, J. M.; Martínez-Rodriguez, A.; Alcaraz, P. E.; Cases, J. *Nutrients* **2021**, *13*, 492. https://doi.org/10.3390/nu13020492

[50] Gutiérrez-Díaz, I.; Salazar, N.; Pérez-Jiménez, J.; De los Reyes-Gavilán, C. G.; Gueimonde, M.; González, S. *European Journal Of Nutrition* **2020**, *60*, 1403-1413. https://doi.org/10.1007/s00394-020-02339-5

[51] Lu, Z.; Chan, Y.; Lo, K. K.; Wong, V. W.; Ng, Y.; Li, S.; Ho, W.; Wong, M.; Zhao, D. *Food Function* **2021**, *12*, 12683-12695. https://doi.org/10.1039/d1fo02529e

[52] Sharma, A.; Shahzad, B.; Rehman, A.; Bhardwaj, R.; Landi, M.; Zheng, B. *Molecules* **2019**, *24*, 2452. https://doi.org/10.3390/molecules24132452

[53] Kumar, K.; Debnath, P.; Singh, S.; Kumar, N. *Stresses* **2023**, *3*, 570-585. https://doi.org/10.3390/stresses3030040

[54] Brown, D. E.; Rashotte, A. M.; Murphy, A. S.; Normanly, J.; Tague, B. W.; Peer, W. A.; Taiz, L.; Muday, G. K. *Plant Physiology* **2001**, *126*, 524-535. https://doi.org/10.1104/pp.126.2.524

[55] Kurepa, J.; Shull, T. E.; Smalle, J. A. *Plants* **2023**, *12*, 517. https://doi.org/10.3390/plants12030517

[56] Kumar, S.; Abedin, M. M.; Singh, A. K.; Das, S. *Plant Phenolics in Sustainable Agriculture* **2020**, 517-532. https://doi.org/10.1007/978-981-15-4890-1_22

[57] Chun, H. J.; Baek, D.; Cho, H. M.; Lee, S. H.; Jin, B. J.; Yun, D.; Hong, Y.; Kim, M. C. *Plant Signaling Behavior* **2019**, *14*, 1625697. https://doi.org/10.1080/15592324.2019.1625697

[58] Pech, R.; Volná, A.; Hunt, L.; Bartas, M.; Červeň, J.; Pečinka, P.; Špunda, V.; Nezval, J. *International Journal Of Molecular Sciences* **2022**, *23*, 6533. https://doi.org/10.3390/ijms23126533

[59] Xue, J.; Qiu, S.; Jia, X.; Shen, S.; Shen, C.; Wang, S.; Xu, P.; Tong, Q.; Lou, Y.; Yang, N.; Cao, J.; Hu, J.; Shen, H.; Zhu, R.; Murray, J. D.; Chen, W.; Yang, Z. *Plant Physiology* **2023**, *193*, 627-642. https://doi.org/10.1093/plphys/kiad313

[60] Singh, S.; Kaur, I.; Kariyat, R. *International Journal Of Molecular Sciences* **2021**, *22*, 1442. https://doi.org/10.3390/ijms22031442

[61] Sugumaran, M.; Barek, H. *International Journal Of Molecular Sciences* **2016**, *17*, 1753. https://doi.org/10.3390/ijms17101753

[62] Franco, R.; Reyes-Resina, I.; Navarro, G. *Biomedicines* **2021**, *9*, 109. https://doi.org/10.3390/biomedicines9020109

[63] Ahn, B. K. *Journal Of The American Chemical Society* **2017**, *139*, 10166-10171. https://doi.org/10.1021/jacs.6b13149

[64] Miller, D. R.; Spahn, J. E.; Waite, J. H. *Journal Of The Royal Society Interface* **2015**, *12*, 20150614. https://doi.org/10.1098/rsif.2015.0614

[65] Nino, M.; Reddivari, L.; Osorio, C.; Kaplan, I.; Liceaga, A. *Journal Of Insects As Food And Feed* **2021**, *7*, 1077-1087. https://doi.org/10.3920/jiff2020.0113

[66] Ito, S.; Sugumaran, M.; Wakamatsu, K. *International Journal Of Molecular Sciences* **2020**, *21*, 6080. https://doi.org/10.3390/ijms21176080

[67] Caridi, A.; Sidari, R.; Giuffrè, A. M.; Pellicanò, T. M.; Sicari, V.; Zappia, C.; Poiana, M. *European Food Research And Technology* **2017**, *243*, 1287-1294. https://doi.org/10.1007/s00217-016-2840-8

[68] Duangkaew, N.; Lacson, C. F. Z.; Grisdanurak, N.; Neramittagapong, S.; De Luna, M. D. G. *Bioresource Technology Reports* **2024**, *25*, 101759. https://doi.org/10.1016/j.biteb.2023.101759

[69] Colombo, R.; Moretto, G.; Barberis, M.; Frosi, I.; Papetti, A. *Antioxidants* **2023**, *13*, 35. https://doi.org/10.3390/antiox13010035

[70] Cuffaro, D.; Bertolini, A.; Bertini, S.; Ricci, C.; Cascone, M. G.; Danti, S.; Saba, A.; Macchia, M.; Digiacomo, M. *Nutrients* **2023**, *15*, 3746. https://doi.org/10.3390/nu15173746

[71] Valle, C.; Grillo, G.; Gaudino, E. C.; Ponsetto, P.; Mazzoli, R.; Bonavita, G.; Vitale, P.; Pessione, E.; Garcia-Moruno, E.; Costantini, A.; Cravotto, G.; Tabasso, S. *ChemSusChem* **2025**, e202402536. https://doi.org/10.1002/cssc.202402536

[72] Wang, Z.; Duan, Y.; Duan, Y. *Journal Of Controlled Release* **2018**, *290*, 56-74. https://doi.org/10.1016/j.jconrel.2018.10.009

[73] Suárez-García, S.; Solórzano, R.; Alibés, R.; Busqué, F.; Novio, F.; Ruiz-Molina, D. *Coordination Chemistry Reviews* **2021**, *441*, 213977. https://doi.org/10.1016/j.ccr.2021.213977

[74] Dai, Q.; Geng, H.; Yu, Q.; Hao, J.; Cui, J. *Theranostics* **2019**, 9, 3170-3190. https://doi.org/10.7150/thno.31847

[75] Mao, X.; Wu, S.; Calero-Pérez, P.; Candiota, A. P.; Alfonso, P.; Bruna, J.; Yuste, V. J.; Lorenzo, J.; Novio, F.; Ruiz-Molina, D. *Cancers* **2022**, *14*, 410. https://doi.org/10.3390/cancers14020410

[76] Mao, X.; Calero-Pérez, P.; Montpeyó, D.; Bruna, J.; Yuste, V. J.; Candiota, A. P.; Lorenzo, J.; Novio, F.; Ruiz-Molina, D. *Nanomaterials* **2022**, *12*, 1221. https://doi.org/10.3390/nano12071221

[77] Gómez-Herrera, R.; Alfonso-Triguero, P.; Mao, X.; Mancebo-Aracil, J.; Montpeyó, D.; Novio, F.; Lorenzo, J.; Ruiz-Molina, D. *Nanotechnology Reviews* **2024**, *13*, 20240118. https://doi.org/10.1515/ntrev-2024-0118

[78] Zhang, J.; Ramu, V.; Zhou, X.; Frias, C.; Ruiz-Molina, D.; Bonnet, S.; Roscini, C.; Novio, F. *Nanomaterials* **2021**, *11*, 3089. https://doi.org/10.3390/nano11113089

[79] García-Pardo, J.; Novio, F.; Nador, F.; Cavaliere, I.; Suárez-García, S.; Lope-Piedrafita, S.; Candiota, A. P.; Romero-Gimenez, J.; Rodríguez-Galván, B.; Bové, J.; Vila, M.; Lorenzo, J.; Ruiz-Molina, D. *ACS Nano* **2021**, *15*, 8592-8609. https://doi.org/10.1021/acsnano.1c00453

[80] Suárez-García, S.; Esposito, T. V. F.; Neufeld-Peters, J.; Bergamo, M.; Yang, H.; Saatchi, K.; Schaffer, P.; Häfeli, U. O.; Ruiz-Molina, D.; Rodríguez-Rodríguez, C.; Novio, F. *ACS Applied Materials Interfaces* **2021**, *13*, 10705-10718. https://doi.org/10.1021/acsami.0c20612

[81] Ma, H.; Qiao, X.; Han, L. *Biomimetics* **2023**, *8*, 128. https://doi.org/10.3390/biomimetics8010128

[82] Quan, W.; Hu, Z.; Liu, H.; Ouyang, Q.; Zhang, D.; Li, S.; Li, P.; Yang, Z. *Molecules* **2019**, *24*, 2586. https://doi.org/10.3390/molecules24142586

[83] Wang, Y.; Zhang, Y.; Yang, Y.; Jin, M.; Huang, S.; Zhuang, Z.; Zhang, T.; Cao, L.; Lin, X.; Chen, J.; Du, Y.; Chen, J.; Tan, W. *Bioactive Materials* **2024**, *35*, 330-345. https://doi.org/10.1016/j.bioactmat.2024.02.010

[84] Ouyang, Y.; Su, X.; Zheng, X.; Zhang, L.; Chen, Z.; Yan, Q.; Qian, Q.; Zhao, J.; Li, P.; Wang, S. *International Journal Of Biological Macromolecules* **2024**, *261*, 129828. https://doi.org/10.1016/j.ijbiomac.2024.129828

[85] Li, Z.; Chen, Z.; Chen, H.; Chen, K.; Tao, W.; Ouyang, X.; Mei, L.; Zeng, X. *Bioactive Materials* **2022**, *17*, 49-70. https://doi.org/10.1016/j.bioactmat.2022.01.038

[86] Zhu, J.; Zhou, H.; Gerhard, E. M.; Zhang, S.; Rodríguez, F. I. P.; Pan, T.; Yang, H.; Lin, Y.; Yang, J.; Cheng, H. *Bioactive Materials* **2022**, *19*, 360-375. https://doi.org/10.1016/j.bioactmat.2022.04.020

[87] Pandey, N.; Soto-Garcia, L. F.; Liao, J.; Zimmern, N. P.; Nguyen, K. T.; Hong, Y. *Biomaterials Science* **2020**, *8*, 1240-1255. https://doi.org/10.1039/c9bm01848d

[88] Shokri, M.; Kharaziha, M.; Tafti, H. A.; Dalili, F.; Aghdam, R. M.; Eslaminejad, M. B. *Advanced Healthcare Materials* **2024**, *13,* 2304349. https://doi.org/10.1002/adhm.202304349

[89] Cheng, F.; Xu, L.; Zhang, X.; He, J.; Huang, Y.; Li, H. *International Journal Of Biological Macromolecules* **2024**, *260*, 129372. https://doi.org/10.1016/j.ijbiomac.2024.129372

[90] Liu, Z.; Ding, Y.; Ding, Y.; Wang, W.; Mao, Z.; Yu, L. *Biomaterials* **2024**, *317*, 123038. https://doi.org/10.1016/j.biomaterials.2024.123038

[91] Zhang, X.; Mu, Y.; Zhao, L.; Hong, Y.; Shen, L. *International Journal Of Biological Macromolecules* **2024**, *270*, 132182. https://doi.org/10.1016/j.ijbiomac.2024.132182

[92] Liu, Y.; Ai, K.; Lu, L. *Chemical Reviews* **2014**, *114*, 5057-5115. https://doi.org/10.1021/cr400407a

[93] Sun, M.; Li, D.; Xi, Y.; Qin, X.; Liao, Y.; Liu, X.; Jia, S.; Xie, Y.; Zhong, C. *International Journal Of Biological Macromolecules* **2024**, *259*, 129033. https://doi.org/10.1016/j.ijbiomac.2023.129033

[94] Zhang, T.; Xu, Z.; Xu, H.; Gu, Y.; Xing, Y.; Yan, X.; Liu, H.; Lu, N.; Song, Y.; Zhang, S.; Zhang, Z.; Yang, M. *Sensors And Actuators B Chemical* **2019**, *288*, 469-475. https://doi.org/10.1016/j.snb.2019.03.027

[95] Gao, Q.; Li, X.; Yu, W.; Jia, F.; Yao, T.; Jin, Q.; Ji, J. *ACS Applied Materials Interfaces* **2019**, *12*, 2999-3010. https://doi.org/10.1021/acsami.9b19335

[96] Xu, K.; Yuan, Z.; Ding, Y.; He, Y.; Li, K.; Lin, C.; Tao, B.; Yang, Y.; Li, X.; Liu, P.; Cai, K. *Applied Materials Today* **2021**, *24*, 101155. https://doi.org/10.1016/j.apmt.2021.101155

[97] Li, D.; Wang, D.; Yang, Y.; Gao, P.; Fan, W.; Zhang, X.; Tang, Y.; Yang, W.; Cai, K. *Advanced Functional Materials* **2023**, *33*. https://doi.org/10.1002/adfm.202212016

[98] Yang, H.; Xu, W.; Du, Y.; Wu, J.; Xu, Z. *RSC Advances* **2014**, *4*, 45415-45418. https://doi.org/10.1039/c4ra04549a

[99] Hong, S.; Schaber, C. F.; Dening, K.; Appel, E.; Gorb, S. N.; Lee, H. *Advanced Materials* **2014**, *26*, 7581-7587. https://doi.org/10.1002/adma.201403259

[100] Ponzio, F.; Houerou, V. L.; Zafeiratos, S.; Gauthier, C.; Garnier, T.; Jierry, L.; Ball, V. *Langmuir* **2017**, *33*, 2420-2426. https://doi.org/10.1021/acs.langmuir.6b04435

[101] Im, B. G.; Do, M.; Kim, Y.; Cho, M.; Jang, J. *ACS Applied Materials Interfaces* **2017**, *10*, 7602-7613. https://doi.org/10.1021/acsami.7b10023

[102] Sun, J.; Li, J.; Liu, D.; Ma, Y.; Yang, S. *Langmuir* **2018**, *34*, 6653-6659. https://doi.org/10.1021/acs.langmuir.7b04339

[103] Luan, Q.; Wang, Y.; Chen, Y.; Chen, H. *Journal Of Food Science* **2025**, *90*, e70016. https://doi.org/10.1111/1750-3841.70016

[104] Xu, J.; Liu, K.; Chang, W.; Chiou, B.; Chen, M.; Liu, F. *Foods* **2022**, *11*, 1657. https://doi.org/10.3390/foods11111657

Chapter 2

Objectives

In accordance with the precedents established for catechol-based materials presented in the introduction, and considering the scope of this thesis, two main general objectives were defined:

1. To obtain catechol-amine based coatings with broad-spectrum antimicrobial properties.

2. To develop novel catechol-amine free-standing membranes for localized Glioblastoma treatment.

To achieve the first objective, the following specific objectives were set:

I. To synthesize and physiochemically characterize of the obtained coatings.

II. To evaluate the antimicrobial properties with different microorganisms and substrates.

III. To validate a proof of concept of the applicability of these coatings on *ex vivo* tissues.

IV. To assess their potential for metallic nanoparticle filtration as an additional property.

To achieve the second objective, the following specific objectives were set:

I. To synthesize and optimize a batch of novel membranes based on different catechol derivatives and amine-based ligands, ensuring their mechanical manipulability.

II. To perform the physiochemical characterization of the hexamethylenediamine-based membranes.

III. To perform an in-depth *in vitro* characterization of the cytotoxic properties of the selected candidate.

IV. To elucidate the mechanism underlying the cell death induced by this membrane.

Chapter 3

Bioinspired Phenol-Based Coatings Against Antimicrobial Resistance and Environmental Applications

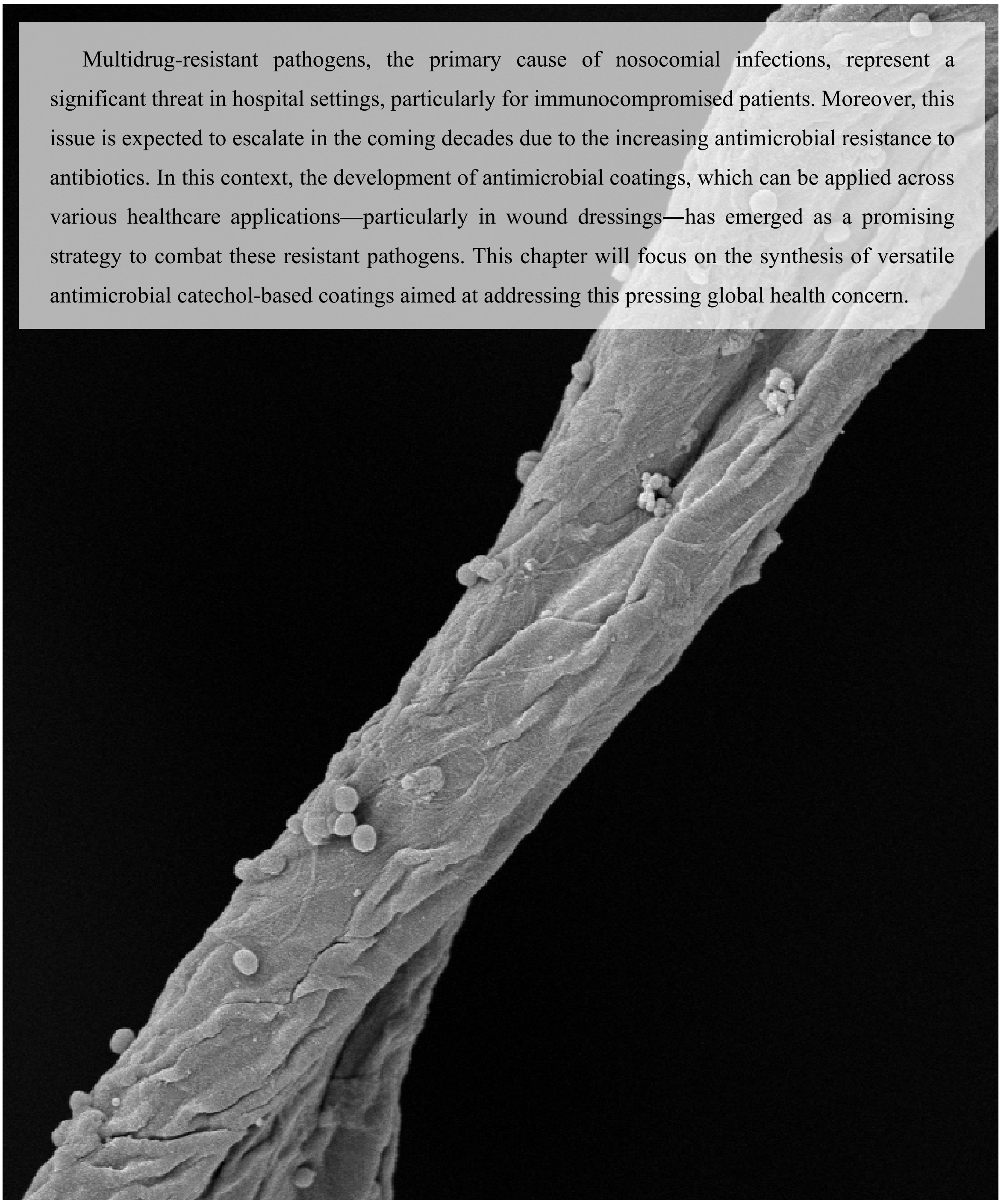

Multidrug-resistant pathogens, the primary cause of nosocomial infections, represent a significant threat in hospital settings, particularly for immunocompromised patients. Moreover, this issue is expected to escalate in the coming decades due to the increasing antimicrobial resistance to antibiotics. In this context, the development of antimicrobial coatings, which can be applied across various healthcare applications—particularly in wound dressings—has emerged as a promising strategy to combat these resistant pathogens. This chapter will focus on the synthesis of versatile antimicrobial catechol-based coatings aimed at addressing this pressing global health concern.

3.1 Introduction

Infections have been a persistent challenge to humanity since the dawn of civilization. They can be described as the process in which a microorganism (e.g., bacteria, fungi, virus) enters the organism of a host and multiplies, causing harm and disrupting normal functions. While some infections can be mild and localized, severe cases may progress to systemic infections, potentially escalating in extreme instances to sepsis. In 2017, an estimated number of 49 million cases of sepsis worldwide and 11 million sepsis-related deaths were recorded, which represented a 20% of all deaths (**Figure 3.1**).[1]

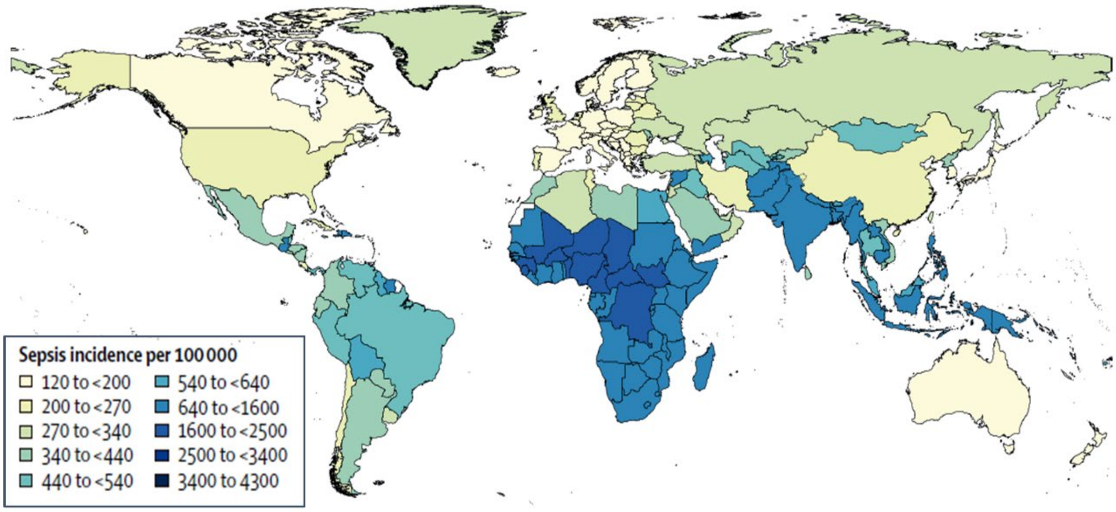

Figure 3.1. Sepsis incidence per 100,000 population in 2017.[1]

3.1.1 Antimicrobial resistance

The overuse of antibiotics in recent decades to combat infections has led to the development of antimicrobial resistance (AMR), a growing threat to public health worldwide.[2] AMR occurs when bacteria change over time and no longer respond to drugs, antibiotics or other related antimicrobial medicines, making infections harder to treat and increasing the risk of pathogen spread, severe illness and death. While in 2021 approximately 5 million deaths globally were associated with bacterial AMR, researchers and clinicians estimate that by 2050, this number could rise to over 10 million (**Figure 3.2**).[3] In fact, the World Health Organization (WHO) and United Nations (UN) have reported that AMR possesses a major threat to human health globally, potentially becoming a leading cause of death by 2050.[2,4,5] Measures such as improving water sanitation, increasing vaccination coverage, minimizing antibiotic exposure unrelated to human diseases (e.g., farming) and reducing an unnecessary use (e.g., for viral infections) are fundamental to prevent the worsening of this problem.[6] Moreover, although the rate of AMR is surpassing the pace of therapeutic innovation, it remains crucial to continue developing new antibiotics. In this scenario, the development of novel and efficient antibacterial materials has become essential to reduce pathogen spread, prevent infections, and combat AMR before it affects a host.

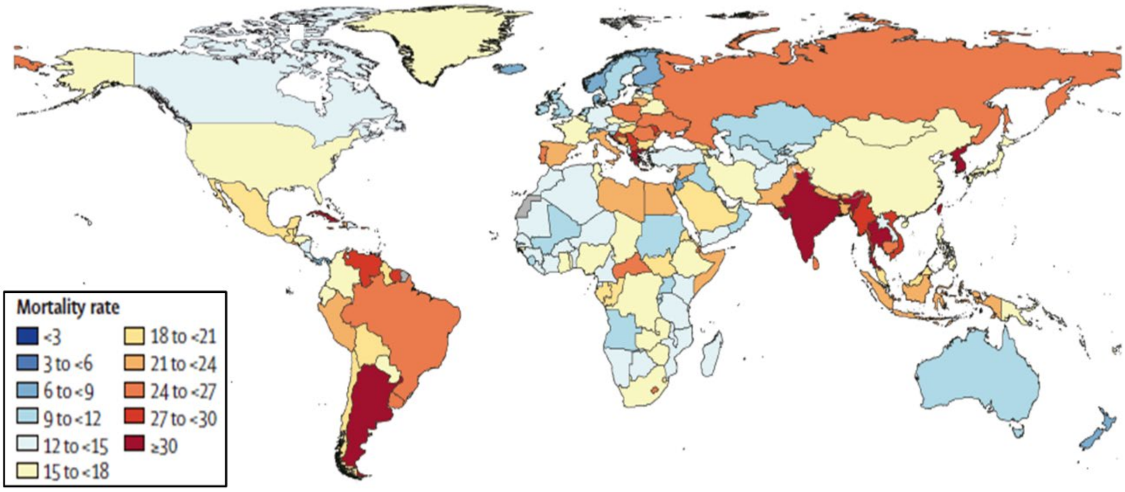

Figure 3.2. Projected mortality rates per 100,000 due to antimicrobial resistance (AMR) in 2050.[3]

Controlling microorganism populations in healthcare environments such as hospitals and other healthcare units is crucial to avoid nosocomial infections, primarily caused by bacterial and fungal colonization on biomedical surfaces. Among bacteria, most of these infections are caused by *Escherichia coli, Staphylococcus aureus* and *Pseudomonas aeruginosa*,[7] while among fungi ,*Candida albicans* is the most relevant.[8] Although bacteria are currently considered a more serious threat due to their fast evolution and resistance acquisition, fungi are becoming increasingly concerning due to the limited availability of effective antifungals and the rise of resistant species, such as *Candida auris.*[9] Nowadays, nosocomial infections are the sixth leading cause of death in industrialized countries (much higher in the developing world), specially affecting immunocompromised and intensive care patients (e.g., burns), and those with chronic conditions such as diabetes.[10] In addition to individual patient health, factors such as the length of hospital stay, patient density (particularly during outbreaks), invasive medical procedures, suboptimal hygiene practices (especially in undeveloped countries) and surface contamination increase the risk of acquiring these infections. Emphasizing the later, fabrics represent an important part of patient care, as they are materials that may spread bacterial populations. From the clothes of doctors, surgeons and nurses to medical curtains, bed sheets, pillow coverings, masks, gloves and bandages, all these fabrics are in direct contact with sutures and wounds. For all these reasons, antibacterial coatings for medical fabrics have become a very active field of research.[11] Their full implementation could represent a groundbreaking shift in the fight against AMR.

3.1.2 Antimicrobial coatings

In base on their characteristics, coatings can be primarily classified according to their composition and mechanism of action.

In terms of composition, two main classes can be identified:[12]

1. Inorganic: metals (e.g., Ag, Cu, Zn), ceramics (e.g., SiO_2, ZrO_2) and graphene-based coatings (e.g., graphene oxide).
2. Organic: polymers (e.g., PDA), biopolymers (e.g., chitosan), peptide-based and hybrid (e.g., metallic nanoparticle polymer or graphene-chitosan coating, among others).

In base on their mechanism of action, they can be divided into:[13]

1. Contact-killing: Activity upon direct contact.
2. Release-based: The antimicrobial agent is spread.
3. Adhesion-modulator: Prevents the adhesion or traps the microorganism.
4. ROS-generation: Induces oxidative damage.

Researchers have prominently developed coatings using metal-based antibacterial materials, thanks to their broad-spectrum biocidal properties, low probability of inducing resistance, versatility and ease of application on different surfaces (**Figure 3.3**).[14,15,16,17] Nevertheless, reliance on a secondary material (hybrid coatings), uncontrolled release of ions, cytotoxic effects due to bioaccumulation and competitive protein complexation have limited their successful translation to clinics.[18]

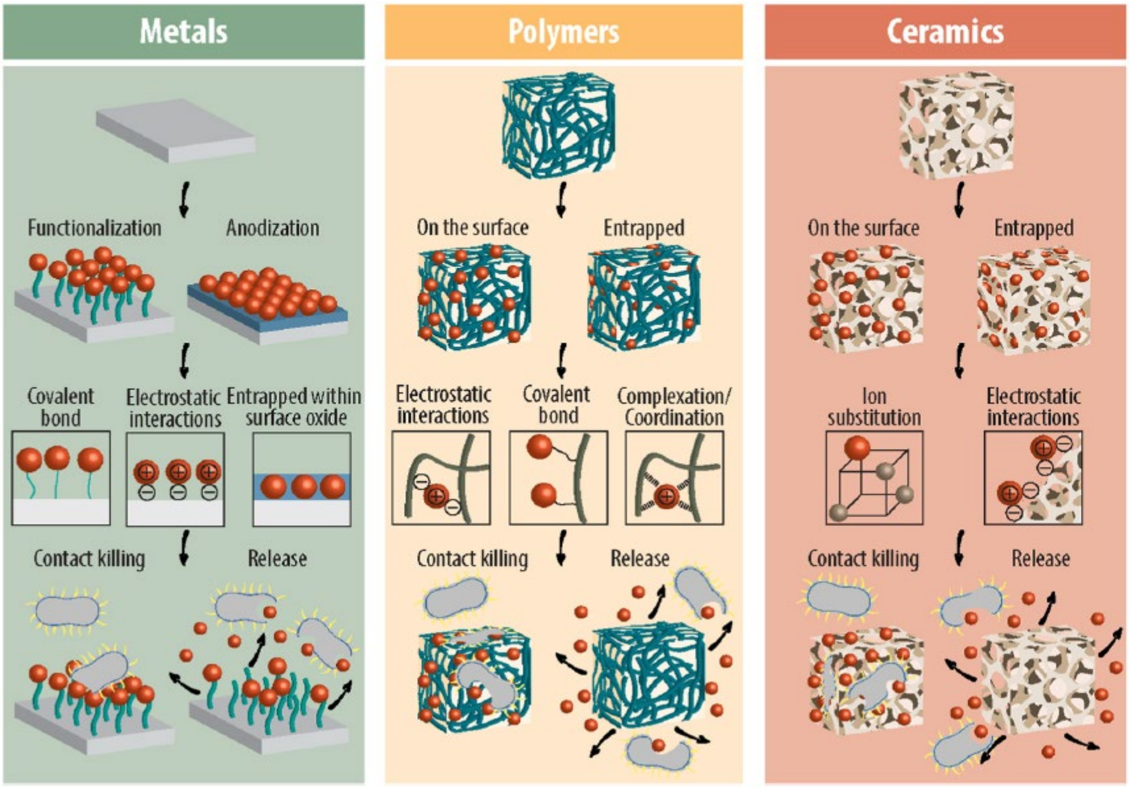

Figure 3.3. **Versatility of metals in antimicrobial coatings.** Schematic representation of the functionalization of diverse materials with metal ions and/or metallic nanoparticles (red circles), endowing them with antimicrobial properties.[17]

Moreover, the environmental outcome of widely endorsing these coatings should be carefully studied, as their persistence and non-degradability could lead to their accumulation in soil microbiota, aquatic ecosystems, plants and higher trophic levels in the food chain, ultimately affecting humans (**Figure 3.4**).[19,20,21] Moreover, metallic nanoparticles can also be produced as by-product of different industrial processes (e.g., mining and electronics), agriculture practices (e.g., fertilizers and pesticides) and urban activities (e.g., construction and waste management).[22,23,24] Their growing presence in our daily life is the reason why some new materials, rather incorporating these nanoparticles and using their properties, are synthetized in order to remove them from the environment.[25] In this context, the ability of certain molecules, such as catechols and polyphenols, to coordinate with metals is a desirable property for developing coatings for filtration membranes, which are essential for effective wastewater treatment.

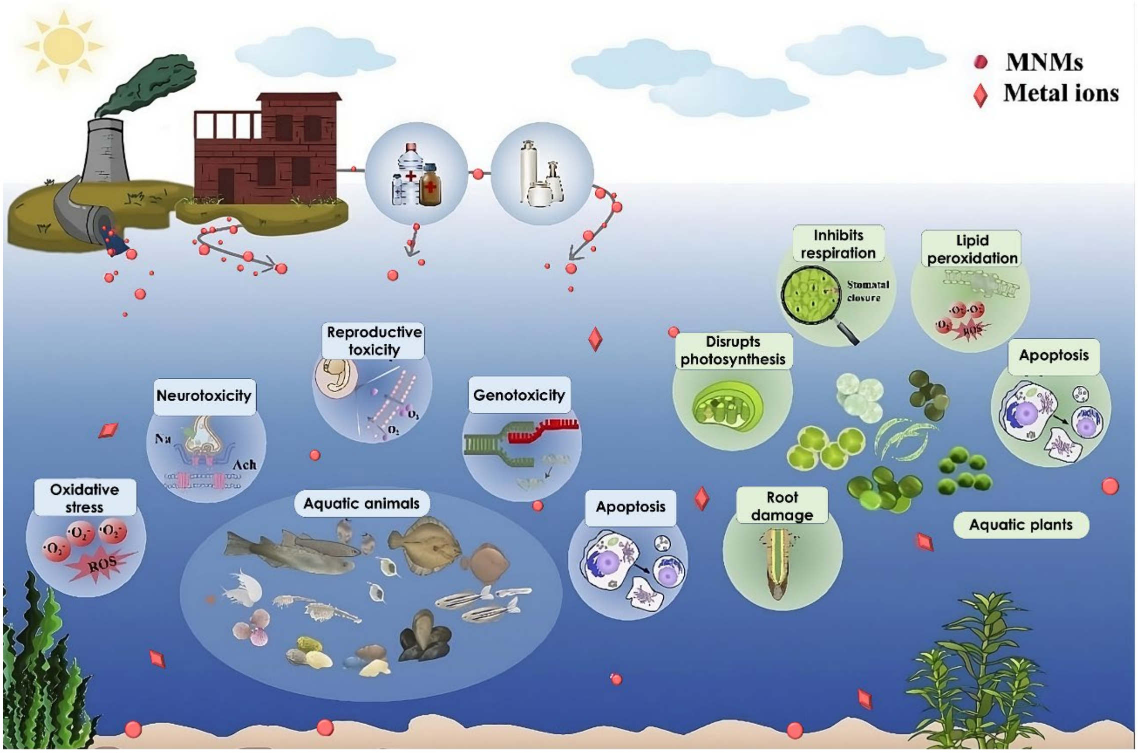

Figure 3.4. Ecotoxicity of metallic nanomaterials in aquatic ecosystems. Schematic representation of how metallic ions and nanoparticles can negatively affect both animals (through oxidative stress, apoptosis, and reproductive, neurological and genetic toxicity) and plants (through root damage, disruption in respiration and photosynthesis and oxidative stress). Adapted from [[21]].

Recently, new antimicrobial materials have been reported and extensively studied, particularly those based on carbon nanotubes and graphene oxide.[26] These materials are noted for their versatility, stability, and strong antibacterial activity, specially through physical interactions. However, alongside their high production costs and scalability challenges, additional concerns regarding public safety and environmental impacts have arisen.[27]

Other reported materials are based on polymeric quaternary ammonium salts (QAS). These versatile molecules can induce cationic membrane disruption and are usually found as a complementary agent in coatings to endow them with antimicrobial properties. [28,29,30] In bacteria, the cell membrane is usually negatively charged, which is even higher in gram-negative due to the additional layer of lipopolysaccharides. When positively charged materials, such as QAS or primary amines, directly interact with a bacterium, they lead to membrane permeabilization (induced by the neutralization of charges) and destabilization (of structures like the lipid bilayer) (**Figure 3.5**).[31] Additionally, it has been observed that this change in the interfacial potential (between the particle and the cell) could also lead to ROS production.[32] These changes, beyond a critical point, result in significant membrane alteration and subsequent cell death. However, besides the heterogeneous antibacterial activity of QAS (less effective in gram-positive due to their less negative surface charge), it has been observed that they can contribute to the co-resistance of antibiotics during plasmid transference.[33]

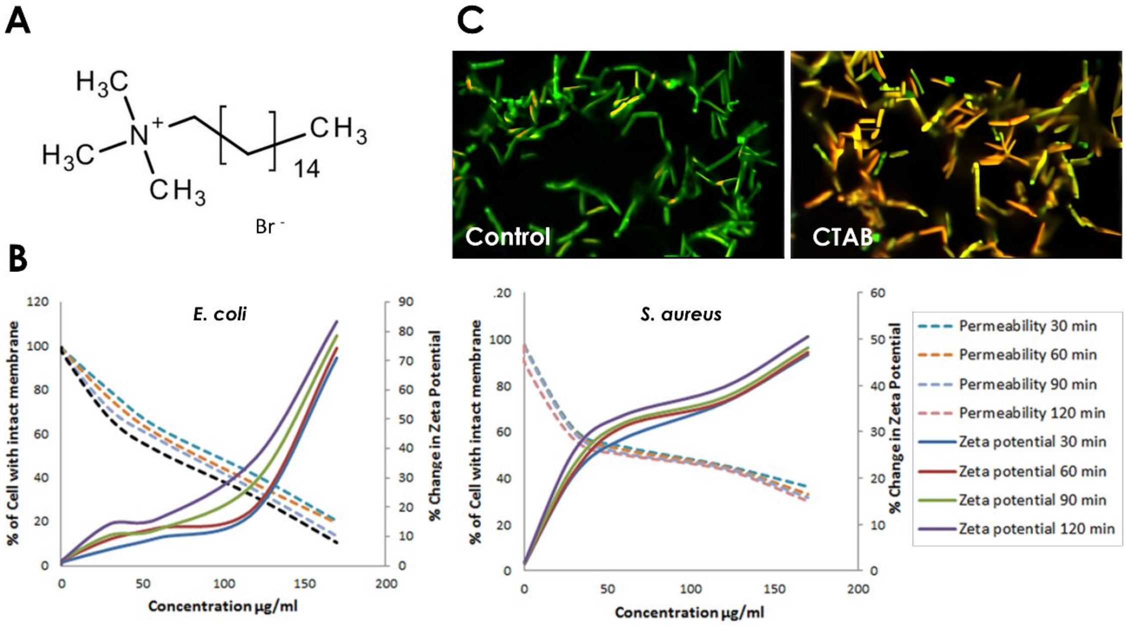

Figure 3.5. Effect of quaternary amines in bacteria. A) The quaternary amine cetrimonium bromide (CTAB) is a potent antiseptic. **B)** It disrupts bacterial membrane integrity and alters the zeta potential in a concentration-dependent manner. **C)** This effect is validated through dual staining with SYTO9 (green, indicating an intact membrane) and propidium iodide (red, signifying membrane permeabilization), confirming the observed results. Adapted from [31].

Some materials, based on a more biological approach, exploit the properties of antimicrobial peptides, notable for they customizability, low potential to develop resistance and degradability. However, their difficult immobilization, high production costs and limited scalability hamper its use.[34,35] As a result, there is a need for novel alternative antibacterial systems that can overcome these limitations and provide effective and safe antimicrobial activity through efficient and controllable mechanisms.

In this scenario, synthetic antibacterial polymers are attracting special attention.[36] Their rationalized chemical design allows for the production of coatings with multiple antibacterial pathways and broad antimicrobial activity against different pathogens, while avoiding the induction of severe drug resistance. Especially relevant is the family of catechol-based polymers. As previously mentioned in Chapter 1, among their several properties, ROS production makes polyphenolic compounds great candidates for developing antimicrobial materials based on the induction of oxidative stress. Furthermore, their wide range of interactions—including hydrogen bonds, π interactions, as well as coordination and covalent bonds—makes them versatile ligands in various hybrid antimicrobial materials, thereby enhancing their properties. Some representative components used in combination with catechols include silver nanoparticles,[37,38] chlorinated catechol moieties,[39,40] antimicrobial peptides[41] or antibacterial compounds such as chitosan.[42] However, their promising potential, the antibacterial properties are still in their early stage and far from being optimized. They often require long and complex synthetic methodologies and/or fabrication processes that are difficult to scale up, in addition to the need for organic solvents that are harmful for the environment. Another challenge is achievement of thr antibacterial activity in the presence of air and humid environments, conditions where the coatings must remain functional, especially in healthcare applications.[43] For these reasons, more efforts must be directed towards the design and development of phenol-based materials to improve their antibacterial capabilities, emphasizing the optimization of their inherent properties rather than the incorporation of secondary elements. This elemental and streamlined approach has been one of the main objectives of this Thesis.

3.1.3 ROS-mediated bacteria cell death

As previously explained in Chapter 1, catechols and their derivatives are characterized by their ability to produce ROS, a useful property that can be incorporated into materials. In this section, the relevance and mechanisms of these molecules from an antibacterials perspective will be discussed.

Oxidative stress occurs when prooxidant molecules overcome the antioxidant capacity of bacteria, rendering them unable to counteract ROS (and also reactive nitrogen species, RNS) levels. This leads to the accumulation of ROS and the consequent cell damage, which can be manifested through alterations and double-stranded breaks in DNA (oxidizing dCTP and dGTP), lipid peroxidation, protein carbonylation and membrane permeabilization (**Figure 3.6**). This multitarget feature is the reason why ROS-mediated antimicrobials have drawn the attention for the development of advanced materials.[44]

Particularly, in the case of the DNA, H_2O_2 can indirectly cause damage by generating $\cdot OH$ radicals through the Fenton reaction, which affects the nucleobase or the deoxyribose of the DNA.

In contrast, $\cdot O_2^-$ exclusively interacts with guanine. Additionally, besides also been converted into H_2O_2 and undergoing the Fenton reaction. It has also been observed that oxidative stress generally inhibits translation process, since tRNA and mRNA are not protected from it.[45]

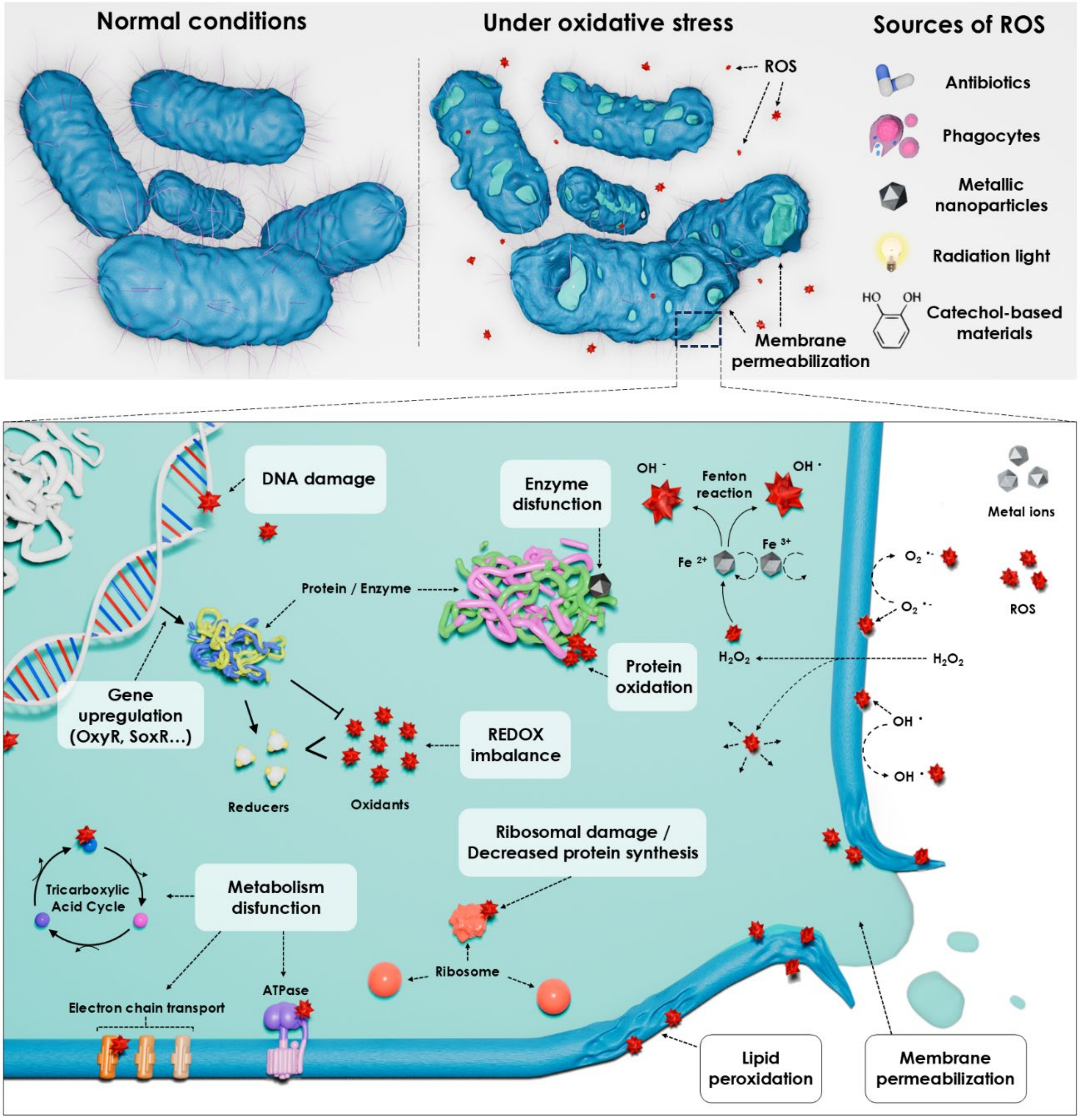

Figure 3.6. Reactive oxygen species (ROS)-mediated antibacterial mechanisms. Antibiotics, phagocytes, metallic nanoparticles, radiation, and catechol-based materials can induce the generation of ROS, which in turn triggers oxidative stress in bacteria. The accumulation of ROS sets off a cascade of cellular damage, including DNA damage, enzyme dysfunction, protein oxidation, ribosomal damage, lipid peroxidation, and metabolic dysfunction, ultimately resulting in redox imbalance and membrane permeabilization.

While the host immune system induces exogenous oxidative stress in pathogens, for instance, due to the ROS-mediated activity of phagocytes, antimicrobials can contribute to endogenous oxidative stress. In response, bacteria can upregulate the transcription factors required for antioxidant defense (e.g., OxyR, OhrR, PerR, SoxR), leading to increased levels of superoxide dismutase, catalase, thioredoxins, machinery biosynthesis, glutathione reductases, ferric uptake regulator or ferritin.[46] This adaptation could allow bacteria to overcome extracellular concentrations of H_2O_2 that are 10^6 times the normal intracellular levels.[45] Moreover, oxidative stress can be mitigated with pigments such as carotenoids, regulation of metal homeostasis, general stress response and SOS response (DNA repair).[44] Although some antibiotics, such as Polymyxin B, have the direct ROS production as primary mechanism of action, this is not a common characteristic. Most antibiotics target the bacterial cell wall, protein synthesis or DNA replication. However, if this primary damage is not enough, the indirectly produced ROS due to structural damage and the overstimulation and dysfunction of specific metabolic pathways (such as the tricarboxylic acid cycle) could lead to higher ROS accumulation, resulting in secondary damage that could compromise the cell.[47]

The use of metals, particularly metallic nanoparticles, such as Ag, Au, Cu, Zn, Fe, Mn and Ti, stands out due to their ROS production properties. Inside bacteria, metals can induce ROS directly through the Fenton reaction and photocatalysis (upon light exposure). Indirectly, they can disrupt protein activities, disturb redox homeostasis, and interact with proteins in the electron transport chain, causing electron leakage and subsequent ROS generation. [17,48]

Finally, among the organic polymers, it is important to highlight the phenolic-based materials, which are the focus of this Thesis. As thoroughly explained in Chapter 1, besides the wide range of ROS that phenols (such as catechols) can produce, their redox cycling and self-oxidation in presence of oxygen confer a strong oxidative capacity (**Figure 3.7**).[49] Moreover, their direct interaction with different structures and chelation of essential metals (free ions or from enzymes), which leads to a disruption in homeostasis, can indirectly induce even higher levels of ROS. This particular ROS-mediated mechanism, without the addition of metals or antibiotics, is characteristic of the materials studied in this Chapter.

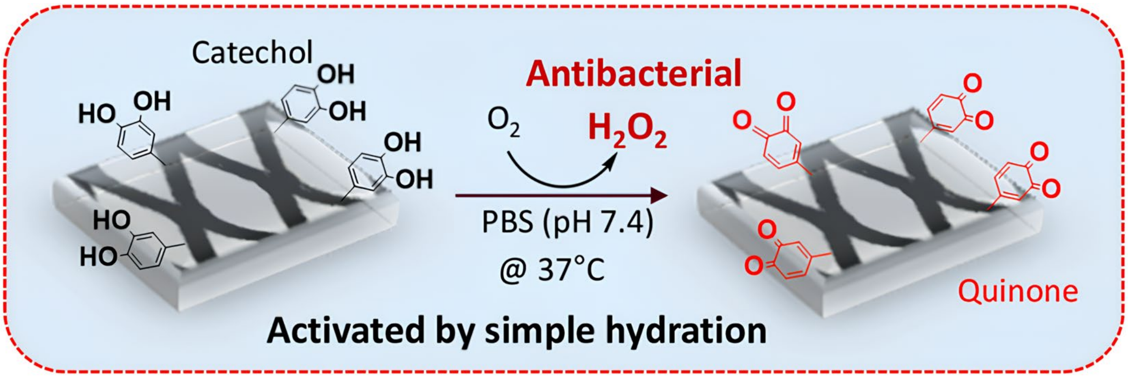

Figure 3.7. Representation example of a polypropylene mesh coated with a dopamine solution (pH 8.5). The resulting polydopamine (PDA) coating can generate hydrogen peroxide by simply hydrating it in PBS. Adapted from [[49]].

3.1.4 Scope of this Chapter

In line with the previous discussion, this Chapter focuses on the development of a novel family of biocompatible coatings, which were optimized, characterized (both physiochemically and biologically) and validated with the goal of combating antimicrobial resistance. These coatings were produced through a catechol-amine based approach by the co-polymerization of catechol derivatives with amino-terminal ligands.

Worth to mention, the Nanosfun research group has previous expertise in the development of this kind of materials, for instance, using them to modulate the surface properties, such as wettability.[50] However, their antimicrobial properties were not yet characterized, in spite of the increasing interest. In view of this, this Chapter has been focused on (**Figure 3.8**):

- The development and optimization of efficient antimicrobial materials based on their ability to chemically evolve with time in the presence of air and humid environments, inducing a continuous formation of ROS.
- Understand the ROS mechanisms of the developed coatings by:
  - Measuring the ROS evolution and assessing their individual levels.
  - Confirming the oxidative capacity and their interaction with antioxidant modulators.
- Endow a strong antimicrobial activity to:
  - Coated woven and non-woven-based materials commonly used in healthcare environments: paper, cotton, surgical masks and commercial band-aids.
  - Against a broad spectrum of pathogenic species, including multi-resistant microorganisms (responsible of nosocomial infections), from both Gram-negative and Gram-positive bacteria and fungi.
  - Validation of these properties, both *in vitro* and *ex vivo*.
- Successful preliminary analysis in the filtration of metallic nanoparticles as environmental remediation model.

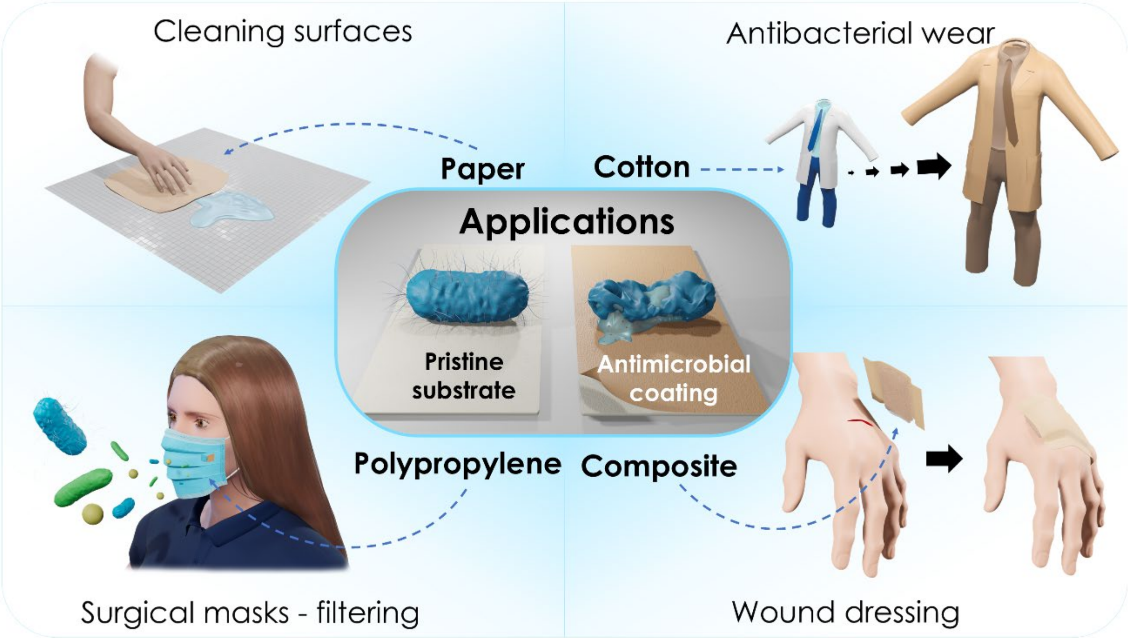

Figure 3.8. Potential healthcare applications for antimicrobial coatings. Different goals can be achieved in base of the selected substrates, for instance: coated paper for surface cleaning, coated cotton and polypropylene to protect patients and personnel and band-aids to avoid infection progression.

3.2 Results and Discussion

3.2.1 Coatings on paper, properties and characterization

The bioinspired coatings were synthesized by combining different catechol derivatives: pyrocatechol (PYRO), caffeic acid (CAFF), pyrogallol (GALL), catechin (CATH), dopamine (DOPI) and 4-methylcatechol (4MET), with two amino-based ligands: hexamethylenediamine (HMDA, H) and tris(2-aminoethyl)amine (TRI2, T). These catechol derivatives were selected due to their chemical differences, like the presence of functional groups (acid, amine, methyl) or the number of hydroxyl groups (two, three or five). The developed coatings were respectively named: **PYRO-H**, **PYRO-T**, **CAFF-H**, **CAFF-T**, **GALL-H**, **GALL-T**, **CATH-H**, **CATH-T**, **DOPI-H**, **DOPI-T**, **4MET-H** and **4MET-T**.

Briefly, the selected catechol derivative and the amines were weighted separately and mixed in ultra-pure water with different molarities (**Table 3.1**), in the presence of a paper substrate (**Figure 3.9A** and **B**). Interestingly, each catechol derivative generated a coating with a specific color, which slightly changed depending on the amine (**Figure 3.9C**). The diverse color palette obtained—including yellow (**GALL-H**), orange (**CATH-H** and **4MET-H**), brown (**DOPI-H/T** and **GALL-T**), green (**CAFF-H/T**), beige (**PYRO-H/T**), and pale rose (**CATH-T** and **4MET-T**)—enables this technology to be customized for different color-dependent applications, such as matching different skin tones.

Table 3.1. Catechol-amine molar ratios used for the coating synthesis. Each catechol derivative was combined separately with hexamethylenediamine (H) or tris(2-aminoethyl)amine (T) to obtain twelve different coatings.

Catechol derivative	Molarity (mM)	Amine	Molarity (mM)	Molar Ratio	Name
Pyrocatechol	10	Hexamethylenediamine	15	1 : 1.5	**PYRO-H**
Pyrocatechol	10	Tris(2-aminoethyl)amine	22	1 : 2.2	**PYRO-T**
Caffeic acid	10	Hexamethylenediamine	25	1 : 2.5	**CAFF-H**
Caffeic acid	10	Tris(2-aminoethyl)amine	24	1 : 2.4	**CAFF-T**
Pyrogallol	10	Hexamethylenediamine	20	1 : 2	**GALL-H**
Pyrogallol	10	Tris(2-aminoethyl)amine	22	1 : 2.2	**GALL-T**
Catechin	10	Hexamethylenediamine	15	1 : 1.5	**CATH-H**
Catechin	10	Tris(2-aminoethyl)amine	16	1 : 1.6	**CATH-T**
Dopamine	10	Hexamethylenediamine	20	1 : 2	**DOPI-H**
Dopamine	10	Tris(2-aminoethyl)amine	24	1 : 2.4	**DOPI-T**
4-Methylcatechol	10	Hexamethylenediamine	25	1 : 2.5	**4MET-H**
4-Methylcatechol	10	Tris(2-aminoethyl)amine	27	1 : 2.7	**4MET-T**

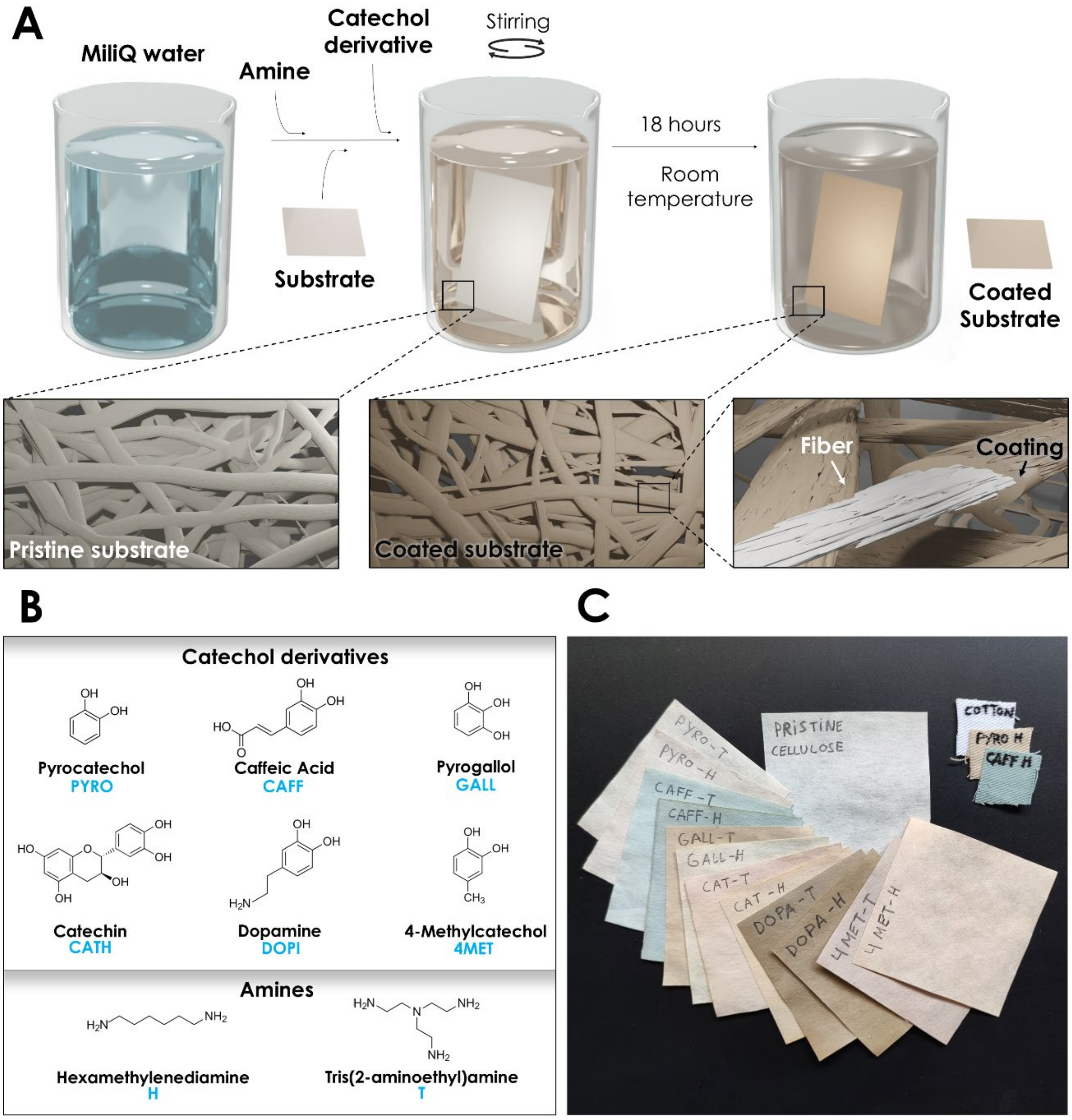

Figure 3.9. Bioinspired catechol-amine-based coatings. **A)** Schematic representation of the coating process of a fiber-based substrate. The used approach allows for the straightforward production of catechol-amine-based coatings under mild conditions using water at room temperature and with the presence of oxygen. After 18 h, functional antimicrobial coatings are obtained ready-to-use. **B)** Catechol derivatives and amino-based ligands selected for the formation of the bioinspired coatings abbreviations in blue). **C)** Color comparison between a pristine substrate (paper or cotton) and the different obtained coatings.

The polymerization and coating formation were confirmed by Fourier-transform Infrared Spectroscopy (FTIR), which clearly showed the presence of both HMDA (H) or TRI2 (T) and catechol/quinonic species (**Figure 3.10**). The broad band around 3240 cm^{-1} and its shoulder at higher wavenumbers around 3400 cm^{-1} could be attributed to the NH_2 and O–H vibrations from catechol and amine moieties, respectively. These observations confirmed the presence of both hydroxyl and free amino groups, which would have a relevant role in the retention and inactivation of pathogens. Interestingly, all spectra presented intense bands around 1575 cm^{-1}, and between 1620 and 1710 cm^{-1}, which could be attributed to C=O quinonic groups. The presence of both hydroxyl and quinone groups is particularly noteworthy for two reasons: firstly, their strong adhesion and interaction with the substrates, and secondly, their role in promoting further oxidation, which results in the production of ROS during the process. FTIR also confirmed the presence of other functional groups. For example, when CAFF was used as a catechol derivative, bands at 1585 cm^{-1} and 1385 cm^{-1} confirmed the presence of carboxylate groups (–COO–). X-ray Photoelectron Spectroscopy (XPS) further confirmed the presence of these functional groups in the surface of the coatings (**Figure 3.11A-C**).

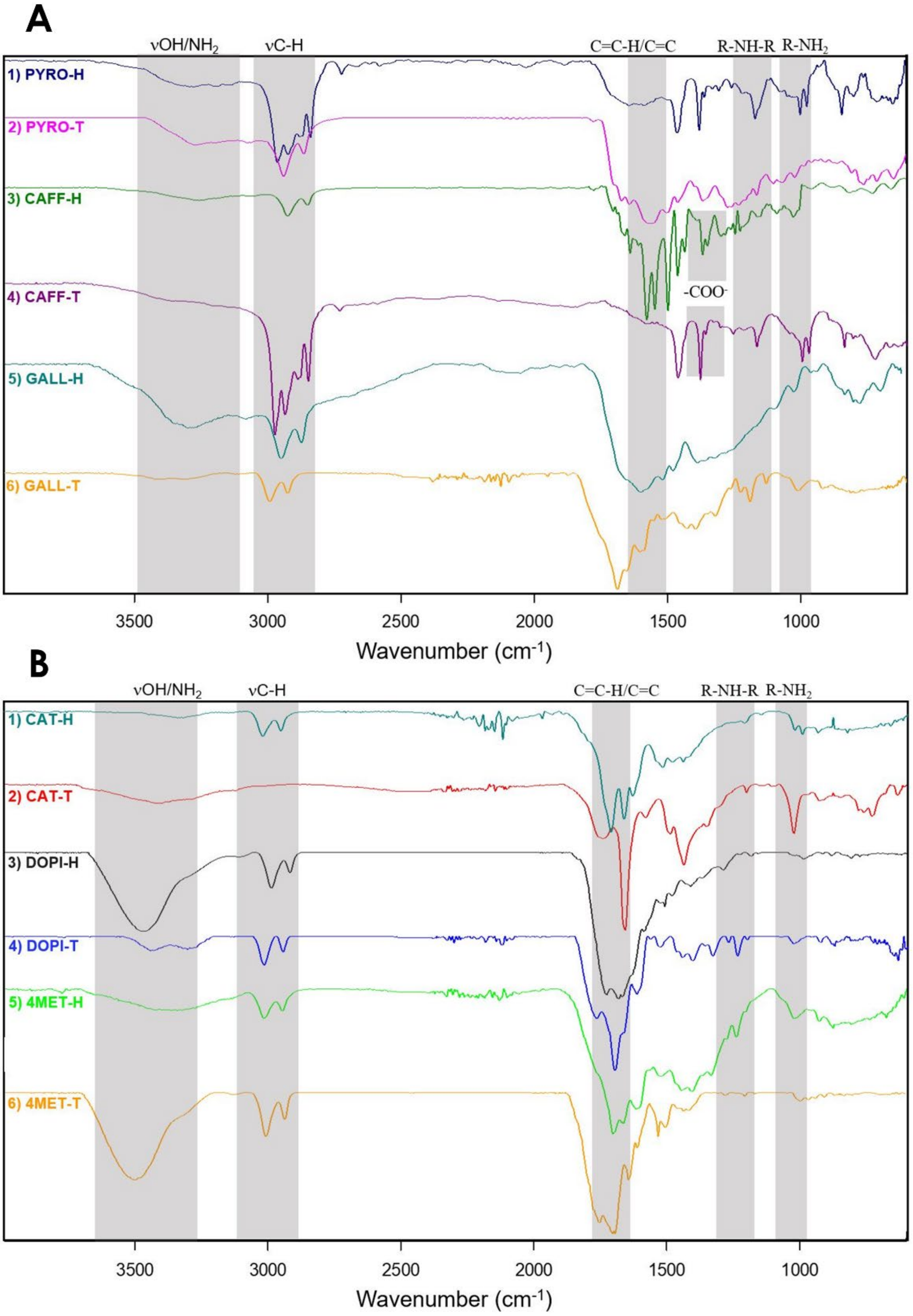

Figure 3.10. Characterization of the twelve coatings by Fourier-transform Infrared Spectroscopy (FTIR). **A)** FTIR spectra of **PYRO-H**, **PYRO-T**, **CAFF-H**, **CAFF-T**, **GALL-H** and **GALL-T**. **B)** FTIR spectra of **CAT-H**, **CAT-T**, **DOPI-H**, **DOPI-T**, **4MET-H** and **4MET-T**

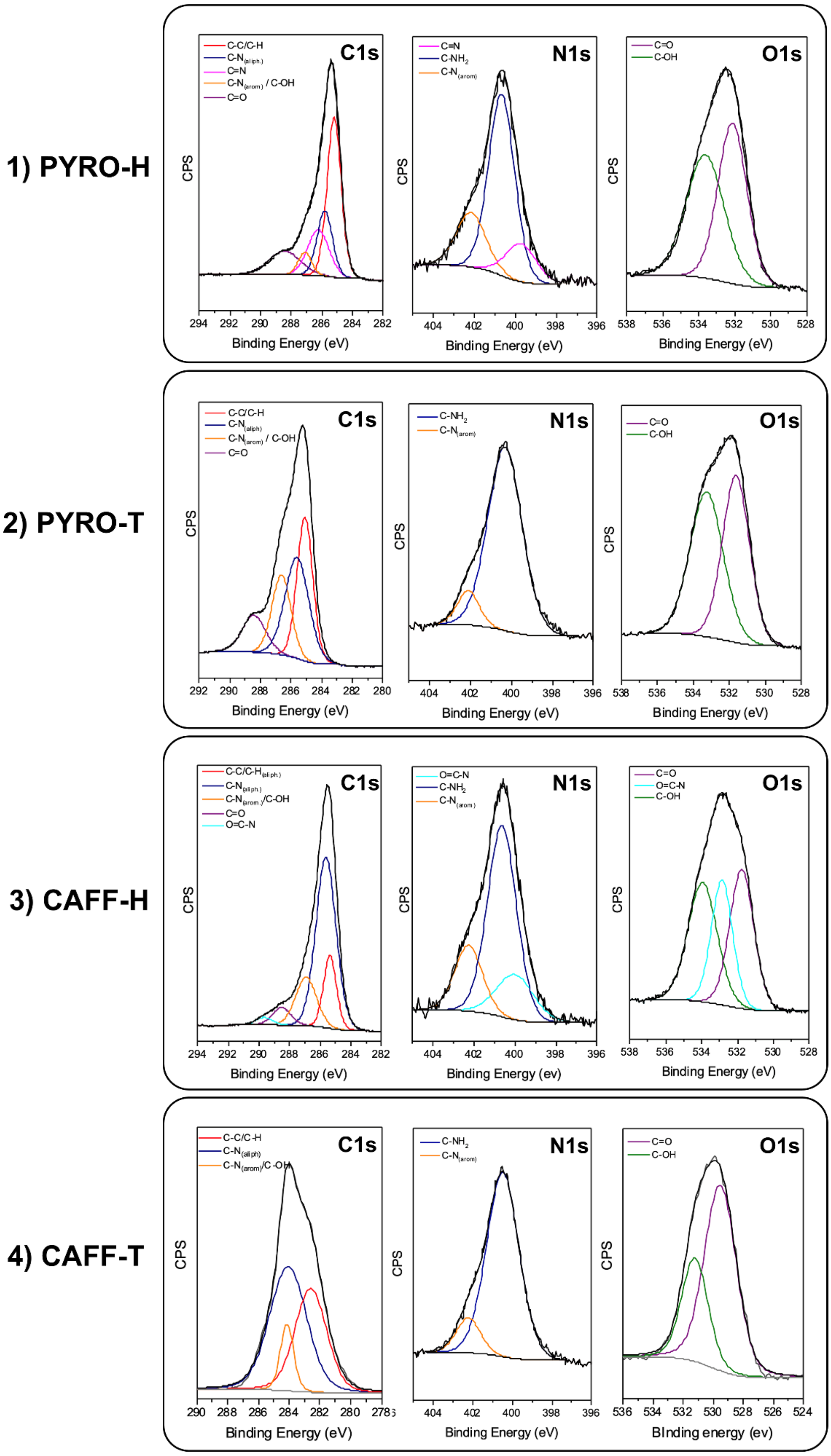

Figure 3.11A. Characterization of the obtained coatings by X-Ray Photoelectron Spectroscopy (XPS). Curve-fitting results for C1s, N1s and O1s high-resolution XPS spectra for 1) **PYRO-H**, 2) **PYRO-T**, 3) **CAFF-H**, and 4) **CAFF-T**. CPS: Counts per second.

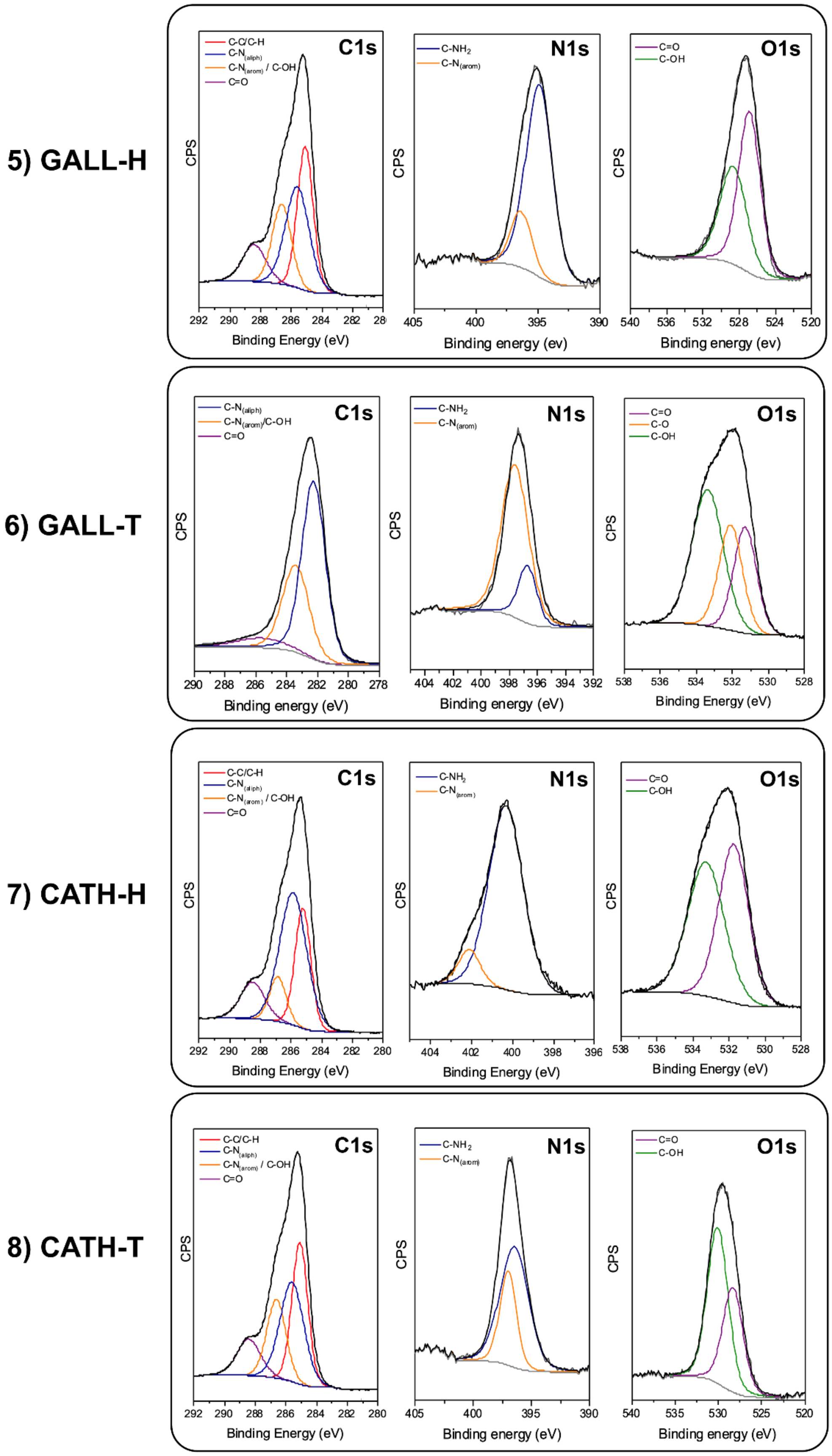

Figure 3.11B. Characterization of the obtained coatings by XPS. Curve-fitting results for C1s, N1s and O1s high-resolution XPS spectra for 5) **GALL-H**, 6) **GALL-T,** 7) **CATH-H**, and 8) **CATH-T**. CPS: Counts per second.

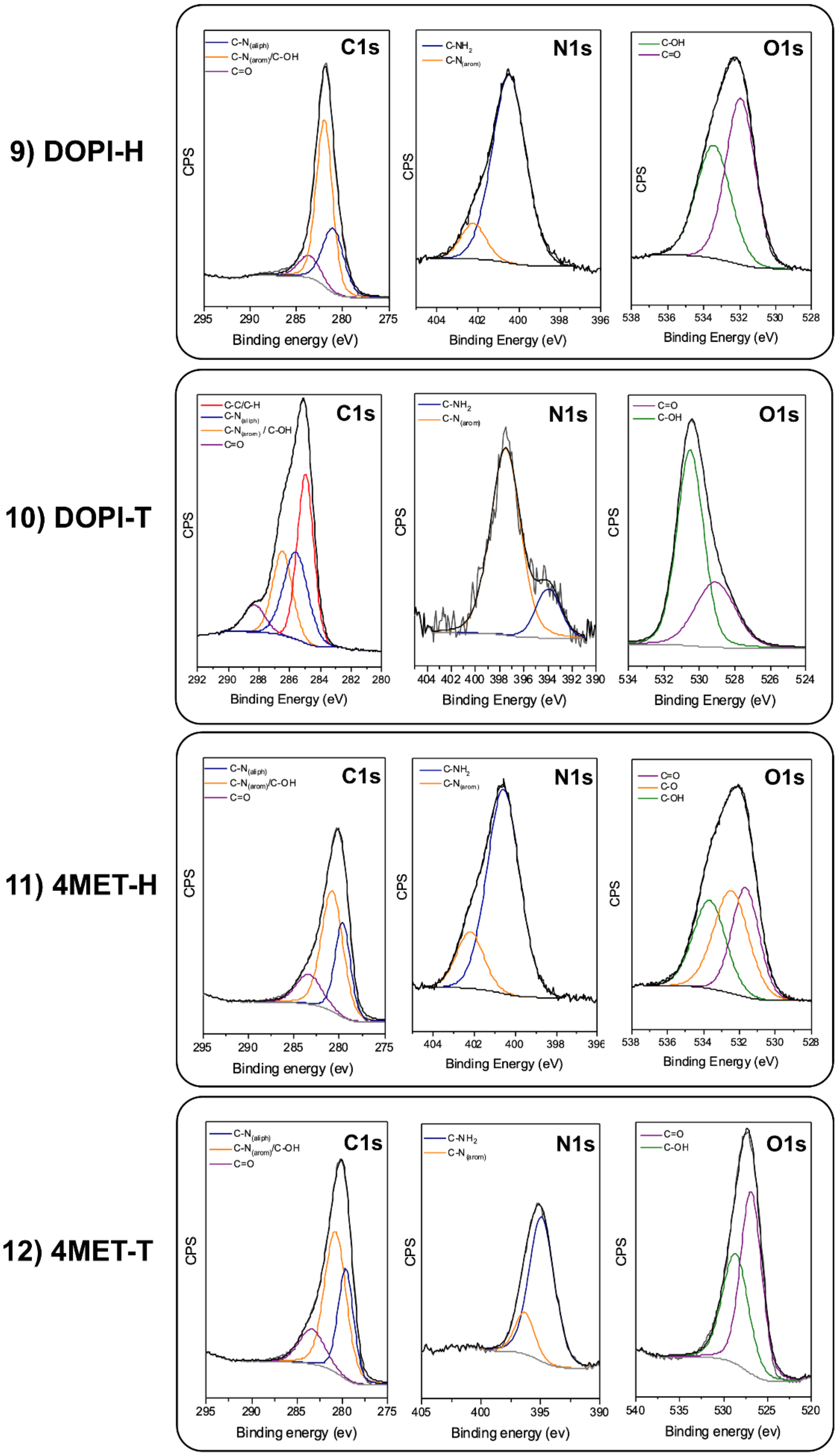

Figure 3.11C. Characterization of the obtained coatings by XPS. Curve-fitting results for C1s, N1s and O1s high-resolution XPS spectra for 9) **DOPI-H**, 10) **DOPI-T**, 11) **4MET-H**, and 12) **4MET-T**. CPS: Counts per second.

The coexistence of the catechol moieties with their oxidized quinone states were confirmed by the simultaneous detection of C–OH and C=O signals at approximately 286 eV and 288 eV, respectively. Furthermore, the presence of aliphatic C–NH at approximately 399 eV would indicate the presence of unreacted terminal amines. Interestingly, this functional group may be protonated/deprotonated under certain conditions, endowing the bioinspired coatings with improved antimicrobial properties and electrostatic interactions at the bio-interface.

To study the coating morphology and thickness on the paper substrates, scanning electron microscopy (SEM) was employed (**Figure 3.12A** and **B**). SEM images revealed a thin layer of catechol-amine coating homogeneously covering the paper fibers, with small variations observed in the morphology between different amino-based reagents (**Figure 3.12C**). When DOPI and CATH were used as polyphenolic ligands, a higher number of nanoparticles as a byproduct were observed on the surface of the resulting coatings. While catechin-derivatives have been reported to be prone to generate particles with different amines,[51] dopamine has the ability to self-polymerize with its own terminal-amine (PDA), leading to the formation of nanoparticles, which would support the obtained results.[52] Moreover, it is important to highlight that the creation of nanoparticles is purposely less favored during the synthesis, since the process is oriented towards the coating development (for instance, low agitation decreases nanoparticles formation). On the other hand, PYRO and specially CAFF yielded fewer nanoparticles as byproducts. Interestingly, when TRI2 was used as amine, particle formation generally decreased for each catechol-derivate.

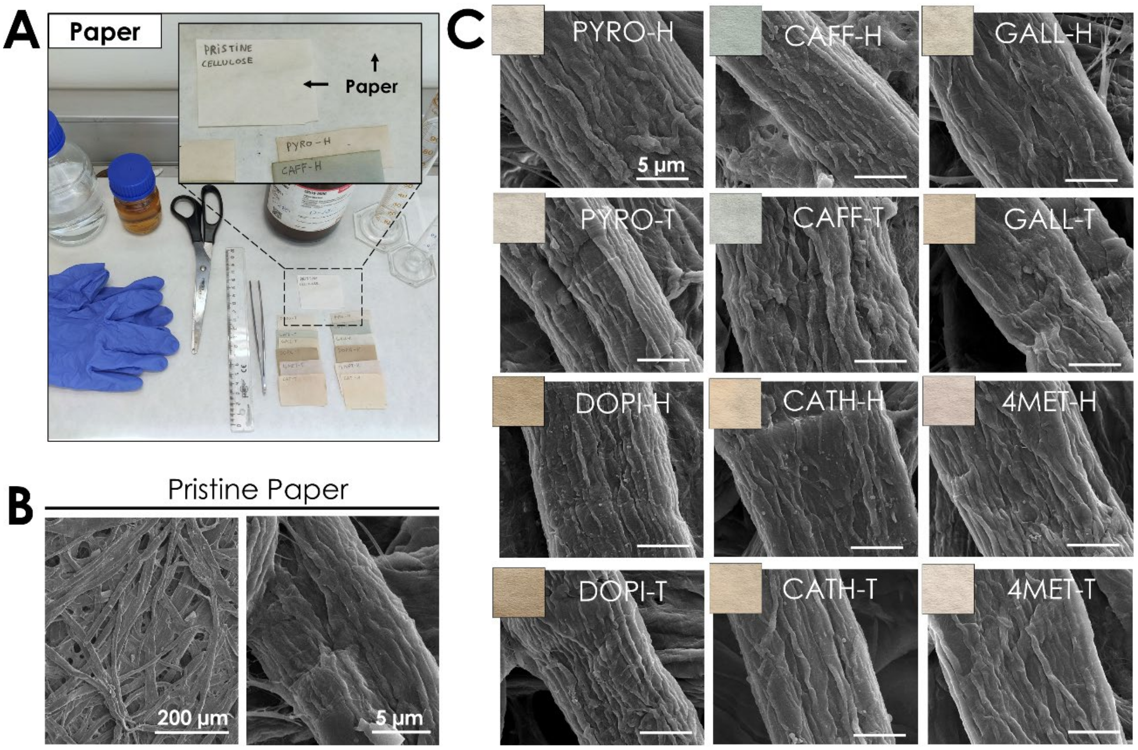

Figure 3.12. Coated paper substrate. **A)** The selected substrate was filter paper, commonly used in laboratories. Scanning electron microscopy (SEM) micrographs of the **B)** pristine paper and **C)** the twelve different coatings**.** The SEM scale bars correspond to 5 µm.

Interestingly, the thicknesses between the different coatings was homogeneous, showing values around 300 nm (**Figure 3.13**). This thickness allows the coatings to retain the intrinsic mechanical properties of the substrate and their porous and permeable nature, while simultaneously endowing them with the properties of the bioinspired coatings. This is especially relevant for those materials with applications in health environments that must meet specific parameters. For instance, coated face masks should have adequate breathability, since coated fibers could decrease the air flux through the material. Similarly, coated paper and fabrics should retain enough humidity, as a thick coating can reduce moisture retention by limiting the interstitial space (i.e. empty space between the fibers).

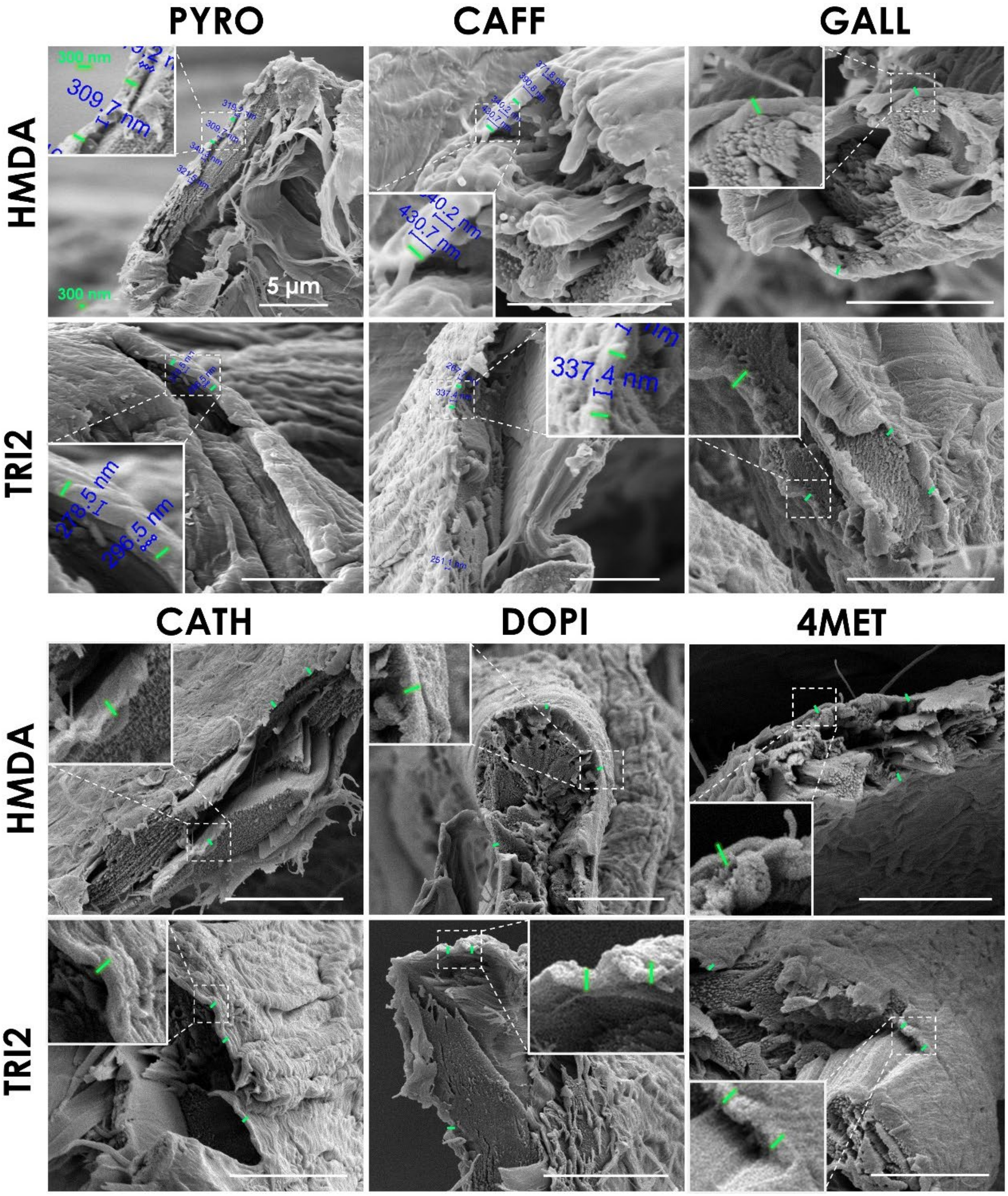

Figure 3.13. Representative thicknesses of the different coatings in paper. Coated fibers of the substrate with the twelve obtained coatings are shown. The thickness measured in blue (in PYRO and CAFF) showed an average value of 300 nm. Green scale bars correspond to 300 nm. White scales bars correspond to 5 µm.

The stability of the coatings, especially in wet environments, is a fundamental property, since most healthcare applications for fiber-like materials occurs under these conditions. The robustness and adhesion of the coating to the fabrics were confirmed after the first post-synthesis cleaning. The material was washed with a continuous flow of distilled water, followed by a subsequent vacuum drying. This washing process was repeated until the rinsing water was completely clear, indicating the removal of any unreacted materials and excess coating. It is important to remark that these washes did not alter the coating, an evidence of its strong adhesion to the underlying fiber substrates. Additionally, the long-term stability of these coatings under wet conditions is crucial to ensure that the material will not degrade upon use. To test this, the coated substrates were immersed in water for 60 days under magnetic stirring. After this period, the water-immersed coatings were compared to those that remained dry. SEM was used to identify any defects or signs of degradation. No considerable variation in the overall morphology of all the coatings were observed, either on the surface or in the amount of coating, suggesting that these catechol-amine coatings possess excellent durability in water (**Figure 3.14**).

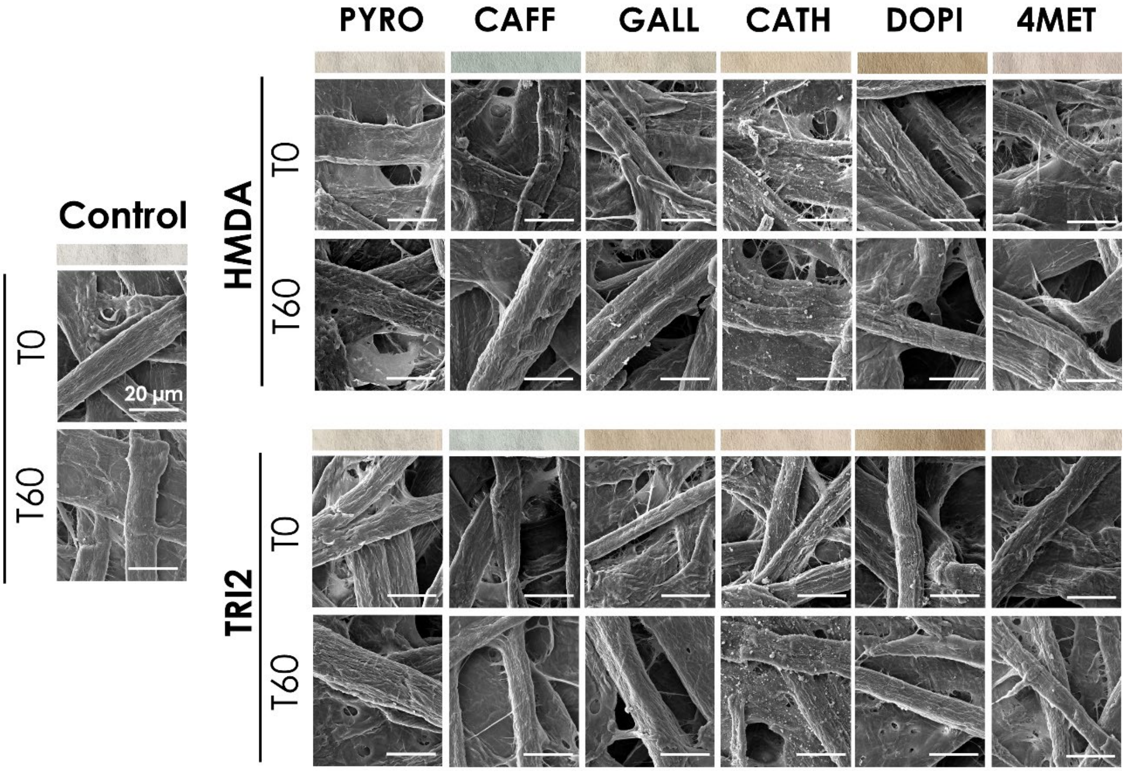

Figure 3.14. Coatings stability before and after 60 days in water. Comparison between each coating obtained by the permutation of catechol derivatives with HMDA or TRI2, showing their natural color and comparing the SEM pictures obtained before and after 60 days in water. No changes in the surface were observed between both times. The scale bars correspond to 20 µm.

After confirming the robustness and stability of the coatings, the next parameter measured was their Zeta potential. Depending on the environment conditions, the amine groups of HMDA and TRI2 can be positively charged under certain conditions. This has a direct influence on antimicrobial properties (as explained in section 3.1.2). This suggests that these coatings could achieve a positively charged surface. However, due to a lack of a specific cell to directly measure the Zeta potential of the coated materials at the time of the execution of this Thesis, it was decided to use an approximation which consisted in measuring the Zeta potential of the colloidal free polymer obtained after the reaction. The results revealed that most of the coatings (their polymer colloidal solution version) exhibited a positive charge, ordered from most to least: PYRO, 4MET, DOPI, GALL, CATH and CAFF (**Table 3.2**). Specifically, all the coatings synthesized with HMDA (except **CAFF-H**) showed positive Zeta potential values ranging from 11 to 37 mV, depending on the catechol derivative used. On the other hand, the **CAFF-H** coating had a nearly neutral charge (-0.3 ± 0.4 mV), likely due to the presence of deprotonated exposed carboxylic acid groups from the caffeic acid ligand. Similarly, but to a lesser extent, the three hydroxyl groups present in GALL and the five in CATH could contribute to decrease the positive charge. When HMDA was replaced with TRI2, the Zeta potential of all the coatings increased, getting values from 17 to 40 mV. This can be attributed to the fact that TRI2 ligand has an extra amine group compared with HMDA. As discussed in the previously, the positive Zeta potential of the coatings plays an essential role in their antimicrobial mechanisms and interactions with pathogens.

Table 3.2. Zeta Potential (ζ) of the different isolated coatings.

	Zeta potential (ζ-potential) (mV)					
	PYRO	**CAFF**	**GALL**	**CATH**	**DOPI**	**4MET**
HMDA	37.1 ± 1.6	-0.3 ± 0.4	11.2 ± 0.4	5.14 ± 3.0	25.0 ± 1.0	26.7 ± 1.4
TRI2	39.8 ± 0.6	3.5 ± 0.6	21.1 ± 0.2	17.5 ± 0.6	28.6 ± 0.7	28.9 ± 6.9

3.2.2 Antimicrobial activity

After performing a physicochemical characterization of the coatings, whereby their morphology, thickness, robustness, stability, and estimated potential charge were assessed, a deep biological characterization, focusing on their antimicrobial properties, was performed.

3.2.2.1 General screening

Initially, a general screening of the antimicrobial activity for all the coatings was performed to determine possible differences. The twelve combinations of catechols and amines (as well as pristine paper for comparison purposes) were tested against *E. coli.* The logarithmic reduction of the colony-forming units (CFUs) was calculated using the single plate-serial dilution spotting (SP-SDS) method (**Figure 3.15A and B**). Worth to mention, the antibacterial tests were performed under conditions similar to those found in real environments (i.e., after the substrate absorbs and retains a specific volume of bacteria suspension). After 24 h of incubation, no CFUs were detected in any of the coatings, revealing an antibacterial activity above 99.999% (**Figure 3.15C**). These results demonstrated the high antibacterial effectiveness of the synthesized coatings against a resistant and widespread bacteria strain, suggesting a common antibacterial pathway for the developed phenolic-based coatings.

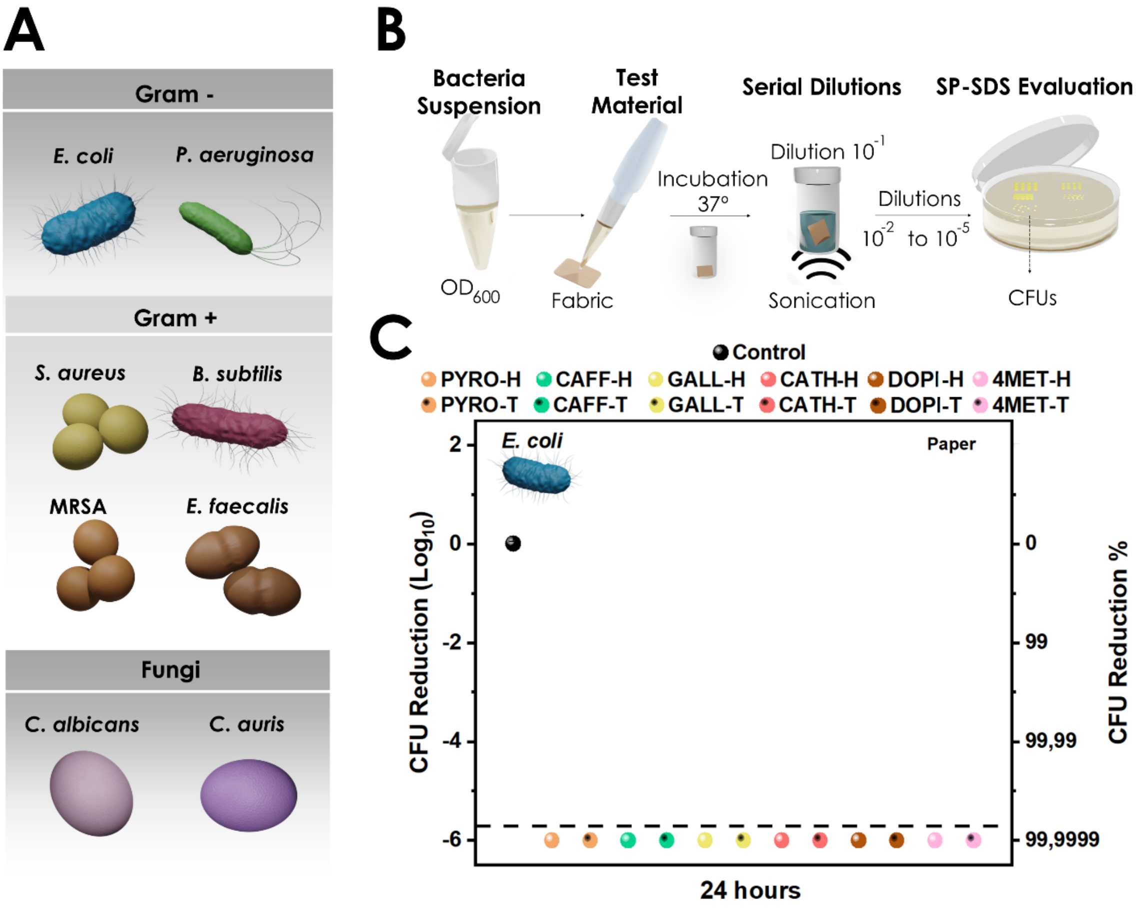

Figure 3.15. Antibacterial properties of the twelve coatings. A) Bacteria and fungi used in this work. **B)** Scheme of the single plate-serial dilution spotting (SP-SDS) methodology. **C)** Screening of the antibacterial properties of the twelve different coatings in paper after being inoculated with *E. coli* for 24 h. In all the cases, the colony-forming units (CFU) logarithmic reduction obtained was below the detection limit (dashed line).

To validate this approach beyond *E. coli*, the antimicrobial properties were studied over a broader range of pathogens. Considering all the coatings, **PYRO-H** and **CAFF-H** were selected for further studies as representative coatings based on their: i) chemical composition (different exposed functional groups), ii) cost-production and iii) optimum coating homogeneity.

3.2.2.2 Determination of the minimum contact-killing time

Prior to the study, the minimum time-exposure for effective antibacterial activity was determined for both **PYRO-H** and **CAFF-H** coatings against Gram-negative (*E. coli*) and Gram-positive (*S. aureus*) bacteria strains in time-lapses of 30, 60 and 180 min (**Figure 3.16**). After 30 min, a CFU log reduction of approximately -1 was observed, without significant differences between both bacteria and coatings. Interestingly, the antibacterial effect increased with time, reaching its maximum activity after 180 min, when CFUs notably decreased and reached the detection limit in almost all the conditions, especially for the *E. coli* strain, while no effect was found for the control sample. Worth to mention, the **CAFF-H** coating was less effective with *S. aureus* in comparison to **PYRO-H**, most probably due to electrostatic repulsion between deprotonated carboxylic acids exposed on the coating surface and the negative charges surrounding bacteria. Overall, 180 min was selected as the optimal incubation period. Additionally, the antibacterial activity of both coatings in contact with *E. coli* and *S. aureus* after 180 min was confirmed by live/dead fluorescent staining. In this double staining kit, SYTO9 enables the staining of all bacteria, while propidium iodide (PI) staining is specifically targeted for dead bacteria. More dead cells (red) than alive-all cells (green) were observed by fluorescence in the coated substrates, especially in *E. coli*, than in the pristine substrate, where almost no death signal was observed (**Figure 3.17**).

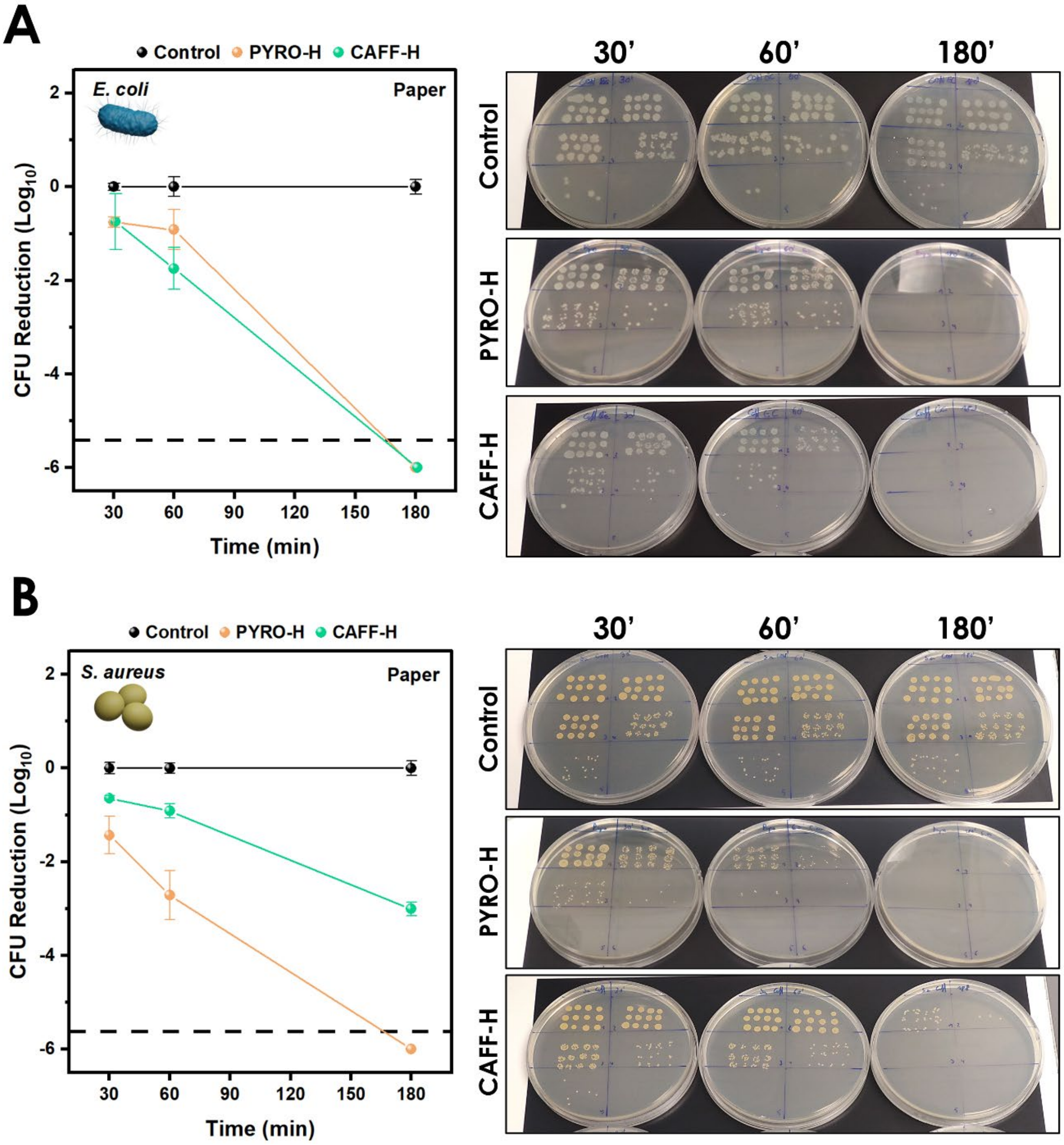

Figure 3.16. PYRO-H and CAFF-H antibacterial time-lapse evaluation. A) CFU logarithmic reduction, in base of exposure time, on paper substrates, with **PYRO-H** or **CAFF-H** coatings against *E. coli* and **B)** *S. aureus*. The dashed line represents the detection limit. In the representative petri plates for each bacterium, when compared the coating (upper row) with the pristine paper (lower row, Control), can be observed a progressive decrease of the *E. coli* and *S. aureus* CFUs in base of the incubation time for both **PYRO-H** and **CAFF-H** coatings.

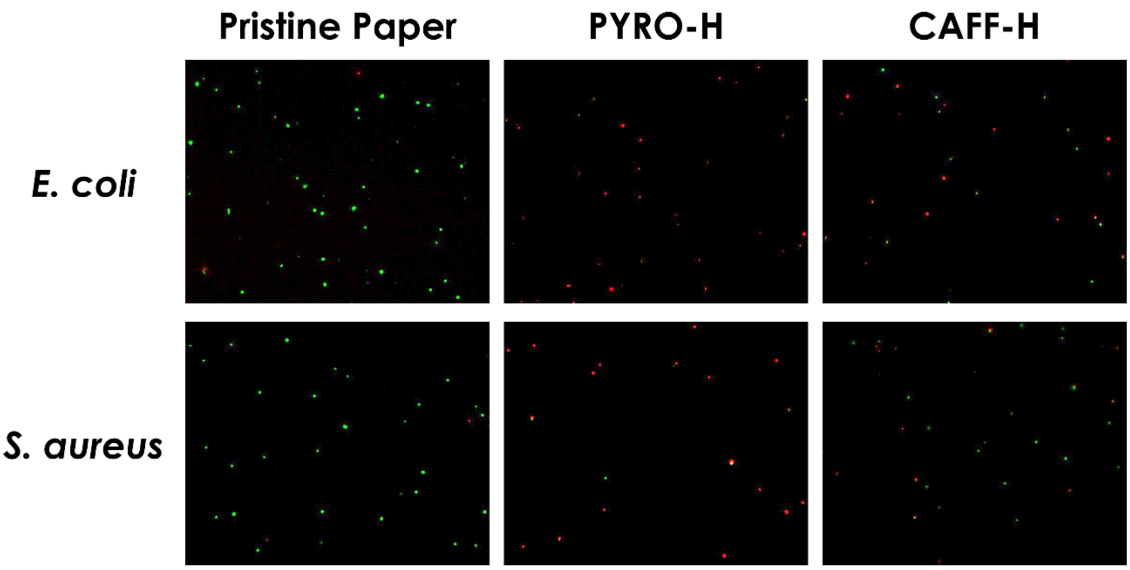

Figure 3.17. Representative images from fluorescence microscopy viability test. Strong green signal represents viable bacteria, whereas those with a damage membrane are shown in red (internalizing propidium iodide). It can be observed that pristine paper is completely innocuous (full green) for both *E. coli* and *S. aureus*, while both coatings, especially the **PYRO-H**, are damaging the membrane of the bacteria (full or mostly red).

3.2.2.3 Spectrum of antimicrobial activity

The antimicrobial activity of **PYRO-H** and **CAFF-H** coatings on paper was studied using four additional bacteria strains (*P. aeruginosa,* MRSA, *E. faecalis* and *B. subtilis*, (**Figure 3.18**) and two fungi (*C. albicans* and *C. auris*) (**Figure 3.19**). For this, the exposition time was set at 180 min and 24 h for bacteria and fungi, respectively. As can be seen in **Figure 3.18**, **PYRO-H** achieved a considerably higher CFU reduction than **CAFF-H** with Gram-positive bacteria, whereas no significant differences were found in the Gram-negative bacteria. As previously discussed, these differences could be attributed to the different electrostatic interactions established between both coatings and the bacteria plasma membrane.

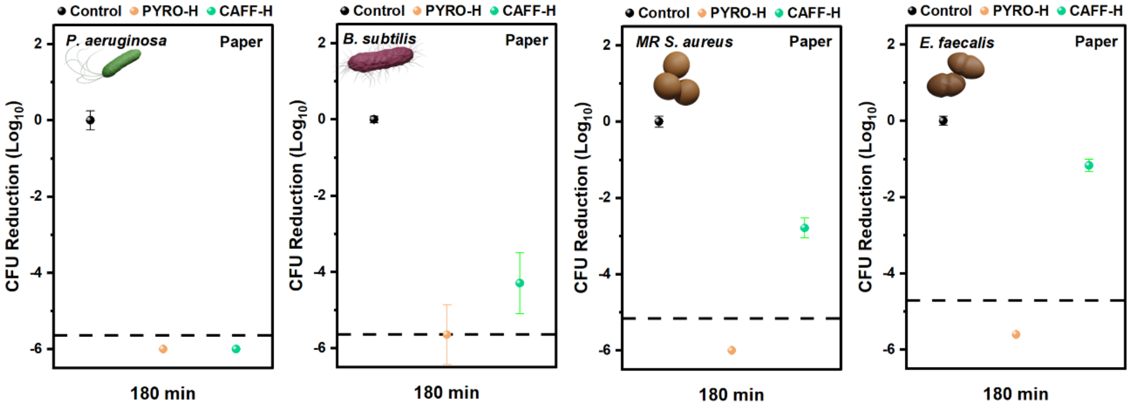

Figure 3.18. Broad antimicrobial spectrum of the two selected catechol-based coatings. CFU logarithmic reduction in coated paper with **PYRO-H** and **CAFF-H** after 3 h of incubation against four different bacteria (*P. aeruginosa,* MRSA, *B. subtilis and E. faecalis*), where **PYRO-H** achieved better results than **CAFF-H**. The dashed line represents the detection limit.

A similar behavior was found for fungi, where both coatings exhibited antimicrobial activity. **PYRO-H** achieved a CFU reduction of nearly 99% with *C. auris* and close to the detection limit (99,99%) with *C. albicans*. **CAFF-H** easily surpassed this reduction in both yeasts (**Figure 3.19**). Instead of quantifying the CFU reduction, this result can also be observed when an inoculated and incubated substrate is directly placed over a plate. This test allowed for seeding in the plate any remaining alive colony that survived to the incubation time in the substrate (**Figure 3.20**). The results showed a considerable decrease in growth density for *C. auris* with **PYRO-H**, but it was much more noticeable with the **CAFF-H** coating (where only a small group of CFUs were observed). On the other hand, *C. albicans* did not show any live colonies for both coatings (only those ones present on the pristine substrate, giving the fungi a squared-shape growth). These results could be attributed to the fact that *C. albicans* presents other non-specific mechanisms, in addition to electrostatic interactions, that allow for its spread. These mechanisms primarily involve physical interactions at the molecular level, allowing the fungus and similar pathogens to adapt to environmental changes and enhance adhesion to different surfaces. [53,54] Besides, it has been recently reported that caffeic acid (precursor of the **CAFF-H** coating) targets the inhibition of key enzymes involved in the survival of fungi.[55,56] All this could explain the higher antifungal efficiency observed in the **CAFF-H** coating compared to **PYRO-H**.

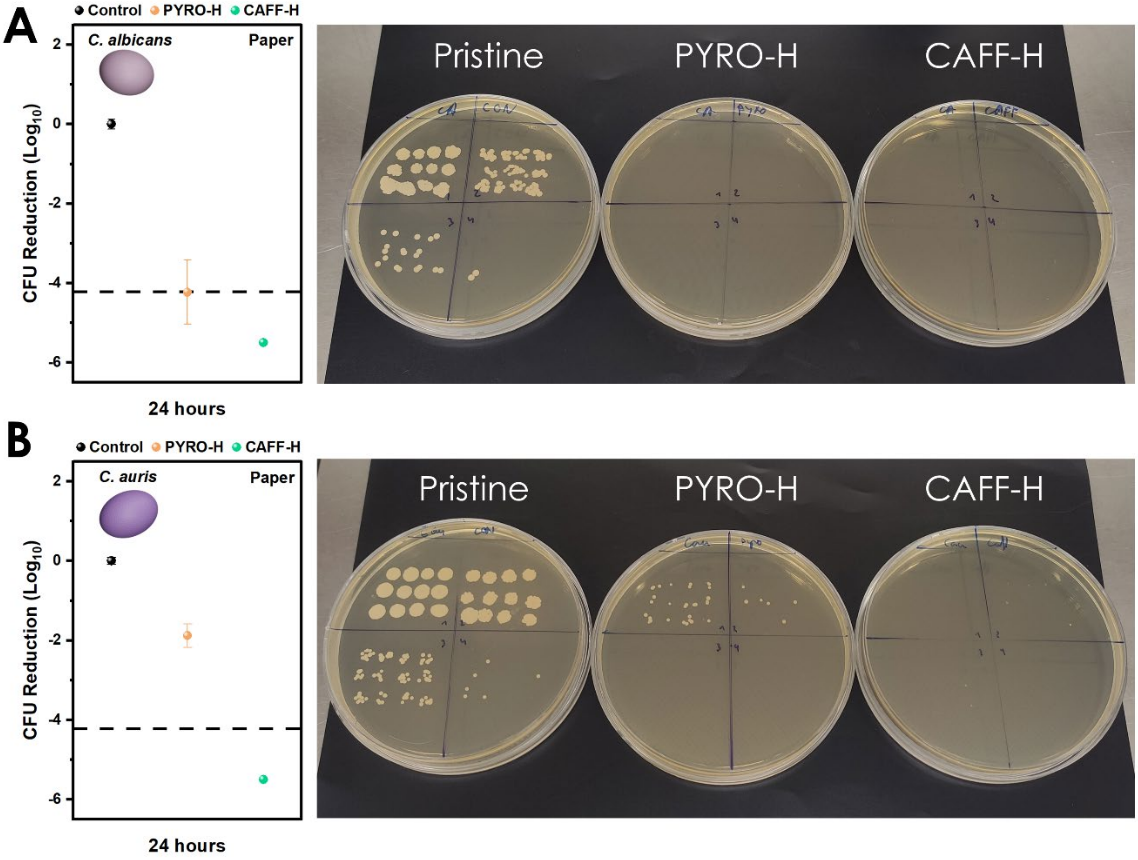

Figure 3.19. Antifungal properties in coated paper. A) CFU logarithmic reduction in coated paper with **PYRO-H** and **CAFF-H** after 24 h against the fungi *C. albicans* and **B)** *C. auris*. Representative plates from the SP-SDS test are also shown. The dashed line represents the detection limit.

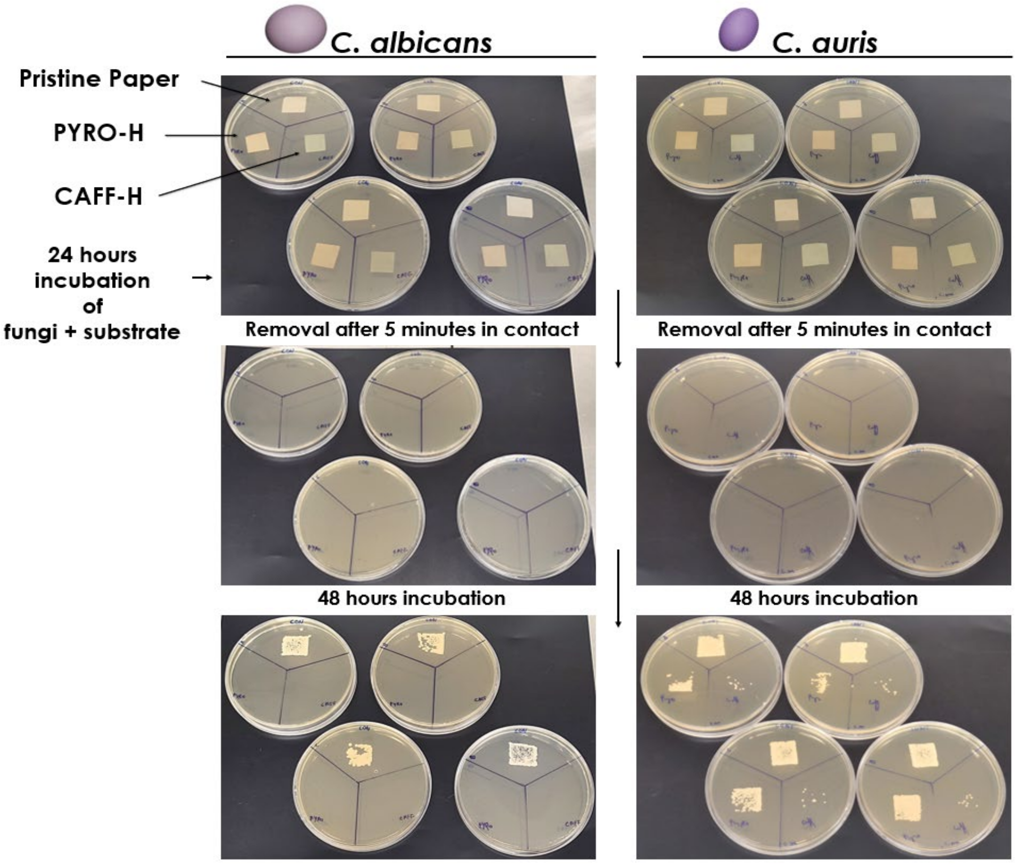

Figure 3.20. Visual representation of the antifungal properties of the coatings. 1.5 x 1.5 cm pristine paper, **PYRO-H** and **CAFF-H** coated substrates tested against *C. albicans* (left) and *C. auris* (right), with 4 repetitions. After 24 h of incubation, each piece stayed in contact with the Petri dish and was removed after 5 min. Both coatings successfully eliminated *C. albicans*. However, in the case of *C. auris*, a slight decrease was observed when incubated in **PYRO-H** and almost a complete elimination in **CAFF-H**.

3.2.3 Antimicrobial mechanism

The remarkable antimicrobial effectiveness previously observed may arise from a complex mechanism that is activated upon direct contact of pathogens with the coated surfaces, favored by the adhesion properties of phenol-based coatings and the electrostatic interactions. It is hypothesized that the primary killing mechanism is the production of ROS. To demonstrate this, the ability of **PYRO-H** and **CAFF-H** coated paper to generate ROS in wet environments was studied. This quantification was performed by fluorescence, where a higher signal correlates with a higher ROS concentration. Initially, the ROS production capacity of **PYRO-H** alone was monitored for 24 h, in the presence or absence of three different antioxidants: 10 mg/ml N-Acetyl-L-Cysteine (NAC), 1 mM Trolox or 10 mM ascorbic acid (AsAc). Interestingly, the results showed that, besides the coating's ability to generate sustained ROS production over time, this production could be decreased (Trolox) or almost completely annulled (NAC and AsAc) (**Figure 3.21A**). Subsequently, a second ROS generation test was performed using both **PYRO-H** and **CAFF-H** coatings and then adding only NAC at concentrations of 1 mg/ml and 10 mg/ml. Results showed that **PYRO-H** induced a higher ROS production (higher fluorescence signal) than **CAFF-H**, which explains why **PYRO-H** achieved better overall results in the antimicrobial assays.

Additionally, it was observed that the addition of NAC induced a slight decrease in the fluorescence signal of both coatings when using 1 mg/ml, reducing it to almost zero at 10 mg/ml. These results confirmed that ROS generation can be both counteracted and modulated by using NAC as antioxidant (**Figure 3.21B**).

Following these preliminary results, the effect of antioxidant addition was analyzed in the presence of bacteria. For this, three suspensions of *E. coli* were supplemented with 10 mg/ml of NAC, 10 mM of AsAc, or nothing (control) and tested for 3 h on pristine, **PYRO-H** and **CAFF-H** coated paper substrates. Despite the slight toxic effect of NAC observed on the pristine paper, the resulting plates showed a clear decrease in the antibacterial activity of both coatings (slightly more in **CAFF-H**) when this ROS-scavenger was present (**Figure 3.21C** and **D**). Both coatings showed similar and successful results when tested with AsAc. However, significant toxic effects were noted on the uncoated paper, which were not found on the **PYRO-H** and **CAFF-H** coatings. This could be attributed to the neutralization between the antioxidant (AsAc) and the oxidant (coatings), thus protecting *E. coli*. Therefore, these results confirmed the suggested mechanism based on sustained ROS production.

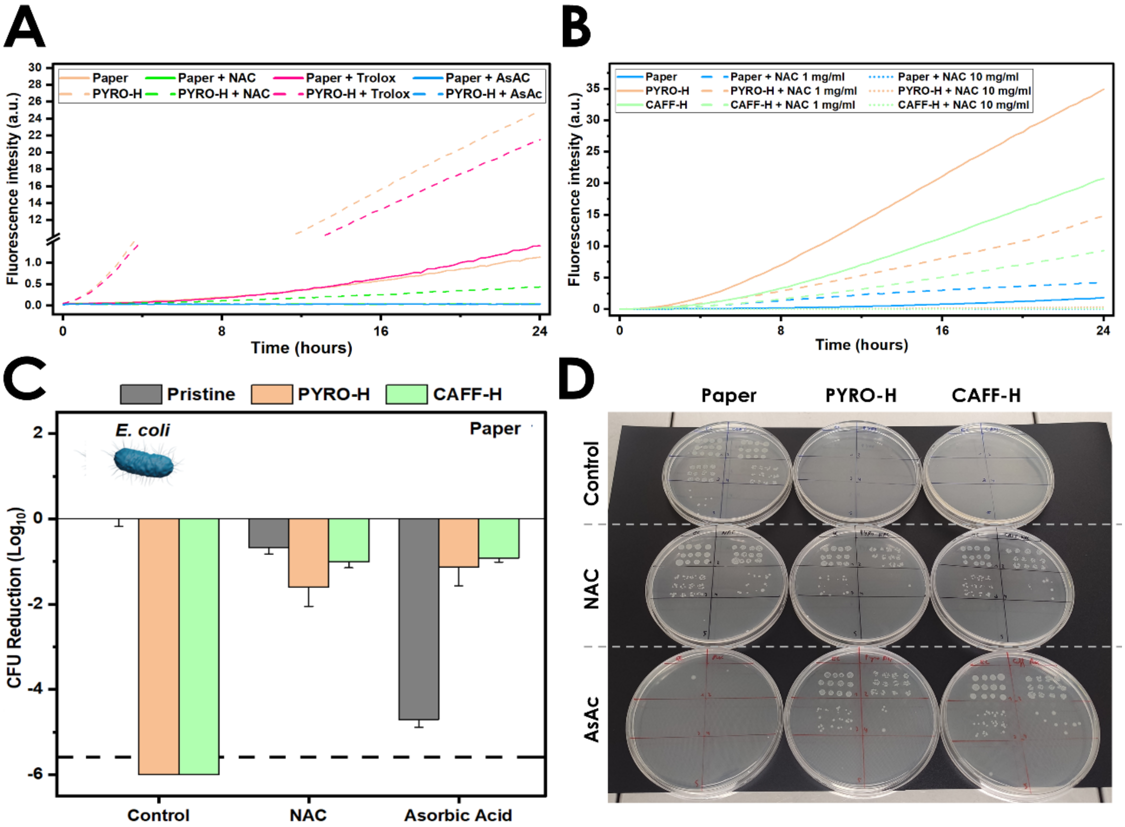

Figure 3.21. Reactive oxygen species (ROS) generation in coated paper. A) Reactive oxygen species generated by pristine and **PYRO-H** coated paper, in presence or absence for 24 hours of N-Acetyl-L-Cysteine (NAC) 10 mg/ml, Trolox 1 mM and ascorbic acid (AsAc) 10 mM. It where can be observed that the three reagents can decrease the signal achieved by the coating. **B)** ROS generated by pristine, **PYRO-H** and **CAFF-H** coated paper in the presence or absence of N-Acetyl-L-Cysteine (NAC) (1 mg/ml and 10 mg/ml) for 24 h, where is demonstrated that NAC can modulate the signal obtained for both coatings. **C)** SP-SDS test in pristine, **PYRO-H** and **CAFF-H** coated paper against an *E. coli* suspension with or without (control), 10 mg/ml of NAC or AsAc 10 mM, showing the CFU logarithmic reduction after 3 h incubation and **D)** the representative plates of the test.

Finally, the production of different types of ROS species was analyzed, providing a detailed understanding of the oxidative processes involved. For this, both **PYRO-H** and **CAFF-H** coated paper were used to determine the type and relative amount of each ROS produced. When compared to the uncoated substrate, both coatings generated hydrogen peroxide, especially **PYRO-H** (**Figure 3.22A**). However, only **CAFF-H** showed remarkable signs of hydroxyl radicals and superoxide radical production (**Figure 3.22B** and **C**).

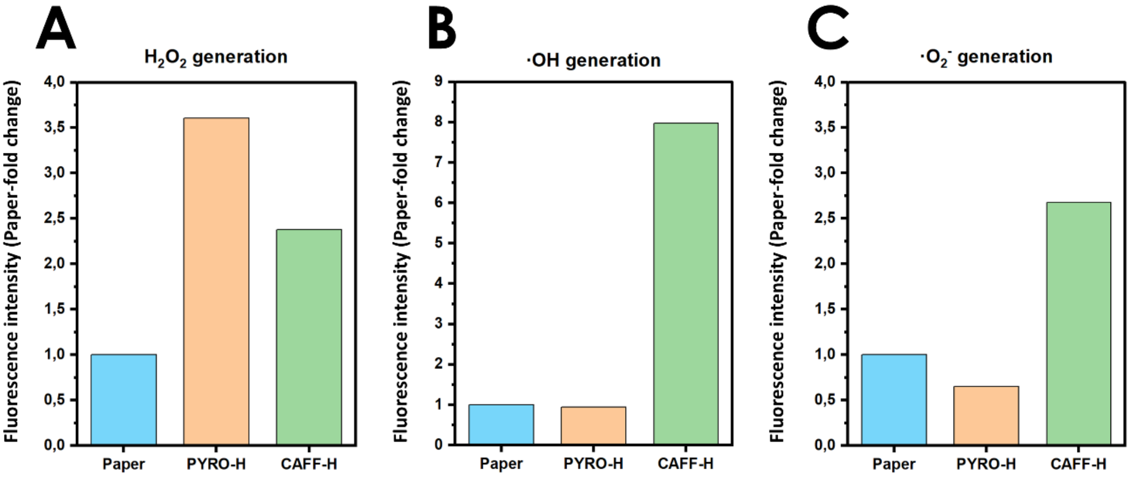

Figure 3.22. Selective detection of reactive oxygen species. Generation of **A)** hydrogen peroxide, **B)** hydroxyl radical and **C)** superoxide radical by pristine, **PYRO-H,** and **CAFF-H** coated paper. In each case, the signal is represented as fold of the obtained vs the pristine paper after subtracting the blank.

It is important to remark that ROS species such as H_2O_2 or ·OH lack potent disinfectant effects or have a short half-life.[57] For this reason, the outstanding antimicrobial effectiveness suggests other interactions. In this sense, a second mechanism could be induced due to the presence of protonated amine groups on the surface, whose positive charges (**Table 3.2**) would interact with the negatively charged cell wall of the bacteria.[31]

The electrostatic attractive interactions play a crucial role in promoting close contact between microorganisms and the coating surface. This process is essential for enhancing both adhesion and the ROS effect. The bioinspired coatings described in this Chapter exhibited a multi-pathway antimicrobial activity, further enhanced by the adhesion properties provided by catechol groups (**Figure 3.23**). The mechanisms and interactions previously described result in irreversible damage to the pathogens based on: i) physical lysis, ii) charge disruption and iii) exudation of cell contents.

To shed more light in this multi-step mechanism, the six bacteria and the two fungi tested were studied by SEM after interacting for 180 min and 24 h, respectively, with PYRO-H and CAFF-H coatings and the pristine paper. In all cases, the direct contact between the coating and the pathogens led to a severely damaged plasma membrane, exhibited an irregular and deflated shape, which compromised their viability. The antimicrobial effect of the coatings was evident when comparing the pathogens in contact with uncoated paper, where bacteria and fungi showed normal morphology and appeared visually viable (**Figure 3.24A**).

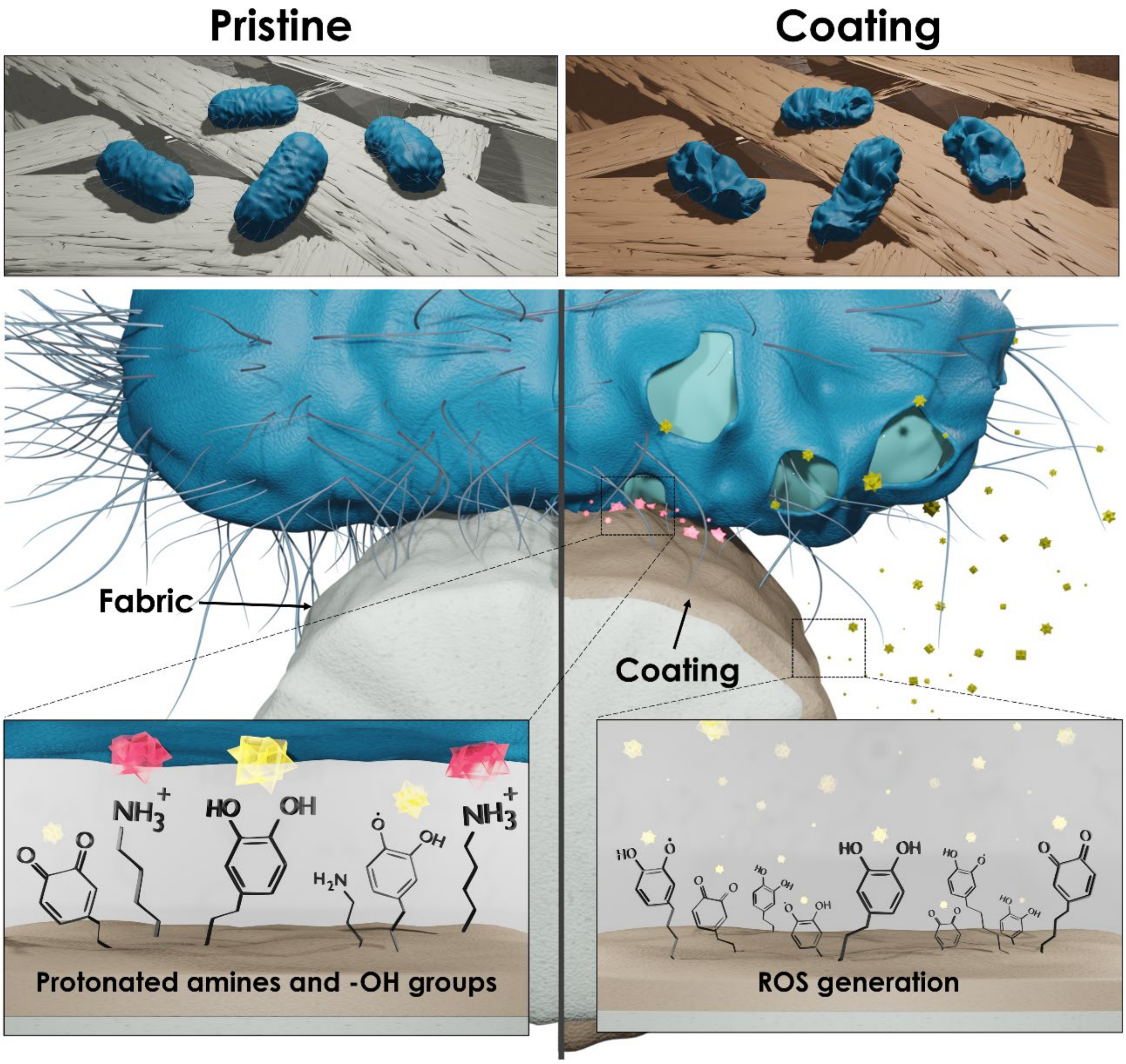

Figure 3.23. Antimicrobial mechanisms of the coatings. Schematic representation of the proposed antimicrobial mechanisms, where the retention of the cells by the catechol groups, the interaction of protonated amines and ROS generated by the active oxidation of exposed functional groups from the coatings are suggested to play a main role.

Isolated cultures provide important information about the overall behavior of the different coatings against groups of microorganisms (Gram-positive, Gram-negative and fungi). However, in real environments (such as a wound), microorganisms are typically found as a mixture of heterogeneous species rather than pure cultures. To mimic this scenario, a bacteria cocktail was generated and used for seeding. A mixture of *E. coli, P. aeruginosa*, *S. aureus*, *E. faecalis* and *B. subtilis* were inoculated on **PYRO-H** and **CAFF-H** coated papers for 180 min. Interestingly, SEM micrographs showed bacteria-damaged morphology simultaneously for all tested strains. Besides, no CFUs were observed on the SP-SDS plates for **PYRO-H** (**Figure 3.24B** and **C**). Overall, these results demonstrated the broad antimicrobial range of action of the developed coatings, effective both against isolated and mixed strains.

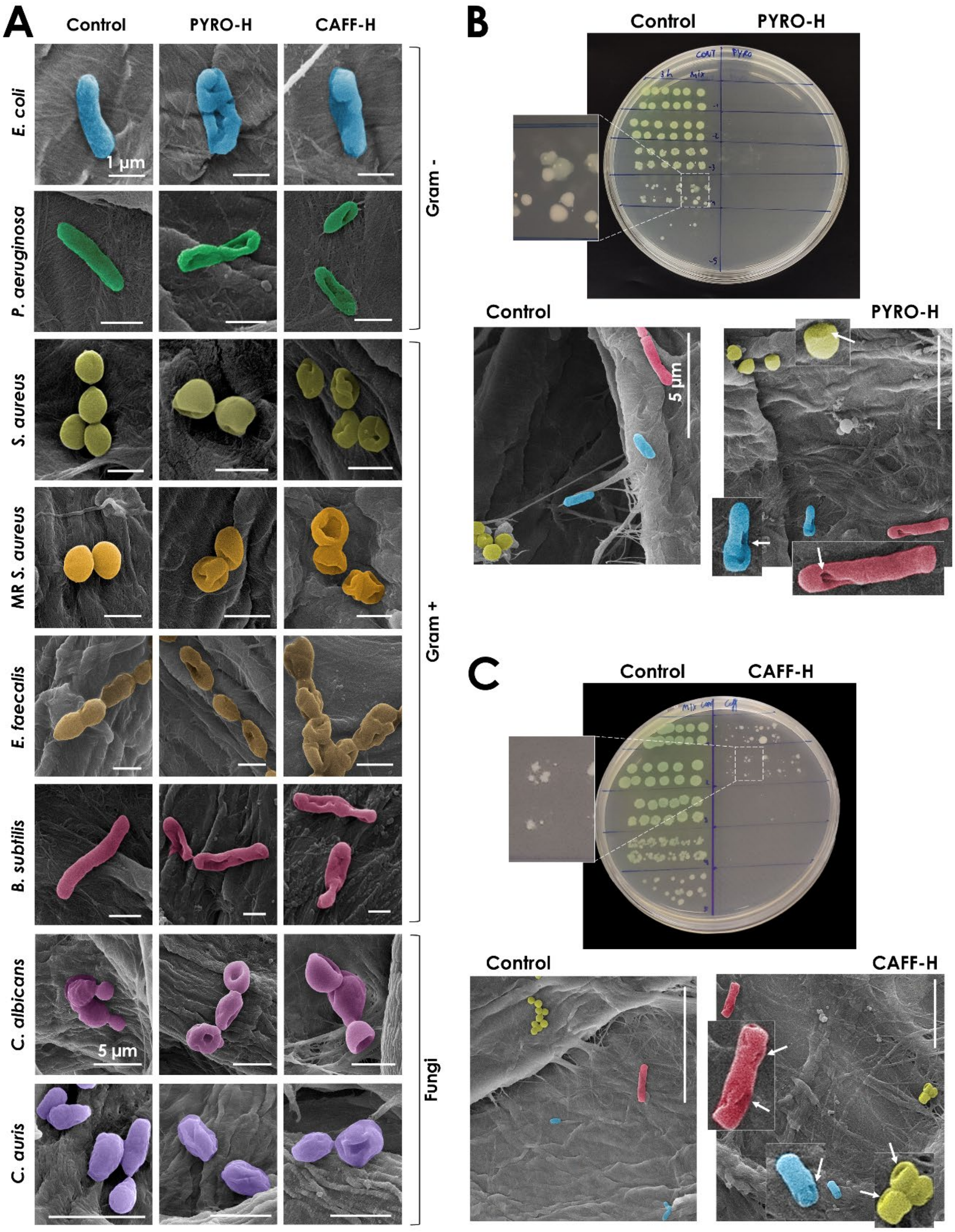

Figure 3.24. Cell membrane damage induced by the coatings. A) Colored SEM images of the eight different microorganisms (Gram-negative: *E. coli* and *P. aeruginosa*, Gram-positive: *S. aureus*, methicillin-resistant *S. aureus* (MRSA), *E. faecalis*, *B. subtilis*, Fungi: *C. albicans* and *C. auris*) in pristine paper (upper row), **PYRO-H** (center row) and **CAFF-H** (bottom row) coatings. Pathogens in the control substrate showed a stable and viable morphology and were visually viable. Those microorganisms in contact with coatings, presented severely damaged membranes and irregular shapes. The scale bars correspond to 1 µm for bacteria (Gram-negative and Gram-positive) and 5 µm for Fungi. **B)** SP-SDS plate and SEM pictures after testing **PYRO-H** and **C) CAFF-H** coated paper against a mixed suspension with *E. coli, P. aeruginosa, S. aureus, E. faecalis* and *B. subtilis* for 3 h. SEM pictures show that the damage (pointed with arrows) and the changes of the cell membrane can be observed simultaneously in different bacteria for both coatings. Scale bars correspond to 5 µm.

3.2.4 Stability and biocompatibility

To further validate the robustness of the developed coatings, an assay to test their long-lasting antibacterial activity was conducted. This assay aimed to determine how the antibacterial properties of **PYRO-H** coatings persisted over different time intervals of 0, 15, 30, 60, 120 and 180 days (**Figure 3.25**). All the samples used in this assay were synthetized the same day and stored in dark and dry conditions until used. In each case, CFU reduction was assessed with *E. coli* and *S. aureus*, following the previous protocols and 180 min of incubation period. After comparing the results over time, no changes in the antibacterial activity for both bacteria for at least 2 months were observed. Although a decrease in activity was observed after 4 months, excellent results were still obtained, with reductions in *E. coli* and *S. aureus* higher than 99.9% and 99%, respectively. Finally, after 6 months, approximately 90% reduction could still be achieved for both bacteria. These results demonstrated the stability and long-lasting ROS generation activity of the developed coatings.

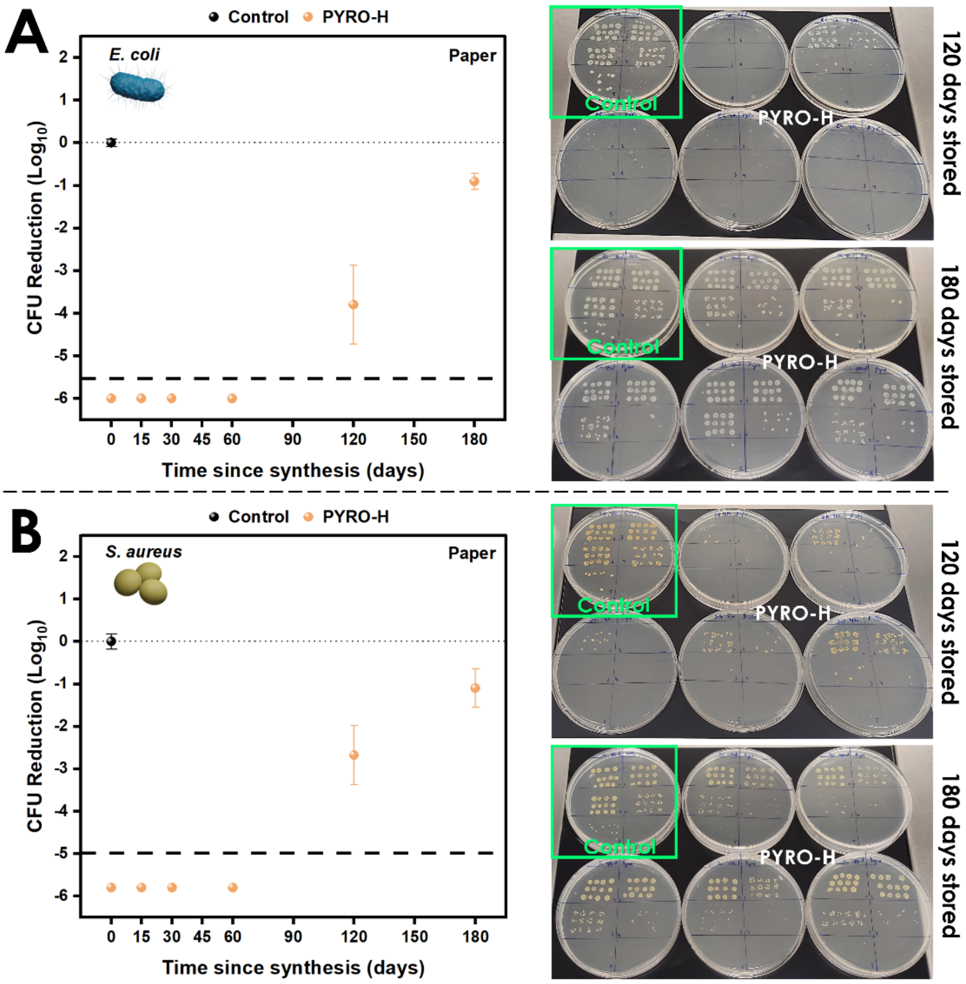

Figure 3.25. Antibacterial properties stability of PYRO-H coating. A) The **PYRO-H** coating was synthetized and tested after being stored for 15, 30, 60, 120 and 180 days against *E. coli* and **B)** *S. aureus* (right). The activity was maintained perfectly at least for 2 months. After 4 months, despite a decrease was observed, a CFU reduction higher than 99.9% and 99% for *E. coli* and *S. aureus* was still obtained*,* respectively. Finally, and after 6 months, approximately 90% reduction could still be achieved in both bacteria. Representative plates for each bacteria strain are also shown, being the control (pristine paper) the one inside a green square, while the **PYRO-H**, the five ones outside it.

Since these coatings are generally used in environments involving direct contact with human tissues, their biocompatibility is fundamental. For its study, NIH/3T3 fibroblasts were exposed to the different catechol-based coatings for 24 h. The results showed no significant differences in all conditions compared with the control (only cells) (**Figure 3.26**), demonstrating a cell viability higher than 90%, and thus corroborating their potential application in healthcare.

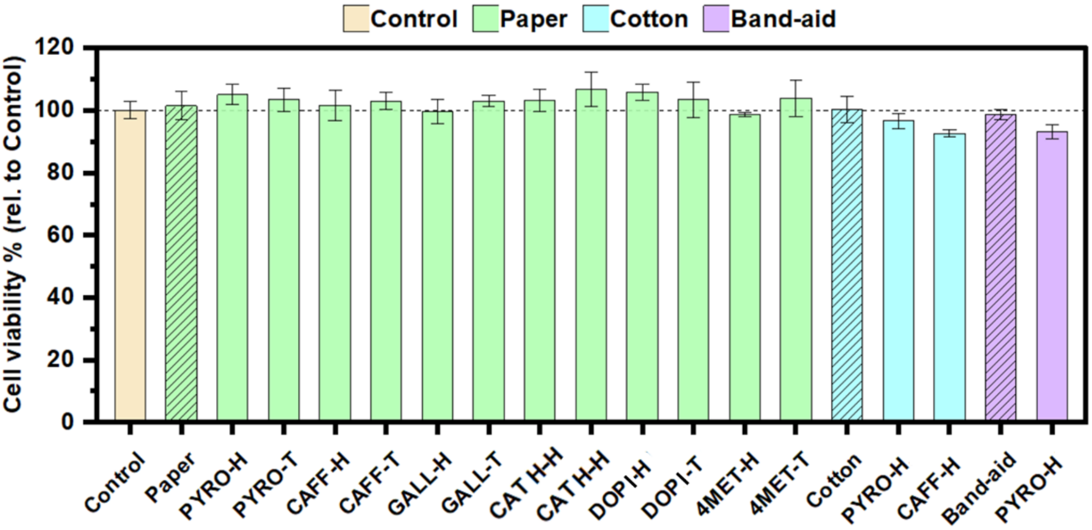

Figure 3.26. Coating biocompatibility. Viability test in NIH/3T3 cell line. The signal shown for each condition is relative to the control with only cells. Stripped bars correspond to pristine substrates while flat ones to coatings. A total of 4 repetitions, each with 3 replicas, were performed.

3.2.5 Antibacterial activity on different substrates

3.2.5.1 Coating universality

The ability of coatings to be used on different substrates was validated by applying both **PYRO-H** and **CAFF-H** to cotton (from a lab coat) and polypropylene (from a surgical mask) (**Figure 3.27A**). Similar to paper, the coatings were homogenously distributed, covering the fibers without clogging the pores (thus retaining their intrinsic permeability properties), with some rugosities of no relevance (**Figure 3.27B**). Overall, these results corroborate the fine-tuned control of the coatings independently from the substrate nature, and without any previous functionalization needed. Additionally, the presence of the coating modified the wettability of the substrates, a feature relevant for a proper performance. For instance, the hydrophobic surface of polypropylene becomes hydrophilic upon coating. This was corroborated by measuring the contact angle of pristine and coated polypropylene, obtaining values of 126° and 0°, respectively (**Figure 3.27C**).

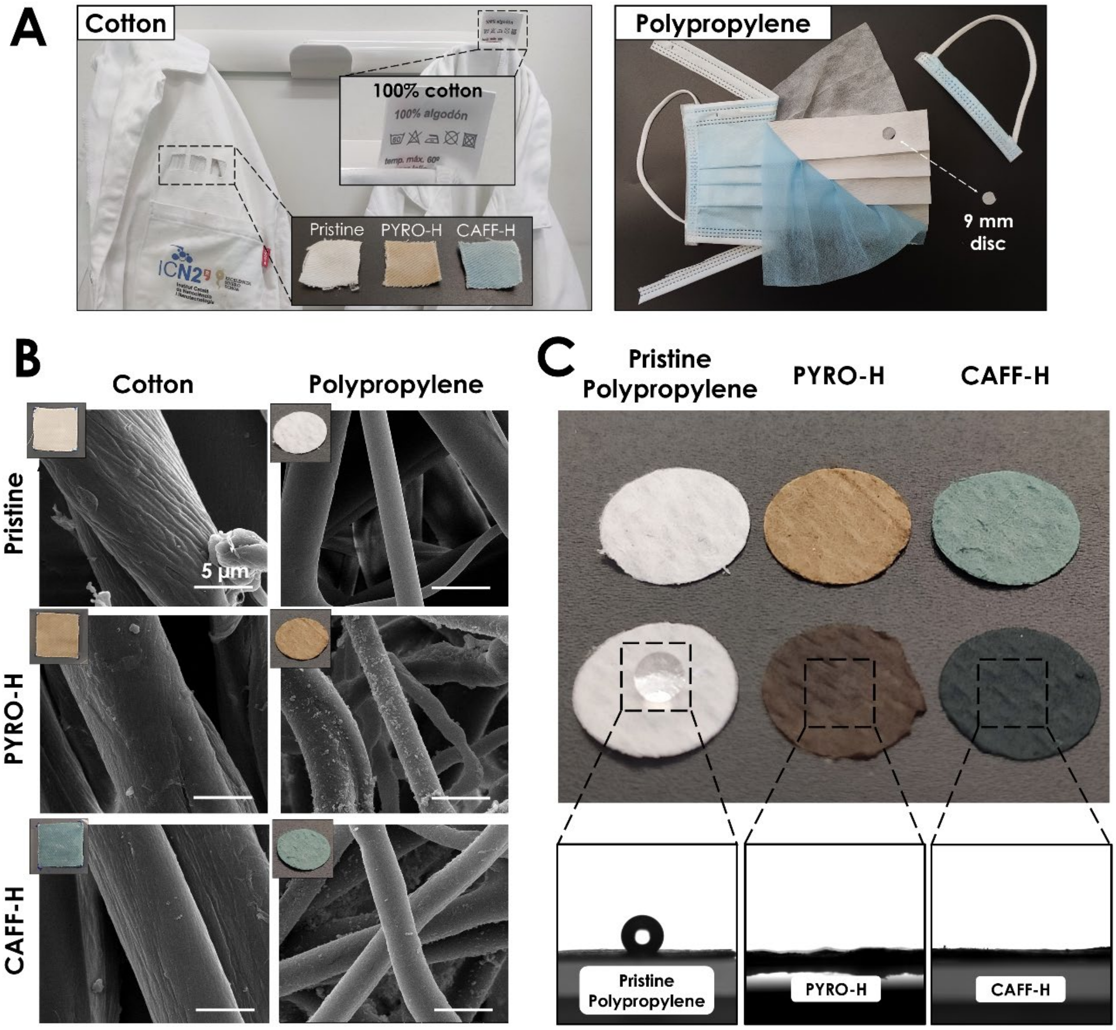

Figure 3.27. Coating of cotton and polypropylene substrates. **A)** Cotton was obtained from a 100% cotton lab coat and polypropylene from the middle layer of a commercial N95 surgical mask. **B)** SEM micrographs of the selected **PYRO-H** and **CAFF-H** coatings in cotton (left) and polypropylene (right) substrates. The SEM scale bars correspond to 5 µm. **C)** Comparison of the dry pristine, **PYRO-H** and **CAFF-H** coated polypropylene in the upper row, while in the lower one the same conditions after applying a drop of 2 µl of water. Despite the hydrophobic nature of the pristine material, both coatings turned its surface strongly hydrophilic, changing the contact angle from approximately 126° to 0° in both cases.

Pristine polypropylene has antifouling properties mainly due to its hydrophobic nature, which repels bacteria but still allows them to spread to other surfaces. The modification of polypropylene with the developed bioinspired coatings results in a hydrophilic substrate, reducing the antifouling effect and allowing direct contact with bacteria. Consequently, these bacteria can be retained and eliminated through the mechanisms previously described, thus stopping their spread. The presence of a hydrophilic environment is crucial, as it promotes interactions between bacteria and surfaces, thereby enhancing the antibacterial effect at the bio-interface.[58]

3.2.5.2 Antibacterial activity

After successfully coating cotton and polypropylene with **PYRO-H** and **CAFF-H**, their antimicrobial activity was tested against *E. coli* and *S. aureus* at 180 min. A visual comparison of the antibacterial properties on paper and cotton for both bacteria is shown in **Figure 3.28A,** following a similar procedure as previously described (section 3.2.2.3). In the case of polypropylene, strong antibacterial activity was observed for both coatings against both bacteria (**Figure 3.28B**). However, a lower antibacterial effect was observed for cotton coated with **CAFF-H**, particularly with *E. coli* (**Figure 3.28C**). These differences could be tentatively attributed to the intrinsic properties of the material such as permeability, fiber content, morphological structure and how it fine-tunes the interactions with bacteria. These properties could influence interactions with bacteria, resulting in varying levels of antibacterial efficiency. Interestingly, the universal application of the developed coatings allows to overcome these differences by selecting the specific coating and adapting the preferred substrate based on the final application.

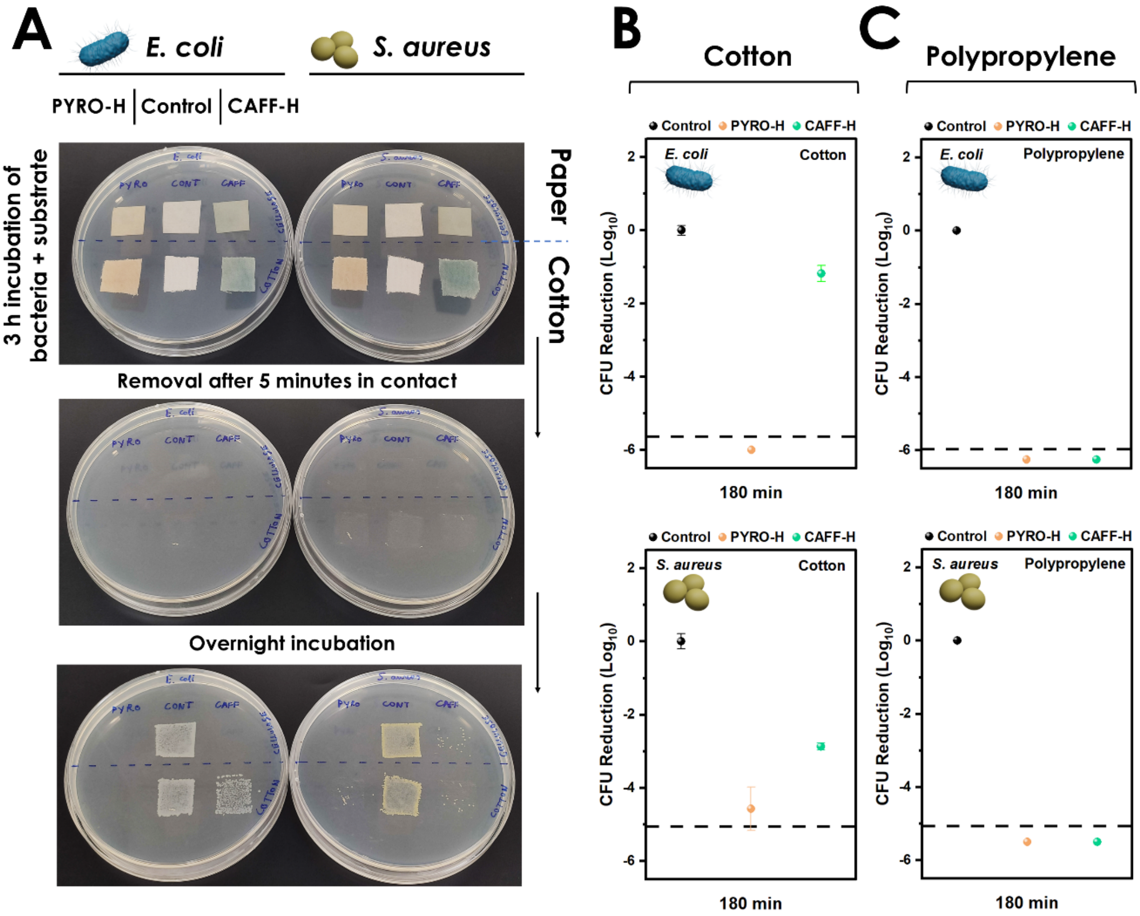

Figure 3.28. **Robustness of the antimicrobial properties. A)** Antibacterial properties of the coatings, where a 1.5 x 1.5 cm paper and cotton substrates (upper and lower row in each Petri dish, respectively) coated with **PYRO-H** and **CAFF-H**, were tested against *E. coli* (left) and *S. aureus* (right). After 3 h of incubation, each piece stayed in contact with the Petri dish and removed after 5 min. The next day, a decrease or complete elimination of CFUs when compared with pristine substrates was observed. These results were in accordance with the obtained by SP-SDS quantification. **B)** CFU logarithmic reduction of *E. coli* and *S. aureus* in coated cotton and **C)** polypropylene with **PYRO-H** and **CAFF-H** after 3 h of incubation. The dashed line represents the detection limit.

3.2.6 Proof-of-concept case: in vitro and ex vivo validation of commercial band-aids

To validate the performance of the developed coatings, a close-real scenario experiment was performed using commercial band-aids. While the two main roles of a band-aid are to act as a physical barrier between the exterior and the wound and absorb the excess moisture produced, it also creates a humid environment where bacteria can easily proliferate, leading to infection and a slower healing process. Therefore, a potential application of the developed bioinspired coatings could be the modification of band-aids to endow them with antimicrobial activity. This would reduce the infection risk of the wound, since the absorbed moisture and surrounding areas would be exposed to in-place generated ROS species, thus inducing antimicrobial activity, which in turn improves wound healing (**Figure 3.29**).

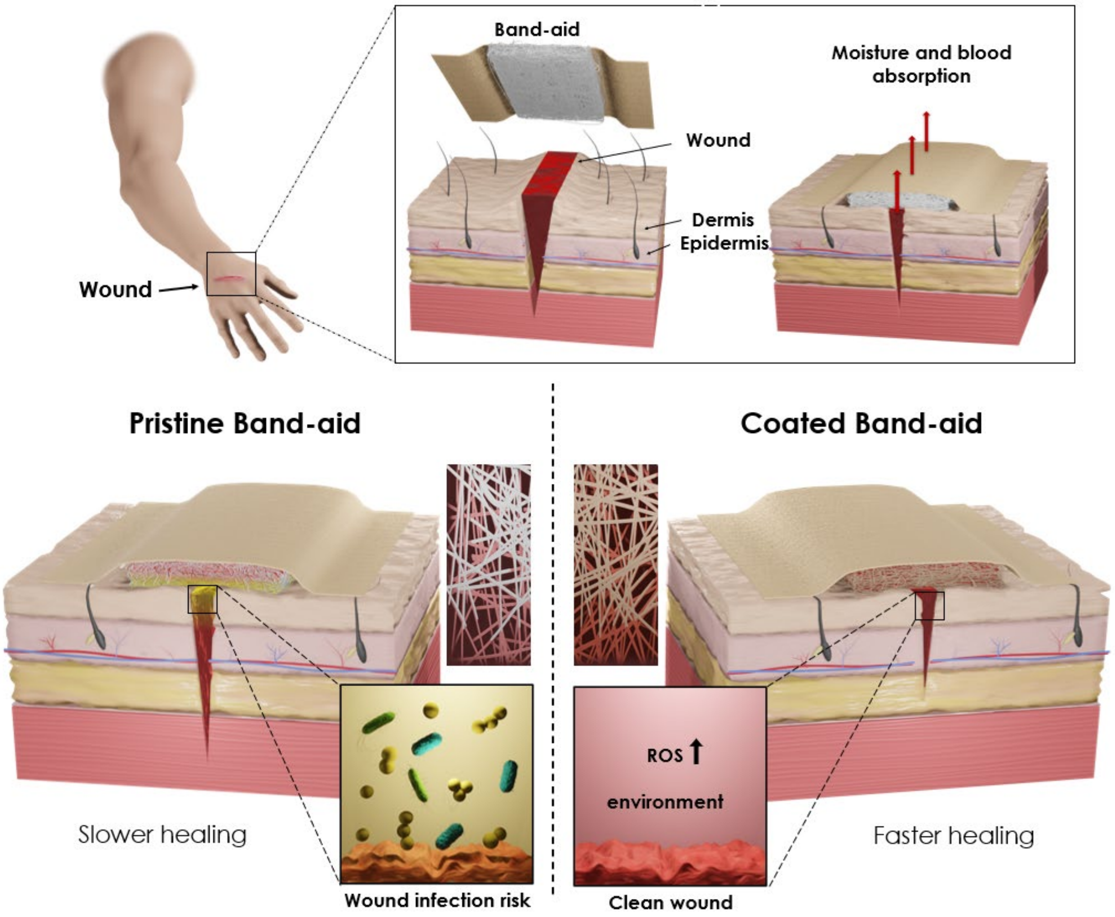

Figure 3.29. Coated band-aid applicability in wound healing. Schematic comparison of a wound covered with a pristine and a coated band-aid. Whereas in the first case the lack of antimicrobial properties entails a risk of wound infection, it is suggested that the ROS generated by the catechol-based coatings could decrease considerably this risk, improving the healing time.

Therefore, as a proof-of-concept for evaluating the developed coatings, both **PYRO-H** and **CAFF-H** coatings were applied to commercial band-aids (a composite material made of: viscose, polyethylene and polypropylene) (**Figure 3.30A**). The coatings were generated for 18 h to ensure a complete and homogenous covering around both the fibers (hydrophobic) composing the band-aids and the plastic net holding them (in contact with the skin, hydrophobic) (**Figure 3.30B**). As previously observed in paper, cotton and polypropylene substrates, **PYRO-H** was more prone than **CAFF-H** to generate nanoparticles on the surface of the coating on this substrate as well.

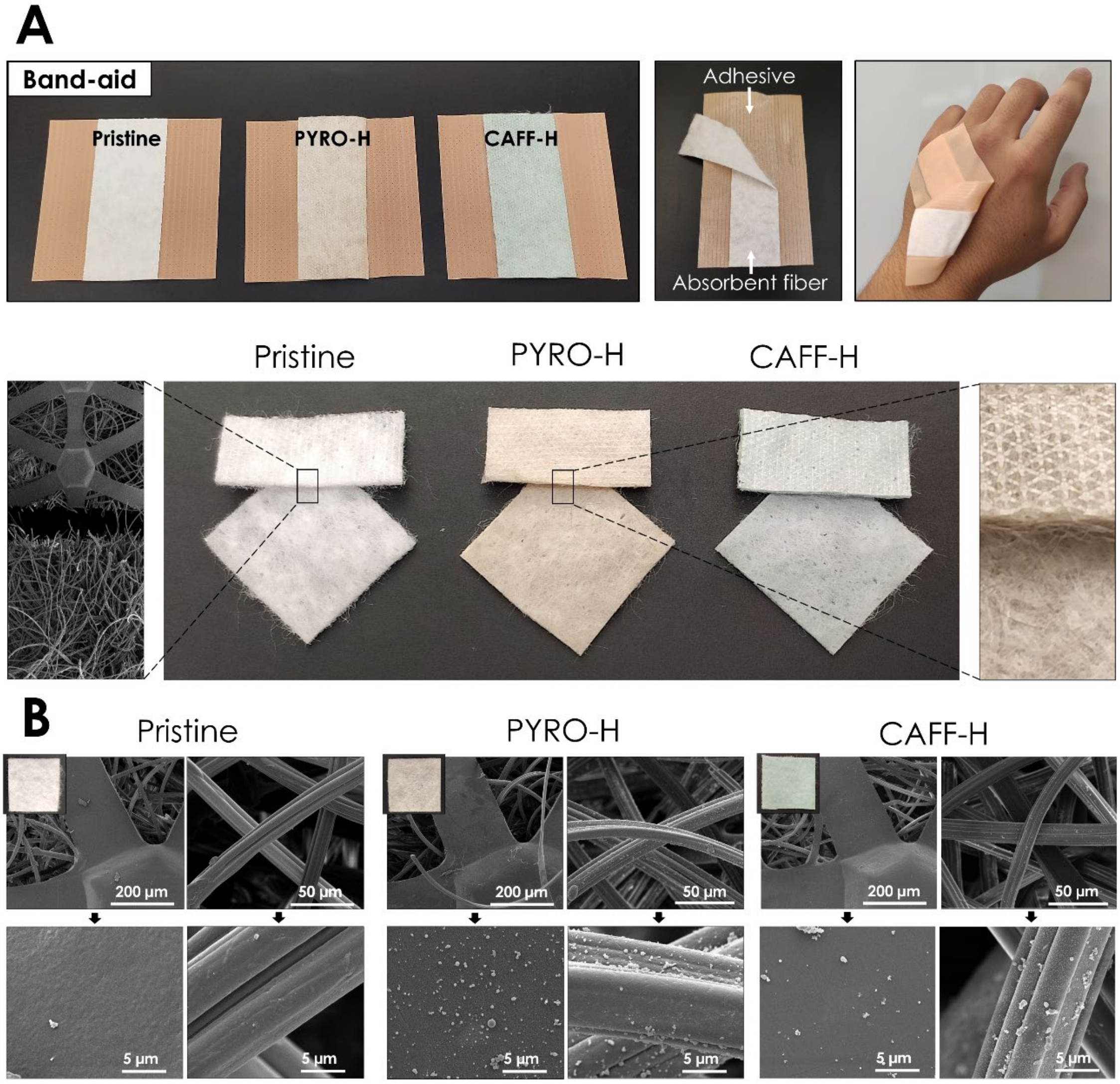

Figure 3.30. Coating of commercial band-aids. A) Visual comparison of pristine, **PYRO-H** and **CAFF-H** coated band-aid, where the absorbent fiber is removed and used as substrate. B) SEM micrographs of the pristine and coated band-aid in both of their sides.

As previously mentioned, the characteristics of the selected substrates, such as fiber content and density, permeability, thickness and morphological structure, may not only affect the antibacterial properties but also influence the homogeneity of the coating and the distribution of particles on the surface (**Figure 3.31A**). In this study, after coating four different substrates, it was observed that the thinnest and most sparsely distributed fibers resulted in the highest number of nanoparticles, in the following order: polypropylene, band-aid, cotton and paper (**Figure 3.31B**). Additionally, greater agitation contributed to an increase in byproducts and nanoparticles formation in the coating, which further explains why polypropylene exhibited the highest amount.

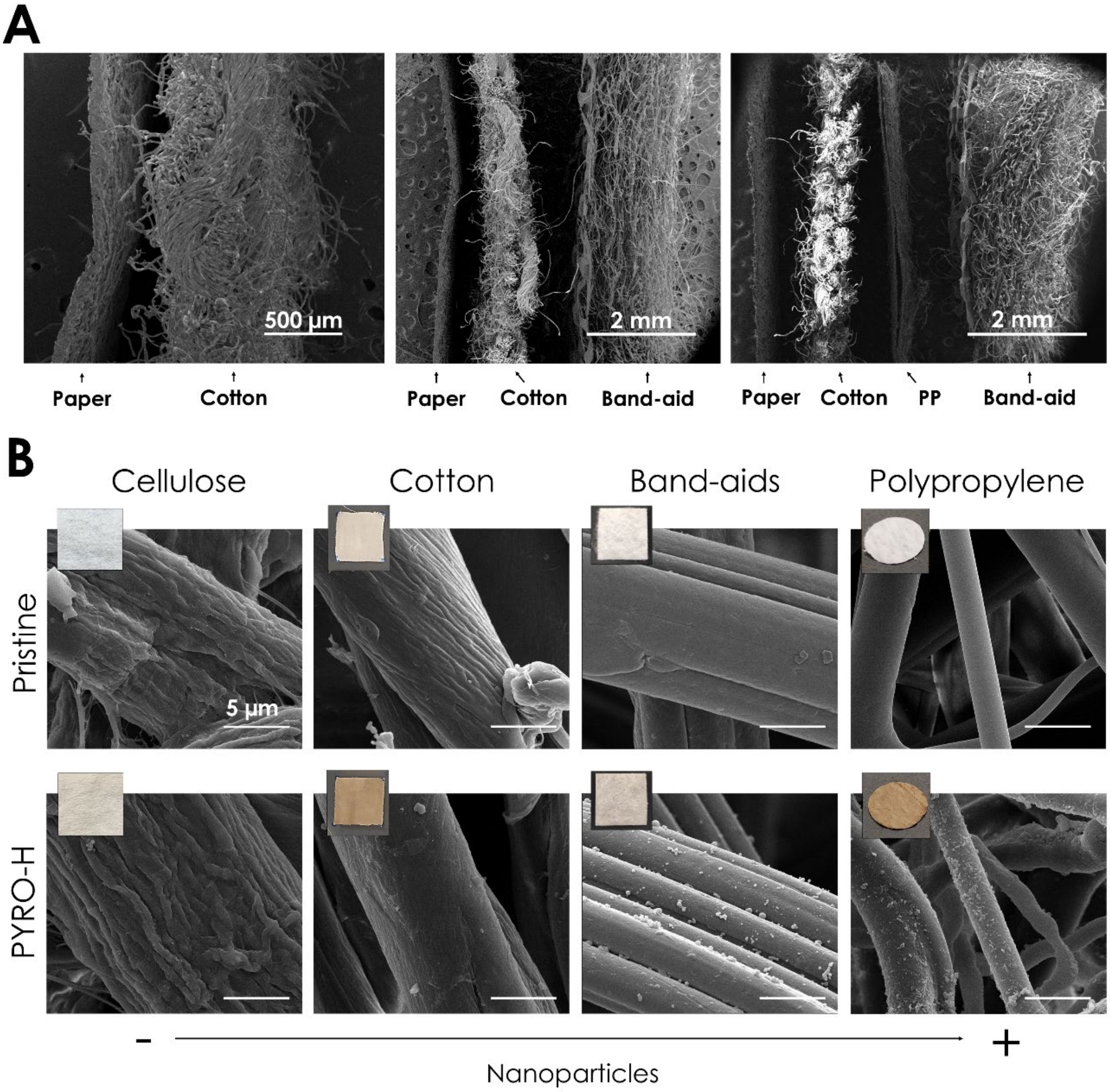

Figure 3.31. Substrates comparison. A) When comparing the thickness of the pristine substrates, it can be observed that the width of paper and polypropylene is approximately eight times smaller than cotton, which is three times smaller than the band-aid. **B)** Changes in thickness and specially the distribution and size of the fibers can affect the coating process. It has been observed that the fiber-like substrates, like polypropylene and band-aid, are more prone to synthetize nanoparticles in the surface of these substrates. The scale bars correspond to 5 µm.

The antibacterial properties of the resulted coated ban-aids were tested against *E. coli* and *S. aureus* for 24 h. When *S. aureus* was analyzed, a CFU reduction of at least 99.99% was observed for both coatings (detection limit). Interestingly, slightly lower results were obtained with *E. coli* for both **PYRO-H** and **CAFF-H** coatings, being approximately 99.9% and 99%, respectively (**Figure 3.32A** and **B**). For further validation, the antibacterial properties were tested in a more realistic environment using *ex vivo* tissue. An infection scenario was mimicked using fresh pieces of pig skin (extracted and immediately used), establishing a wound model by performing a hole in the skin and subsequently inoculating it with *E. coli* (**Figure 3.32C**). The mimicked infected wound was then covered with either pristine or coated band-aids. In this case, **PYRO-H** was selected as a candidate due to its overall superior antimicrobial properties as previously discussed. Remarkably, after 24 h of incubation, **PYRO-H** achieved an outstanding 90% CFU reduction in the infected *ex vivo* wound (**Figure 3.32D**). Although the antimicrobial activity may seem limited, it is important to note that it was achieved in tissue that has been in a decomposing state since extraction, and especially during the incubation period. Therefore, these results suggested the excellent ability of the coatings for their potential application against bacterial spread, thereby preventing infection progression.

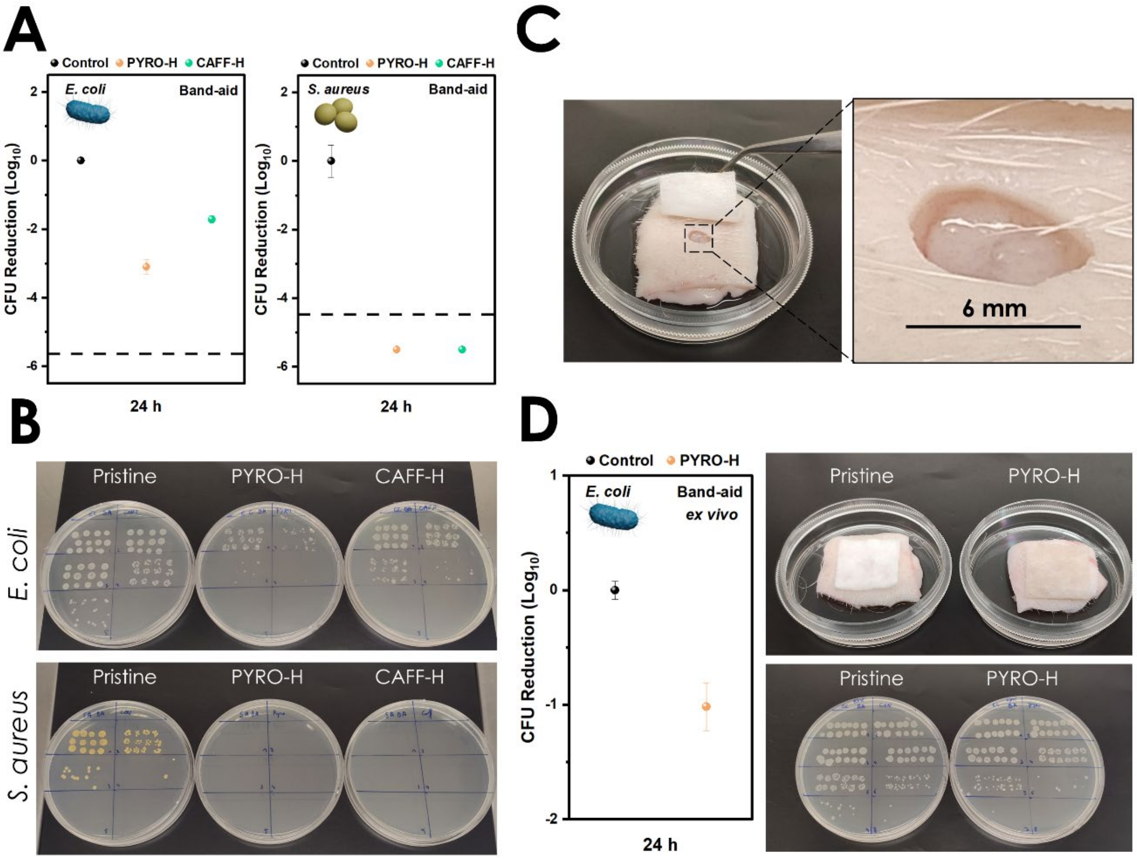

Figure 3.32. Antibacterial properties in commercial band-aids. A) CFU logarithmic reduction of the **PYRO-H** and **CAFF-H** coatings against *E. coli* and *S. aureus* after 24 h incubation (dash line represents the detection limit) and the **B)** representative SP-SDS plates of the test. **C)** *Ex vivo* assays performed in pig skin, where *E. coli* was inoculated inside a 6 mm induced wound in the skin. **D)** CFU logarithmic reduction achieved by **PYRO-H** against *E. coli* after 24 h over the inoculated *ex vivo* tissue and the representative SP-SDS plates of the test.

3.2.7 Bioinspired coatings for enhanced filtration

Besides the outstanding antimicrobial activity of these coatings, the broad properties of catechols give them the potential for a broad spectrum of applications, including environmental uses, for example the removal of metallic nanoparticles from water, which is crucial for protecting both environmental and human health. As previously explained (section 3.1.2), these particles, often originated from industrial processes and agriculture, have a risk of accumulation in aquatic life and the food chain.[21] To address this problem, the ability of the obtained catechol-based coatings to retain CuO and ZnO nanoparticles was tested. Specifically, PYRO, GALL and CAFF (catechol derivatives less prone to generate particles during the coating synthesis), with both HMDA and TRI2 in polypropylene substrates were used in this study.

3.2.7.1 Retention of metallic nanoparticles

In order to compare the amount of CuO and ZnO nanoparticles (93 ± 44 nm and 56 ± 16 nm of diameter, respectively) (**Figure 3.33A**) that each coating could retain, solutions of 0.5 mg/ml of each metal oxide were prepared. Freshly synthetized coatings and pristine polypropylene substrates were then introduced into vials containing these solutions, and placed in a shaking platform for 18 h. Pristine and coated substrates were then washed and placed in a new vial containing 20 ml of water and shaked for 10 min in order to remove unretained nanoparticles (**Figure 3.33B**). The resulting pristine and coated polypropylene discs shifted to a blacker or whiter when exposed to CuO or ZnO, respectively, indicating high retention of nanoparticles. Whereas immersion in the solutions led to a visible heterogeneous retention of nanoparticles in the pristine substrate, the coated ones achieved a homogeneous dispersion, specially noticed with CuO (**Figure 3.33C**).

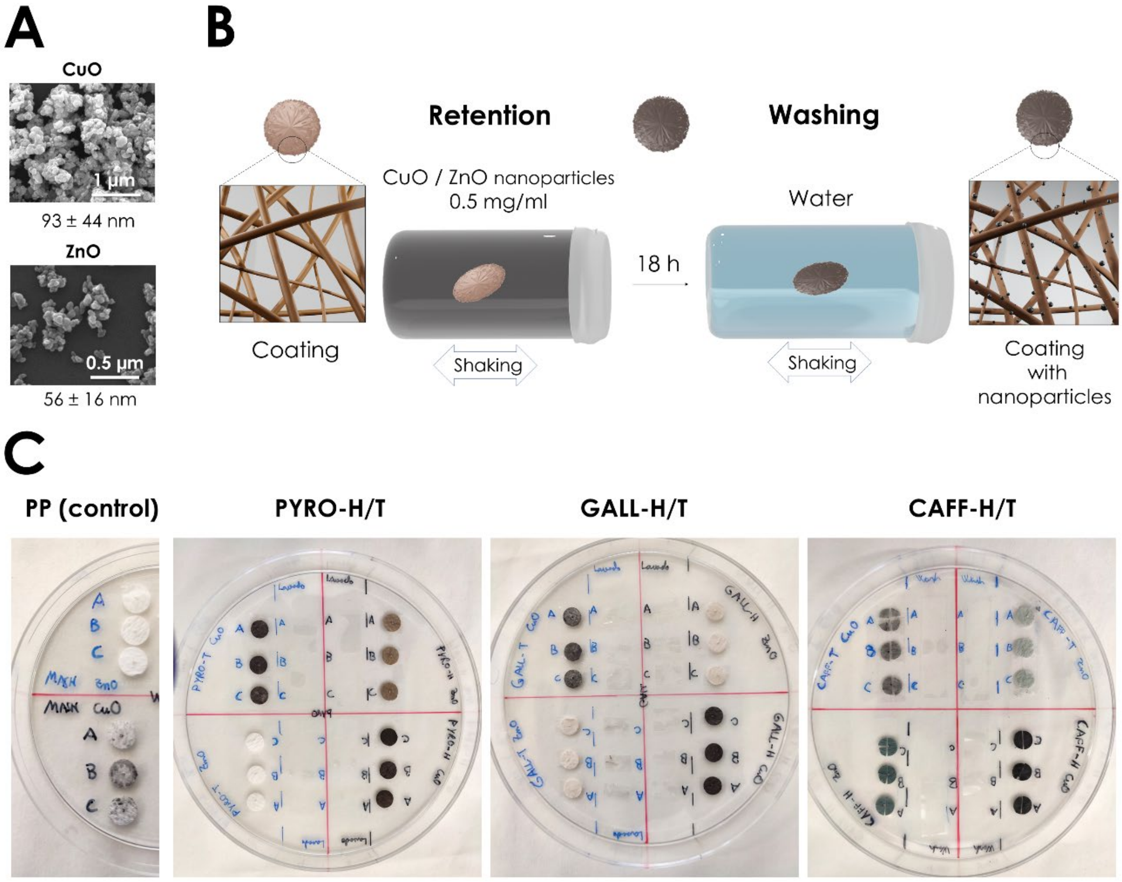

Figure 3.33. Coating retention test. A) Schematic representation of the retention protocol with **B)** CuO and ZnO nanoparticles. **C)** Pristine, **PYRO**, **GALL** and **CAFF -H/T** coated polypropylene discs after the assay, becoming darker or whiter when exposed to CuO and ZnO, respectively.

In the case of copper oxide, SEM micrographs revealed that the **CAFF-T** coated substrates generally retained the fewest nanoparticles within their fibers, closely followed by the pristine polypropylene. On the other hand, **CAFF-H**, **PYRO-H** and **PYRO-T** coatings demonstrated similar retention capabilities. Notably, GALL (especially **GALL-H**) emerged as the catechol derivative that captured the largest quantity of CuO nanoparticles in its fibers (**Figure 3.34A**). Considering that catechols can form coordination bonds with metal ions thanks to their hydroxyl groups in ortho- positions, it was initially suggested that GALL might achieve the best performance due to its additional hydroxyl.

In the case of ZnO nanoparticles, the differences were less pronounced compared to CuO, but similar trends were evident. Pristine polypropylene visually trapped an amount of ZnO comparable to the **PYRO-H**, **PYRO-T** or **CAFF-T** coatings. However, **CAFF-H** and, particularly, **GALL-H** and **GALL-T** exhibited the highest retention of ZnO nanoparticles (**Figure 3.34B**).

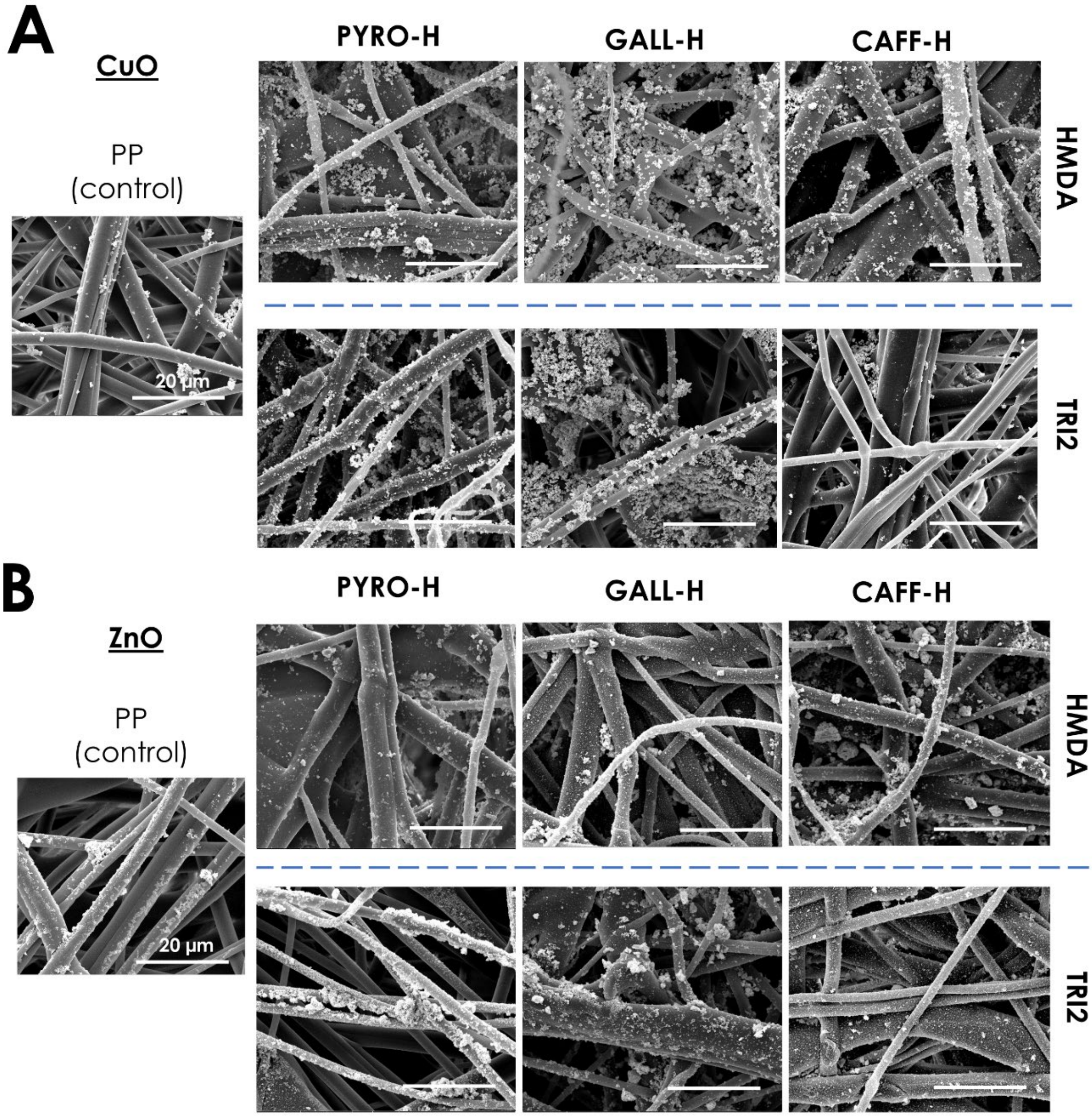

Figure 3.34. Retention of CuO and ZnO nanoparticles in the six selected coatings. SEM micrographs of pristine, **PYRO**, **GALL** and **CAFF -H/T** coated polypropylene discs after being in contact with the **A)** CuO and the **B)** ZnO nanoparticles solution. The scale bars correspond to 20 µm.

Additionally, it is worth mentioning that, whereas the ZnO nanoparticles attached to the pristine polypropylene tended to form small aggregates, the coatings provided a more uniform coverage. This likely occurred due to the smaller size of the particles, which formed aggregates only when the surface of the fibers became saturated.

Energy dispersive X-ray spectroscopy (EDX) measurements of these substrates confirmed the presence of the nanoparticles and evaluated the percentage of Cu and Zn in them. Consistent with previous results, the catechol derivative with the highest retention of Cu and Zn was GALL, specifically with HMDA and TRI2 in the case of Cu and Zn, respectively (**Figure 3.35**). While both **PYRO-H** and **PYRO-T** increased or kept the same amount of nanoparticle retention as the pristine polypropylene, **CAFF-H** consistently increased retention, whereas **CAFF-T** always decreased it. Furthermore, the ability to retain these nanoparticles was assessed after a 7-day washing period. Interestingly, Cu levels remained relatively stable with minimal reduction in most cases. In contrast, Zn levels decreased sharply in the pristine substrate, whereas most coatings retained about half of the initial Zn amount (**Figure 3.35**). Overall, HMDA-based coatings outperformed TRI2-based ones in terms of retention both before and after washing.

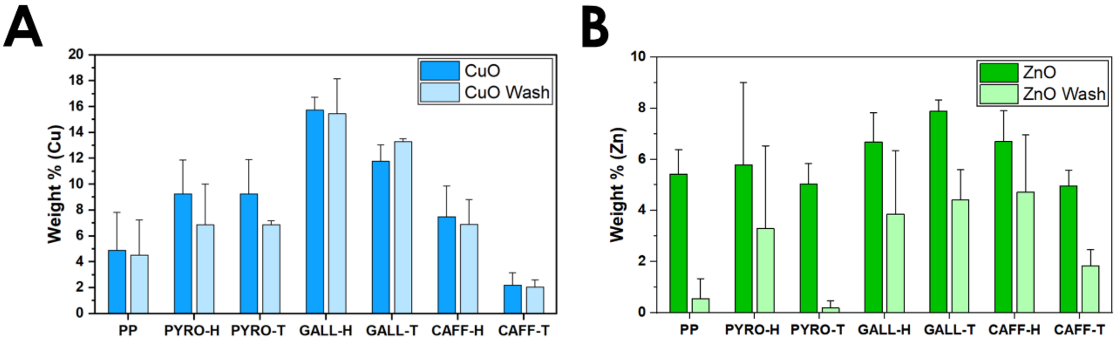

Figure 3.35. Weight of Cu and Zn retained in the six selected coatings. A) Energy dispersive X-ray spectroscopy (EDX) performed in the same samples (without metalizing), measuring the weight % of Cu and **B)** Zn for each condition and coating before and after a 7-day washing period. Can be observed that the catechol **GALL** and specially its combination with **HMDA** (**GALL-H**) retained the highest number of metallic nanoparticles in both cases.

3.2.7.2 Filtering of metallic nanoparticles

A dynamic filtration setup with continuous water flow was established to assess the ability of the coatings to retain nanoparticles. By analyzing the behavior of the pristine and coated polypropylene under these conditions, we aimed to gain insights into their long-term performance and durability. Pristine and coated polypropylene were used as filtration membranes. CuO or ZnO solutions (2 ml of 0.5 mg/ml) were forced to pass through the polypropylene discs after inducing negative pressure (**Figure 3.36A** and **B**). After collecting the filtered solution, a washing step of the disc was performed with water, which was also collected for further analysis. After drying the substrates, a black or white circle (CuO or ZnO, respectively) could be observed in every case at the center of the filter, which corresponds to most of the metallic nanoparticles (**Figure 3.36C**). Inductively coupled plasma mass spectrometry (ICP-MS) measurements of the filtrate and the washing water were performed to analyze the concentration of Cu or Zn after each filtration step. Results showed that all the coatings substantially improved the filtration of the metallic nanoparticles, with a decrease concentration of the Cu or Zn in the filtrates and washing waters (**Figure 3.36D**). Interestingly, the solutions filtered by the coatings contained from 5 to 20 times fewer ppm of Cu or Zn than the pristine polypropylene (**Figure 3.36E**). However, it is essential to emphasize that **GALL-H** was able to reduce these values by approximately 60 to 80 times, demonstrating its superior filtration capabilities in this test.

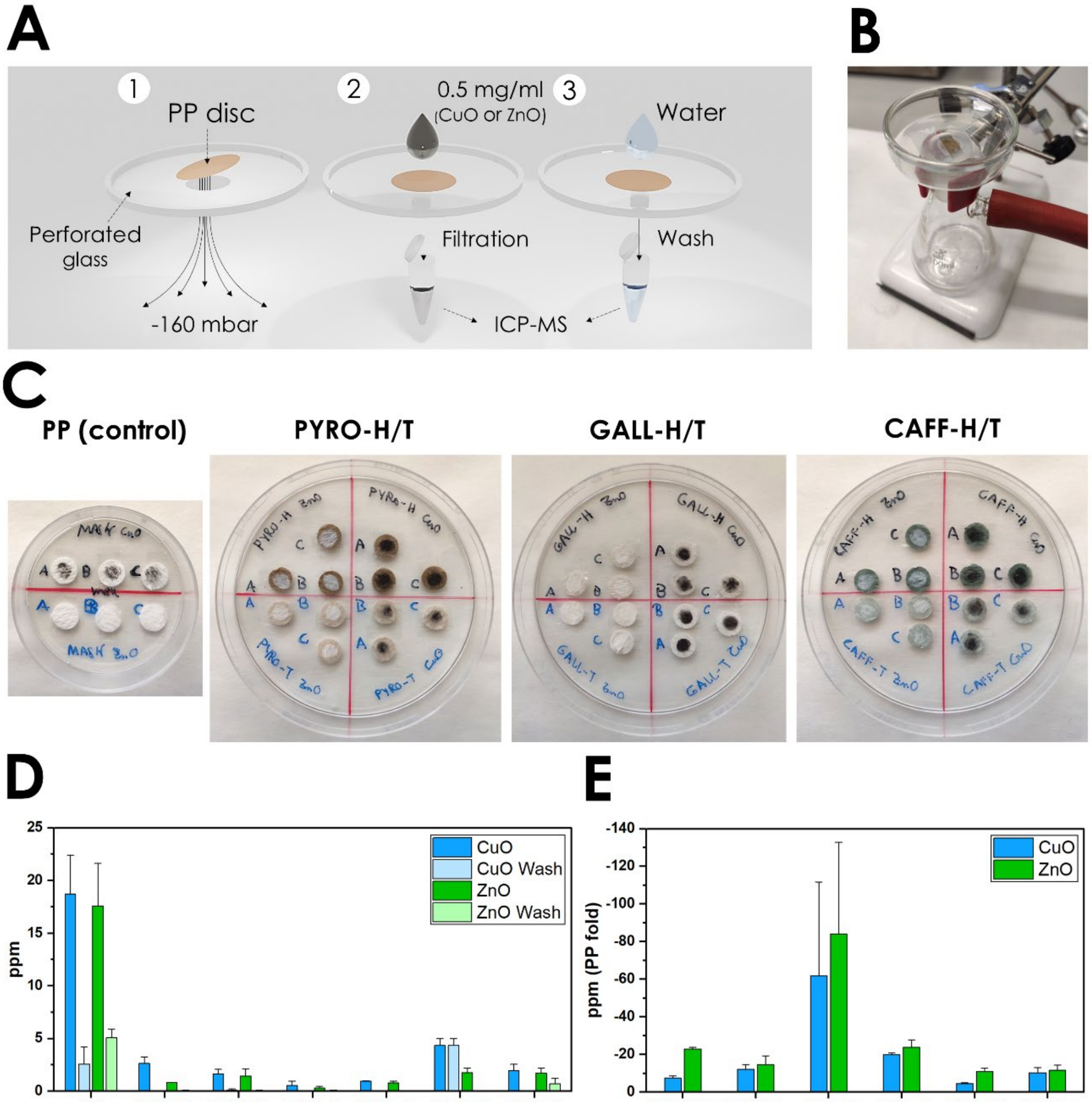

Figure 3.35. Coating filtering test. A) Schematic representation of the filtering protocol. **B)** Setup used for the experiment. **C)** Pristine, **PYRO**, **GALL** and **CAFF -H/T** coated polypropylene discs after the assay. A darker or whiter spot in the center of the substrate after the filtration of CuO or ZnO, respectively, can be observed. **D)** Inductively coupled plasma mass spectrometry (ICP-MS) of the resultant water after filtration of the CuO and ZnO nanoparticles solution through pristine, **PYRO**, **GALL** and **CAFF -H/T** coated polypropylene discs and their wash. **E)** Representation of the data in base (fold) of the pristine polypropylene. Results are represented as PPM of Cu (blue spectrum) and Zn (green spectrum).

3.3 Conclusions

i. Catechol-amine-based coatings were applied to different substrates relevant in healthcare environments: paper, cotton, surgical mask middle layer and commercial band-aids. The resulting coated materials effectively eradicate different bacteria (*E. coli*, *P. aeruginosa*, *S. aureus*, MRSA and *E. faecalis*) and fungi (*C. albicans* and *C. auris*), which are considered global health threats due to their AMR.

ii. The developed coatings are obtained following a simple one-step and scalable synthesis under mild conditions, using affordable materials and green chemistry-based methodologies.

iii. Their efficient application was demonstrated in wet atmospheres, such as those found in healthcare environments where respiratory droplets and other biofluids are present. This reduces the risk of indirect contact transmission.

iv. The antimicrobial activity is attributed to a direct contact killing process, where the pathogen is initially attached to the coating by catechol molecules and other polyphenol derivatives.

v. A multi-pathway antibacterial effect is then activated, mainly due to: i) a sustained generation of biosafety levels of ROS and ii) electrostatic interactions with protonated amino groups exposed to the surface. These antibacterial mechanisms induced a fast (180 min for bacteria and 24 h for fungi) and efficient (more than 99%) response against pathogens, causing irreversible damage.

vi. Furthermore, preliminarily assays showed excellent filtration properties of metallic nanoparticles (up to 80 times better) thanks to the coordination capabilities of catechols.

3.4 Future work

In view of the outstanding results obtained with the developed coatings for different materials and microorganisms offered outstanding results, a preclinical assay with coated band-aids remains pending to definitively confirm their use in wound healing, useful to avoid and treat infections, such as in ulcers or other skin-related damage. Additionally, the retention capacity of new contaminants with these coatings, also at lower concentrations, remains an interesting and promising property that could be definitely exploited in the field of environmental remediation.

To ensure proper scalability and reproducibility, faster and more efficient approaches, such as spray-coating are being already implemented by the research group. Additionally, the simplicity of this synthesis allows for the partial sourcing of essential reagents from biomass waste, thereby promoting the circular economy.

3.5 Experimental section

All reagents, solvents and kits were purchased and used without further purification from Sigma-Aldrich (Merck, Madrid, Spain) unless otherwise specified. Four substrates were selected: paper, cotton fabric (100% cotton), surgical mask middle layer (100% polypropylene) and commercial band-aids (viscose, polyethylene and polypropylene) (Auchan Brand). Type 1 ultrapure water from in-house Milli-Q® filtration systems (Millipore, Burlington, MA) was used in all experiments, unless otherwise specified.

Catechol-amine coating synthesis. The coatings were synthesized by combining different catechol derivatives: pyrocatechol (PYRO), caffeic acid (CAFF), pyrogallol (GALL), catechin (CATH), dopamine (DOPI) and 4-methylcatechol (4MET), and two amino-based ligands: hexamethylenediamine (HMDA, H) and tris(2-aminoethyl)amine (TRI2, T). The coatings obtained and the molarity (mM) of the catechol derivative and amine selected were: **PYRO-H** (10-15), **PYRO-T** (10-22), **CAFF-H** (10-25), **CAFF-T** (10-24), **GALL-H** (10-20), **GALL-T** (10-22), **CATH-H** (10-15), **CATH-T** (10-16), **DOPI-H** (10-20), **DOPI-T** (10-24), **4MET-H** (10-25) and **4MET-T** (10-27). The selected catechol derivative and the amine were weighted separately and dissolved (in the case of CATH, also heated to ease its mixture) in 200 ml of water. Both reagents were mixed and remained under stirring at 300 rpm and room temperature until its complete dissolution. Subsequently, 11 x 5 cm pieces of paper or cotton substrates were introduced into the solution, holding it with a needle, in order to avoid the substrate to touch the magnetic stirrer. For band-aids, pieces of 10 x 2 cm were chosen. In the case of polypropylene (directly extracted from the surgical mask middle layer), due to its natural hydrophobicity, ten discs of 9 mm in diameter were cut and introduced in a final volume of 100 ml, stirring them initially at 1200 rpm for 10 minutes (in order to force substrate to enter inside the solution and slowly become less hydrophobic), to then change it to 600 rpm for the rest of the experiment. All the recipients were covered with a four times pierced Parafilm to allow for oxygen exchange. The reaction only remained fully uncovered when catechin was involved in the synthesis. After 18 h, coated substrates were removed from the solutions, generously cleaned with a continuous flux of distilled water and subsequently dried under vacuum. In the case of the 10 mm diameter non-treated petri plate, the whole plate was introduced inside a recipient containing the mixture reagents of the PYRO-H coating. After 18 h, the plate was removed, washed with water and ultraviolated for 1 hour (as well for the non-treated control, and the treated control plate). All the procedures were performed inside a biosafety cabinet in sterile conditions in order to perform a clean synthesis.

Scanning electron microscopy imaging (SEM). The morphological characterization of the coatings was determined by scanning electron microscopy (SEM, FEI Quanta 650 FEG, Thermo

Fisher Scientific, Eindhoven, The Netherlands) in secondary electron mode with a beam voltage of 10 kV (5kV in the case of band-aids). Samples were coated with a 5 nm layer of gold/palladium 60/40 layer (Emitech K550X Sputter Coater). The thicknesses of the coatings were measured by previously freezing in nitrogen the samples and breaking in small pieces attached to low profile 45º/90º SEM mount pin.

Fourier Transformed Infrared (FTIR). Surface FTIR experiments have been performed with the Hyperion 2000 FTIR microspectrometer (Bruker Optik GmbH, Ettlingen, Germany) in reflection mode, equipped with a nitrogen-cooled mercury–cadmium–telluride (MCT) detector (InfraRed Associates, Inc., Stuart, FL, USA). The samples were analyzed using a 15× reflection objective, a gold mirror as a reference and scanning for 30 min with a resolution of 4 cm^{-1}. All the data was treated with OPUS version 7.5 (Bruker) and OriginPro version 8.0988 (OriginLab Corporation, Northampton, MA, USA) software.

Energy Dispersive X-ray spectroscopy (EDX). The composition of the samples was determined by SEM in EDX mode. After obtaining a specific sample, it was divided into two pieces, one metalized and observed by secondary electron mode, while the other one not and analyzed by EDX (N=3).

Inductively coupled plasma mass spectrometry (ICP-MS). The analysis was performed at Servei d'Anàlisi Química from Univeristat Autonòma de Barcelona (SAQ-UAB). The equipment used was an Agilent 7900 ICP-MS equipped with an SPS 4 autosampler. The ICP-MS setup includes a MicroMist Nebulizer for samples without HF, a Spray Chamber for sample introduction, and a High Matrix Introduction technology to handle samples with high salt content. The system also features a Cone Interface with sampling cones and skimmer cones made of nickel, an Omega Lens, a Collision Reaction Cell (Octopole Reaction System). The data acquisition and analysis were performed using MassHunter software. The samples were properly digested using nitric acid using a total of N=3 for each condition.

X-ray Photoelectron Spectroscopy. X-ray photoelectron spectroscopy (XPS) measurements were performed with a Phoibos 150 analyzer (SPECS EAS10P GmbH, Berlin, Germany) in ultra-high vacuum conditions (based pressure 10^{-10} mbar, residual pressure around 10^{-7} mbar). A monochromatic Al Kα line was used as X-ray source (1486.6 eV and 300 W). The electron energy analyzer was operated with pass energy of 50 eV. The hemispherical analyzer was located perpendicular to the sample surface. The data was collected every eV with a dwell time of 0.5 s. A flood gun of electrons, with energy lower than 20 eV, was used to compensate the charge. All the data was treated with CasaXPS version 2.3.17PR1.1 (Casa Software LTD, Teignmouth, UK) and OriginPro version 8.0988 software.[59]

Coating stability. The stability in aqueous media of all the coatings produced by the permutation of the six catechol derivatives and HMDA or TRI2, was tested. Subsequently to obtain a coated substrate, part of the initial piece was divided into two pieces of 1 x 1 cm^2. The first one, which remained dry, was considered T=0, while the other half was stored in a vial with 20 ml of water and maintained under 300 rpm for 60 days (T=60). Finally, both pieces were compared with SEM pictures to assess the possible changes after the time lapse.

Contact angle. Changes in wettability were measured before and after the coating. For that, 2 µl of water were dropped over each sample and the contact angle was measured (Drop Shape Analyzer-DSA25S, KRÜSS GmbH, Hamburg, Germany).

Zeta potential (ζ-potential). The surface zeta potential of the coatings was indirectly measured using a Zetasizer Nano ZS 3600 (Malvern Instruments, U.K.). The polymer (free in media and precipitated) of the 12 different coatings were isolated by centrifugation (Thermo Scientific™ Sorvall™ Legend™ Micro 17R, centrifuged at 16200 rcf for 5 min) and washed twice with ultrapure water. The obtained pellet was resuspended in 2 ml ultrapure water and 1 ml introduced in a disposable capillary cell. The data was collected by Zetasizer 7.13 software.

Bacteria and fungi growth conditions. Six different bacteria and two yeast were selected due to their impact in current human health and relevance in research stated by the WHO and UN.[2,4] *Escherichia coli* (MG 1655) and *Pseudomonas aeruginosa* (PAO1) as representative gram-negative bacteria, while *Staphylococcus aureus* (CECT 86), methicillin-resistant *Staphylococcus aureus* (MRSA, CECT 9951), and *Enterococcus faecalis* (CECT 795) as gram-positive. Specifically, *Bacillus subtilis* (CECT 461) is not considered a pathogenic strain. Nonetheless, the selection of this microorganism was made from a research perspective in order to thoroughly examine the bactericidal properties of the coatings. This choice was based on the microorganism's unique reproduction mechanism, which involves the formation of resilient protective endospores. This protection endows the pathogen with special resistant capabilities to tolerate extreme environmental conditions. Initially, an aliquot from all bacteria was streaked on a 100 mm Petri dish containing Miller's Luria-Bertani (LB) with agar and incubated for 24 h at 37°C (Forma™ Series II Water-Jacketed CO_2 Incubator) under a saturating humidity atmosphere composed of 95% air and 5% CO_2. For each experiment, a single colony was selected and grown in 10 ml of Miller's LB for 24 h at 37°C. Bacteria cultures were resuspended in NaCl saline solution at 0.9% and the optical density (OD_{600}) of the suspension was adjusted (Fisherbrand™ Cell Density Meter Model 40) to 0.2 for *E. coli*, 0.15 for *P. aeruginosa* and 0.3 for Gram-positive bacteria (*S. aureus, E. faecalis* and *B. subtilis*), unless otherwise specified. To obtain the OD_{600} with NAC, a saline solution was supplemented with NAC at 10 mg/ml. To achieve a mixed suspension of 5 of these bacteria, 1/5 of the volume of each desired bacteria suspension was combined. Same procedure was followed for the selected fungi, *Candida albicans* (CECT 1394) and *Candida auris* (ATCC MYA-5001), but growing them in Yeast Peptone Dextrose (YPD) media (with or without agar in the base of the step) and adjusting the cell suspension OD_{600} to 0.5. In every case, 100 mm Petri dish plates with Miller's LB with agar were used for bacteria growth and antibacterial tests, while YPD with agar was used for yeast. All procedures were performed under biosafety level 2 laminar flow cabins and sterile conditions.

Single plate-serial dilution spotting (SP-SDS) methodology. Dried pristine and coated substrates (paper and cotton) were cut into pieces of 1.5 x 1.5 cm, introducing four of them (total area of 9 cm^2) in 10 ml glass vials, followed by 1 h of UV light for their sterilization. After obtaining the corresponding OD_{600} for all bacteria and fungi suspension, 120 µl were inoculated in the paper substrates and 300 µl in cotton. In the case of polypropylene, 4 discs of 0.9 cm (total area ≈ 2.5 cm^2) were inoculated with 30 µl. The volume selected in each case was the maximum capable of being retained by the material. For band-aids, 2 x 2 cm pieces were used and 150 µl for inoculation. After the desired incubation time of 30, 60, 180 min and 24 h, dilution -1 was obtained directly with the sample inside the glass vial in which it was incubated. Subsequently, it was sonicated for 5 min (Elmasonic S 30 H) and the remaining serial dilutions (-2 to -5) were also created. Plates were seeded following the already described methodology for SP-SDS.[60] Then, the plates were incubated at 37°C for 24 and 48 h for bacteria and fungi, respectively. Extra 24 hours incubation for both bacteria (specially gram positive) and fungi were also performed in order to determine the presence or not of "late bloomer" CFUs. Viable colony-forming units (CFU) were counted afterwards, with a total number of repetitions of N=5 for each condition and N=8 in the case of fungi. Additionally, right after obtaining **PYRO-H** coated paper substrates, samples were kept in dry conditions and protected from light. The antibacterial activity of this coating was tested after being stored for 15, 30, 60, 120 and 180 days against *E. coli* and *S. aureus* after 3 h incubation.

Fluorescence viability test. To observe the cytotoxic effect of the coated substrate on the bacteria, the LIVE/DEAD™ BacLight™ L7012 Bacterial Viability Kit (Molecular Probes™, Invitrogen™) was used. This kit consists of two dyes, SYTO9 3.34 mM (which labels all bacteria populations) and propidium iodide (PI) 20 mM (which only penetrates when the membrane is damaged). Bacterial suspension was adjusted to OD_{600} 0.4 and 0.5 for *E. coli* and *S. aureus*, respectively. **PYRO-H**, **CAFF-H** coatings and pristine paper were inoculated with 120 µl of suspension and incubated for 3 h at 37°C. Then, dilution -1 was obtained directly with the sample inside the vial and sonicated for 10 s. Afterwards, 500 µl of each sample were mixed with 1.5 µl of SYTO9 and 1.75 µl of PI and incubated at room temperature in darkness for 15 min. Finally, samples were observed with the Nikon ECLIPSE TE2000-E microscope, equipped with epifluorescence optics and a Hamamatsu ORCA-ER photographic camera. Pictures obtained for each dye in the same position were colored (Red-PI and Green-SYTO9) and merged with Image J software.

Microorganism visualization by SEM. Substrates containing bacteria were fixed with paraformaldehyde 2% in a NaCl 0.9% saline solution for 1 h. Subsequently, samples were dehydrated through an ethanol serial dilution series until 100%. Then, samples were dried under cabin airflow, coated with a 5 nm layer of gold/palladium and finally observed by SEM. Bacteria SEM micrographs were colored using Adobe Photoshop CS6.

Generation of reactive oxygen species (ROS) test. ROS was measured with the fluorogenic kit MAK143. To measure the fluorescence generated by ROS from the coatings, black 96-well plates were selected. The antioxidants N-Acetyl-L-cysteine (NAC), Trolox and ascorbic acid (AsAc) were used to regulate the ROS generation of the coatings. Firstly, 180 µl of Master-Reaction-Mix (MRM) were mixed with 20 µl of water (control), NAC, Trolox or AsAc (in a final concentration of 10 mg/ml, 1 mM or10 mM, respectively). Then, pristine or **PYRO-H** coated paper substrates (6 x 0.5 cm^2) were introduced in the corresponding conditions and the fluorescence was measured every 20 min during 24 h, keeping a temperature of 25°C (Varioskan™ LUX, Thermo Scientific™ and $\lambda_{excitation}$ = 490 nm/$\lambda_{emission}$ = 525 nm for excitation and emission wavelength, respectively). A similar test (following the same setup) was also performed with pristine, **PYRO-H** and **CAFF-H** coated paper substrates, but using only NAC in different concentrations (1 mg/ml or 10 mg/ml) or water, in order to determine if the antioxidant could modulate the signal obtained from both coatings. For both experiments, three repetitions of each condition were performed.

Antioxidant protection effect in bacteria. Starting with a liquid culture of *E. coli*, three suspensions with an OD_{600} of 0.2 were obtained, supplemented with NAC 10 mg/ml, AsAc 10 mM or nothing (control). Right after, **PYRO-H** and **CAFF-H** coated paper substrates were inoculated with each of the suspensions separately, incubated for 180 min at 37°C and followed by SP-SDS evaluation to compare the CFU reduction. For each condition, 5 repetitions were performed.

Detection of different reactive oxygen species (ROS). Three different fluorogenic kits were used to detect three specific reactive oxygen species: OxiVision™ 21505 (KIT A), MitoROS™ OH580 16055 (KIT B) and MitoROS™ 580 16052 (KIT C), for hydrogen peroxide (H_2O_2), hydroxyl radicals ($\cdot OH$) and superoxide anions ($\cdot O_2^-$), respectively (AAT Bioquest, US, California). Samples of pristine, **PYRO-H** and **CAFF-H** coated paper of 6 x 0.5 cm^2 were introduced in a black 96-well plate, while no substrate was counted as blank. The protocols described in each kit were followed unless otherwise specified. KIT A: after preparing the working-solution at 20 µM on 20 mM Hepes buffer, 200 µl were added to each condition; KIT B: after preparing the working-solution on the assay buffer as described, 200 µl were added to each condition; Kit C: after preparing the working-solution 2X in 20 mM Hepes buffer, 200 µl were added to each condition. All the samples and kits were prepared simultaneously and incubated for 30 min at room temperature and protected from light. Right after, KIT A was read at $\lambda_{excitation}$ = 490 nm/ $\lambda_{emission}$ = 525 nm, while KITs B and C at $\lambda_{excitation}$ = 510 nm/$\lambda_{emission}$ = 580 nm. At least 4 repetitions of each condition were performed, and the results were represented with OriginPro version 9.8.0.200 software.

Cell culture procedure. Fibroblasts (NIH/3T3, CRL-1658 ATCC) and LN229 human Glioblastoma-derived cells (ATCC CRL-2611, 2010) were cultured and maintained in 100 mm culture dishes (Falcon™ 353003, Fisher Scientific), using 10 ml of Dulbecco's modified Eagle's medium (DMEM), which was supplemented with 100 µg/ml streptomycin, 100 U/ml penicillin, and 10% heat-inactivated fetal bovine serum (FBS) (Invitrogen). Cells were incubated at 37°C in a saturating humidity atmosphere composed of 95% air and 5% CO_2 (Fisherbrand™ CO_2 Incubator Isotemp™). After achieving 80-90% of confluence, cells were rinsed with phosphate-buffered saline (PBS, 100 mM pH 7.4) and incubated at 37°C for 3 min with 0.05% trypsin-EDTA until dissociated. Afterwards, DMEM with 10% FBS was added to neutralize the trypsin and the resulting suspension was centrifuged at 200 g for 5 min. Finally, the pellet was resuspended in a complete medium and the density was adequately adjusted for the experiments. All procedures were performed in a biosafety level 2 laminar flow cabins in sterile conditions.

Cell viability assay. PrestoBlue™ cell viability kit (Invitrogen™) was used to evaluate the possible cytotoxic effects of the pristine and coated substrates in the NIH/3T3 cell line. Initially, a total of $5x10^4$ cells/well with 100µl medium were seeded in a 96-well plate (Falcon™ 353072, Fisher Scientific) and incubated at 37°C for 24 h. Then, the medium was changed to 100 µl of fresh one; cells without substrate were used as controls, while 5 mm^2 substrates (UV sterilized) were incorporated into each well, followed by incubation at 37°C for 24 h. Afterwards, substrates and medium were removed and 10 µl of PrestoBlue™ cell viability kit were added to each well, incubated for 30 min following the manufacturer specifications and finally read (Victor3, PerkinElmer). In each plate, three replicates were done for each condition and a total of four repetitions (N=4) were performed.

***Ex vivo* antibacterial test.** Fresh pig skin was extracted and stored in Krebs-Ringer HEPES-buffered solution at 4°C until used (same day of extraction). After cutting pieces of 3 x 3 cm of skin, a hole of approximately 3 mm of depth was performed in the center of the sample using a 6 mm of diameter biopsy punch. Then, each piece was abundantly washed in sterile saline solution, placed in individual 6 cm sterile Petri dishes and 1 ml of saline solution added to the bottom. Subsequently, 50 µl of *E. coli* (OD 0.2) were inoculated in each hole, covered with pristine or **PYRO-H** coated band-aid and incubated for 24 h. Finally, SP-SDS counting was performed, with an N=3 for each condition. All procedures were performed under biosafety level 2 laminar flow cabins and sterile conditions.

Metallic nanoparticles retention. In this test, the catechol derivatives characterized for synthesis with a low number of nanoparticles (PYRO, GALL and CAFF, with both amines), were selected. A previously washed and dried coated or pristine substrate (circle of 9 cm diameter and square of 1.5 x 1.5 cm for polypropylene and paper, respectively) was pierced with a needle (in order to stabilize it) and introduced in a vial containing 20 ml of 0.5 mg/ml nanoparticles solution of CuO or ZnO. After 18 h in a rocking platform, samples were removed, introduced in new vials with 20 ml of water and washed for 10 minutes in the rocking platform. Then, the substrates were removed and dried. Additionally, half of the sample was washed in 20 ml of water for 7 days in a rocking platform. A total number of 3 repetitions were performed for each substrate/coating/nanoparticle.

Metallic nanoparticles filtration. Same coatings (composition, substrate and shape) described in the previous section were also selected in this one. A previously washed and dried coated or pristine substrate was set (and secured with tape) over a glass with a 4 mm diameter hole. The hole was connected to a vacuum flask that performed a suction of 160 mbar. Then, 2 ml of 0.5 mg/ml of CuO or ZnO nanoparticle solution was forced to be filtered through the substrate. The filtered solution was stored, the flask double acetone-cleaned and 2 ml of water (as washing) were also filtered, followed by also storing the resulting volume. Filtered and washing solutions were analyzed by ICP-MS spectroscopy. A total number of 3 repetitions were performed for each substrate/coating/nanoparticle.

Statistical analysis. For SP-SDS logarithmic reduction test, the CFU number obtained for each plate/condition was transformed to a logarithm and represented as the mean ± standard deviation minus the control mean log(CFU) “ $\bar{x}$ ”. The detection limit was calculated following the next equation (A), where “CFU$_{\text{limit}}$” were the lowest countable colonies per plate (1 colony), “N” number of repetitions (5 for bacteria and 8 for fungi), “d” dilution in which colonies were counted and “ml seeded” were 0.02 ml.

$$Detection\ limit = log\ (\frac{CFU_{limit}}{N} \cdot \frac{0{,}1\ ml}{mL\ seeded} \cdot 10^{d+1}) - \overline{x} \quad \text{(A)}$$

For the overall ROS generation test, the signal obtained for each time-measurement (every 20 minutes during 24 h) was represented as the mean ± standard deviation of the 3 repetitions of each condition. In the specific ROS generation test, the results obtained from each of the 3 kits were analyzed separately, subtracting the mean of the blank from the mean achieved by the 4 repetitions of each condition (pristine, **PYRO-H** and **CAFF-H**) and represented as fold vs. the pristine paper mean signal. In the case of the NIH/3T3 cell viability test, results were normalized as a percentage of the control mean and represented as the mean ± standard deviation. For the EDX data, the results were represented as mean ± standard deviation of three repetitions for each condition.

Similarly, for the ICP-mass, the results obtained were represented as mean ± standard deviation from three repetitions (or as fold change relative to the pristine polypropylene). Unless otherwise specified, all the graphs were represented using OriginPro version 9.8.0.200 software.

3.6 References

[1] Rudd, K. E.; Johnson, S. C.; Agesa, K. M.; Shackelford, K. A.; Tsoi, D.; Kievlan, D. R.; Colombara, D. V.; Ikuta, K. S.; Kissoon, N.; Finfer, S.; Fleischmann-Struzek, C.; Machado, F. R.; Reinhart, K. K., Rowan, K.; Seymour, C. W.; Watson, R. S.; West, T. E.; Marinho, F.; Hay, S. I.; et. al. *The Lancet* **2020**, *395*, 200-211. https://doi.org/10.1016/s0140-6736(19)32989-7

[2] Bracing for Superbugs, *United Nations Environment Programme* **2023**, ISBN:978-92-807-4006-6.

[3] Naghavi, M.; Vollset, S. E.; Ikuta, K. S.; Swetschinski, L. R.; Gray, A. P.; Wool, E. E., Aguilar, G. R., Mestrovic, T.; Smith, G.; Han, C.; Hsu, R. L.; Chalek, J.; Araki, D. T.; Chung, E.; Raggi, C.; Hayoon, A. G.; Weaver, N. D.; Lindstedt, P. A.; Smith, A. E.; et. al. *The Lancet* **2024**, *404*, 1199-1226. https://doi.org/10.1016/s0140-6736(24)01867-1

[4] Antimicrobial resistance, World Health Organization. https://www.who.int/news-room/fact-sheets/detail/antimicrobial-resistance , **2021** (accessed: 30 August 2023).

[5] Jim O'Neill, Tackling drug-resistant infections globally: final report and recommendations the review on antimicrobial resistance, **2016**. https://amr-review.org/sites/default/files/160518_Final%20paper_with%20cover.pdf

[6] Murray, C. J. L.; Ikuta, K. S.; Sharara, F.; Swetschinski, L.; Aguilar, G. R.; Gray, A.; Han, C.; Bisignano, C.; Rao, P.; Wool, E.; Johnson, S. C.; Browne, A. J.; Chipeta, M. G.; Fell, F.; Hackett, S.; Haines-Woodhouse, G.; Hamadani, B. H. K.; Kumaran, E. A. P.; McManigal, B.; et. al. *The Lancet* **2022**, *399*, 629-655. https://doi.org/10.1016/s0140-6736(21)02724-0

[7] Raoofi, S.; Kan, F. P.; Rafiei, S.; Hosseinipalangi, Z.; Mejareh, Z. N.; Khani, S.; Abdollahi, B.; Talab, F. S.; Sanaei, M.; Zarabi, F.; Dolati, Y.; Ahmadi, N.; Raoofi, N.; Sarhadi, Y.; Masoumi, M.; Hosseini, B. S.; Vali, N.; Gholamali, N.; Asadi, S.; et. al. *PLoS ONE* **2023**, *18*, e0274248. https://doi.org/10.1371/journal.pone.0274248

[8] Perlroth, J.; Choi, B.; Spellberg, B. *Medical Mycology* **2007**, *45*, 321-346. https://doi.org/10.1080/13693780701218689

[9] Rahman, M. A.; Victoros, E.; Shanjana, Y.; Thomas, M. R.; Islam, M. R. *Health Science Reports* **2024**, 7, e70160. https://doi.org/10.1002/hsr2.70160

[10] Cloutier, M.; Mantovani, D.; Rosei, F. *Trends In Biotechnology* **2015**, *33*, 637-652. https://doi.org/10.1016/j.tibtech.2015.09.002

[11] Yang, L.; Wang, C.; Li, L.; Zhu, F.; Ren, X.; Huang, Q.; Cheng, Y.; Li, Y. *Advanced Functional Materials* **2021**, *32,* 2108749. https://doi.org/10.1002/adfm.202108749

[12] Jose, A.; Gizdavic-Nikolaidis, M.; Swift, S. *Applied Microbiology* **2023**, *3*, 145-174. https://doi.org/10.3390/applmicrobiol3010012

[13] Bäumler, W.; Eckl, D.; Holzmann, T.; Schneider-Brachert, W. *Critical Reviews In Microbiology* **2021**, *48*, 531-564. https://doi.org/10.1080/1040841x.2021.1991271

[14] Menge, H. G.; Huynh, N. D.; Choi, K.; Cho, C.; Choi, D.; Park, Y. T. *Advanced Functional Materials* **2022**, *33,* 2210571. https://doi.org/10.1002/adfm.202210571

[15] Cao, M.; Wang, S.; Hu, J.; Lu, B.; Wang, Q.; Zang, S. *Advanced Science* **2021**, *9,* 2103721. https://doi.org/10.1002/advs.202103721

[16] Kwon, K. Y.; Cheeseman, S.; Frias-De-Diego, A.; Hong, H.; Yang, J.; Jung, W.; Yin, H.; Murdoch, B. J.; Scholle, F.; Crook, N.; Crisci, E.; Dickey, M. D.; Truong, V. K.; Kim, T. *Advanced Materials* **2021**, *33,* 2104298. https://doi.org/10.1002/adma.202104298

[17] Godoy-Gallardo, M.; Eckhard, U.; Delgado, L. M.; De Roo Puente, Y. J.; Hoyos-Nogués, M.; Gil, F. J.; Perez, R. A. *Bioactive Materials* **2021**, *6*, 4470-4490. https://doi.org/10.1016/j.bioactmat.2021.04.033

[18] Vimbela, G.; Ngo, S. M.; Fraze, C.; Yang, L.; Stout, D. A. *International Journal of Nanomedicine* **2017**, *12,* 3941-3965. https://doi.org/10.2147/ijn.s134526

[19] Wu, J.; Bosker, T.; Vijver, M. G.; Peijnenburg, W. J. G. M. *Environmental Science & Technology* **2021**, *55*, 16563-16572. https://doi.org/10.1021/acs.est.1c05006

[20] Kahlon, S. K.; Sharma, G.; Julka, J. M.; Kumar, A.; Sharma, S.; Stadler, F. J. *Environmental Chemistry Letters* **2018**, *16*, 919-946. https://doi.org/10.1007/s10311-018-0737-4

[21] Zhang, L.; Cui, Y.; Xu, J.; Qian, J.; Yang, X.; Chen, X.; Zhang, C.; Gao, P. *The Science Of The Total Environment* **2024**, *924*, 171660. https://doi.org/10.1016/j.scitotenv.2024.171660

[22] Alengebawy, A.; Abdelkhalek, S. T.; Qureshi, S. R.; Wang, M. *Toxics* **2021**, *9*, 42. https://doi.org/10.3390/toxics9030042

[23] Long, Z.; Huang, Y.; Zhang, W.; Shi, Z.; Yu, D.; Chen, Y.; Liu, C.; Wang, R. *Environmental Monitoring And Assessment* **2021**, *193,* 20. https://doi.org/10.1007/s10661-020-08807-z

[24] Fadel, M.; Farah, E.; Fakhri, N.; Ledoux, F.; Courcot, D.; Afif, C. *Sustainability* **2024**, *16*, 8739. https://doi.org/10.3390/su16208739

[25] Staszak, K.; Wieszczycka, K. *Membranes* **2023**, *13*, 114. https://doi.org/10.3390/membranes13010114

[26] Maas, M.; Wehling, J. *Surface-Functionalized Ceramics* **2022**, 337-368. https://doi.org/10.1002/9783527698042.ch9

[27] Makaras, T.; Jakubowska-Lehrmann, M.; Jurgelėnė, Ž.; Šemčuk, S. *Journal Of Xenobiotics* **2024**, *14*, 484-496. https://doi.org/10.3390/jox14020029

[28] Zhao, Y.; Xiu, Z.; Wu, R.; Zhang, L.; Ding, X.; Zhao, N.; Duan, S.; Xu, F. *Advanced NanoBiomed Research* **2022**, *2,* 2200111. https://doi.org/10.1002/anbr.202200111

[29] Saverina, E. A.; Frolov, N. A.; Kamanina, O. A.; Arlyapov, V. A.; Vereshchagin, A. N.; Ananikov, V. P. *ACS Infectious Diseases* **2023**, *9*, 394-422. https://doi.org/10.1021/acsinfecdis.2c00469

[30] Sorci, M.; Fink, T. D.; Sharma, V.; Singh, S.; Chen, R.; Arduini, B. L.; Dovidenko, K.; Heldt, C. L.; Palermo, E. F.; Zha, R. H. *ACS Applied Materials & Interfaces* **2022**, *14*, 25135-25146. https://doi.org/10.1021/acsami.2c04165

[31] Halder, S.; Yadav, K. K.; Sarkar, R.; Mukherjee, S.; Saha, P.; Haldar, S.; Karmakar, S.; Sen, T. *SpringerPlus* **2015**, *4,* 672. https://doi.org/10.1186/s40064-015-1476-7

[32] Arakha, M.; Saleem, M.; Mallick, B. C.; Jha, S. *Scientific Reports* **2015**, *5*, 9578. https://doi.org/10.1038/srep09578

[33] Murray, L. M.; Hayes, A.; Snape, J.; Kasprzyk-Hordern, B.; Gaze, W. H.; Murray, A. K. *Npj Antimicrobials And Resistance* **2024**, *2*, 9. https://doi.org/10.1038/s44259-024-00026-7

[34] Kong, H.; Yang, G.; He, P.; Zhu, D.; Luan, X.; Xu, Y.; Mu, R.; Wei, G. *Nano Futures* **2023**, *7*, 012001. https://doi.org/10.1088/2399-1984/acafbe

[35] Rai, A.; Ferrão, R.; Patricio, T.; Parreira, P.; Anes, E.; Tonda-Turo, C.; Martins, M.; Alves, N.; Ferreira, L. *Journal Of Materials Chemistry B* **2022**, *19,* 2384–2429. https://doi.org/10.1039/D1TB02617H.

[36] Luo, H.; Yin, X.; Tan, P.; Gu, Z.; Liu, Z.; Tan, L. *Journal Of Materials Chemistry B* **2021**, *9*, 2802-2815. https://doi.org/10.1039/d1tb00109d

[37] Qu, L.; Liu, J.; Liu, Y.; Zhang, G.; Xu, Y.; Zhu, P.; Wang, Y. *Progress In Organic Coatings* **2023**, *176*, 107397. https://doi.org/10.1016/j.porgcoat.2022.107397

[38] Bryaskova, R.; Philipova, N.; Georgiev, N.; Ganchev, D.; Lalov, I.; Detrembleur, C. *Journal Of Polymer Research* **2023**, *30*, 199. https://doi.org/10.1007/s10965-023-03572-2

[39] Liu, B.; Li, J.; Zhang, Z.; Roland, J. D.; Lee, B. P. *Chemical Engineering Journal* **2022**, *441*, 135808. https://doi.org/10.1016/j.cej.2022.135808

[40] Nazi, N.; Marguier, A.; Debiemme-Chouvy, C.; Humblot, V. *Colloids And Interfaces* **2022**, *6*, 9. https://doi.org/10.3390/colloids6010009

[41] Hussain, M.; Suo, H.; Xie, Y.; Wang, K.; Wang, H.; Hou, Z.; Gao, Y.; Zhang, L.; Tao, J.; Jiang, H.; Zhu, J. *ACS Applied Materials & Interfaces* **2021**, *13*, 29380-29391. https://doi.org/10.1021/acsami.1c07656

[42] Caro-León, F. J.; López-Donaire, M. L.; Vázquez, R.; Huerta-Madroñal, M.; Lizardi-Mendoza, J.; Argüelles-Monal, W. M.; Fernández-Quiroz, D.; García-Fernández, L.; Roman, J. S.; Vázquez-Lasa, B.; García, P.; Aguilar, M. R. *Biomacromolecules* **2023**, *24*, 613-627. https://doi.org/10.1021/acs.biomac.2c01012

[43] Pinnataip, R.; Lee, B. P. *ACS Omega* **2021**, *6*, 5113-5118. https://doi.org/10.1021/acsomega.1c00006

[44] Alfei, S.; Schito, G. C.; Schito, A. M.; & Zuccari, G. *International Journal Of Molecular Sciences* **2024**, *25*, 7182. https://doi.org/10.3390/ijms25137182

[45] Fasnacht, M.; Polacek, N. *Frontiers In Molecular Biosciences* **2021**, *8*, 671037. https://doi.org/10.3389/fmolb.2021.671037

[46] Li, H.; Zhou, X.; Huang, Y.; Liao, B.; Cheng, L.; Ren, B. *Frontiers In Microbiology* **2021**, *11*, 622534. https://doi.org/10.3389/fmicb.2020.622534

[47] Vaishampayan, A.; Grohmann, E. *Microorganisms* **2021**, *10*, 61. https://doi.org/10.3390/microorganisms10010061

[48] Mammari, N.; Lamouroux, E.; Boudier, A.; Duval, R. E. *Microorganisms* **2022***, 10*, 437. https://doi.org/10.3390/microorganisms10020437

[49] Forooshani, P. K.; Polega, E.; Thomson, K.; Bhuiyan, M. S. A.; Pinnaratip, R.; Trought, M.; Kendrick, C.; Gao, Y.; Perrine, K. A.; Pan, L.; Lee, B. P. *Frontiers In Chemistry* **2019**, *7*, 631. https://doi.org/10.3389/fchem.2019.00631

[50] Suárez-García, S.; Sedó, J.; Saiz-Poseu, J.; Ruiz-Molina, D. *Biomimetics* **2017**, *2*, 22. https://doi.org/10.3390/biomimetics2040022

[51] Yi, Z.; Chen, G.; Chen, X.; Sun, Z.; Ma, X.; Su, W.; Deng, Z.; Ma, L.; Ran, Y.; Tong, Q.; Li, X. *ACS Sustainable Chemistry & Engineering* **2020**, *8*, 9833-9845. https://doi.org/10.1021/acssuschemeng.0c02538

[52] Chen, T.; Liu, T.; Su, T.; Liang, J. *Langmuir* **2017**, *33*, 5863-5871. https://doi.org/10.1021/acs.langmuir.7b01127

[53] Jones, L.; O'Shea, P. *Experimental Mycology* **1994**, *18*, 111-120. https://doi.org/10.1006/emyc.1994.1013

[54] Tian, W.; Li, F.; Wu, S.; Li, G.; Fan, L.; Qu, X.; Jia, X.; Wang, Y. *ACS Biomaterials Science & Engineering* **2019**, *5*, 3270-3278. https://doi.org/10.1021/acsbiomaterials.9b00069

[55] Cheah, H.; Lim, V.; Sandai, D. *PLoS ONE* **2014**, *9*, e95951. https://doi.org/10.1371/journal.pone.0095951

[56] Cantelli, B. A. M.; Bitencourt, T. A.; Komoto, T. T.; Beleboni, R. O.; Marins, M.; Fachin, A. L. *Biomedicine & Pharmacotherapy* **2017**, *96*, 1389-1394. https://doi.org/10.1016/j.biopha.2017.11.051

[57] Pinnataip, R.; Lee, B.P. *ACS Omega* **2021**, *6*,5113–5118. https://doi.org/10.1021/acsomega.1c00006.

[58] Esplandiu, M.; Bastus, N.; Fraxedas, J.; Ihmaz, I.; Puntes, V.; Radjenovic, J.; Sepúlveda, B.; Serrá, A.; Suárez-García, S.; Franzese, G. *Encyclopedia of Solid-Liquid Interfaces* **2023**, *3*, 465-484. https://doi.org/10.1016/b978-0-323-85669-0.00066-0

[59] Fairley, N.; Fernandez, V.; Richard-Plouet, M.; Guillot-Deudon, C.; Walton, J.; Smith, E.; Flahaut, D.; Greiner, M.; Biesinger, M.; Tougaard, S.; Morgan, D.; Baltrusaitis, J. *Applied Surface Science Advances* **2021**, *5*, 100112. https://doi.org/10.1016/j.apsadv.2021.100112

[60] Thomas, P.; Sekhar, A. C.; Upreti, R.; Mujawar, M. M.; Pasha, S. S. *Biotechnology Reports* **2015**, *8*, 45-55. https://doi.org/10.1016/j.btre.2015.08.003

Chapter 4

Bioinspired Phenol-Based Membrane for Post-Surgical Glioblastoma Treatment

Catechol-based membranes still face several challenges that must be addressed before they can be effectively utilized in biomedical applications, such as cancer treatment. In this context, Glioblastoma—the most prevalent and aggressive brain tumor—poses a significant therapeutic challenge due to its rapid proliferation, invasive behavior, and resistance to conventional treatments. Current therapeutic strategies often lead to tumor recurrence, highlighting the urgent need for innovative approaches. This chapter will focus on the development and evaluation of bioinspired catechol-based membranes specifically designed to mitigate Glioblastoma recurrence after the surgical resection, with a particular emphasis on their reactive oxygen species production mechanism.

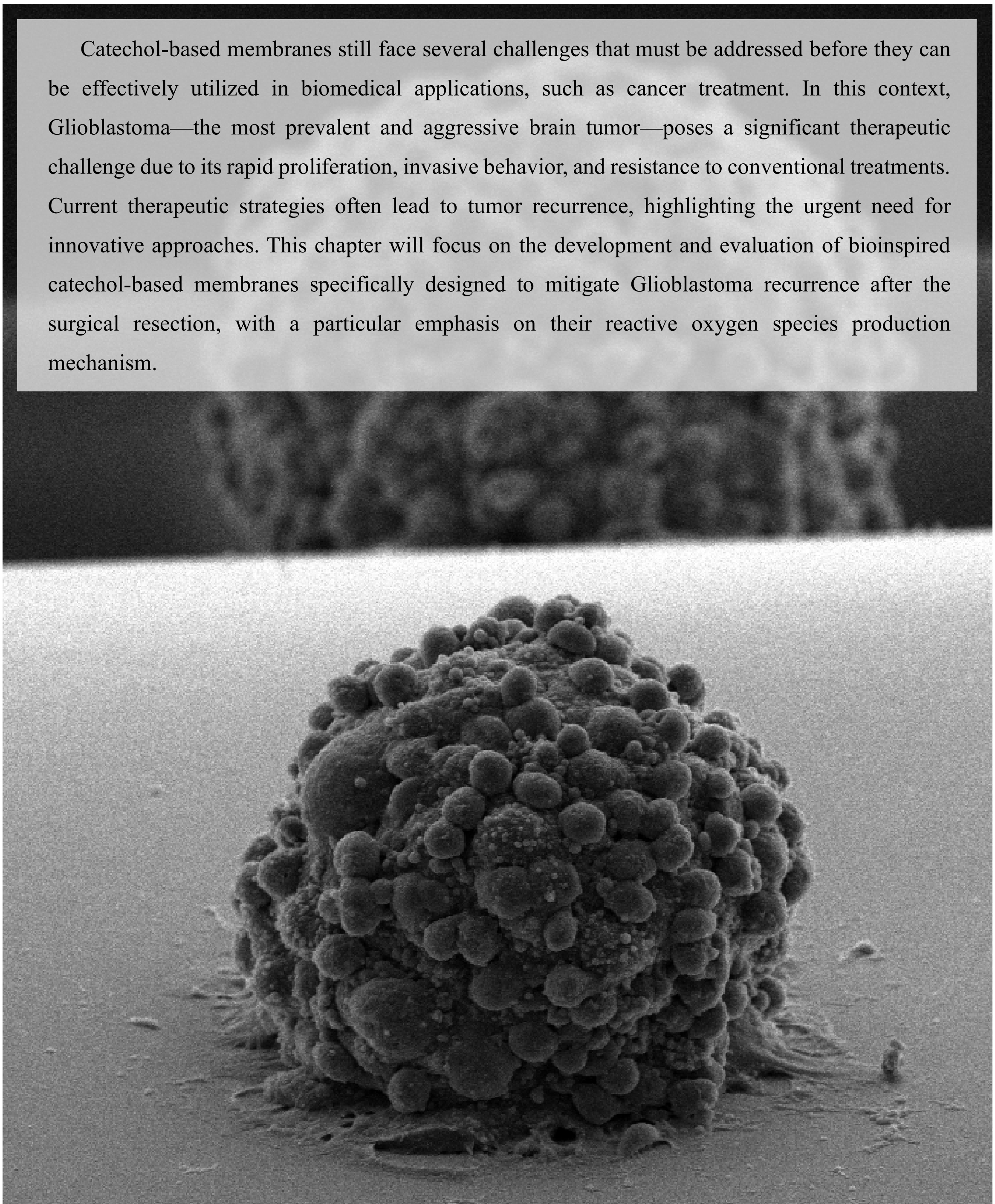

4.1 Introduction

The development of advanced materials as functional scaffolds, such as organic polymeric membranes, has emerged as a promising solution in the fields of biomedical engineering and regenerative medicine.[1,2,3] These materials are designed to provide structural support and enhance the biological functions of damaged tissues or organs. The need for such materials is driven by the increasing demand for effective treatments for various medical conditions, including chronic wounds, age-associated tissue atrophy, and cancer. In this Chapter, particular focus will be given to the latter example, highlighting the development of a novel approach for its treatment.

4.1.1 Cancer: its importance and impact

Nowadays, cancer is one of the leading causes of death in humans, particularly linked to the process of aging. The National Cancer Institute describes it as a disease in which some of the cells of the body grow uncontrollably and eventually spread to other parts (becoming metastasis).[4] This abnormal growth competes with healthy tissues for nutrients, invades their niche and ultimately destroys them, leading to the death of the host in the later stages.

Despite the recent advances in science, cancer remains one of the most formidable challenges in modern medicine. It is estimated that one in every five people will develop this disease over the course of their lifetime. In 2018,[5] 2020 [6] and 2022,[7] an estimated number of 18.1, 19.3, and 20 million cases of cancer worldwide were recorded, respectively, indicating a sustained annual rise of approximately 1 million cases (**Figure 4.1**). Only in the United States more than 2 million new cancer cases were projected during 2024.[8] Furthermore, predictions indicate that by 2050, the number of new cases could rise to 35 million worldwide.[7]

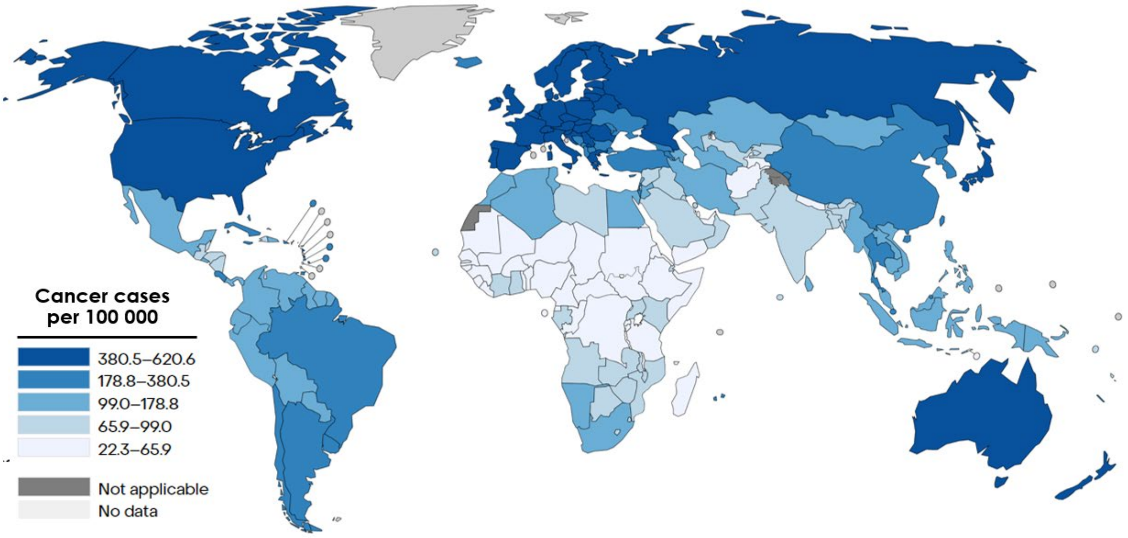

Figure 4.1. Cancer incidence. Cases of cancer worldwide in 2020 per 100,000 people. Adapted from [6].

The aggressiveness of a tumor can be classified into grades based on the appearance of the cells. The grading system primarily evaluates how abnormal (or undifferentiated) the cells are. Tumors with more abnormal cells are generally more aggressive, growing and spreading more quickly. The grades range from 1, indicating a low grade with well-differentiated cells, to 4, representing a high grade with undifferentiated cells.[9]

4.1.2 Glioblastoma multiforme

While some cancers, such as lung, breast, liver and colorectal, achieve the highest incidence and associated mortality rates, other tumors, particularly Grade IV types like Glioblastoma multiforme (GBM), can be considerably more lethal due to their poor prognosis. Unfortunately, Glioblastoma is associated with a median survival of approximately one year following diagnosis, with only 5-10% of patients surviving beyond five years.[10,11,12] Glioblastoma multiforme is a malignant brain cancer, characterized by its rapid growth. It represents 15% of all central nervous system (CNS) tumors and approximately 50% of malignant CNS tumors.[13] Glioblastoma cells exhibit a high degree of cellular heterogeneity, expressing a variety of molecular markers, exhibiting diverse biological behaviors, and achieving different morphologies, which is why the term “multiforme” is attributed to it.[14] This heterogeneity allows Glioblastoma cells to hijack normal brain signaling pathways, promoting tumor survival and resistance to conventional therapies.

4.1.3 GBM standard of care

Due to the aggressiveness of Glioblastoma, the standard of care focuses on improving the quality of life and extending the survival of the patient. It usually involves a multimodality approach, combining surgery, radiation therapy, and chemotherapy (**Figure 4.2**).[15,16] Surgical

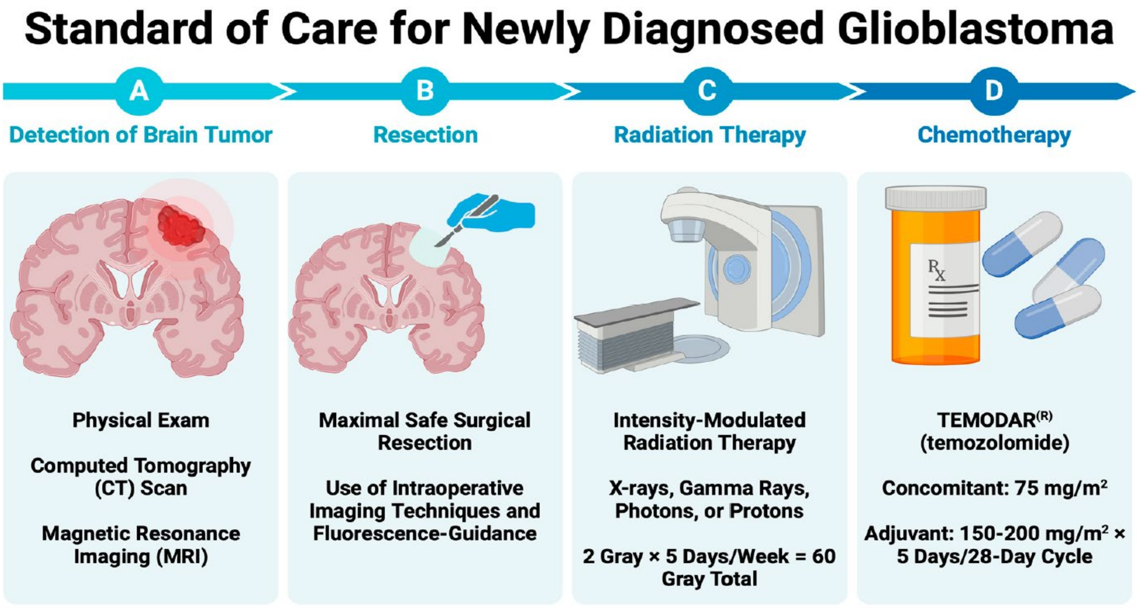

Figure 4.2. Glioblastoma standard of care. Adapted from [16].

resection is often performed to remove as much of the tumor as possible, followed by a systemic approach of radiation therapy, and concurrent and adjuvant temozolomide (TMZ) (the most commonly used drug for Glioblastoma) as chemotherapy. While these systemic treatments are characterized by using less invasive administration routes, their lack of selectivity implies secondary negative effects in the health of the patient due to their non-specificity. For instance, radiotherapy has been reported to induce neurocognitive decline,[17] while in the case of TMZ, myelosuppression, leukopenia and lymphopenia, among others, are common side effects.[18] Another significant challenge is that every chemotherapeutic agent intended to treat Glioblastoma must overcome the blood-brain barrier (**Figure 4.3A**).[19,20] This structure is an extremely selective barrier that protects the brain from large molecules, toxins and pathogens, but simultaneously hinders drug delivery, affecting its effectiveness. Additionally, despite novel approaches, such as immunotherapy (boosting the immune system or decreasing the immunosuppressive effect of cancer cells)[21] and targeted therapy (aiming at specific targets involved in the cancer cell cycle, migration, growth or angiogenesis)[22] have arisen hope in the treatment of Glioblastoma, considerable efforts are still required in their development.[23] In addition, treatments based on oxidative stress are also attracting considerable attention due to their complex and dual role in Glioblastoma, driving the exploration of new materials capable of generating ROS.

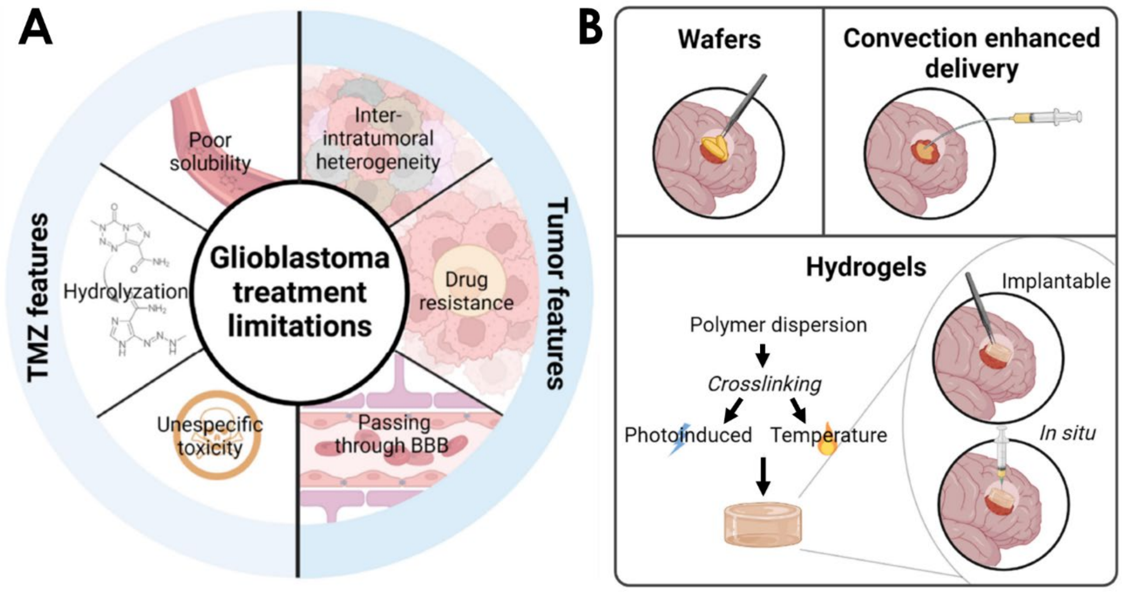

Figure 4.3. Challenges in current GBM treatments. A) Limitations of the chemotherapeutic TMZ and **B)** local GBM therapies. Adapted from [20].

Unfortunately, even with the aggressive treatment regimen of surgery, radiotherapy and chemotherapy, recurrence is the norm, generally before one year of initial therapy.[24] The hallmark feature of Glioblastoma is its infiltrative growth pattern, which makes complete surgical resection challenging and often leads to recurrence.[25] Notably, even after seemingly complete resection of the tumor, most recurrences occur in the surgical bed.[26] This observation has significant implications for the management and research of Glioblastoma, suggesting that the surgical site, despite meticulous efforts to remove the tumor completely, retains a considerable risk of harboring residual tumor cells. Therefore, future methodologies should focus on localized approaches to simultaneously counteract these remnant cells, bypass the blood-brain barrier, and mitigate negative systemic side effects. A notable example is the direct administration of the treatment right into the surgical cavity. It is important to note that the stiffness-induced inflammation associated with rigid materials (e.g., wafers), as well as the challenges in securely fixing scaffolds, continue to pose significant obstacles to their practical application (**Figure 4.3B**).[20] In this context, the development of novel solid yet flexible therapeutic materials might offer effective solutions to these issues.

4.1.4 ROS and their role in cancer

In this context, ROS play a significant role in the biology of cancer. Cancer cells often exhibit elevated ROS levels, which are involved in several signaling pathways that promote tumor growth and survival (e.g., MAPK/ERK activation),[27] resistance to therapy (e.g., enhanced antioxidant production),[28] migration (e.g. actin dynamics),[29] angiogenesis, and metastasis (**Figure 4.4**).[30]

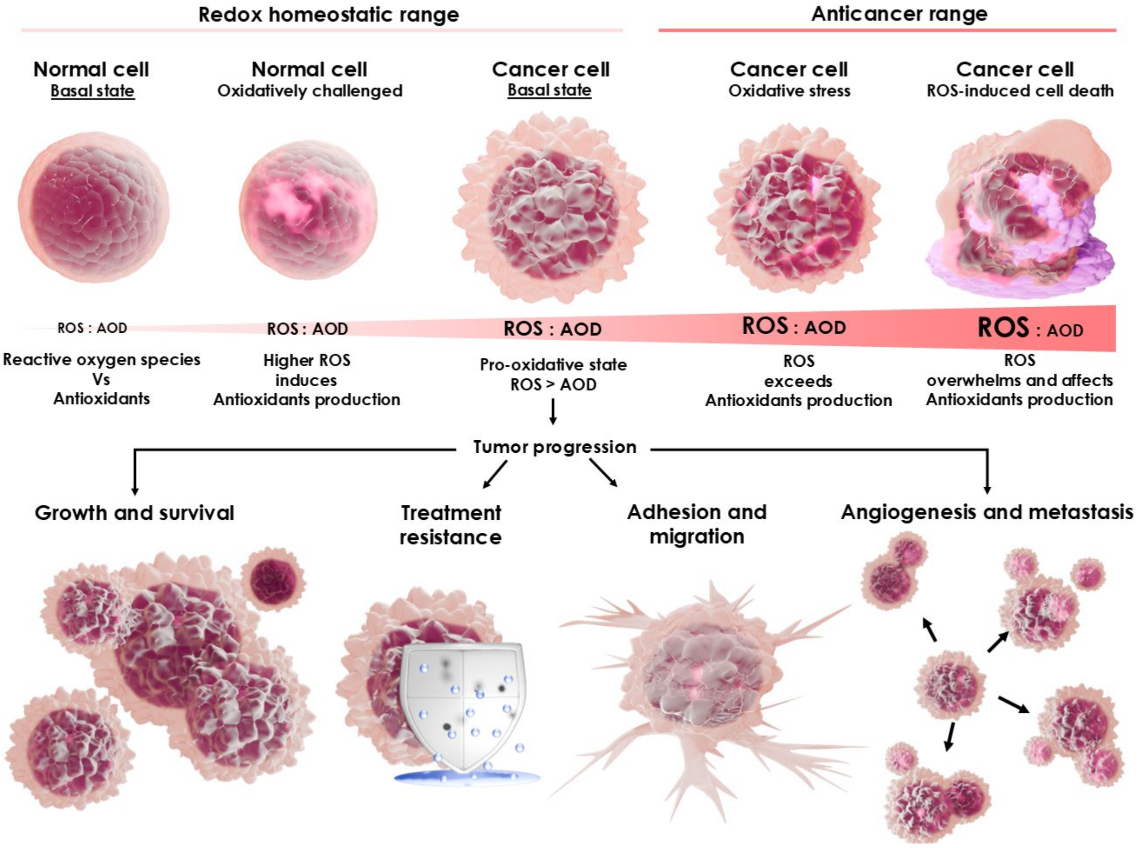

Figure 4.4. **ROS in tumor development and progression.** Normal cells maintain a balanced equilibrium between reactive oxygen species (ROS) and antioxidants (AOD). Under oxidative stress, antioxidant levels increase to mitigate potential mutagenic events and inhibit the initiation of cancer. However, once a tumor has formed, the pro-oxidative state of cancerous cells enhances their metabolic activity and upregulates specific pathways associated with cell adhesion, migration, angiogenesis, and metastasis. If ROS levels are further increased due to cancer treatments, the cellular homeostasis between ROS and AOD becomes unsustainable, leading to cellular damage. If this oxidative stress persists, the tumor cell undergoes irreversible damage, ultimately resulting in cell death.

Inside the cell, different ROS are interrelated, often acting as precursors of each other. The superoxide radical $\cdot O_2^-$ is primarily generated in the mitochondria due to the electron transport chain. It can be later transformed into H_2O_2 (through superoxide dismutase) or into RNS (nitrogen reactive species). RNS, such as peroxynitrite ($ONOO^-$), are also involved in signaling and oxidative stress, although to a lesser extent than ROS. While $\cdot O_2^-$ cannot pass through the cell membrane due to its charge, H_2O_2 can. Hydrogen peroxide plays a fundamental role in signaling (1-10 nM), but high concentrations cause oxidative stress (>100 nM). Although H_2O_2 is poorly reactive, it allows precise signaling when interacting with specific protein domains (such as cysteine).[31] This molecule is generated by metabolic reactions in the cytoplasm, peroxisomes, and the lumen of endoplasmic reticulum and mitochondria.[30] On the contrary, it is mostly detoxified through peroxidases (e.g. catalase, glutathione peroxidase, peroxiredoxins) (**Figure 4.5**). Through the Fenton reaction, H_2O_2 can produce hydroxyl radicals, as well as through Haber-Weiss reaction (reduction of Fe_{3+} to Fe_{2+}) via $\cdot O_2^-$.[32] Hydroxyl radicals are an extremely reactive form of ROS, often inducing damage to membranes (causing lipid peroxidation) and DNA.[31]

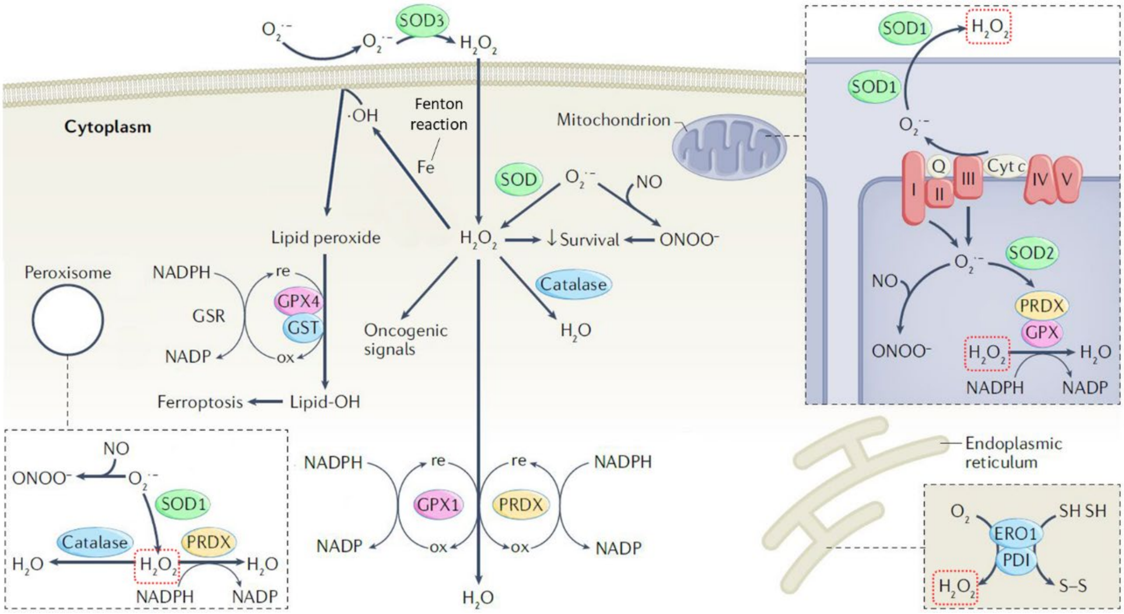

Figure 4.5. Generation and metabolism of ROS. Superoxide dismutases (SOD) generates H_2O_2 from $\cdot O_2^-$ in different compartments of the cell; peroxiredoxins (PRDX), glutathione peroxidases (GPX), and catalases are able to metabolize them; non-metabolized H_2O_2 can produce hydroxyl radicals through the Fenton reaction. Endoplasmic reticulum oxidoreductase 1 (ERO1), protein disulfide isomerase (PDI), cytochrome c (Cyt c), glutathione reductase (GSR), glutathione-s-transferase (GST). Adapted from [30].

Despite their important role in cancer cell signaling and survival, ROS represent a double-edged sword, as cancer cells are more susceptible to ROS-induced damage due to their elevated basal ROS levels. Some of the reasons of this accumulation in cancer cells include altered energetic metabolism due to Warburg effect (relying heavily on glycolysis and lactate, producing additional byproducts such as ROS),[33] higher mitochondrial activity (and consequent ROS during oxidative phosphorylation), and faster metabolism (to support the faster growth and proliferation rates, leading to a higher accumulation of ROS). Nevertheless, to maintain redox homeostasis, cancer cells also increase the levels of antioxidants. For instance, the nuclear factor erythroid 2 (NRF2), which promotes the transcription of several genes related to the antioxidant system, is commonly found to be overactivated in cancer.[34] However, despite this enhanced antioxidant mechanism, the high basal ROS level of the cell reduces its capacity to tolerate further accumulation. As a result, even a moderate increase in ROS can surpass the cell's survival threshold, leading to cell dysfunction or death. This vulnerability in the metabolism of cancer cells offers an excellent—and crucial—target for the novel approaches. Moreover, modulating ROS levels can be exploited as therapeutic strategy for sensitizing the cell against other agents or directly inducing their death due oxidative stress (**Figure 4.6A**).[35] For instance, the combination of mitochondrial ROS-inducing methodologies with radiotherapy (a well-known source of ROS)[36] or chemotherapeutics, such as temozolomide (TMZ), has shown superior therapeutic outcomes and cell death compared to the administration of these treatments alone (**Figure 4.6B**).[37]

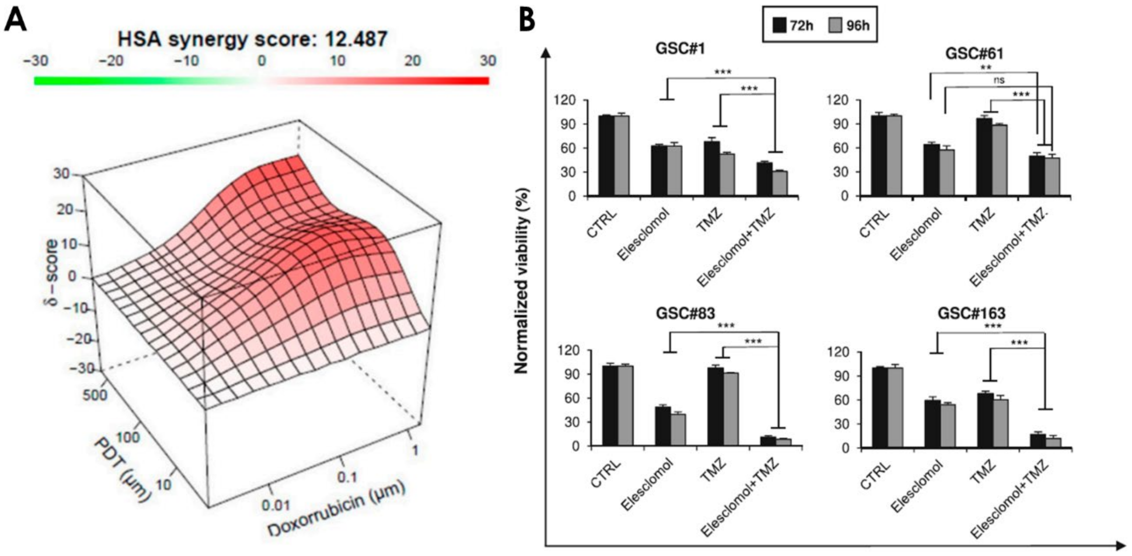

Figure 4.6. Enhanced effects of dual treatments based in pro-oxidants. A) Highest single agent (HAS) score measuring the effect of photodynamic therapy (PDT) and the pro-oxidant doxorubicin alone and simultaneously in the U87 cell line (higher scores represent synergy).[35] **B)** Comparison between the viability of different Glioblastoma cell lines after being treated with the pro-oxidant elesclomol and temozolomide (TMZ) together or alone. Adapted from [[37]].

Although excessive ROS can induce or influence cell death, it does so through various mechanisms. These mechanisms can be divided in non-programmed (necrosis) and programmed (e.g., apoptosis, autophagy, ferroptosis, parthanatos, necroptosis) cell death. Necrosis can be stimulated by external factors, such as physical injuries, infections, or toxins, like ROS, which lead to fatal morphological alterations and the eventual death of the cell. On the other hand, programmed cell deaths are driven by tightly regulated intracellular transduction pathways.[38] Nevertheless, oxidative stress can also trigger them in different ways, usually based on the affected molecules and structures. For instance, ferroptosis is due to lipid peroxidation, parthanatos is due to DNA damage, and apoptosis is due to mitochondria, endoplasmic reticulum or overall oxidative damage in structures.[39]

Therefore, by carefully modulating ROS levels, it is possible to exploit the balance between ROS's role in promoting tumor survival and its potential to induce tumor cell death, offering a promising approach for developing more effective treatments for Glioblastoma. However, most ROS-based therapies are also based on systemic methodologies, highlighting the urgent need for innovative approaches to address this devastating disease and fulfil the significant unmet clinical needs.

4.1.5 Innovative approaches for Glioblastoma

In this scenario, one disruptive approach could be the development of specific scaffolds, such as membranes or bioadhesive patches, that could be placed in the surgical bed after tumor resection during a post-surgery to actively target Glioblastoma recurrence (**Figure 4.7**).[40] Such membranes must demonstrate bioadhesion, biocompatibility and the capacity to eliminate cancer cells, for example, by modulating their redox homeostasis via ROS production. As previously mentioned in Chapter 1, catechol and polyphenolic-based compounds are well known as ROS modulators and key players in natural-based adhesive structures,[41,42,43] thus emerging as excellent candidates in advance scaffolds.[44]

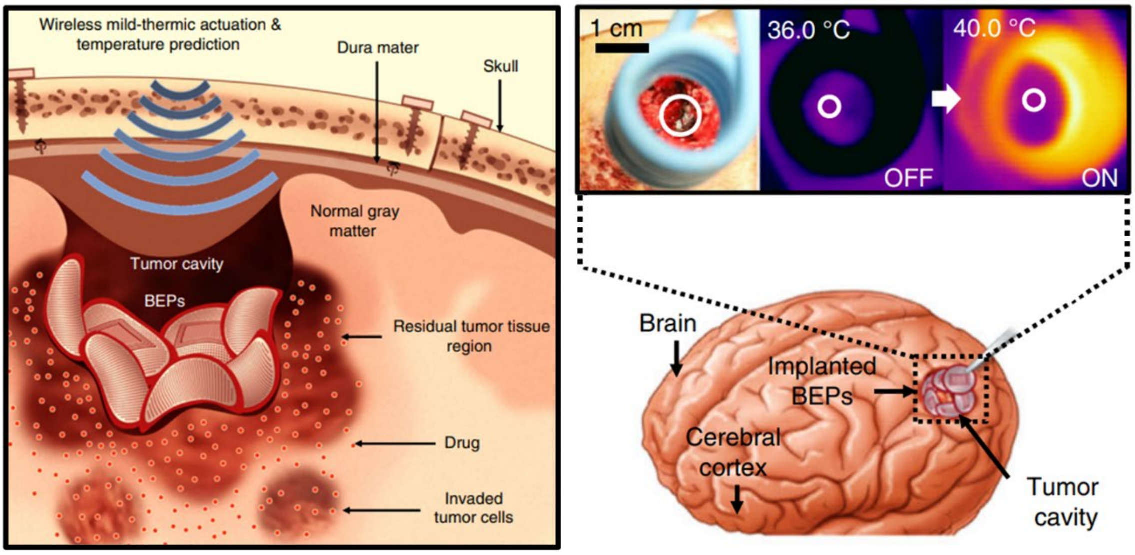

Figure 4.7. Flexible device for GBM treatment. The bioresorbable electronic patch (BEP) can be loaded with a drug and released upon thermal activation. Adapted from [40].

However, the currently available catechol-based membranes (discussed in section 1.4.5) do not meet the necessary requirements to serve as scaffolds for localized therapy: they are inadequate for therapeutic use via ROS production, and, these membranes are highly constrained by their reliance on other catechol-based compounds, severely limiting their potential applications in medicine. For these reasons, finding a new strategy that allows for the formation of a wide range of catechol-based membranes in an easy, eco-friendly and reproducible way is a pressing concern. The final product obtained should be easy to handle (robust and flexible) without the need for substrate or side molecules (e.g., PEI or chitosan).[45]

Besides the complications that may occur during a craniotomy, the patient not only has to deal with the wound and the healing process, but also the possibility of infection during the surgery and the recovery. As detailed in Chapter 3, addressing the risks of infections during medical procedures, such as surgeries, and the growing threat of AMR has become a significant concern.[46] In this specific scenario, craniotomies can result in an incidence of intracranial infections close to 7% in Glioblastoma patients.[47] Consequently, despite the challenges it entails, it is crucial to endow materials used in healthcare applications with antimicrobial properties.[48] However, the real challenge remains in developing these materials into ready-to-use membranes that actively treat tissue-related diseases by incorporating antimicrobial, anticancer and bioadhesive properties. In this context, this Chapter will demonstrate how these goals have been successfully accomplished.

4.1.6 Scope of this Chapter

Consistent with the previous discussion, this Chapter presents a series of novel free-standing membranes based exclusively on catechol derivatives and amines, obtained by a similar synthesis protocol as the described in Chapter 3. Therefore, it was hypothesized that the materials synthetized during this Chapter might also have antimicrobial properties, since both share a similar catechol-amine composition, with the advantage that they are free-standing. Most of these membranes have been optimized and characterized both physiochemically and biologically. Furthermore, particular emphasis has been stablished in the deep analysis and validation of the catechin-based membrane as localized treatment against cancer cells (**Figure 4.8**).

The obtained results can be summarized in:

- Development and optimization of a family of free-standing membranes, only by the permutation of catechol derivatives and amine-ligands.
- Obtention of a specific membrane (including the natural polyphenol compound catechin) with an outstanding ability to continuously produce ROS, including:
    - Determination of the ROS generation profile in specific environments (including biological medium), stability over time and the individual ROS levels generated.
    - Confirmation of the oxidative properties and their modulation with antioxidants
- Validation of the antitumoral properties:
    - In a broad spectrum of different cancer cell lines, Glioblastoma cell lines, primary cultures and 3D cultures (spheroids).
    - Correlation of the cell death with ROS production. Confirmation of oxidative stress mediated cell-death (using several metabolic-pathway inhibitors).
- Influence on the metabolism and development of the cell:
    - Internal and external morphological changes.
    - Effects on survivability, migration, adhesion, and energetic metabolism.
    - Protein profiling.

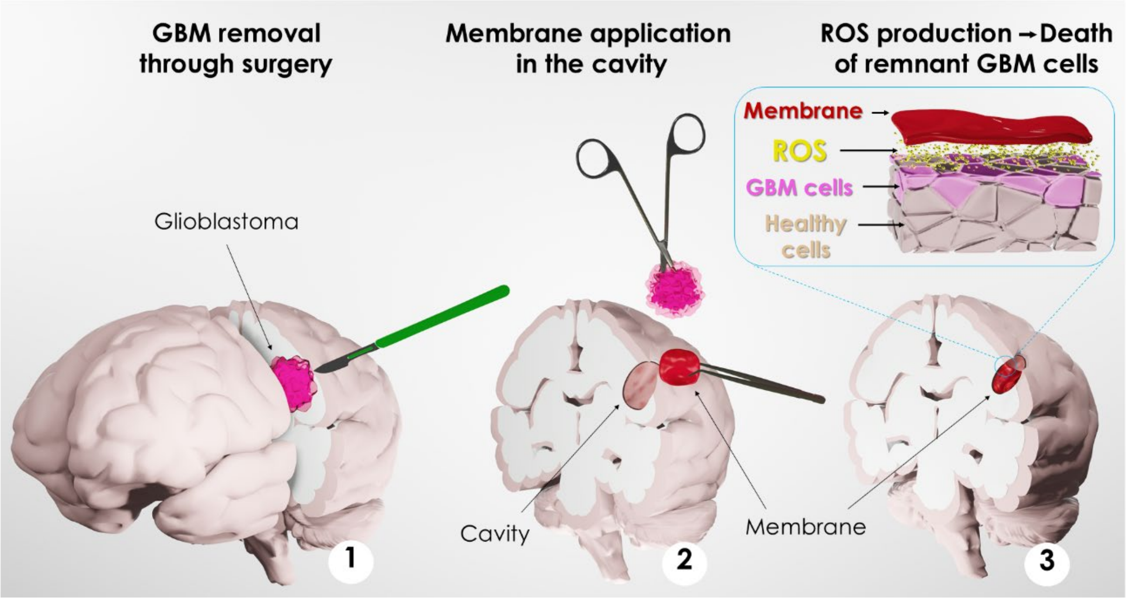

Figure 4.8. Representation of the applicability of the catechol-amine membrane **CATH-M** for Glioblastoma treatment. This approach is based on local ROS-mediated release mechanism in the surgical bed (cavity).

4.2 Results and Discussion

In this Chapter, the process of synthesis, optimization and validation of bioinspired membranes is presented. These membranes have been produced following the catecholamine-based polymerization approach, which is well established in our research group.[49,50,51] The influence of different synthesis parameters has been studied, and their significance is explained. New combinations have also been designed and obtained, highlighting the remarkable versatility of the approach employed. Notably, among all the candidates from the obtained membranes, one in particular, named as **CATH-M**, was chosen for its superior characteristics, making it a prime candidate for a further comprehensive characterization, from both physicochemical and biological perspectives, as well as for its validation in the treatment of Glioblastoma.

4.2.1 Synthesis of the catechol-based free-standing membranes

As demonstrated in the previous Chapter 3 (**Figure 4.9A**), the innovative approach followed for the formation of catecholamine-based polymers enables the efficient and straightforward production of adhesive coatings on virtually any surface. Remarkably, by fine-tuning the reaction parameters, the formation of floating membranes at the air-liquid interface can be significantly optimized. This intriguing observation suggests that the advantageous properties observed in the adhesive coatings may also be effectively transferred to the polymeric membranes. Consequently, these membranes possess the potential to be used in various fields without the need of support, thereby broadening their application scope.

Similar to the approach used for coatings, the synthesis of these membranes depends on two key components: catechol- (**Figure 4.9B**) and amine- (**Figure 4.9C**) based derivatives. The most extensively used amine has been HMDA, which has facilitated an in-depth investigation of the influence of various parameters. However, the versatility of this approach has also been demonstrated by using other amines, such as TRI2 and tris(4-aminophenyl)amine (3PHEN), among others.

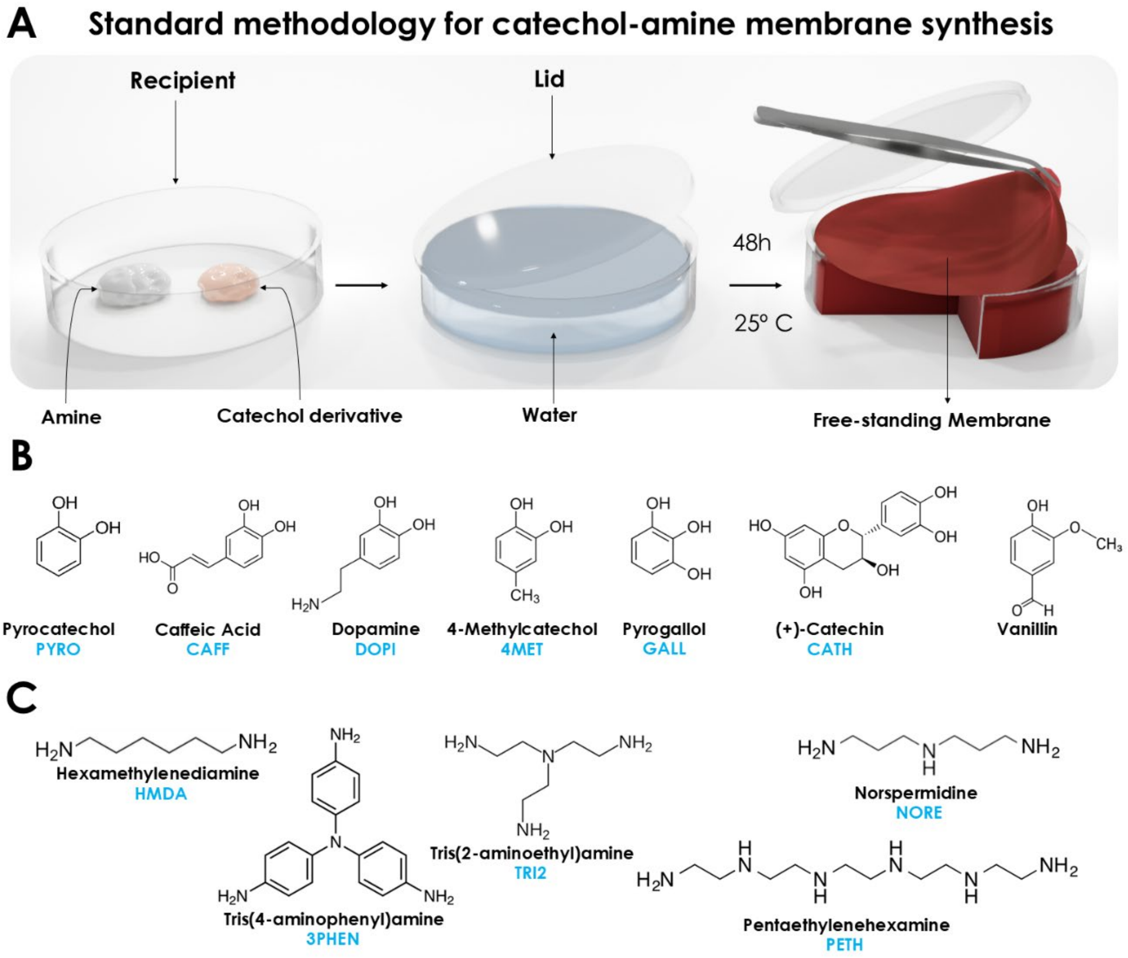

Figure 4.9. Catechol-amine free-standing membrane synthesis protocol. A) The standard conditions are based on the mixture of a catechol derivative **B)** and a **C)** di/tri-amine. Both reagents were dissolved in water and after 48 hours at room temperature, the membranes were synthetized. Here, all the molecules tested during this chapter are shown. Below each molecule, their name and abbreviation are shown in black and blue, respectively.

4.2.1.1 HMDA

The first-generation membranes developed by our group were based on HMDA and four catechol derivatives: PYRO, DOPI, CAFF and 4MET. Although some of these membranes, particularly those based on PYRO, exhibited significant manipulability, their mechanical properties required substantial improvement as many of them were extremely brittle. The initial synthesis parameters were:

1. A catechol concentration of 10 mM.
2. The addition of the amines in a ratio 1.5 to 2.5 times higher than catechol
3. Conducting the synthesis in 6 cm diameter glass Petri dishes, using 10 mL of water, with a reaction time of 48 h at room temperature, low magnetic stirring and restricted oxygen exchange.

The optimization of these conditions allowed for stablishing a standardized protocol for the production of new functional catecholamine-based membranes. Most of the optimization process focused primarily on **PYRO-M,** since it was the most manipulable membrane. The identified optimization parameters (**Figure 4.10**) and its influence in the process of membrane formation provide a comprehensive overview of the standardized procedure (**Table 4.1**). The primary goal of the optimization process was to develop different HMDA-based membranes with sufficient mechanical resistance to be handled.

Different parameters were adjusted in order to test the versatility of the approach:

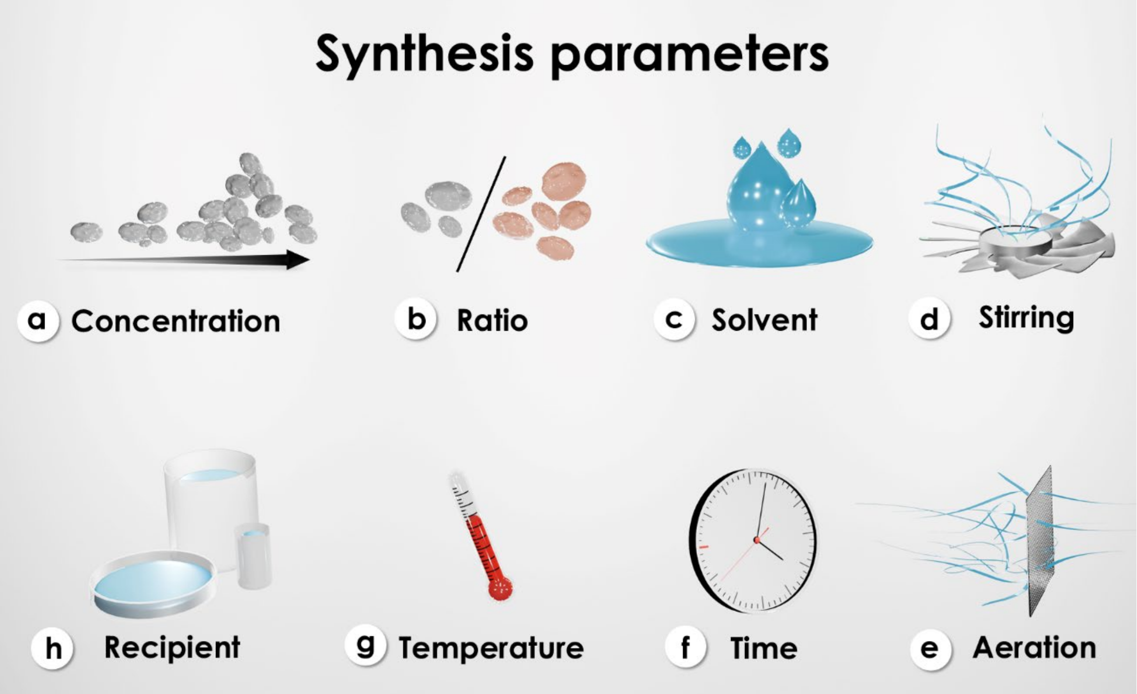

Figure 4.10. Parameters involved in the synthesis of catechol-amine membranes. The optimization process stablished as standard conditions: 50 mM of catechol (1:2 catechol-amine) in MiliQ water, without stirring, restricted air flux (lid perforation), using a 15 cm petri plate (50 ml volume), for 48 h at room temperature (20 to 25 °C). Among the different catechol derivatives and amines, PYRO and HMDA, respectively, have shown to be the most versatile (higher probability to obtain a membrane).

a) Concentration. Adjusted up to 100 mM, although higher concentrations generally resulted in increased byproducts precipitation. The concentration increase facilitated the manipulation of

CAFF- and 4MET-based membranes and induced considerable differences in the **PYRO-M** morphology (**Figure 4.11A**).

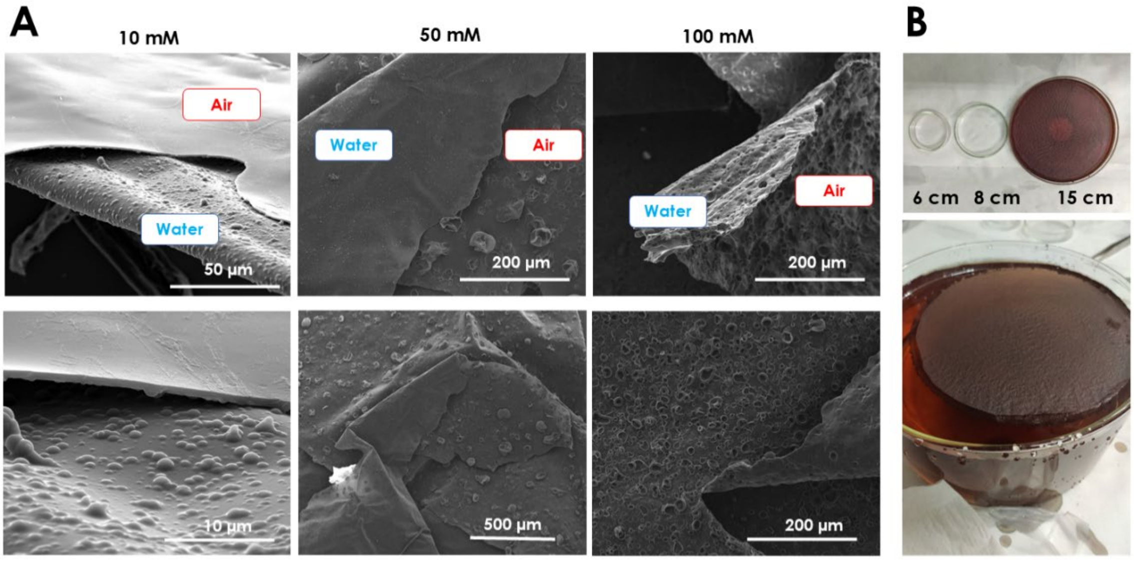

Figure 4.11. Effect of the increase of PYRO-M concentration and size scalation. A) Scanning electron microscopy (SEM) micrographs showing the morphology of the **PYRO-M** membrane in both air- and water-facing sides, when the molarity of pyrocatechol is 10, 50 or 100 mM (ratio 1:1.5 **PYRO-H**). **B)** The different recipients used during the scalation process (up) and the resulting 15 cm membrane floating during the washing step (bottom).

b) Catechol-amine ratio. The optimal proportion of catechol to amine was approximately 1:2, becoming the standard approach for synthesizing HMDA-based membranes. Ratios close to 1:1, or exceeding 1:3 negatively impacted the synthesis process. For example, a ratio of 1:1.5 was ideal for PYRO and 4MET, whereas a ratio of 1:2 was optimal for CAFF and GALL. Conversely, 1:2.5 the was most effective for DOPI and CATH. A precise adjustment of the ratio was crucial for ensuring the structural integrity and functionality of the membrane.

c) Solvent. Type 1 ultra-pure water proved to be the perfect medium for these reactions, making the process safer, cleaner, affordable and environmentally friendly.

d) Stirring. Initial conditions included using spherical magnetic stirrers set in the center of the plate to maintain a constant homogeneity. However, a system without turbulences (no stirring) improved the homogeneity of the membrane by decreasing byproducts or precipitates.

e) Aeration. The oxidation reaction driving membrane synthesis relies on ambient oxygen. To allow the entrance of air, while minimizing the evaporation, all synthesis containers were covered with a pierced Parafilm®. During the scalation process, pierced plastic lids were used to cover the reaction.

f) Time. While the reaction between catechol derivatives and HMDA is considerably fast (inducing an instant color change when mixed), the polymerization of a homogeneous membrane at the air-water interface requires more time. Formation can be visually noticed after

2 to 4 h of reaction, followed by a thickness increase and a darker color. In most cases, 48 h was established as the standard reaction time, since no considerable thickness increase was observed beyond this point (**Figure 4.12**).

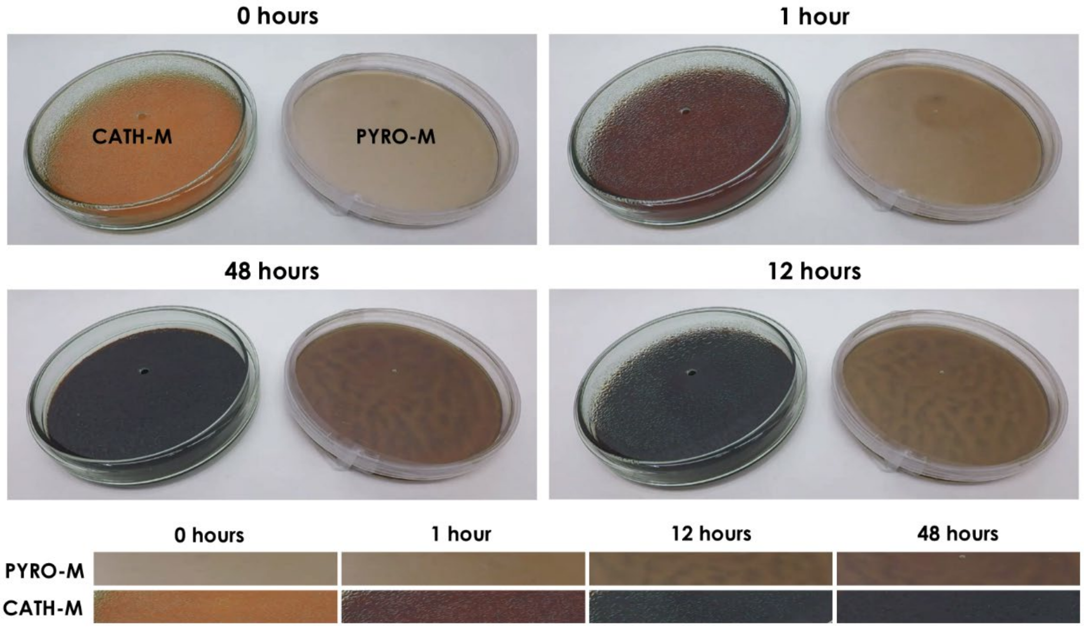

Figure 4.12. 48 h time-lapse of the CATH-M and PYRO-M membranes synthesis. It can be observed how the solutions become darker with time due to the oxidation, leading to the formation of the membranes.

g) Temperature. Temperature was found to play no significant role in the reaction. Synthesis of **CATH-M** and **PYRO-M** at 4º C (fridge), 20º C (desk) and 37º C (incubator) showed no considerable differences between them. However, temperature influenced solvent evaporation (leading to its concentration) and humidity levels.

h) Lab scale (bigger membranes). After obtaining highly manipulable HMDA-based membranes, the synthesis Petri plate was scaled from 6 cm to 8 cm and finally to 15 cm diameter. Volumes of each recipient (10, 20 and 50 ml, respectively) were established to maintain a consistent height while only increasing the surface in contact with the air, minimizing changes in the surface-to-volume ratio (**Figure 4.11B**).

Table 4.1. Optimized synthesis parameters.

Synthesis parameters	Tested conditions	Selected (average)
Concentration	10, 20, 50, 75, 100 and 200 mM (catechol)	50 – 100 mM
Ratio	1 : 1-4 (catechol : amine)	1 : 2
Solvent	Water and buffer pH8	Water
Stirring	Stirring (different sizes and speed) and no stirring	No stirring
Aeration	Sealed, pierced lid, uncovered	Pierced lid
Time	1-7 days	2 days
Temperature	4, 15, 20, 25 and 37 C°	20-25 C°
Recipient	Plates with diameters of 6, 8, and 15 cm	15 cm

4.2.1.2 Post-synthesis manipulation

Initially, the catechol-based membranes could only be handled under wet conditions. After their synthesis, the membranes were thoroughly washed with water and then cut using a biopsy punch or blade, allowing for high precision, especially after their optimization (due to their improved mechanical properties) (**Figure 4.13A**). The adhesive properties of these membranes caused them to firmly adhere to different surfaces once dried, making their removal impossible in most cases. After different approaches, a tool made from metallic wire was developed to dry the membranes, reducing the contact surface and, consequently, the adhesion points. Finally, this process was further improved by the implementation of metallic nets (**Figure 4.13B**).

Aiming to obtain a sterile material, the synthetized membranes were initially autoclaved after being washed. However, this process was eventually avoided due to its extreme conditions, which altered the mechanical (and probably chemical) properties of the material. Therefore, a sterile synthesis protocol was performed inside a biosafety laminar flow cabin, establishing it as a standard clean-method for the future biological characterization. In this case, the properties of the material were ensured to remain stable until they were tested in cell culture.

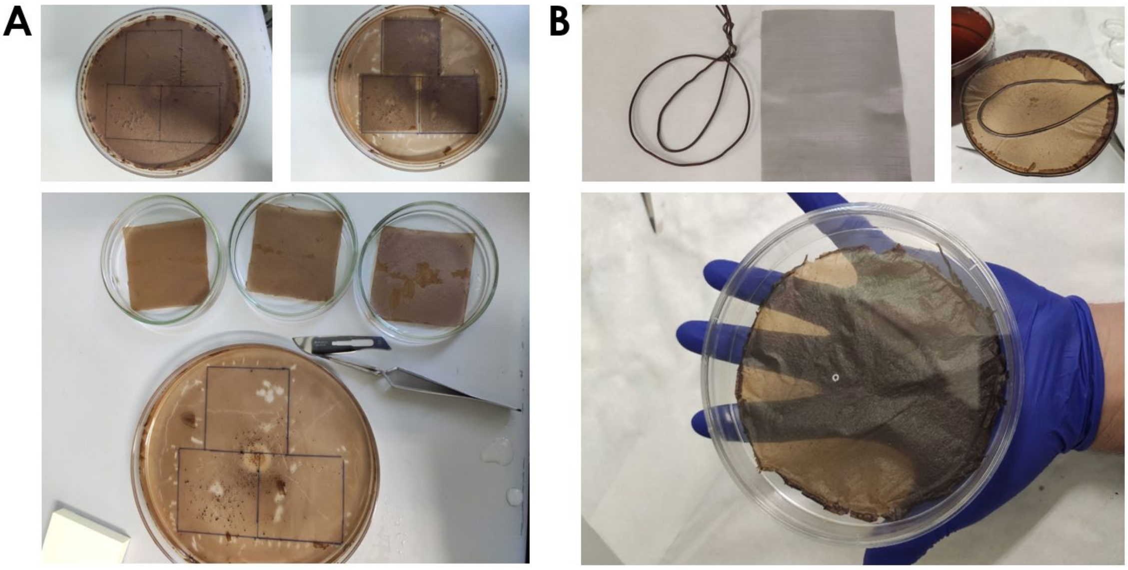

Figure 4.13. Manipulation of the membranes A) Example of the precision that can be achieved when cutting the membrane into three perfect squares. **B)** Tools used for drying the membranes (up) and a 15 cm **PYRO-M** membrane already dry.

4.2.1.3 Other amines

TRI2: In consistency with the previous results obtained with HMDA, the TRI2 was used as ligand for the synthesis of new membranes. In contrast to HMDA, a higher catechol-amine ratio was required to produce a manipulable material, averaging 1:3 instead of 1:2. The resulting membranes were generally smoother and more fragile, exhibiting a darker color while maintaining a morphology similar to that of HMDA. Notably, no membrane formation was observed in the case of CAFF (**Figure 4.14**). It is worth mentioning that the remaining post-synthesis solution (after extracting the membrane) was considerably more homogeneous and precipitate-free than those achieved with HMDA.

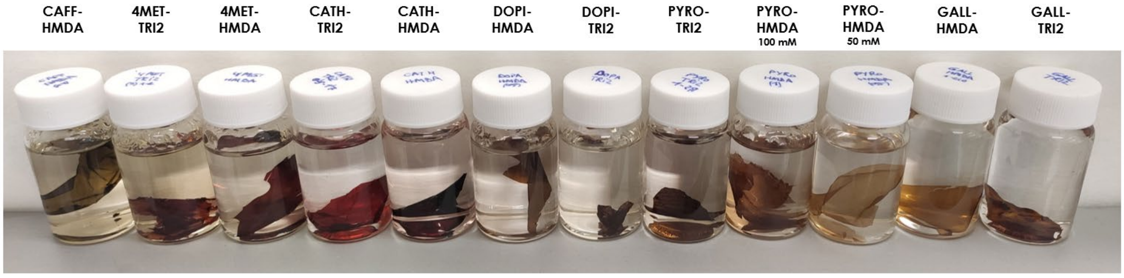

Figure 4.14. HMDA and TRI2-based membranes.

Based on this and previous observations, which showed that the post-synthesis solutions were able to behave like water-based adhesives, the adhesion properties of the 12 permutations (HMDA or TRI2 with the 6 catechols) were further evaluated, demonstrating that **GALL-TRI2**, **GALL-M** and **CATH-M** produced satisfactory adhesive results. This finding led to a new method for producing water-based catechol-amine adhesives in our research group.[52,53]

3PHEN: Going one step forward, 3PHEN was also tested to produce new membranes. This molecule, characterized by three free amines and also three aromatic rings, was theoretically able to confer conductive properties. Interestingly, this membrane achieved electrical conductivity values of 300 ± 50 kΩ/cm in wet conditions. These results established a new research line for the development of conductive membranes with applications in neuroelectronic interfaces, which is currently carried out by PhD Student Sara Pugliese.

Alkylated polyamines: Having a similar structure to the HMDA, the additional amine groups in these molecules were expected to stablish an additional bond with the catechol-derivatives, increasing the possibilities of obtaining a stronger membrane. Whereas the norspermidine (NORE)-based membranes were successfully synthetized without highlighting any distinct characteristic, the pentaethylenehexamine (PETH)-based membranes exhibited a unique feature not observed in any other membranes: elasticity. Interestingly, the ideal ratio for **PYRO-PETH** was the lowest among all the amines observed (1:1), suggesting that the additional amino groups in the PETH chain might be used as anchoring points. In wet conditions, this membrane could be considerably stretched and return to its initial shape (**Figure 4.15A**). Furthermore, after drying, this property can be recovered upon rewetting (**Figure 4.15B**). In contrast, all other membranes tore when subjected to the same force, showing significantly less elasticity. This exceptional property of the PETH-based membrane makes it a promising material for applications in elastic tissues, such as skin.

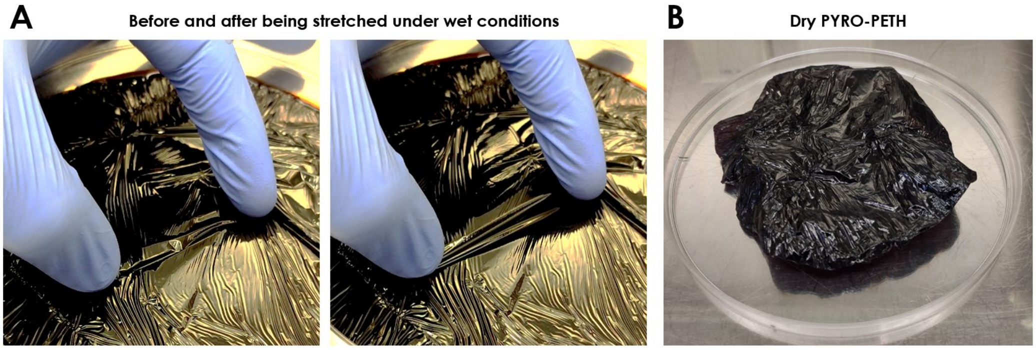

Figure 4.15. **PETH-based membrane. A)** Elasticity of the **PYRO-PETH** membrane in wet conditions and its appearance when **B)** dry.

Among the various catechol derivatives and amines, HMDA-based membranes demonstrated superior properties, including enhanced manipulability, homogeneity, affordability and versatility, as they successfully formed membranes with most of the tested catechol derivatives. Consequently, HMDA-based membranes were the candidates chosen for further physicochemical and biological characterizations, with a particular focus on Glioblastoma treatment.

4.2.2 Characterization of the bioinspired polyphenol-HMDA-based membranes

Among the different combinations, six HMDA-based membranes (**PYRO-M**, **CAFF-M**, **GALL-M**, **DOPI-M**, **4MET-M** and **CATH-M**) (**Figure 4.16A**) were finally chosen as candidates for further analysis, where their chemical structure, exposed functional groups, morphology and cytotoxicity were assessed.

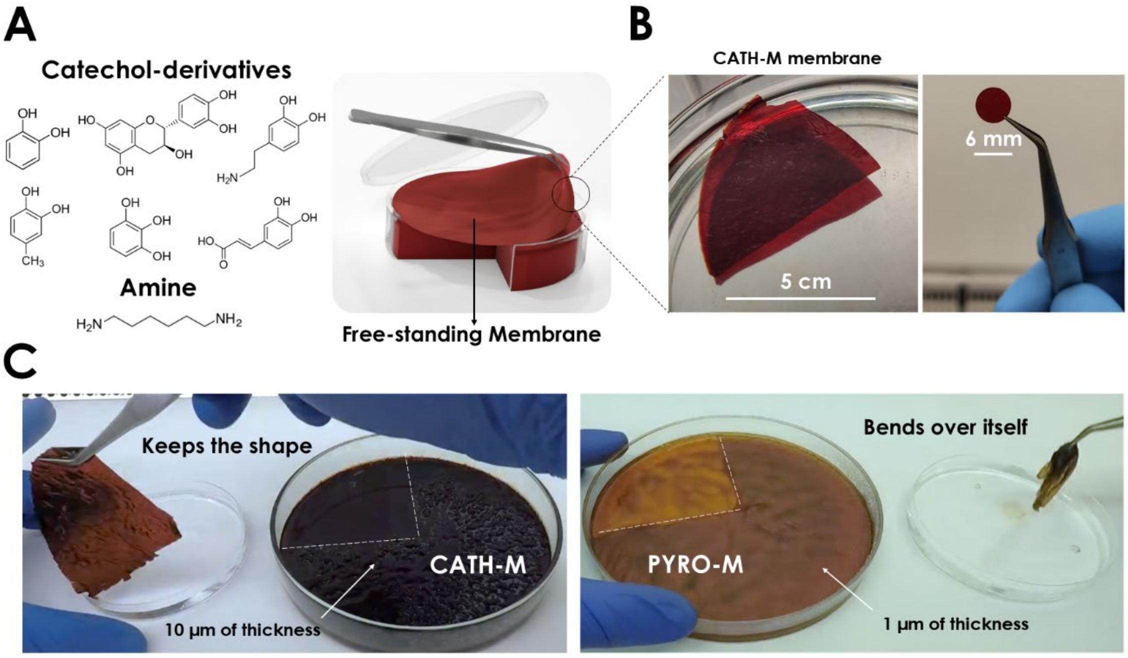

Figure 4.16. Catechol-HMDA membranes synthesis. A) The six catechol derivatives that enabled the synthesis of a membrane with HMDA. **B)** The catechin-HMDA based membrane (**CATH-M**), highlighting its manipulability. **C)** Pieces of both **CATH-M** and **PYRO-M** when removed from a liquid environment. While **CATH-M** retains its shape outside the medium, remaining flat, **PYRO-M** collapses onto itself.

It is worth mentioning that the higher number of rings and hydroxyl groups of catechin, compared to other catechol derivatives, play a crucial role in the significant differences observed in the membranes, particularly regarding their thickness and manipulability (**Figure 4.16B**). The enhanced mechanical properties of **CATH-M** allowed for maintaining its shape outside of water, in contrast to **PYRO-M**, for example (**Figure 4.16C**).

4.2.2.1 Physicochemical and morphological characterization

Once the membranes were synthesized and isolated, their polymerization was thoroughly investigated using various techniques. Initially, FTIR spectroscopy was conducted to identify the main bonding structures. The results clearly indicated the presence of both amine and catechol/quinonic moieties in all membranes (**Figure 4.17**). The spectra consistently exhibited similar features, including a characteristic broad band around 3250 cm^{-1}, attributed to the stretching vibrations of hydroxyl and amine ($-NH_2$) groups from phenol and amine molecules, respectively. Additionally, the peak around 2850 cm^{-1} was associated with aliphatic carbons (C–H), mainly present in the HMDA ligand. Notably, the peak at 1260 cm^{-1} could be assigned to a secondary amine binding to an alkyl or aromatic ring, indicating a successful catecholamine polymerization. Finally, the peaks at 1700 cm^{-1} and around 1500 cm^{-1} were attributed to quinones (C=O) and C=C–H and C=C vibrations from the catecholic/quinonic rings, respectively. Furthermore, other specific functional groups were identified. For instance, in **DOPI-M**, a peak at 1000 cm^{-1} could be assigned to free amine ($-NH_2$) groups, present in both HMDA and DOPI. On the other hand, the carboxylic groups (–COOH) present in **CAFF-M** were confirmed by a distinct band at 1270 cm^{-1}. Notably, in the case of **CATH-M**, the intensity of the peak corresponding to –OH groups were significantly higher compared to the other membranes (**Figure 4.17B**). This indicated a greater abundance of free hydroxyl groups incorporated by the catechin molecules. Such an increase in hydroxyl groups could lead to higher reactivity in the presence of oxygen and wet environments, directly impacting the production of ROS and its biological implications.

After confirming the polymerization process, the surface composition of the membranes was analyzed to identify the exposed functional groups. This is particularly important, as these groups can play a key role in mediating interactions at the biointerface between the membrane, tissue, and cells. To achieve this, X-ray photoelectron spectroscopy (XPS) curve-fitting was performed (**Figure 4.18**), enabling detailed analysis of the chemical bonding environment within the outermost 10 nm of the membrane surface. In all the synthesized membranes, C1s spectra showed three different chemical environments. In addition to the aliphatic component, the existence of the other two contributions confirmed that catechol coexists in its two forms: fully reduced (C–OH) and quinonic (C=O). In the case of **CATH-M**, the C=O band was significantly higher, thus

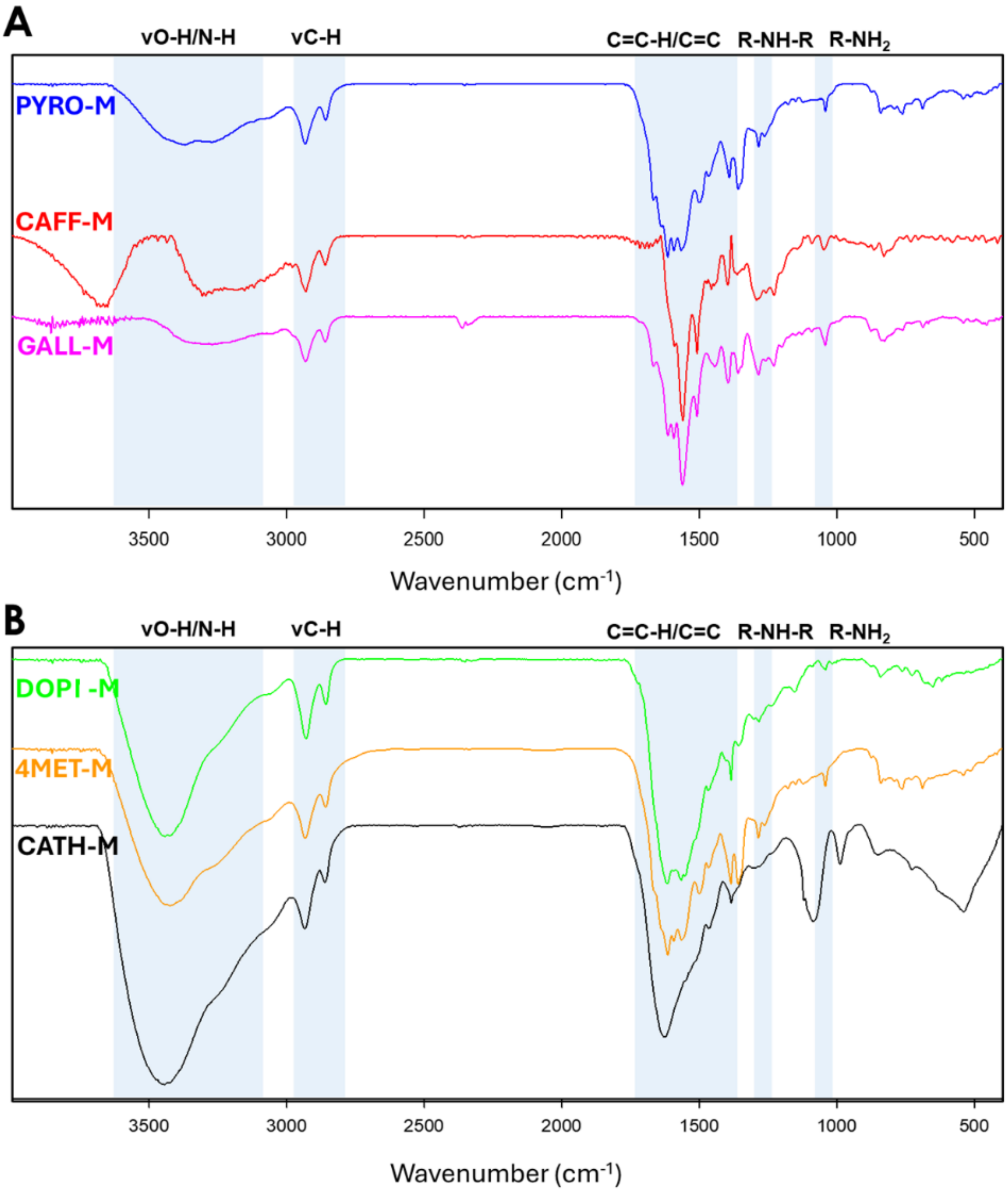

Figure 4.17. Fourier transformed Infrared (FTIR) analysis of the synthesized membranes. FTIR spectra of **A) PYRO-M**, **CAFF-M** and **GALL-M** and **B) DOPI-M**, **4MET-M** and **CATH-M**.

confirming its potential for ROS production by undergoing further oxidation in atmospheric environments. O1s spectra support this statement, as the same contributions appeared, including a third one corresponding to the semiquinone form (C–O$^{\cdot}$). In the case of N1s spectra, it showed free (R–NH_2) and aliphatic (R–N–R) amine-related contributions, associating the first one to unreacted amine tail ends of the HMDA and the second one to the result of cross-linking. The presence of hydroxyl and quinones groups is of special interest due to: i) offering interaction and strong adhesion and ii) be further oxidized, thus producing ROS during the process.

After identifying the exposed functional groups, elemental analysis was conducted to determine the CHON composition of the synthesized membranes, in order to provide fundamental insights into their chemical composition (**Table 4.2**). The obtained results allowed for determining the ratio between catechol and amine molecules in the polymer. Notably, **DOPI-M** showed the lowest ratio, probably due to the capability of dopamine to self-polymerize, thus requiring less HMDA molecules to generate the membrane. In contrast, **CAFF-M** exhibited the highest ratio. **GALL-M** displayed a similar ratio to **PYRO-H**, as did **CATH-M**, despite existing significant structural differences between them. The lower number of HMDA molecules in the **4MET-M** membrane

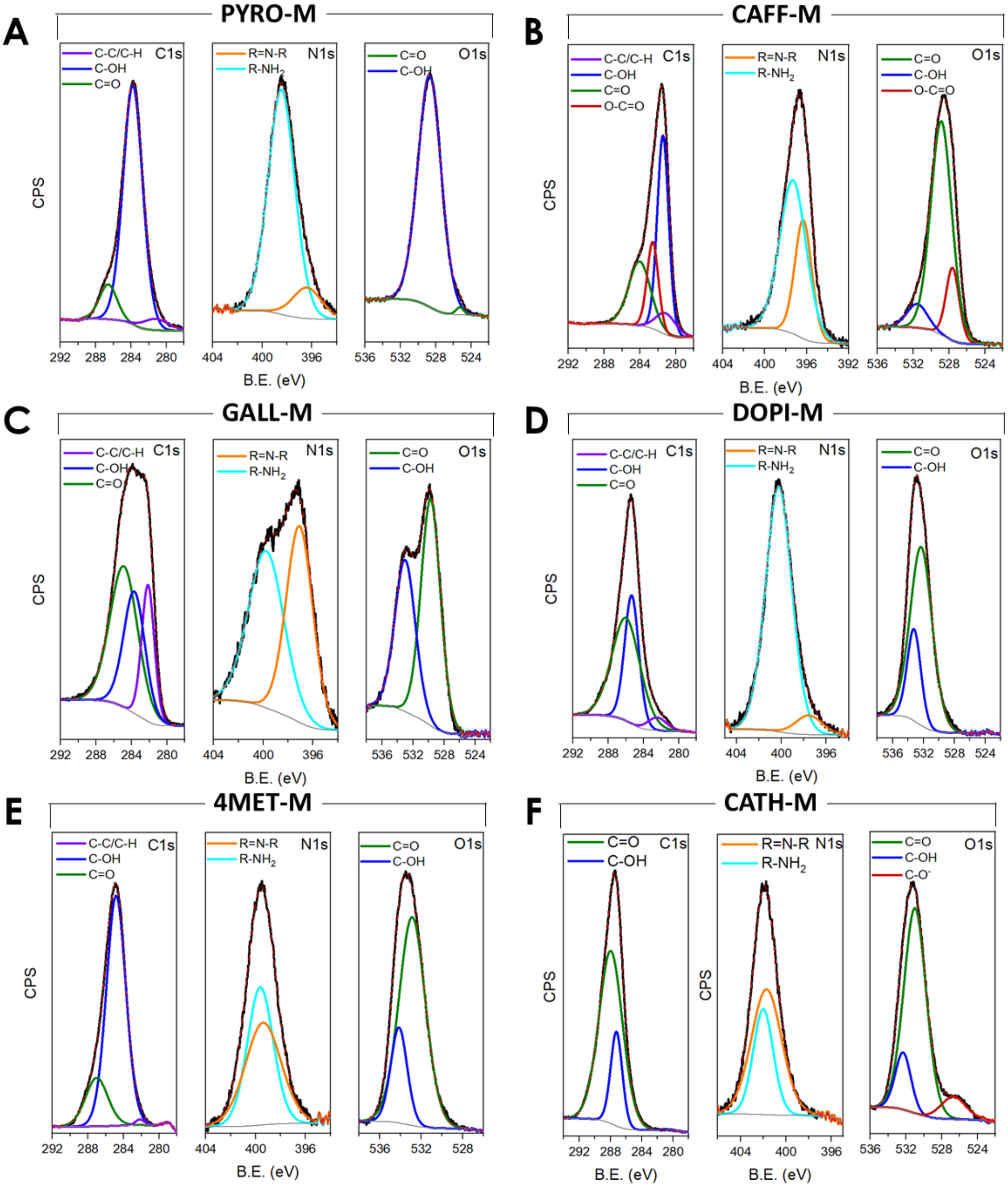

Figure 4.18. X-ray photoelectron spectroscopy (XPS) curve-fitting of the synthesized membranes. Curve-fitting results for C1s, N1s and O1s high-resolution XPS spectra for **A) PYRO-M**, **B) CAFF-M**, **C) GALL-M**, **D) DOPI-M**, **E) 4MET-M** and **F) CATH-M**. CPS: Counts per second.

Table 4.2. Elemental analysis.

Membrane	Catechol : Amine Synthesis ratio	Catechol : Amine Polymer ratio	Empiric formula			
			C	H	O	N
PYRO-M	1 : 1.5	1 : 0.81 ± 0.03	6.09 ± 0.17	9.26 ± 0.28	1.23 ± 0.04	1 ± 0 .03
DOPI-M	1 : 2.5	1 : 0.42 ± 0.01	5.38 ± 0.15	7.7 ± 0.04	1.1 ± 0.02	1 ± 0.02
CAFF-M	1 : 2	1 : 1.24 ± 0.02	7 ± 0.05	10.26 ± 0.14	1.62 ± 0.02	1 ± 0.01
GALL-M	1 : 2	1 : 0.87 ± 0.02	6.37 ± 0.11	9.77 ± 0.06	1.73 ± 0.05	1 ± 0.01
4MET-M	1 : 1.5	1 : 0.62 ± 0.13	8.72 ± 0.07	12.21 ± 0.04	1.71 ± 0.42	1 ± 0.01
CATH-M	1 : 2.5	1 : 0.87 ± 0.03	9.71 ± 0.18	15.07 ± 0.17	3.45 ± 0.12	1 ± 0.02

compared to **PYRO-M** suggests that the methyl group in the para-position decreases the reactivity of the catechol towards HMDA. This observation further supports the brittle nature of the **4MET-M** membrane. Interestingly, despite the reactions start with an excess of amine, the average ratio found in the membranes was of 0.88 amines per catechol molecules (without taking into consideration the particular case of dopamine). Notably, these results underscored the reproducibility, as measurements from three different batches displayed low error rates.

The choice of the catechol derivative not only influenced the color and chemical composition, but also the physical properties of the resulting membranes (**Figure 4.19A**). **PYRO-M** was characterized as the most homogeneous, mechanically resistant and flexible (ability to bend over itself) membranes. In contrast, **GALL-M** exhibited significant heterogeneity, but appeared to have enhanced surface adhesion. As previously mentioned, the hydroxyl groups of catechols play a crucial role in adhesion and the establishment of a broad range of molecular interactions. GALL, containing three hydroxyl groups, exhibited enhanced adhesion due to increased surface interactions, endowing it with greater adhesion capacity. Besides, membranes derived from the combination of HMDA with catechol derivatives DOPI or CAFF demonstrated easy manipulability and flexibility, respectively. Conversely, 4**MET-M** resulted to be the most brittle membrane, whereas CATH allowed for the formation of the thickest and most manipulable membrane.

From a morphological perspective, SEM showed that all six different membranes shared some patterns in their topography and exhibited a Janus-like morphology (**Figure 4.19B**). Whereas the air-facing side in all the cases was characterized by a smooth or mostly flat surface (though “bubbles” could be observed), the water-facing side yielded a particle-embedded surface, displaying higher variability between membranes (with **PYRO-M** being the softest and **CATH-M** the roughest). In terms of thickness, most membranes measured between 1 and 3 µm. **PYRO-M** was the thinnest, ranging from 0.7 to 1 µm, whereas **CATH-M** was significantly thicker, measuring between 10 and 12 µm. This explains why **PYRO-M** was flexible and easily manipulable. On the contrary, **CATH-M** maintained its shape without bending when removed from water. Additionally, the considerable morphological differences between the two sides of

CATH-M allow for easy distinction at a glance: the air-facing side appears shiny, while the water-facing side looks opaque.

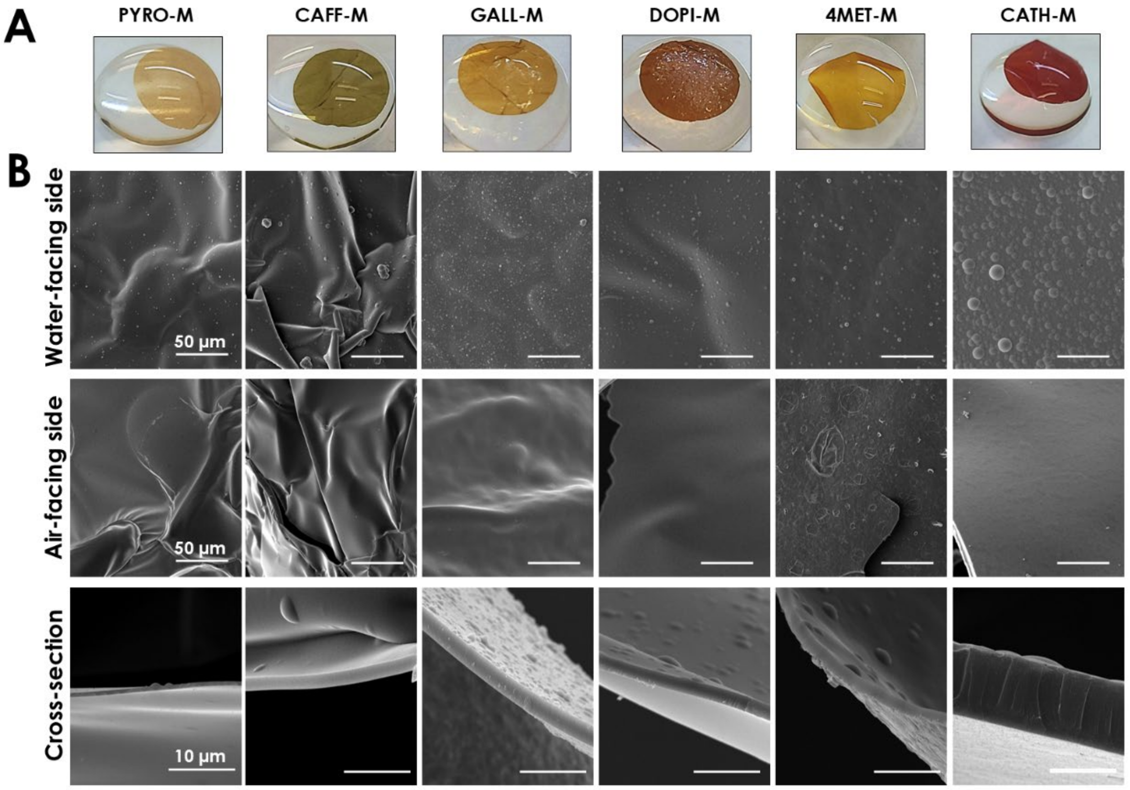

Figure 4.19. Morphology of the membranes. **A)** Macroscopic appearance of the six different HMDA-based membranes floating in a drop of water. **B)** Scanning electron microscopy (SEM) images comparing the cross-section, air-facing side and water-facing side.

Although the membranes were initially hydrophobic when completely dried, they were able to absorb water and become turgid, thereby turning hydrophilic. This suggests a porous nature, despite the absence channels in the cross-section analysis, especially in the case of the **CATH-M**, the thickest membrane (**Figure 4.19B** and **4.21C**).

To elucidate the polymerization process of **CATH-M** from a morphological perspective, the synthesis was monitored by SEM at different time points between 3 and 60 h (**Figure 4.20**). It is suggested that since oxidation is maximized in the air-water interface, the synthesis of the polymer is also confined in this region (**Figure 4.21A**). The formation of an extremely thin film at this interface may serve as a nucleation and/or anchoring site for these particles during the early-stage (0-3 h). As the particles grow, they progressively embed adjacent ones, forming a network of spherical units in the mid-stage (3 to 6 h). Over time, this process continues, filling the remaining voids and ultimately resulting in a uniform membrane in the late stage (from 12 h onward), after which only an increase in thickness was observed (**Figure 4.21C**). This increase in thickness reached a plateau after 48-60 h. Finally, particles that were not incorporated into the membrane precipitate, making easily to discard them (**Figure 4.21B**).

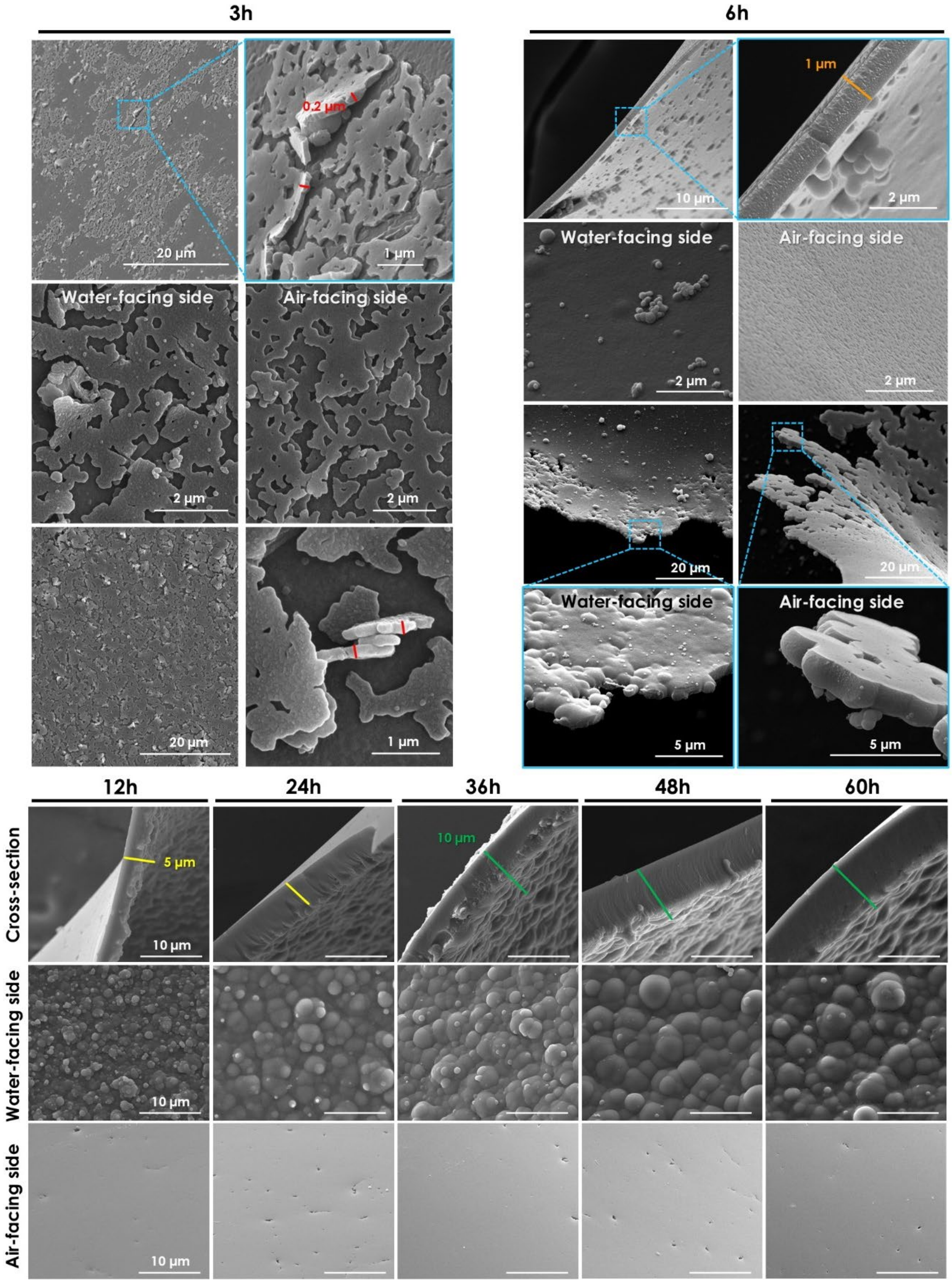

Figure 4.20 Time course of the CATH-M synthesis. SEM micrographs showing the evolution of membrane morphology as a function of synthesis time. After 3 h, a heterogeneous, net-like structure is observed. By 6 hours, the membrane thickness increases approximately fivefold, resulting in a more homogeneous and flat morphology. At 12 hours, the membranes become mechanically stable and can be manipulated. After 24 h, the membrane maintains its shape on both faces, with further changes limited to thickness increase. The thickness grows exponentially, progressing from approximately 0.2 µm at 3 h to 1, 3, 5, 7, 9, and 10 µm at 6, 12, 24, 36, 48, and 60 h, respectively. This plateau in thickness growth may be attributed to a reduction in oxygen diffusion, which could slow the reaction rate. Red, orange, yellow, and green lines indicate thicknesses of 0.2, 1, 5, and 10 µm, respectively.

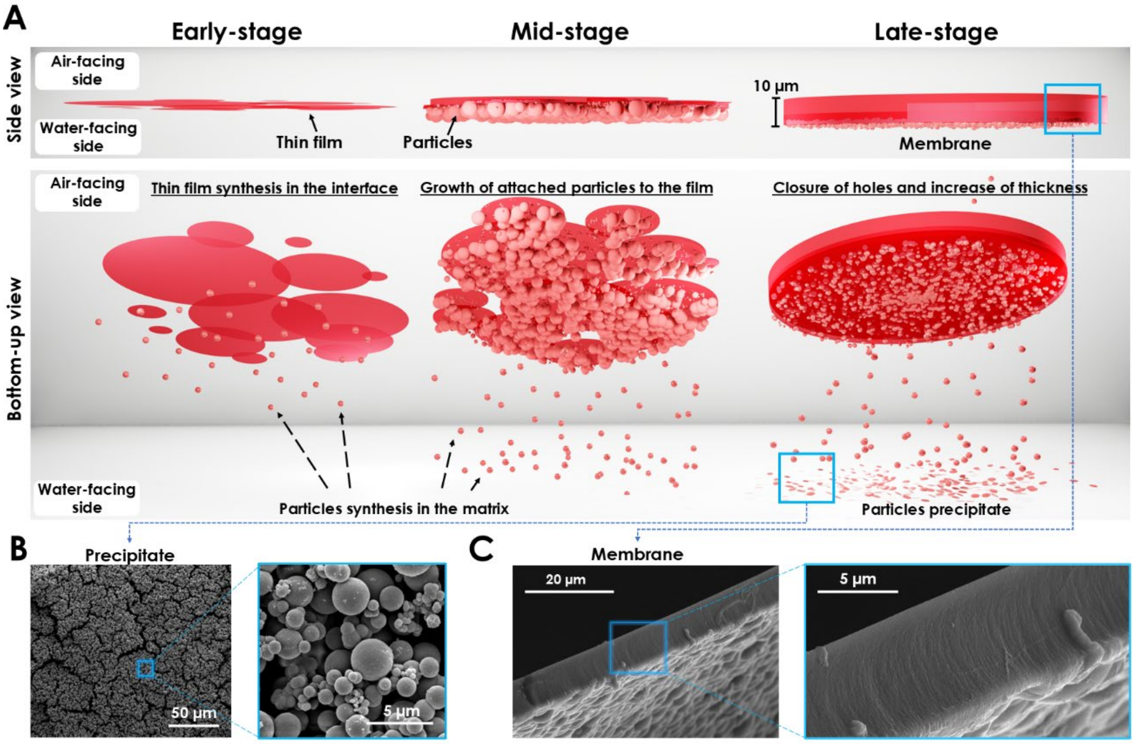

Figure 4.21 Synthesis scheme of the CATH-M membrane. **A)** Representation of the three suggested main stages identified during the synthesis of this membrane. The process begins with the formation of an extremely thin and heterogeneous film in the early stage, followed by the growth of particles attached to the membrane surface (mid stage). In the late stage, the membrane reaches a homogeneous thickness, although some particles remain visible on the water-facing side. **B)** The particles generated in the solution that were not incorporated into the membrane precipitate as a byproduct, with sizes ranging between 0.5 and 3 µm. **C)** The particles that contributed to membrane formation remained partially visible on the water-facing side, thereby contributing to its final thickness of approximately 8-10 µm.

4.2.2.2 Cytotoxicity activity screening against Glioblastoma cells

To comprehensively evaluate the cytotoxic activity against Glioblastoma, the six HMDA-based membranes and its precursors (catechol derivatives and HMDA) were subjected to a first screening assessment against the human Glioblastoma cell line LN229. A standardized experimental protocol was followed, involving the incubation of 2 × 10^4 LN229 cells with increasing molarities of each molecule (**Figure 4.22A**), or with an individual 6 mm diameter membrane discs (**Figure 4.22B**) for 24 h. Following this incubation period, the negative *in vitro* effects of the different molecules (catechols or HMDA) were visually approximated. Increasing concentrations of each molecule were added until morphological changes were observed, in comparison with the control. In the case of the membranes, the percentage of induced cell death was quantified using a combination of H42 and PI staining. The results of this cytotoxicity assay were both intriguing and remarkable. On the one hand, CATH precursor was shown to be the most biocompatible catechol derivative, not affecting the LN229 cells even at concentrations up to 1 mM (similar to HMDA); while the remaining catechol derivatives were considerably less biocompatible (**Figure 4.22A**). On the other hand, whereas most of the polyphenol-based membranes exhibited minimal cytotoxicity, the **CATH-M** membrane demonstrated a remarkable higher level. **CATH-M** induced cell death in approximately 90% of the LN229 cells, far surpassing the cytotoxicity levels observed with the other five membranes (**Figure 4.22C**). In contrast, the remaining membranes failed to induce substantial cell death, with cytotoxicity rates remaining similar to the control (**Figure 4.22D**).

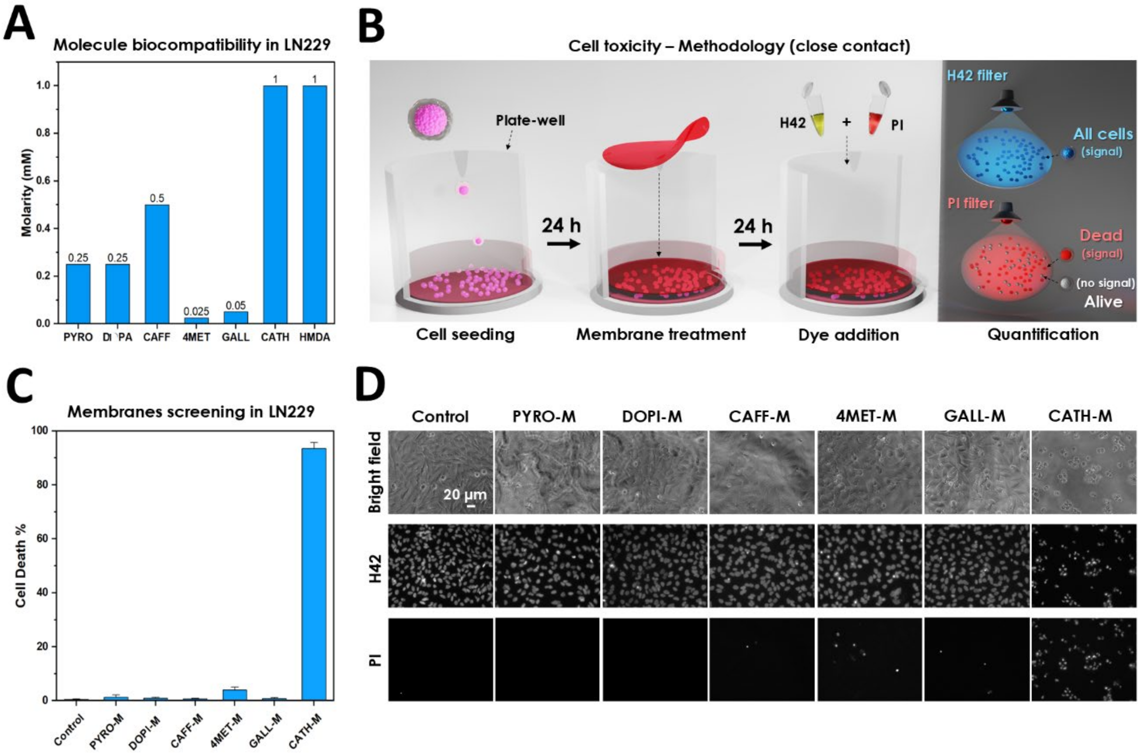

Figure 4.22. Molecules and membranes cytotoxicity. A) Biocompatibility of various concentrations of the six catechol derivatives and HMDA in the LN229 cell line, indicating the highest concentration that the cells can withstand without exhibiting morphological or visual changes. **B)** Methodology used to study the percentage of cell death in a cell monolayer, in which the membrane was used as a "close contact" treatment (not touching the cells but near them). Cell death was measured after the treatment with a Hoechst33342 (H42) and propidium iodide (PI) staining. **C)** Comparison of the cytotoxicity between the different HMDA-based membranes in the LN229 cell line, where **CATH-M** was the only one achieving a considerable cell death percentage. **D)** Cytotoxicity analysis of each membrane under fluorescence microscopy using the H42, which can pass through intact cell membranes, and PI, which can only enter cells that have suffered membrane damage.

Based on the previous results, the cytotoxic effect observed in the **CATH-M** was further explored through a time-course study in LN229 cells, using three different batches of **CATH-M** to determine the cell death profile. The results revealed a linear increase in the percentage of cell death within the first 24 h. Notably, initial changes in cell morphology were observed as early as 9 h, with a consistent rate of cell killing evident after 12 h, suggesting a necrosis-like cell death (deeply analyzed in section 4.2.3.8) (**Figure 4.23**).

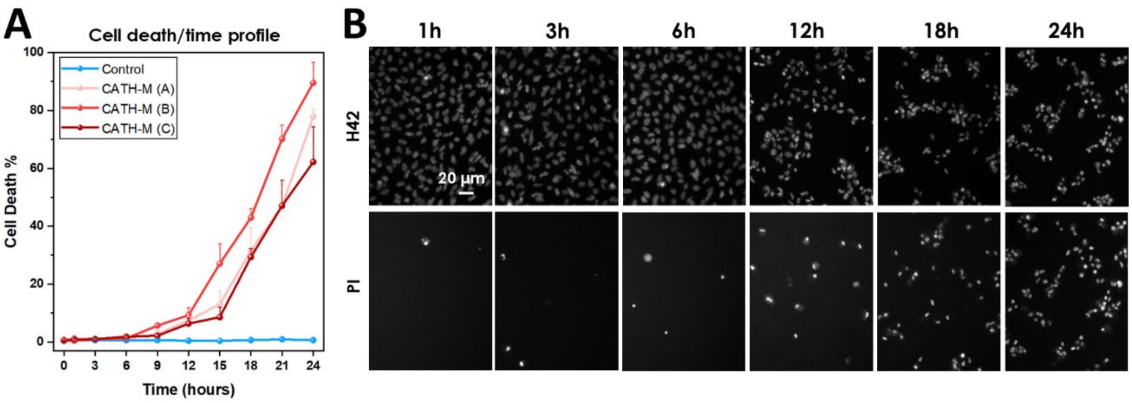

Figure 4.23. CATH-H cell death profile with time. **A)** Percentage of cell death when the LN229 are exposed to 3 different **CATH-M** membranes from 1 to 24 hours. **B)** Representative H42 and PI images of the LN229 cells after gradually raising the exposure time to the **CATH-M** from 1 to 24 h, where an increasing signal was observed in the PI in base of the time.

4.2.3 CATH-M and its suitability for Glioblastoma post-surgical treatment

Given the exceptional cytotoxic activity displayed by the **CATH-M** membrane, it emerged as a highly promising candidate for further investigation. Conversely, the **PYRO-M** membrane, which exhibited a low cytotoxicity activity, was selected as an appropriate negative control for comparison purposes (**Figure 4.22C**). The selection of **PYRO-M** as a negative control provided a valuable benchmark for comparing the cytotoxic effects of **CATH-M**, ensuring a robust and reliable assessment of their cytotoxic potential. Furthermore, besides its interesting physical properties, **PYRO-M** also served as an excellent control for the mechanical stress (and potential damage) induced to the cells due to the manipulation of a solid, thereby minimizing the risk of false positives. Consequently, a thorough characterization was subsequently conducted for both membranes equally (**Figure 4.24).**

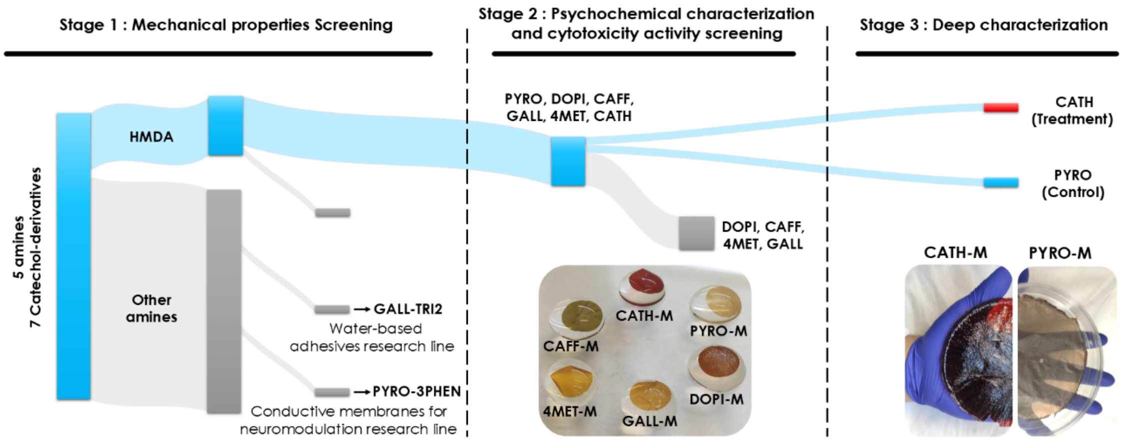

Figure 4.24. Scheme of the stages of this Chapter. In the first stage, the most manipulable membranes (HMDA-based) were selected**.** During the second stage, the only membrane that exhibited cytotoxic properties, **CATH-M**, was selected along with an inert candidate, **PYRO-M** (control), for a thorough characterization in the third stage.

4.2.3.1 Physiological degradation and stability

To evaluate the biodegradability of the selected membranes in different media, **CATH-M** and **PYRO-M** were stored for up to eight months at 37 ºC in different environments, including water, 100% ethanol, pH 4 and pH 10 solutions, phosphate-buffered saline (PBS, pH 7.3), culture media or trypsin. The evolution of the membranes was monitored monthly (**Figure 4.25A**) and characterized using SEM (**Figure 4.26A**). The results showed that **PYRO-M** did not present significant changes after eight months. Only its macroscopic shape was slowly altered when immersed in a pH 10 solution, eventually rolling up on itself after this period (**Figure 4.25B**).

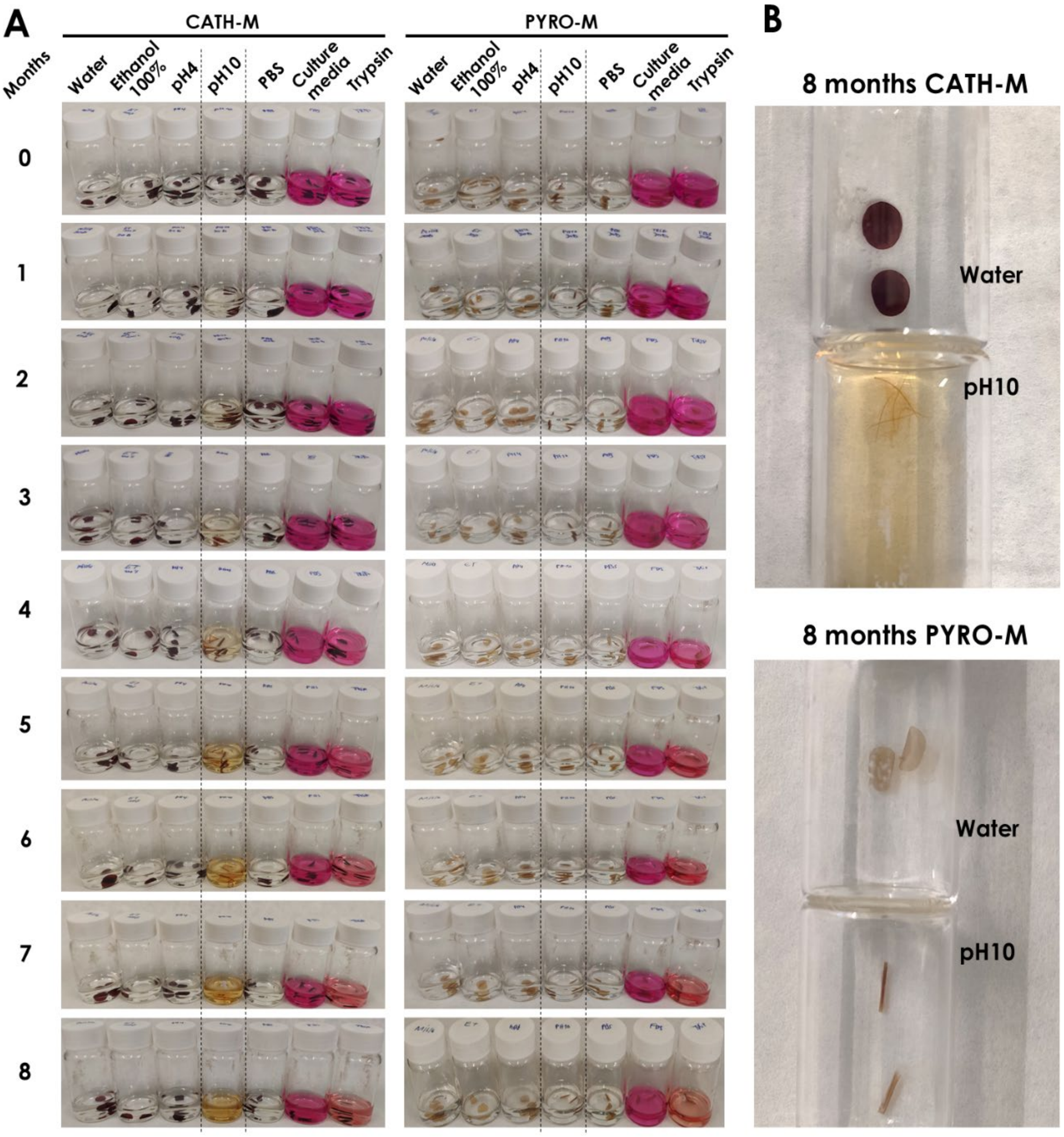

Figure 4.25. Long-term degradation test. A) Macroscopic evolution of both **CATH-M** and **PYRO-M** in different media, where a clear difference is observed when stored inside pH 10 solution. **B)** In this media, the catechin membrane became almost transparent (passing its color to the solution) when compared to those stored in water for the same time, whereas the only perceptible change in the pyrocatechol was the rolling of the material.

However, the membrane remained easily manipulable, not falling apart or breaking when extracted from the solution. In contrast, **CATH-M** displayed more noticeable changes under basic conditions, becoming more transparent within the first month and exhibiting the roll-up change in shape observed in **PYRO-M**, but at much faster rate, causing a subtle change in the color of the medium. After four months, the membrane became extremely thin, brittle and transparent, yet retained its previous shape. Ultimately, **CATH-M** almost fully degraded after eight months under these conditions, becoming nearly unnoticeable and impossible to manipulate (**Figure 4.26C**). These observations suggested that the change in pH accelerated oxidation of the membrane, thus inducing changes in the bonding structure and leading to membrane weakening, which highlights its reactivity in basic and oxidative environments. Additionally, subtle differences were observed on the surface of **CATH-M** after eight months when comparing water, culture medium, and trypsin (**Figure 4.26B**). In cell culture medium, the **CATH-M** surface became smoother, with nearly complete closure of the pores on the air-facing side. This was likely attributed to interactions with proteins and amino acids present in the culture medium. Conversely, exposure to trypsin resulted in a slightly eroded surface with more rugosities and membrane protuberances, particularly on the air-facing side. This effect was attributed to the protease activity of the components of the trypsin, which degrade overtime. However, apart from these differences, no variations in thickness, manipulability or macroscopic morphology were observed. Finally, in the case of water, pH 4 solution, ethanol and PBS, no changes were observed, suggesting that these membranes could be both stored or cleaned in these solutions without losing their mechanical properties.

These findings highlight the **CATH-M** potential for its application in the human body, thanks to both its stability and potential biodegradability. The membrane remains stable during the necessary period for the expected treatment, ensuring its functionality and effectiveness. Over time, it progressively degrades, thus minimizing the risk of long-term complications. It is worth mentioning that this process may be accelerated in a real environment due to the interaction with different proteases (which could be more efficient that trypsin) along with the immune system. Furthermore, while catechin is a natural molecule broadly found in the human diet, HMDA, despite being synthetic, has a chemical structure similar to the biogenic amines putrescine and cadaverine, which are present in human metabolism and diet. This consideration suggests that HMDA could have also the potential to be metabolized, nevertheless, more experiments should be performed to confirm it.

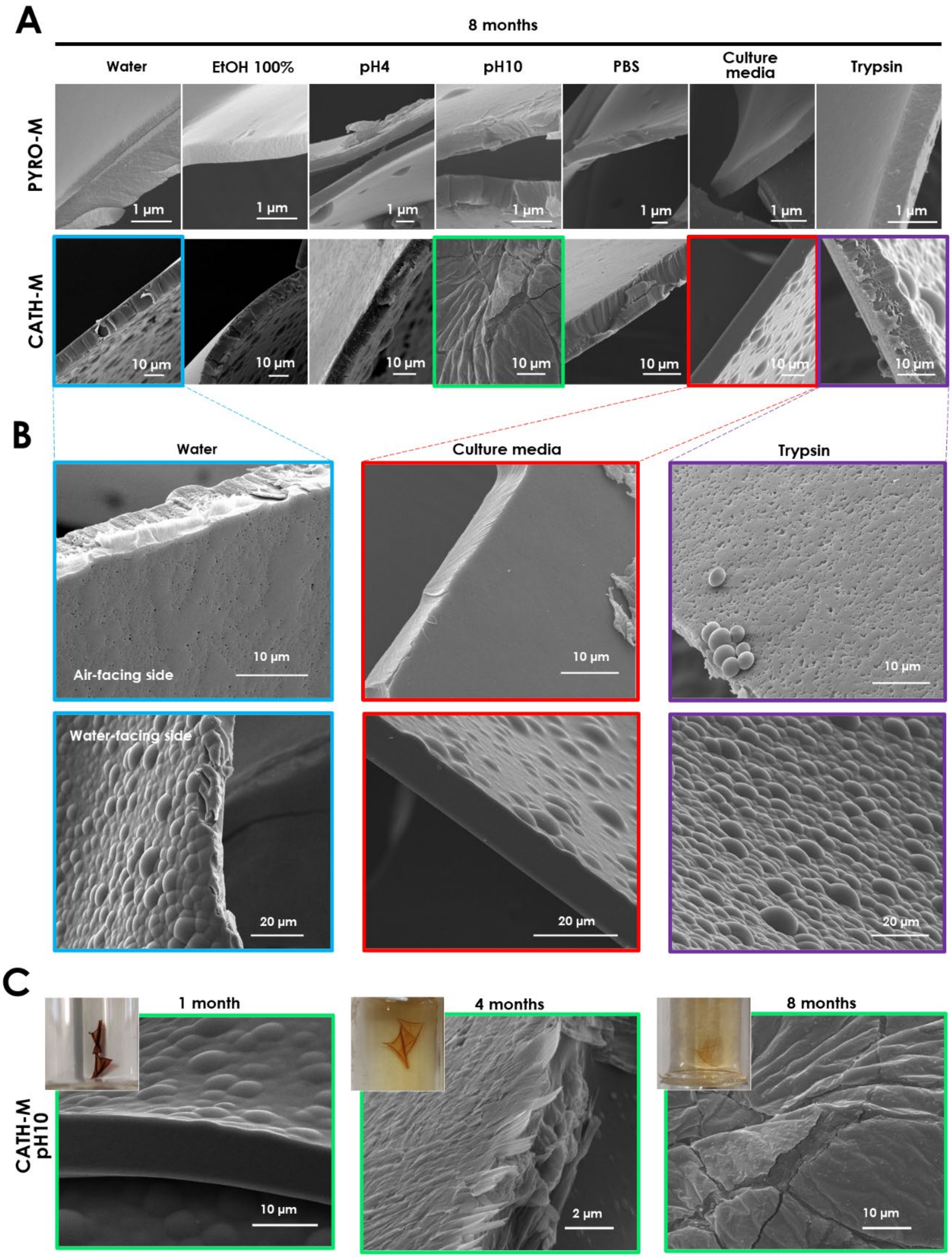

Figure 4.26. Morphological changes after degradation test. SEM images of the **A)** microscopic evolution of both **PYRO-M** and **CATH-M** in different media after eight months. No big differences can be distinguished in the first one, whereas substantial changes can be detected in the second membrane. **B)** Taking into account the **CATH-M** in water (blue frame) as a control, a slight thickening and smother appearance is observed when stored in culture media (red frame). Conversely, in the case of Trypsin (purple frame), more the details of the membrane (especially in the air-facing side) can be observed. **C)** In the case of pH 10 (green frame), a gradual change in the thickness and integrity was noticed with the time.

4.2.3.2 Antibacterial activity

Considering the cytotoxic potential of **CATH-M** against Glioblastoma, in addition to the antimicrobial activity found in coatings with a similar formulation (Chapter 3), the antibacterial properties were also evaluated. Methicillin-Resistant *S. aureus* (MRSA) and *E. coli*, common microorganisms found in post-craniotomy infections, were selected as representative Gram-positive and Gram-negative bacteria, respectively.[54,55]

Two different approaches were performed to quantify this property: in suspension (relying completely on the leaking effect) and close contact (leaking in direct surroundings and surface interaction) (**Figure 4.27F**). In the first method, after **CATH-M** remained inside a dense bacterial suspension for 24 h, the membrane demonstrated exceptional antibacterial activity, achieving a CFU reduction of over 99.999% for MRSA and 99.99% for *E. coli*. In contrast, **PYRO-M** exhibited a slight reduction (approximately 50%) in Gram-negative *E. coli* (**Figure 4.27A** and **B**). ROS generation was measured in the bacterial solutions after the incubation period. The observed ROS levels for both membranes and bacteria, aligned with the CFU reduction results, further supported the antibacterial efficacy of **CATH-M** (**Figure 4.27C**). However, despite not achieving a substantial antibacterial property in suspension, previous *in vivo* experiments of the group (to be published) suggested that **PYRO-M** had the potential to decrease the infection risk when applied to open wounds. Consequently, in order to quantify this observation, the close contact approach was performed. This methodology could be considered an approximation of the antibacterial tests performed in Chapter 3 with catechol-amine coatings. It consisted in attaching the membrane to a coverslip, which was then placed in contact with a drop of bacterial suspension deposited on glass, allowing the drop to be homogeneously dispersed by capillarity along the membrane. The face of the membrane in contact with the bacteria was randomly selected. In this case, both **CATH-M** and **PYRO-M** reached a CFU reduction above 99.99% for *E. coli* after 24 h of incubation (**Figure 4.27D**), with **PYRO-M** capable of achieving this results in 6 h (**Figure 4.27E**). Therefore, the antibacterial properties of both membrane types were confirmed, highlighting the effectiveness of **CATH-M** in both approaches.

The importance of having intrinsic antimicrobial activity in a patch for potential Glioblastoma post-surgery treatment cannot be overstated. The objective is to reduce the risk of post-operative infections, which are a major concern in neurosurgical procedures. By effectively eliminating pathogenic bacteria, these membranes can enhance patient outcomes, minimize the need for additional antibiotic treatments and ultimately contribute to a more successful recovery process.

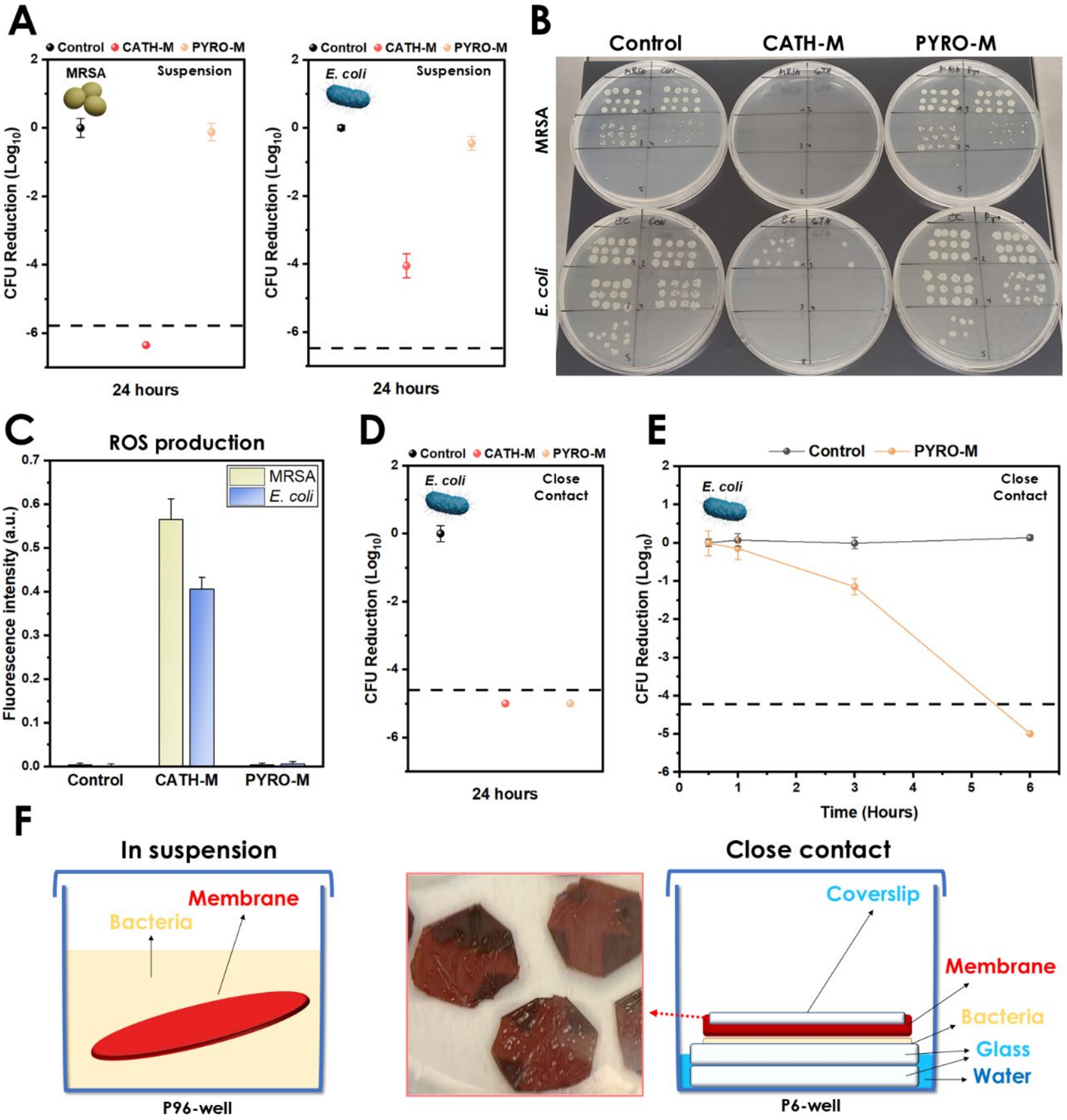

Figure 4.27. Antibacterial properties. A) Colony forming units (CFU) logarithmic reduction of MRSA and *E. coli* after being exposed to **CATH-M** or to a **PYRO-M** for 24 h in suspension. **B)** Representative SP-SDS plates for both bacteria and membranes. **C)** Reactive oxygen species (ROS) generated in the bacteria suspension in which the membranes were introduced after also 24 h. Error bars represent the standard deviation of a data set relative to the mean. **D)** CFU logarithmic reduction of *E. coli* after being exposed to **CATH-M** or to a **PYRO-M** for 24 h in close contact. **E)** Reduction in function of the exposure time of *E. coli* against **PYRO-M**. **F)** Comparison between the “suspension” and “close contact” methodologies in the antibacterial tests used for both membranes.

4.2.3.3 Ex vivo adhesion and brain conformability of ***CATH-M***

The assessment of adhesion properties of **CATH-M** is crucial to ensure its suitability for brain and Glioblastoma post-surgical treatment, particularly where adhesion in humid environments is fundamental. To this end, *ex vivo* assays were conducted to evaluate the adhesion properties of **CATH-M**. The membrane was cut into round discs and placed as patches in various gyrus-sulcus areas of an *ex vivo* pig brain (**Figure 4.28**). Notably, **CATH-M** demonstrated excellent conformability, adapting its shape to the brain surface regardless of its position, and could be effortlessly introduced or removed from the cavity without breaking. Once positioned in the desired area, **CATH-M** remained securely in place, maintaining its adhesion even under high humidity conditions.

Taking a step further, the adhesion was tested by applying shear force between a rabbit brain and a **CATH-M** membrane (with a contact area of 2 cm^2), to which different weights were attached. The membrane remained adhered under weights of up to 10 g (**Figure 4.29**). This ensures that **CATH-M** can effectively remain in place and perform its intended function without displacement, which is vital for brain applications and successful post-surgical treatment.

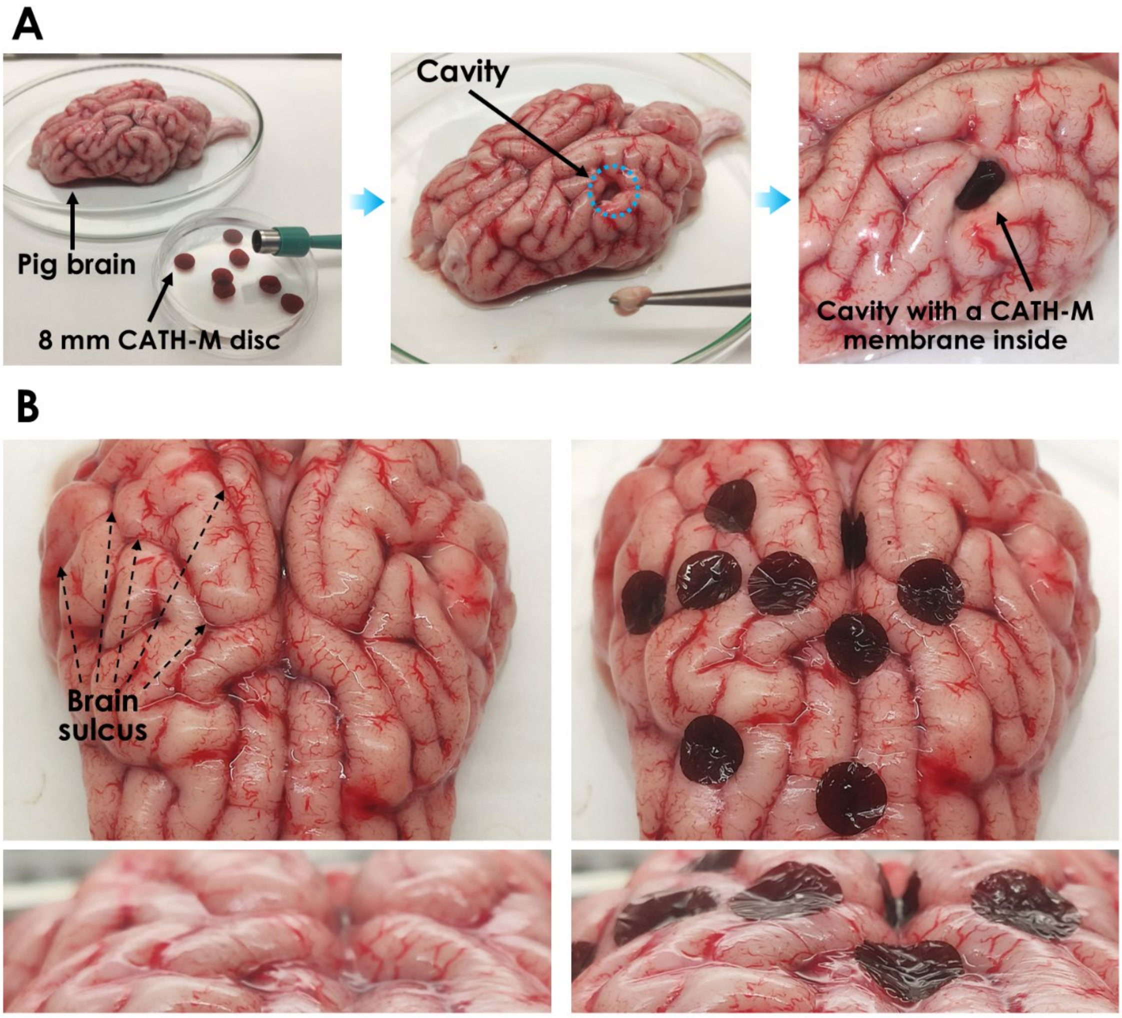

Figure 4.28. CATH-M membrane manipulability in a real environment. A) Representation of a **CATH-M** application in a Glioblastoma-resection cavity using an *ex vivo* model (pig brain). **B)** Comparison of a pig brain without (left) and with (right) several membrane discs adhered to distinct parts of its surface, being able to bend and adapt to the different shapes of the brain, especially in the sulcus.

*4.2.3.4 Cell death spectrum of the **CATH-M** membrane*

Focusing on the promising results observed in the LN229 cell line, the research was expanded to four additional stablished human Glioblastoma-derived cell lines (LN18, A172, U87, and U251) and two primary cultures isolated from patients (MSO4 and MSO7). Initial seeding densities were set at 1.8 × 10^4, 1.8 × 10^4, 1.5 × 10^4, 1 × 10^4, 2.4 × 10^4, and 2.6 × 10^4 cells/well respectively. After a 24 h incubation period, all six Glioblastoma-derived cell lines exhibited a similar pattern of cell death as previously observed in LN229. **PYRO-M** remained innocuous, whereas **CATH-M** consistently induced cell death rates around 80% in most of the cases, reaffirming its broad cytotoxic spectrum against Glioblastoma cells (**Figure 4.30A** and **4.31**).

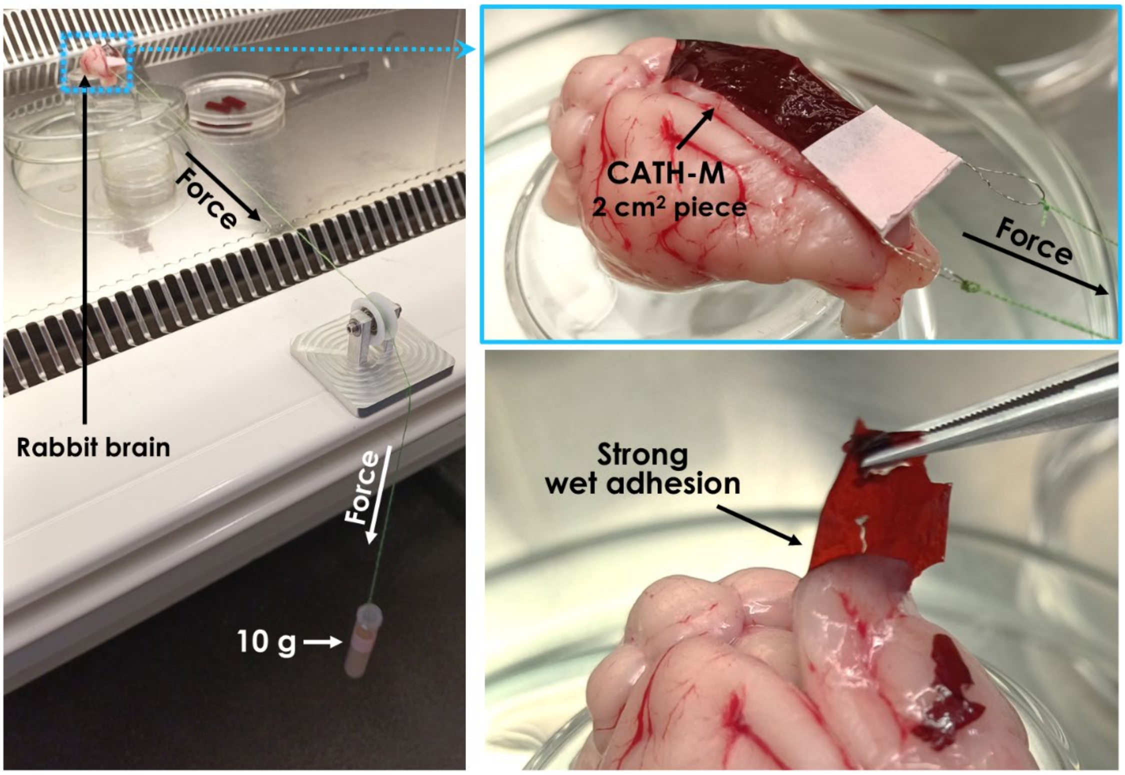

Figure 4.29. CATH-M *ex vivo* adhesion. Setup established to test the shear force that a 2 cm^2 piece of **CATH-M** can withstand when adhered to a rabbit brain, demonstrating resistance up to 10 g. It can also be observed how the membrane gently pulls the tissue when attempts are made to remove it.

To further demonstrate the broad applicability of **CATH-M**, the same experiment was performed with the tumor cell lines A549, PANC-1, CACO-2, SAOS-2 and HELA, which are derived from human lung carcinoma, pancreatic carcinoma, colorectal adenocarcinoma, osteosarcoma and cervical carcinoma, respectively. In this case, 1 × 10^4, 2 × 10^4, 2 × 10^4, 2.5 × 10^4 and 1 × 10^4 cells/well were seeded. After 24 h of incubation, the cell death induced by **CATH-M** remained around 80% in all the cases. Conversely, **PYRO-M** exhibited some cytotoxicity in certain cases (**Figure 4.30B** and **4.32**). These results, aligned with previous findings, confirmed the broad spectrum of **CATH-M** against different cancers, which highlights its potential application scope (**Figure 4.30D**).

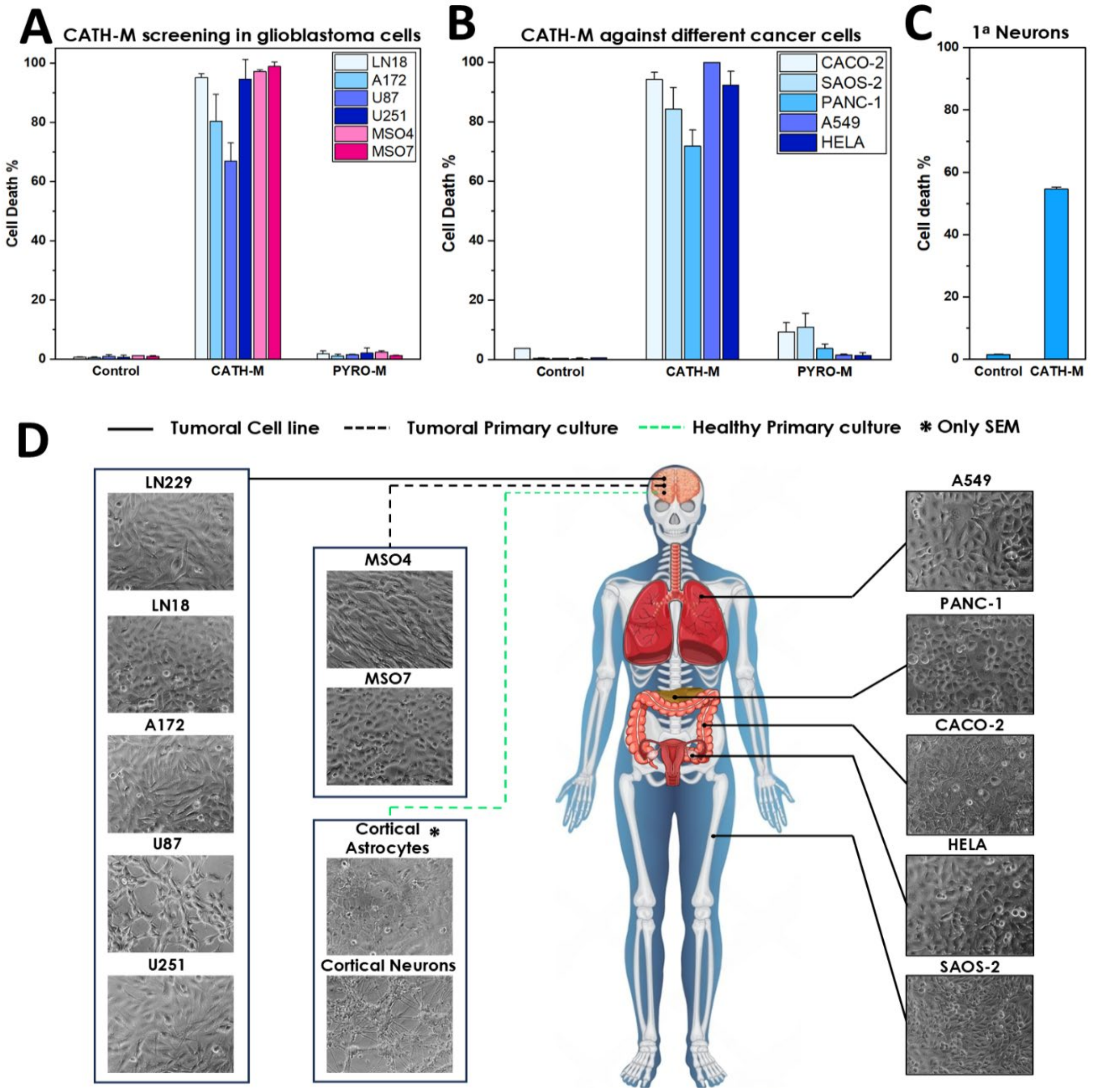

Figure 4.30. CATH-M cytotoxicity broad spectrum in tumor-derived cells. Cell death screening of the **CATH-M** and **PYRO-M** membranes against **A)** 6 human-derived Glioblastoma cells (4 cell lines and 2 primary cultures) and **B)** 5 human-derived tumor cells (from different organs). In all the cases, **CATH-M** achieved a percentage of cell death around 80%. **C)** The membrane was also tested against cortical neurons (rat primary culture), surprisingly obtaining lower results than the tumoral cells. **D)** Schematic representation of all the cells tested against the CATH-M membrane and their origin. A total of eleven different tumoral cell where tested (five Glioblastoma cell line, two Glioblastoma primary cultures and five different organ-derived tumor cell lines). Two healthy primary cultures from rat (cortical astrocytes and neurons) were also used.

Going a step forward, it was necessary to ensure that CATH-M have no cytotoxic effects on healthy tissue. This is particularly critical for treatments targeting diseases like Glioblastoma, where the proximity of healthy brain tissue is a constant concern. Preserving the viability of non-tumoral cells is essential to avoid additional complications and support overall patient recovery. To test the cytotoxicity in non-tumoral cells, primary cortical neurons from rat were used. Interestingly, only a 55% cell death rate was observed, which is an outstanding result considering the fragile nature of the neurons (**Figure 4.30C** and **4.32**).

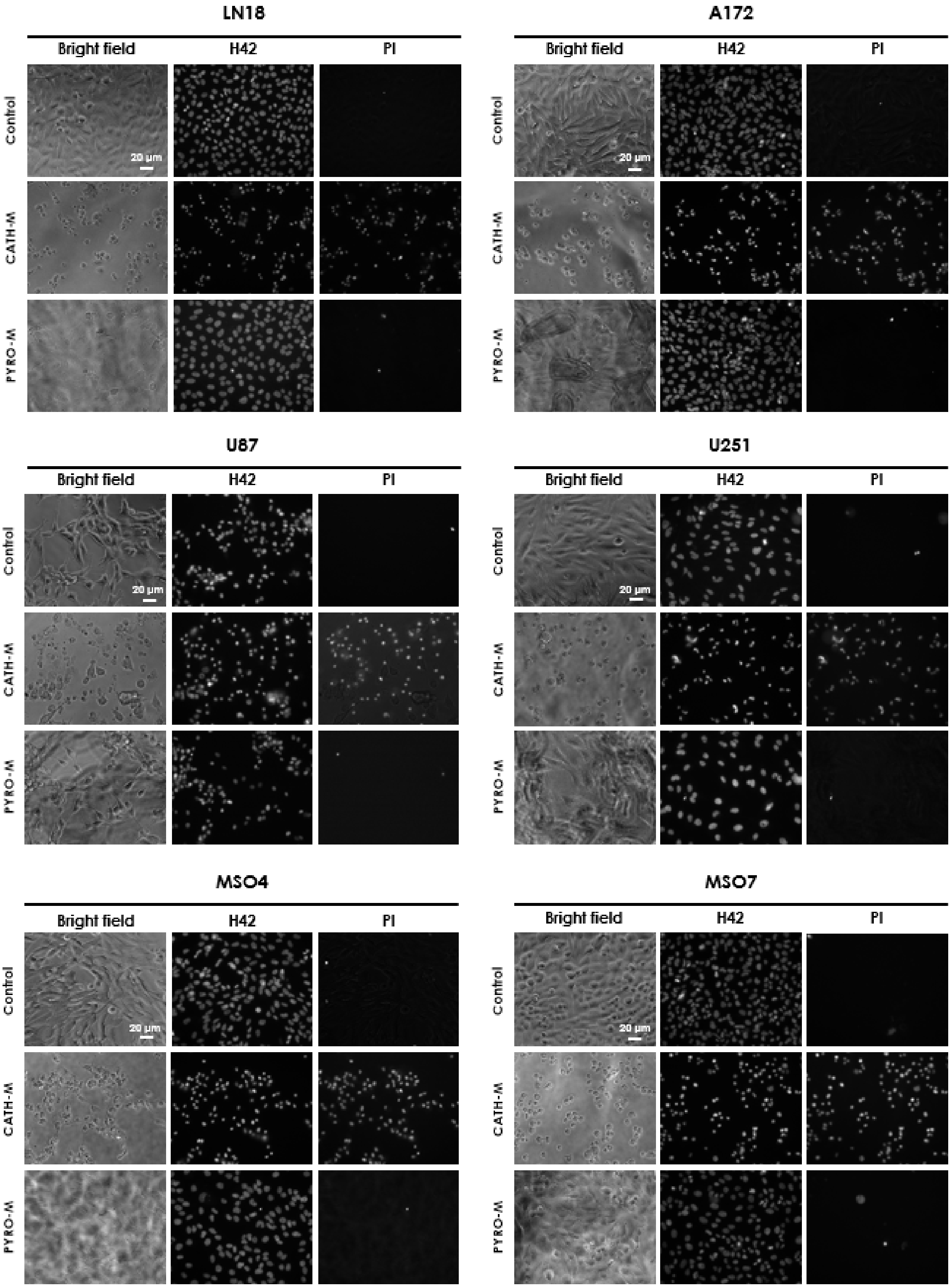

Figure 4.21. Glioblastoma cells cytotoxic screening. Representative bright field, Hoechst 33342 (H42) and propidium iodide (PI) images of the four additional Glioblastoma cell lines (LN18, A172, U87 and U251) and the two Glioblastoma primary cultures (MSO4 and MSO7) after being treated with the **CATH-M** and **PYRO-M** membranes, where a clear difference in the PI of **CATH-M** can be observed in all the cases.

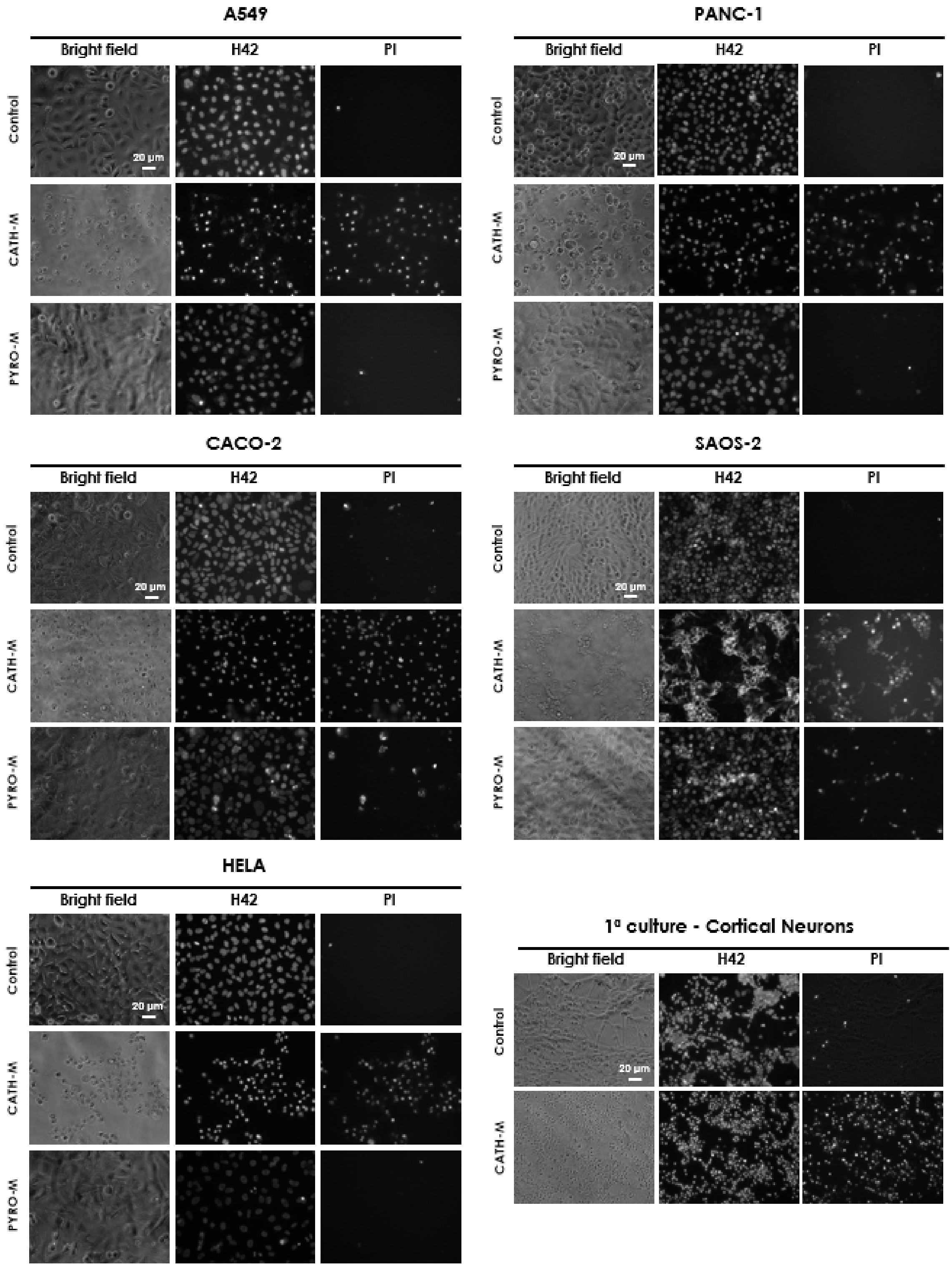

Figure 4.32. CATH-M cytotoxic effect against different tumor cells lines and healthy cells. Representative bright field, Hoechst 33342 (H42) and propidium iodide (PI) images of four tumor cell lines from different organs (A549, PANC-1, CACO-2, SAOS-2 and HELA) after being treated with the **CATH-M** and **PYRO-M** membranes, where a clear difference in the PI of **CATH-M** can be observed in all the cases. Regarding the primary culture of cortical neurons, although the effect of **CATH-M** is evident, it is considerably lower than that observed in all the studied cancer cell lines.

4.2.3.5 Survivability and viability

To comprehensively evaluate the survivability and viability of LN229 cells exposed to **CATH-M**, a clonogenic assay was performed. Initially, a monolayer of 250,000 cells was treated with a 21 mm diameter membrane for 24 h (**Figure 4.33A**). After its removal, one plate was fixed and stained with crystal violet, serving as the starting point of the experiment (T0) (**Figure 4.33B**). Then, the ability of the damaged cells to recover and proliferate over a 20-day period (T20) was assessed using four additional plates, comparing their growth to that of a control group of 1,000 cells (growth control). While **PYRO-M** treatment resulted in minimal changes beyond expected

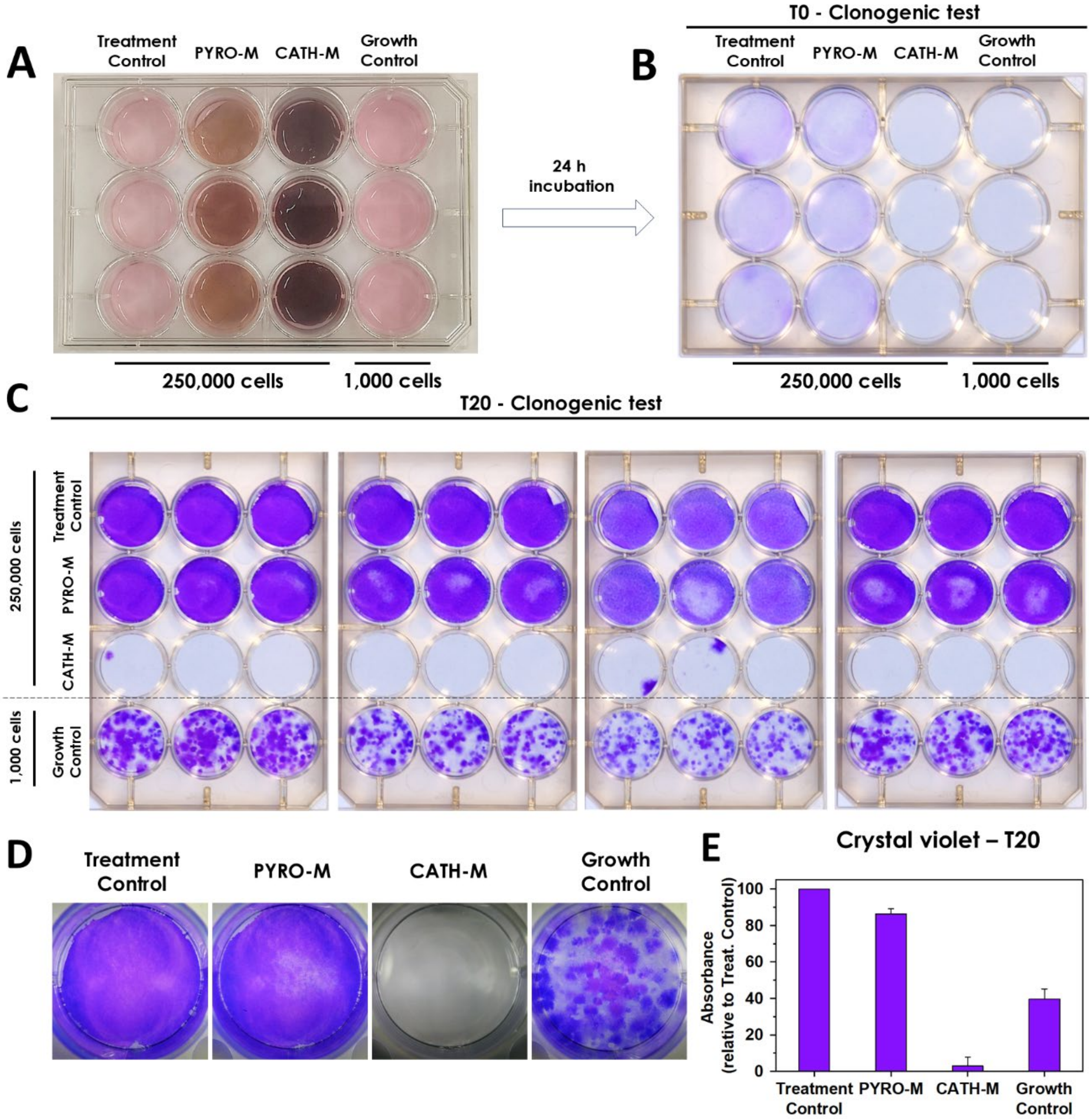

Figure 4.33. Clonogenic test. A) Visual example of the test setup, where a disc with a similar dimension of the well's diameter was cut and used as treatment. **B)** Crystal violet revealed plate after the first 24 h incubation (where no coloration in the case of **CATH-M** can be observed) and **C)** after 20 days (four plates), where the homogeneity of the results can be confirmed (only 3 of the 12 repetitions shown some marginal growth of colonies). **D)** Representative close images of a repetition from each condition after 20 days. **E)** Quantification of the retained crystal violet by the cells in each condition (present in the 20 days plates) of the clonogenic test**.**

mechanical damage, primarily observed in the center of each well (the zone where the membrane mostly interacted during its setting and removal), a remarkable 9 out of 12 replicates of **CATH-M**-treated cells exhibited no signs of survival after the 20-day incubation period (**Figure 4.33C** a**nd D**).The relative cell numbers in each condition were quantified by measuring crystal violet absorption following fixation after the 20-day period (**Figure 4.33E**). Notably, the surviving clones in the **CATH-M**-treated group were predominantly located at the well edges, where the leaking-effect was probably less concentrated than in the center, and direct contact with the membrane was limited (due to the subtle roll-up of the edges or gaps generated during the cutting/manipulation of the pieces).

To assess whether this membrane could induce a local cytotoxic effect, LN229 cells were cultured on plates with **PYRO-M** and **CATH-M** applied to only half of the plate (**Figure 4.34A**). After 24 h, it was observed that the cells in close contact with the membrane were eliminated, while the cells in the untreated half of the plate remained unchanged. In contrast, **PYRO-M** did not show any signs of cytotoxicity (**Figure 4.34B**). This observation supports the concept of the local effect of **CATH-M**, which is a desirable characteristic for cancer treatment as it may minimize side effects and collateral damage to nearby healthy tissues.

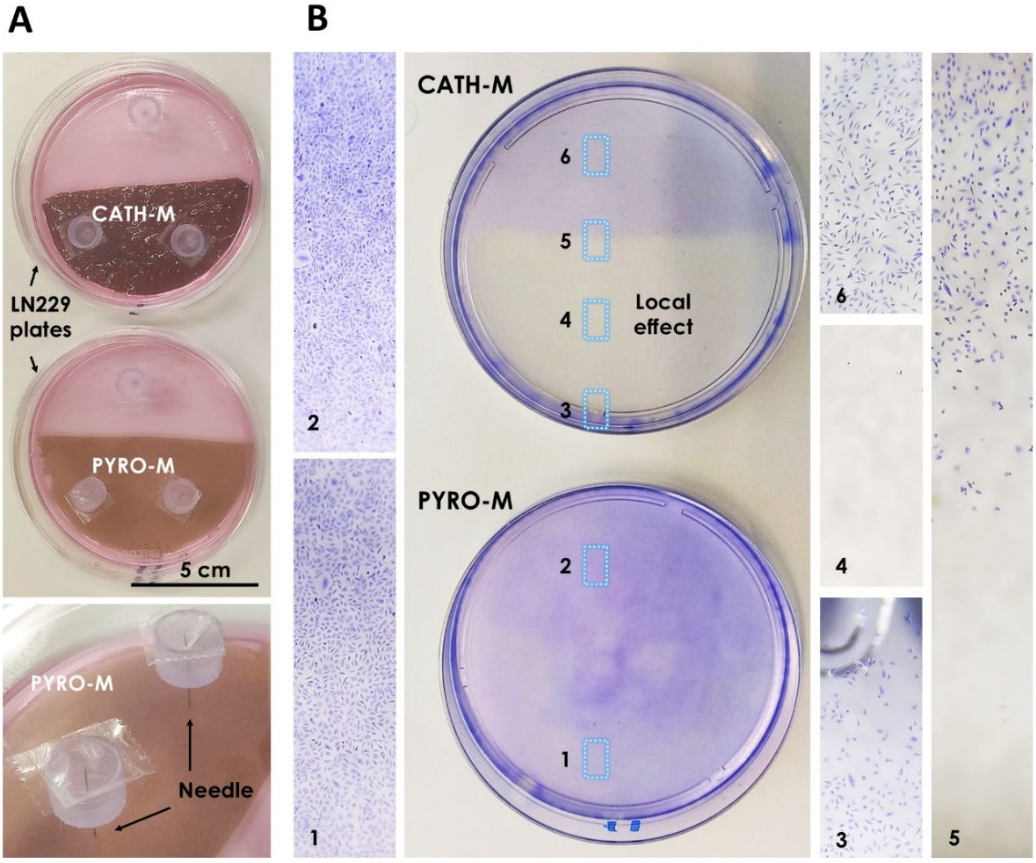

Figure 4.34. CATH-M local effect. A) LN229 cells were exposed to **PYRO-M** and **CATH-M** membranes placed on only half of each culture plate, fixed in position using needles. **B)** After 24 h, crystal violet staining revealed that **CATH-M** exerted a localized cytotoxic effect, eliminating the cells directly under the membrane, while the other half of the plate remained viable. In contrast, **PYRO-M** did not exhibit any cytotoxic effect either in close contact (under) or adjacent to the membrane. These results confirm the localized cytotoxicity of the **CATH-M** membrane.

4.2.3.6 Comparison with standard-of-care treatments

To investigate the potential interactions between **CATH-M** treatment and existing Glioblastoma therapies, a comparative analysis of its cytotoxicity against TMZ was conducted. Furthermore, their combined effects on LN229 cells (4.0×10^4 cells/well) subjected to irradiation doses of 10, 20 or 40 Gray (Gy) was assessed. Following 48 and 96 h incubation, the cells were treated with **CATH-M** for 24 h. The results revealed that **CATH-M** consistently exhibited superior cytotoxicity compared to TMZ (**Figure 4.35**). Moreover, the concurrent administration of **CATH-M** and TMZ (0.25 mM) yielded a higher effect across all exposure time, often surpassing the sum of both individual treatments. These results suggested that integrating **CATH-M** with current Glioblastoma treatment protocols (irradiation plus TMZ) could potentially enhance therapeutic outcomes without compromising the existing standard-of-care.

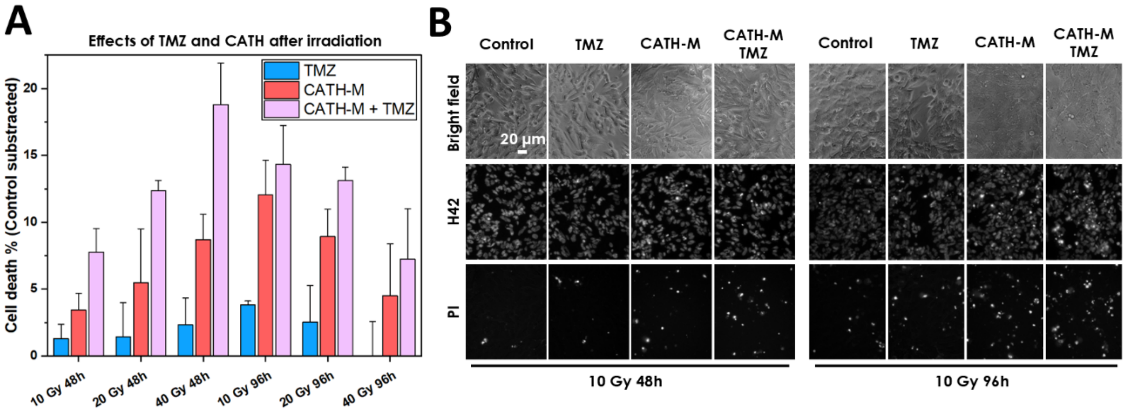

Figure 4.35. Clonogenic A) Comparison of the **CATH-M** and temozolomide (TMZ) treatment over irradiated LN229 cells, together or separated, at different irradiation intensities (Gy) and treatment time. **B)** Representative images of the 10 Gy and 48h or 96h combination. Error bars represent the standard deviation of a data set relative to the mean.

4.2.3.7 Similarities in the catechin-stereoisomers-based membranes

Chirality and structural similarities between molecules can determine the difference between a desired effect and its absence or even lead to adverse outcomes (e.g., thalidomide).[56] The catechin enantiomer used for obtaining **CATH-M** was the (+)-catechin hydrate, chosen for cost-related reasons. To determine if different formulations, enantiomers or diastereomers, could affect the properties of this membrane, (+)-catechin, (-)-catechin and (-)-epicatechin (**Figure 4.36A**) were used as catechol derivatives during the synthesis of the **CATH-M** membrane, following the same protocol. Interestingly, in all cases, membranes with the same color and macroscopic appearance as the original **CATH-M** were obtained. A closer examination by SEM also revealed no apparent differences in the thickness and topography of both faces of the membranes (**Figure 4.36B**). It is worth mentioning that the chirality was retained after the synthesis of the catechin-based membranes, as observed by vibrational circular dichroism (**Figure 4.36C**). These results suggested that the polymerization reaction occurs at the ends of the catechin molecules, thereby preserving the chiral center of the molecule. The preservation of this chirality provided an opportunity to explore if specific stereochemistry of the catechin molecules influences their behavior in biological systems.

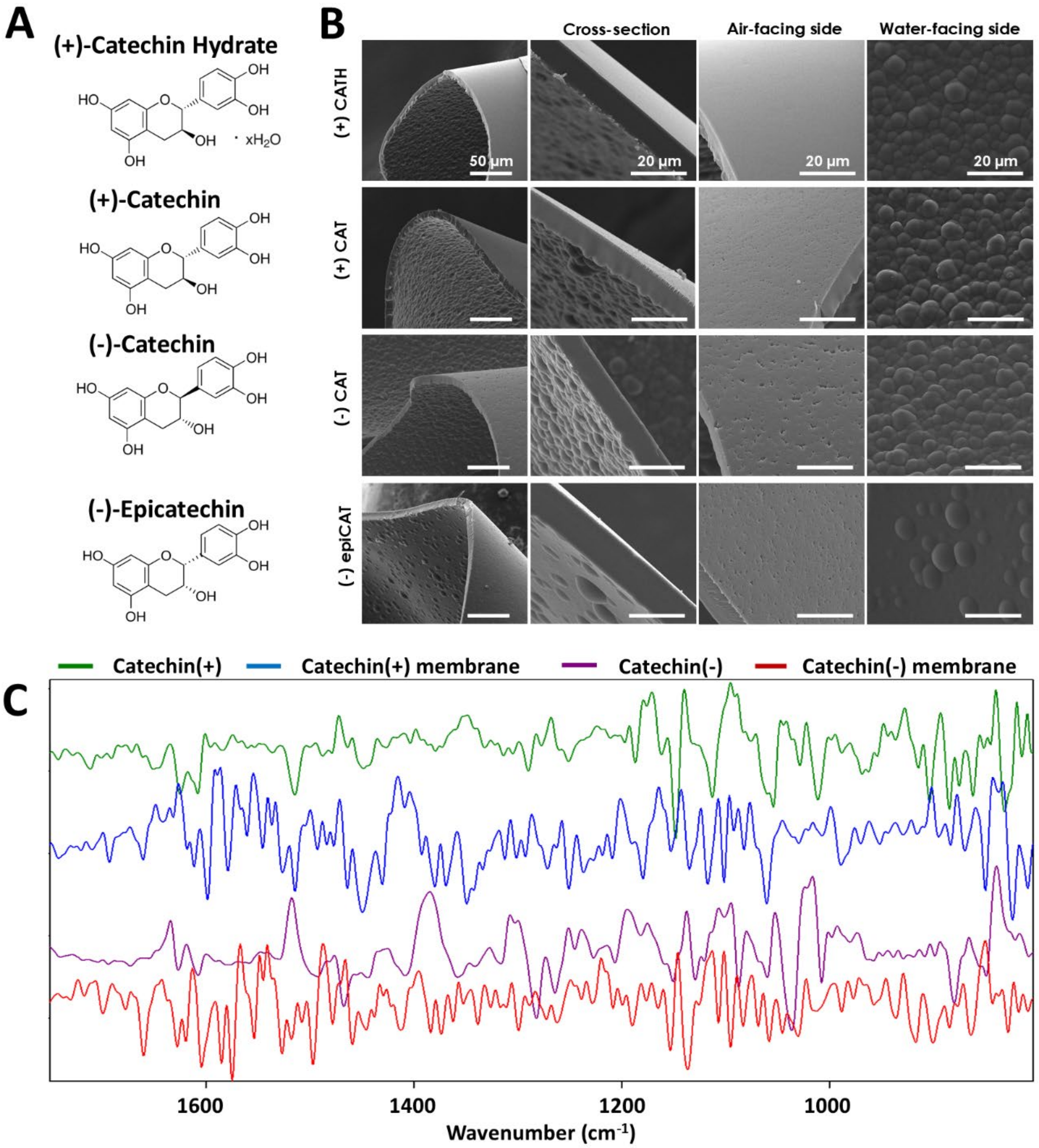

Figure 4.36. Catechin stereoisomers synthetize similar membranes. A) Molecular structure of the "(+) catechin hydrate (CATH), a non-hydrated formulation "(+) CAT", its enantiomer "(-) CAT" and its diastereomer "(-) epiCAT". **B)** SEM images of the membranes obtained with each stereoisomer and HMDA, where no differences between them can be observed. **C)** Vibrational circular dichroism of each membrane confirms that the chirality has been retained after the synthesis.

To study the effect of chirality, the cytotoxicity of the four membranes obtained from these stereoisomers was also determined. Interestingly, no differences were observed in the percentage of cell death in LN229 cells after treatment with each membrane (**Figure 4.37**). Therefore, while the cytotoxic properties of **CATH-M** appear to be related to non-specific ROS radicals formed after the interaction of the membrane with the surrounding media, the lack of observed differences between the different stereoisomers does not rule out the possibility that chirality may play a specific role in interactions with certain cellular receptors. Further research is needed to explore the potential for specific receptor-chiral center recognition within the membrane.

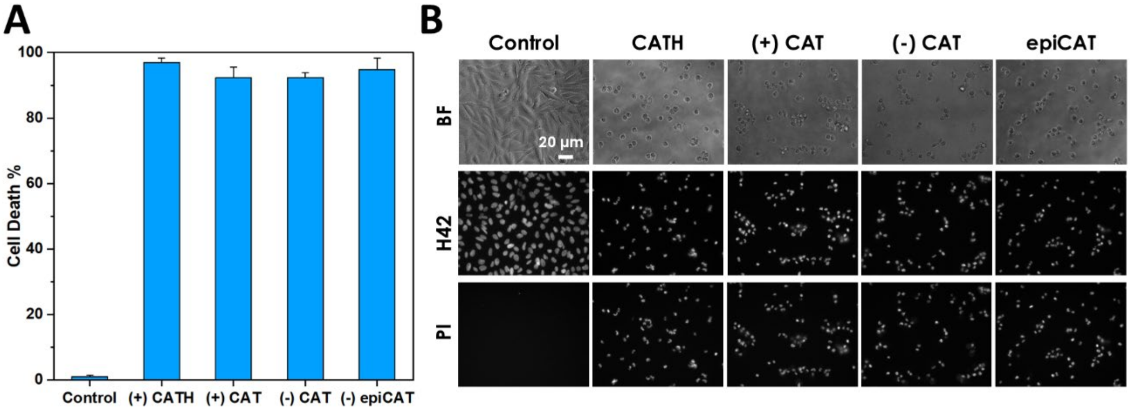

Figure 4.37. Catechin stereoisomers membranes exert similar cytotoxic properties. A) Cell death percentage of the LN229 cells after being treated with membranes obtained from HMDA and CATH, a non-hydrated formulation "(+) CAT", its enantiomer "(-) CAT" or its diastereomer "(-) epiCAT", where no differences were found between the four membranes. **B)** Representative bright field, H42 and PI images of the test.

*4.2.3.8 Identification of the cell death subroutine(s) engaged by **CATH-M** in GBM cells*

To elucidate the underlying mechanism of cell death induced by **CATH-M**, various inhibitors targeting different pathways were tested in conjunction with the membrane:

- Apoptosis: Q-VD-OPH (QVD) 50 µM, staurosporine (STAURO) 1 µM
- Necroptosis: necrostatin-1 (NEC1) 50 µM
- Autophagy: 3-methyladenine (3MA) 10 mM, bafilomycin (BAFI) 100 nM, hydroxychloroquine (HCLQ) 20 µM
- Parthanatos (PARP inhibitors): rucaparib (RUCA) 10 µM, olaparib (OLAP) 10 µM, PJ34 10 µM; E) cycloheximide (CHX) 10 µg/ml, actinomycin D (ACTD) 10 nM
- Ferroptosis: ferrostatin-1 (FER1) 10 µM, deferoxamine (DEF) 100 µM, erastine (ERA) 10 µM
- Oxidative damage: n-acetylcysteine (NAC) 5 mM

Results showed that QVD effectively inhibited apoptosis induced by staurosporine, a well-known apoptosis inducer.[57] However, it failed to protect LN229 cells from **CATH-M**-induced cell death, suggesting a non-apoptotic mechanism (**Figure 4.38A** and **4.39A**). Similarly, the necroptosis inhibitor NEC1 did not provide protection (**Figure 4.38B** and **4.39C**), thus indicating that necroptosis was also not the primary mechanism of cell death triggered by **CATH-M**. Autophagy (**Figure 4.38C** and **4.40A**) and parthanatos (**Figure 4.38D** and **4.40B**) inhibitors both displayed marginal reductions in cell death, suggesting that these pathways might play a minor role in the overall cell death process. Macromolecular synthesis inhibitors also showed no considerable difference compared to the membrane alone (**Figure 4.38E** and **4.39B**). Whereas ferroptosis inhibitors, DEF and FER1, successfully protected cells from the ferroptosis inducer (ERA), only the iron chelator DEF achieved a significant decrease in cell death against **CATH-M**, with FER1 showing a slight effect (**Figure 4.38F**). However, it is important to consider that, although deferoxamine resulted in less than a 10% cell death, the cell morphology remained similar to that observed with **CATH-M** alone (**Figure 4.40C**). This suggested that this protection might be enough to avoid cell death, but could be inefficient to keep long-term cell viability, potentially leading to eventual death if the stimulus persists. These findings entail that, whereas the **CATH-M**-induced cell death may not be strictly ferroptosis, the protective mechanisms involved in this pathway could still play a relevant role in modulating the death process.

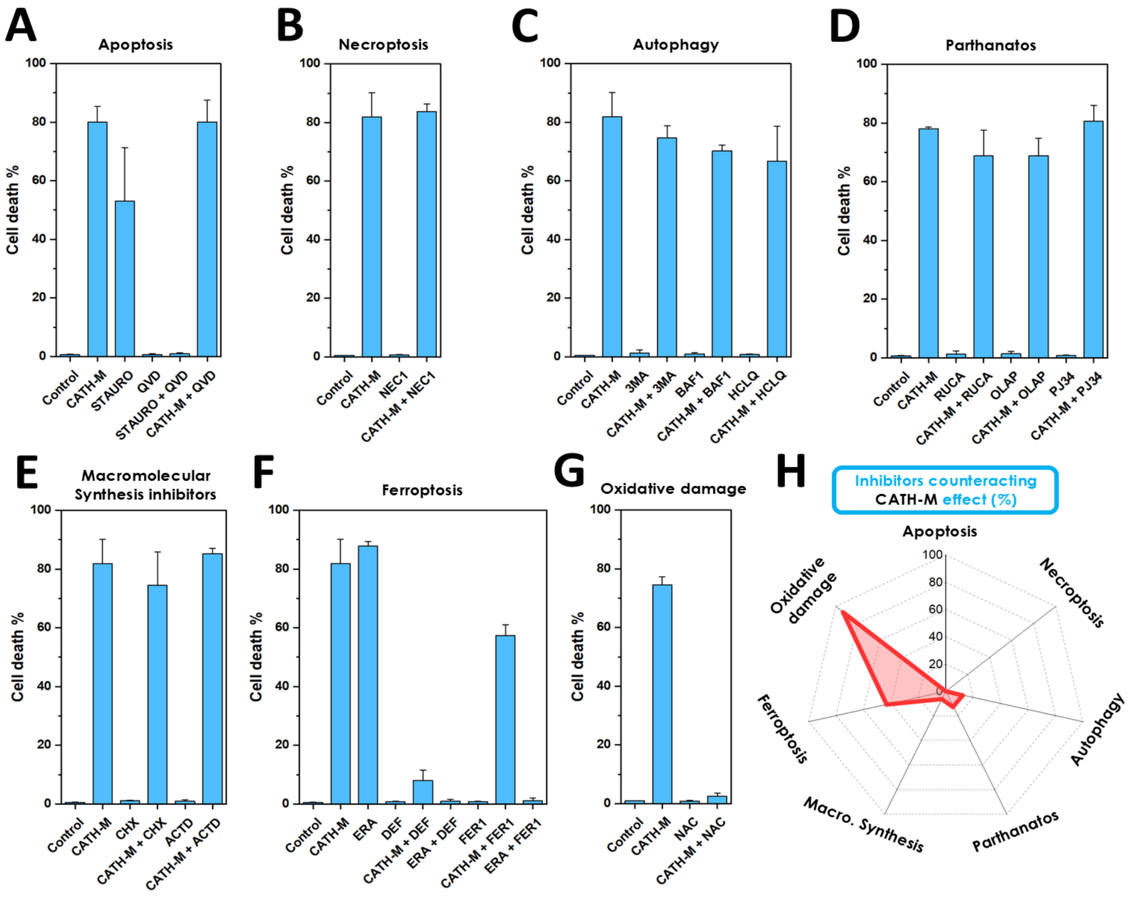

Figure 4.38. CATH-M-triggered cell death analysis. LN229 Cell death percentage when exposed to **CATH-M** and simultaneously with inhibitors of **A)** apoptosis, **B)** necroptosis, **C)** autophagy, **D)** parthanatos, **E)** macromolecular synthesis, **F)** ferroptosis, and **G)** oxidative damage. From the inhibitors selected, only the chelating agent deferoxamine (DEF) and, especially, the antioxidant NAC showed a significant decrease in the percentage of cell death. Error bars represent the standard deviation of a data set relative to the mean. **H)** Influence of each pathway towards **CATH-M**-mediated cell death in base of the selected inhibitors.

Finally, it was observed that N-acetylcysteine (NAC), an inhibitor of oxidative damage, completely protected cells from **CATH-M**-induced cell death (**Figure 4.38G** and 4.**39D**). This result was consistent with findings from Chapter 3, where NAC also protected bacteria against catechol-amine based coatings. Unlike deferoxamine, NAC also managed to maintain the normal morphology of the cells, which suggests that this protection might be robust enough to preserve cell viability.

These findings strongly suggest oxidative stress as the primary driver of cell death induced by **CATH-M**. Considering the lack of protection from apoptosis and necroptosis, coupled with the slightly protection observed from ferroptosis inhibitors and the complete protection afforded by NAC, it is proposed that the cell death induced by **CATH-M** was predominantly necrosis due to oxidative damage (**Figure 4.38H**).

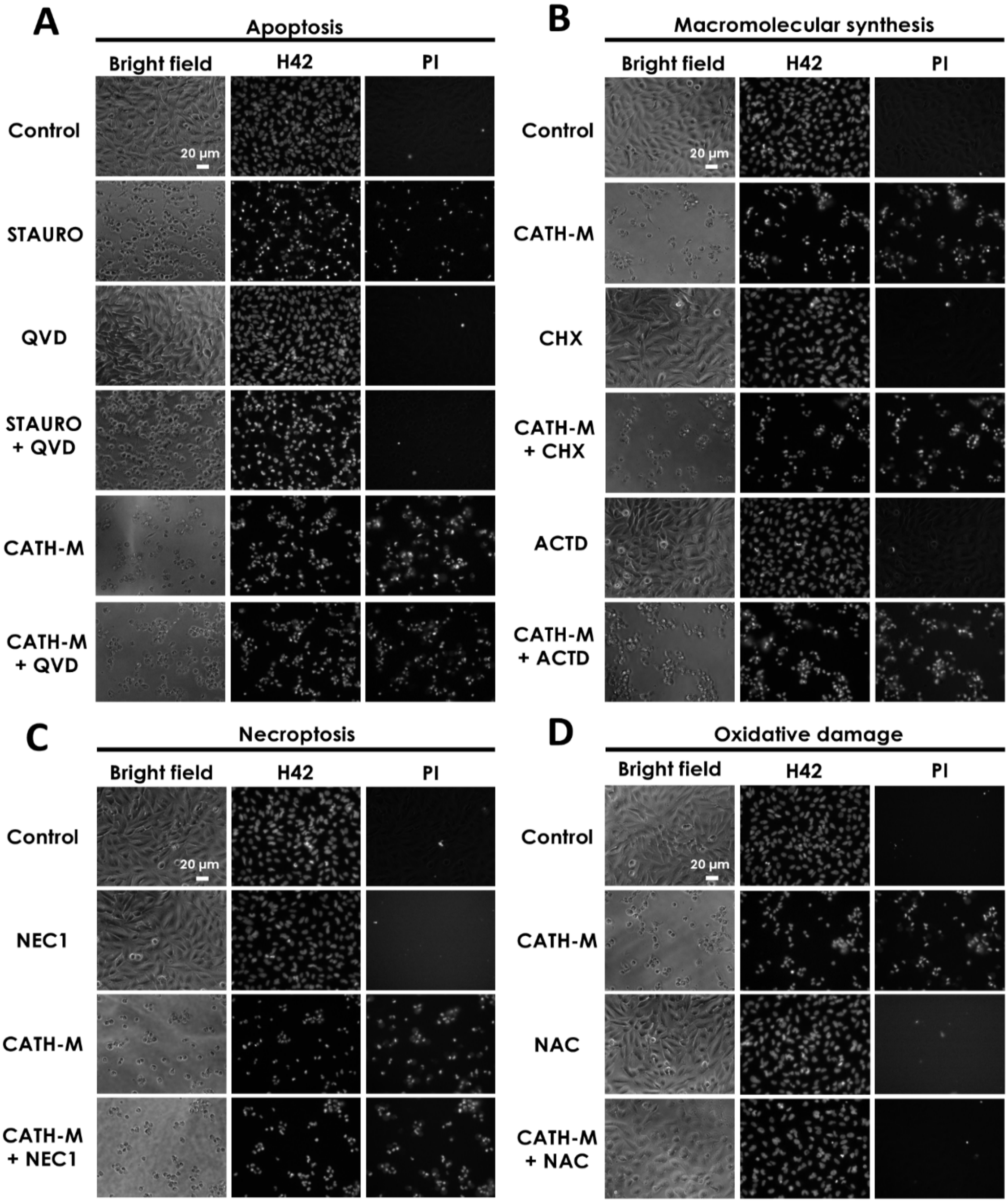

Figure 4.39. CATH-M and apoptosis, macromolecular synthesis, necroptosis and oxidative damage inhibitors. **A)** Representative bright field, H42 and PI images of the LN229 cells after using pan-caspase inhibitor QVD simultaneously with staurosporine (apoptosis inducer); **B)** cycloheximide and actinomycin D; **C)** necrostatin-1; and **D)** n-acetylcysteine.

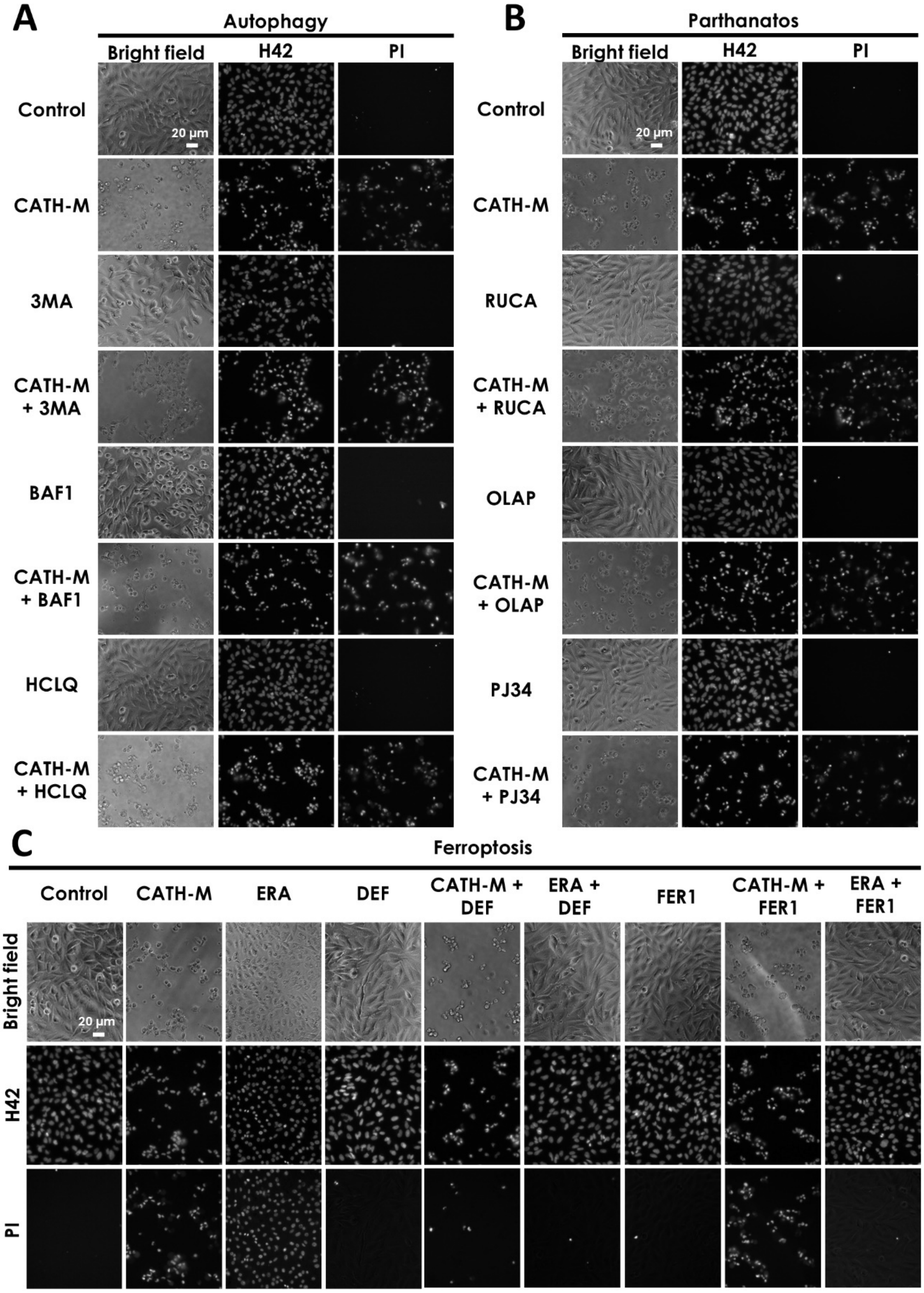

Figure 4.40. CATH-M and autophagy, parthanatos and ferroptosis inhibitors. A) Representative bright field, H42 and PI images of the LN229 cells after using the inhibitors 3-methyladenine, bafilomycin, and hydroxychloroquine; **B)** rucaparib, olaparib, and PJ34; and **C)** deferoxamine or ferrostatin-1, as well as the ferroptosis inducer erastine.

4.2.4 Influence of CATH-M in cell adhesion and migration

4.2.4.1 Cell morphology and tumor-like environment

The initial methodology stablished to assess the cell death induced by the leaking effect of the membrane was named as “close contact”. However, in order to examine the impact of **CATH-M** or **PYRO-M** on cell behavior and morphology, an alternative approach named as “direct contact” was implemented (**Figure 4.41**). For this, 4 × 10^4 LN229 cells/well were seeded directly onto glass without (control) and with H_2O_2 0.5 mM (positive control), or on the membranes, followed by 24 h incubation. For the **PYRO-M**, no specific side of the membrane was selected for cell culture since the morphology of both sides was relatively smooth. In the case of **CATH-M,** the air-facing side was selected due its extremely flat surface compared to the particle-embedded morphology of the water-facing side, which would difficult cell identification. In any case, empirical data (not shown) indicated that LN229 cells behaved similarly on both sides of the membrane. Subsequent SEM analysis revealed that LN229 cells exhibited normal morphology on control substrates and **PYRO-M** (**Figure 4.42**), confirming the innocuous nature of this membrane. On the contrary, those seeded on **CATH-M** displayed significant morphological

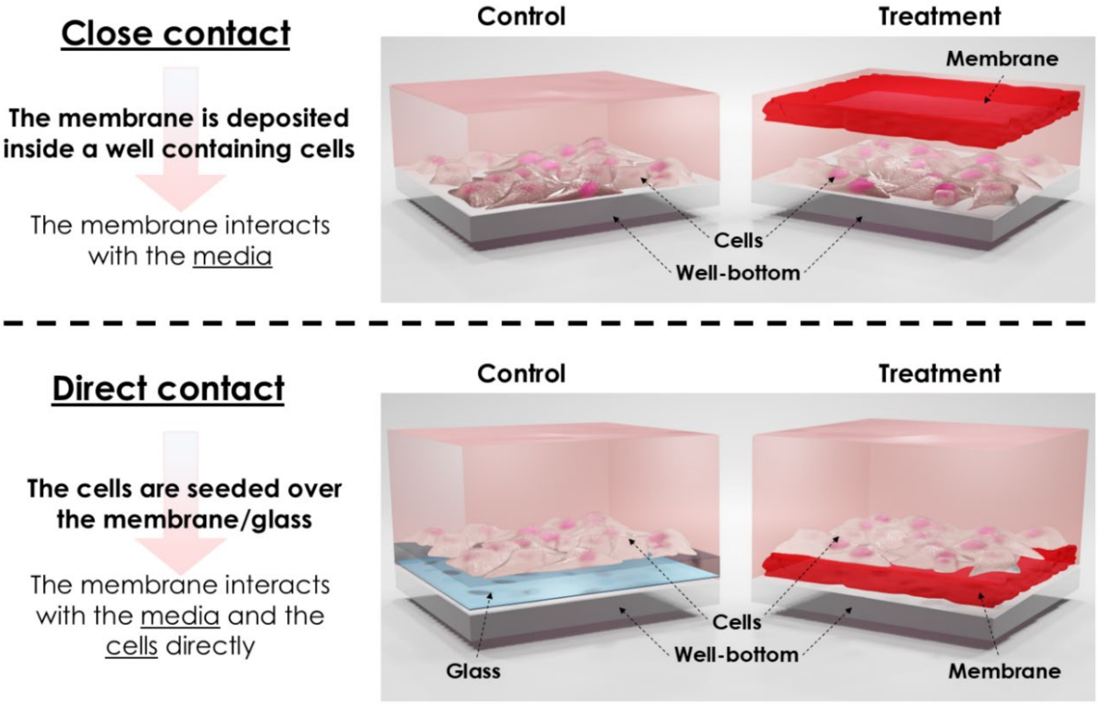

Figure 4.41. Methodologies used to test the membranes. The close contact (above), is characterized for testing only the radical production of the membranes (interaction with media) close to the cells, but without being physically in contact with them. The membranes are tested on an already stablished monolayer. On the contrary, the direct contact (right) is characterized for using the membrane as substrate for the cell seeding (and a glass coverslip as control) Therefore, in this case, not only the interaction with media is tested (which would be even stronger due the proximity of the cells to the membrane), but also the interaction of the cells with the surface of the membrane. No specific face was selected for the close contact treatment or direct contact (seeding) in the case of **PYRO-M**. For **CATH-M**, the water-face was oriented to the cells in the case of the close contact treatment, whereas the cells (in direct contact) were seeded over the air-face. Therefore, the air/water faces of the **CATH-M** membrane were always oriented as up/down, respectively.

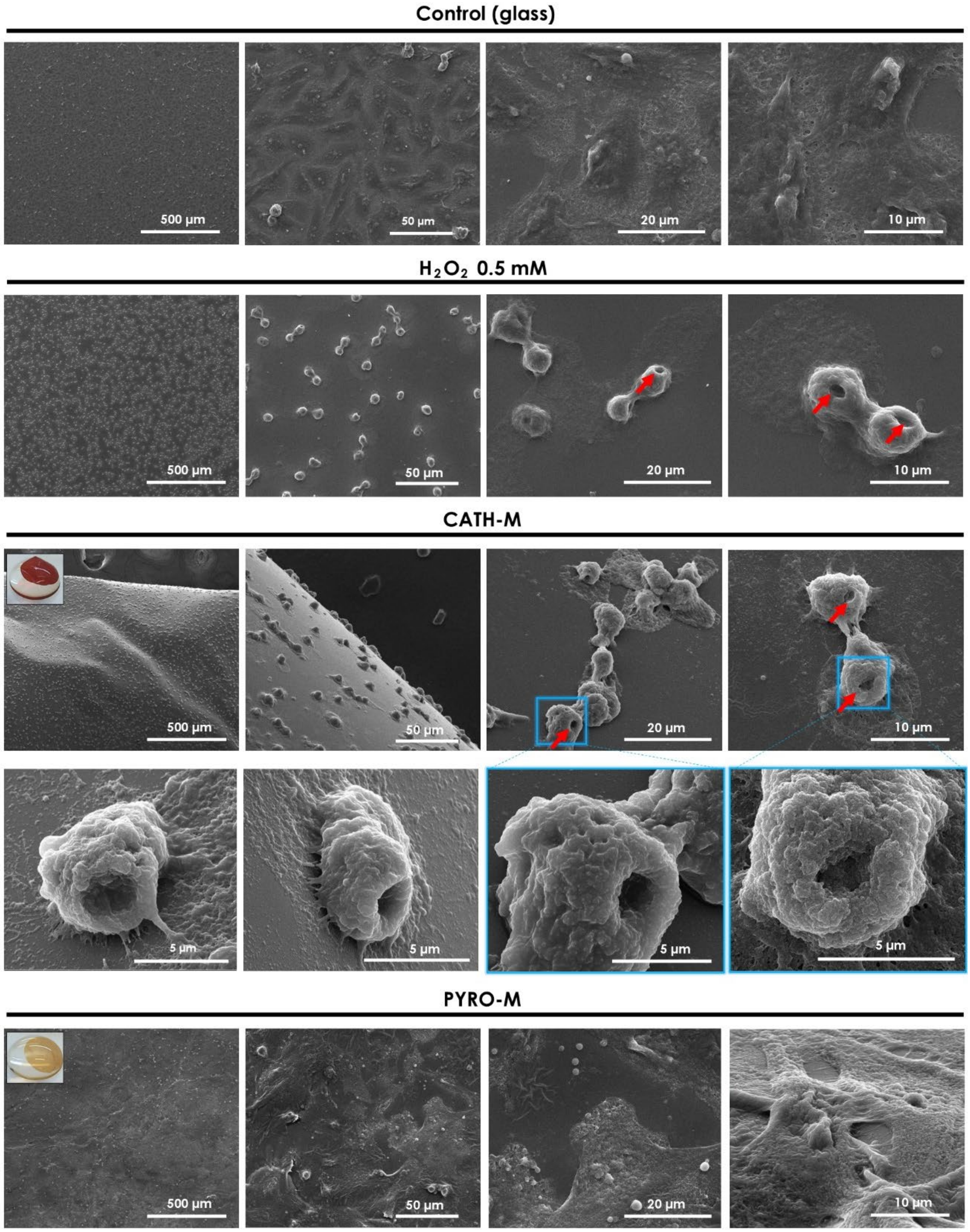

Figure 4.42. LN229 morphology over the membranes. Representative scanning electron microscopy (SEM) micrographs of the LN229 cells cultured over glass (control), as well as exposed to 0.5 mM H_2O_2 (positive control), or over **CATH-M / PYRO-M** for 24 h**.** Red arrows highlight evident invaginations in the cell membrane on the positive control and the **CATH-M.** In the catechin membrane, it is also evident that the cells exhibit a strong interaction with the material, indicating robust adhesion. At the same time, remnants of cytoplasm can be observed being expelled from the cells (in their surroundings), particularly in those that are perforated. In the case of the **PYRO-M**, no main differences were noticed when compared to the control (glass).

alterations. These alterations were characterized by invaginations, perforations, retraction, and signs of membrane damage, similar to the effects observed with H_2O_2. Interestingly, the results obtained with **CATH-M** and LN229 cells resembled the pores, invagination, and deflation observed in bacteria, and the catechol-amine coatings shown in Chapter 3. Additionally, H42/PI staining confirmed that LN229 cells exposed to H_2O_2 and those cultured on **CATH-M** were dead after 24 h, whereas those on glass substrates or **PYRO-M** remained viable (**Figure 4.43**).

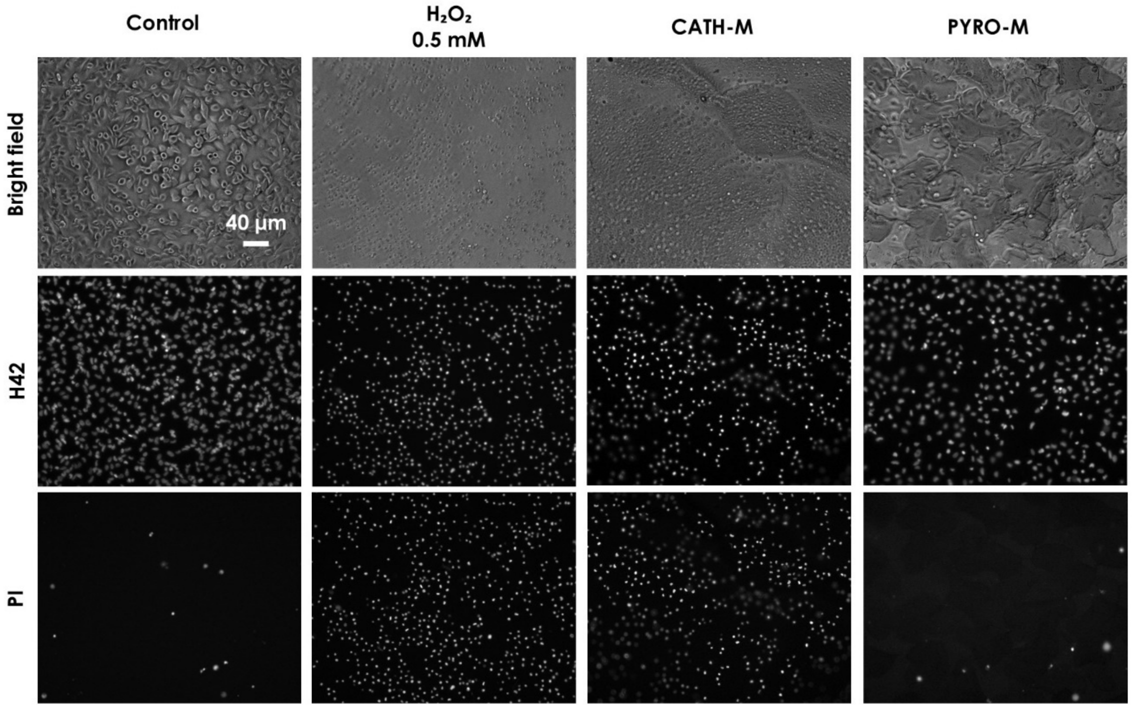

Figure 4.43. LN229 cell death on the membranes. Representative Bright field, H42 and PI images of the LN229 cells cultured on glass (control), as well as exposed to 0.5 mM H_2O_2, or on **CATH-M** / **PYRO-M** for 24 h.

To compare the effects of **CATH-M** on non-tumoral healthy cells, 2 × 10^4 cells/well rat primary cortical astrocytes were cultured directly on the membranes. Interestingly, SEM observations revealed that cells exposed to H_2O_2 0.5 mM abruptly changed their morphology (becoming spherical, and in some cases, showing perforations and cytoplasm leakage). Conversely, cells seeded on **CATH-M** remained largely unaffected, maintaining a morphology similar to the control, completely extended and flat (**Figure 4.44**). These results highlighted that **CATH-M** has a specific targeting cytotoxic effect on tumoral cells whereas healthy cells are unaffected, being able to further grow and proliferate.

Going a step further, in order to mimic a tumor-like environment, both **CATH-M** and **PYRO-M** were tested with LN229 spheroids (approximately 100 µm in diameter). The spheroids were seeded on glass (control) or membranes and their evolution was monitored over 7 days using SEM and optical microscopy. Within the first hour, the spheroids cultured on **CATH-M** exhibited early signs of membrane damage in the outer layer cells, showing similar morphological changes (invaginations, membrane unevenness and more rounded shape) as observed with separated cells in the previous section. In contrast, spheroids seeded on **PYRO-M** or glass remained largely unaffected, characterized by a more even outer layer cell, visually fused between them (**Figure 4.45**).

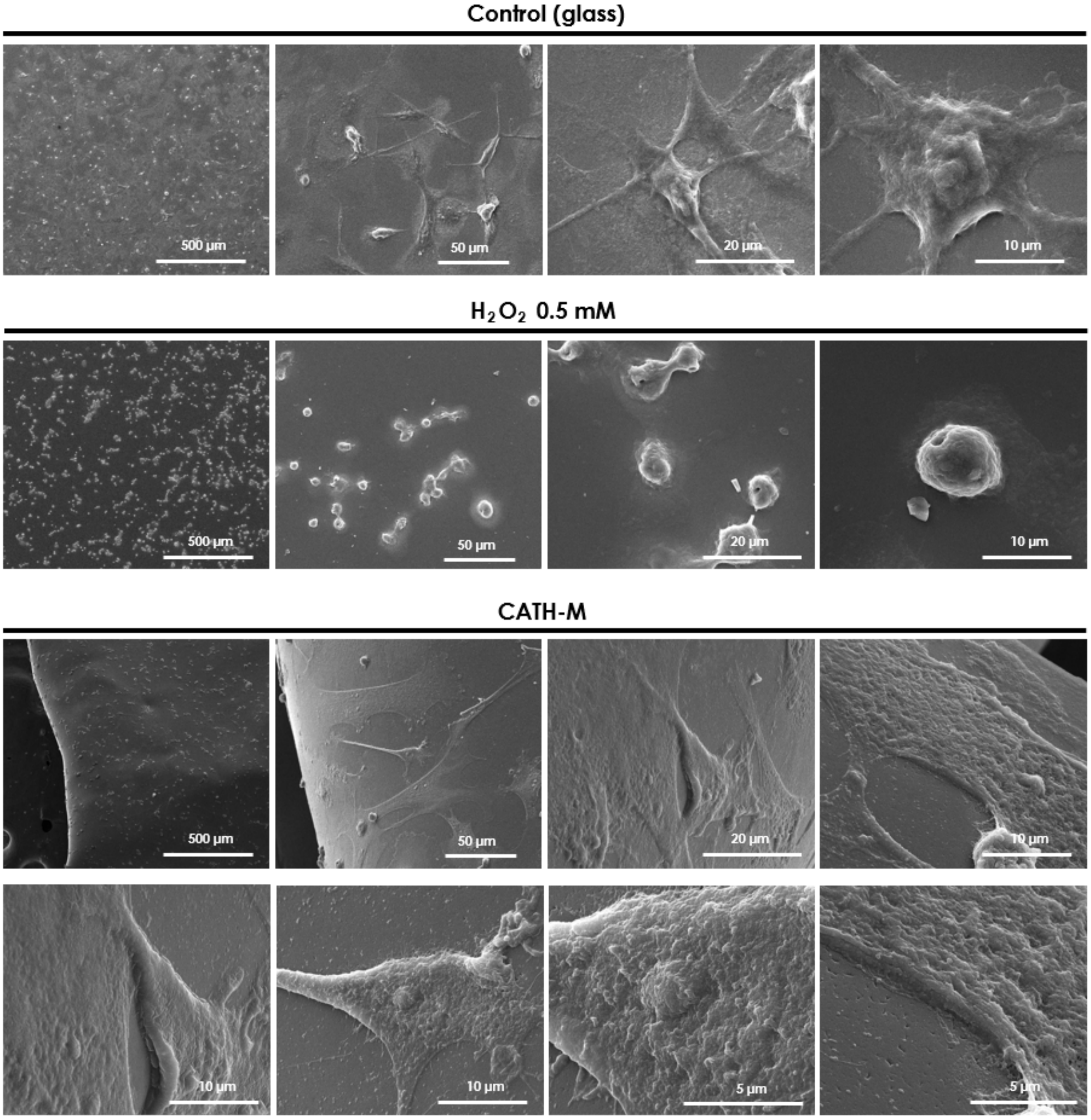

Figure 4.44. Primary cortical astrocytes morphology on the membranes. Representative SEM images of healthy astrocytes cultured for 24 h on glass (control) without and with $H_2O_2$0.5 mM (positive control) and **CATH-M.** Whereas the cells affected by the peroxide, changed their natural morphology, becoming spherical and, in some cases, showing perforations in their membranes in the case of the **CATH-M** no differences with the control were noticed. In the case of the control and **CATH-M**, the spherical cells observed, rather than damaged cells, correspond to microglia that remained in the culture after the extraction of the astrocytes.

After 24 h, spheroids on glass and **PYRO-M** demonstrated vigorous and uniform migration without signs of cell death. In contrast, spheroids on **CATH-M** exhibited subtle, irregular migration, and a damaged spherical morphology, particularly in peripheral cells (**Figure 4.46A**). The evolution of specific spheroids in each condition was compared by optical microscopy after 1 and 24 h of incubation. Only **CATH-M** showed a range of expansion almost imperceptible (**Figure 4.46B**). These differences became more pronounced after 3 days, when spheroids on glass and **PYRO-M** achieved sizes of approximately 1 cm, whereas **CATH-M** spheroids remained practically unchanged (**Figure 4.47A**). After 7 days, spheroids on glass and **PYRO-M** grew significantly, with **PYRO-M** inducing a distinctive star-like shape in the membrane, probably due to the tension created by strong cell adhesion (which often resulted in membrane tearing during the sample preparation for SEM) (**Figure 4.47B**). Interestingly, spheroids on **CATH-M** remained partially or completely intact, with limited migration and damaged cells at their edges.

These findings indicate that **CATH-M** significantly reduces the invasiveness of Glioblastoma spheroids by inhibiting migration and inducing cell damage (a promising therapeutic effect for targeting Glioblastoma).

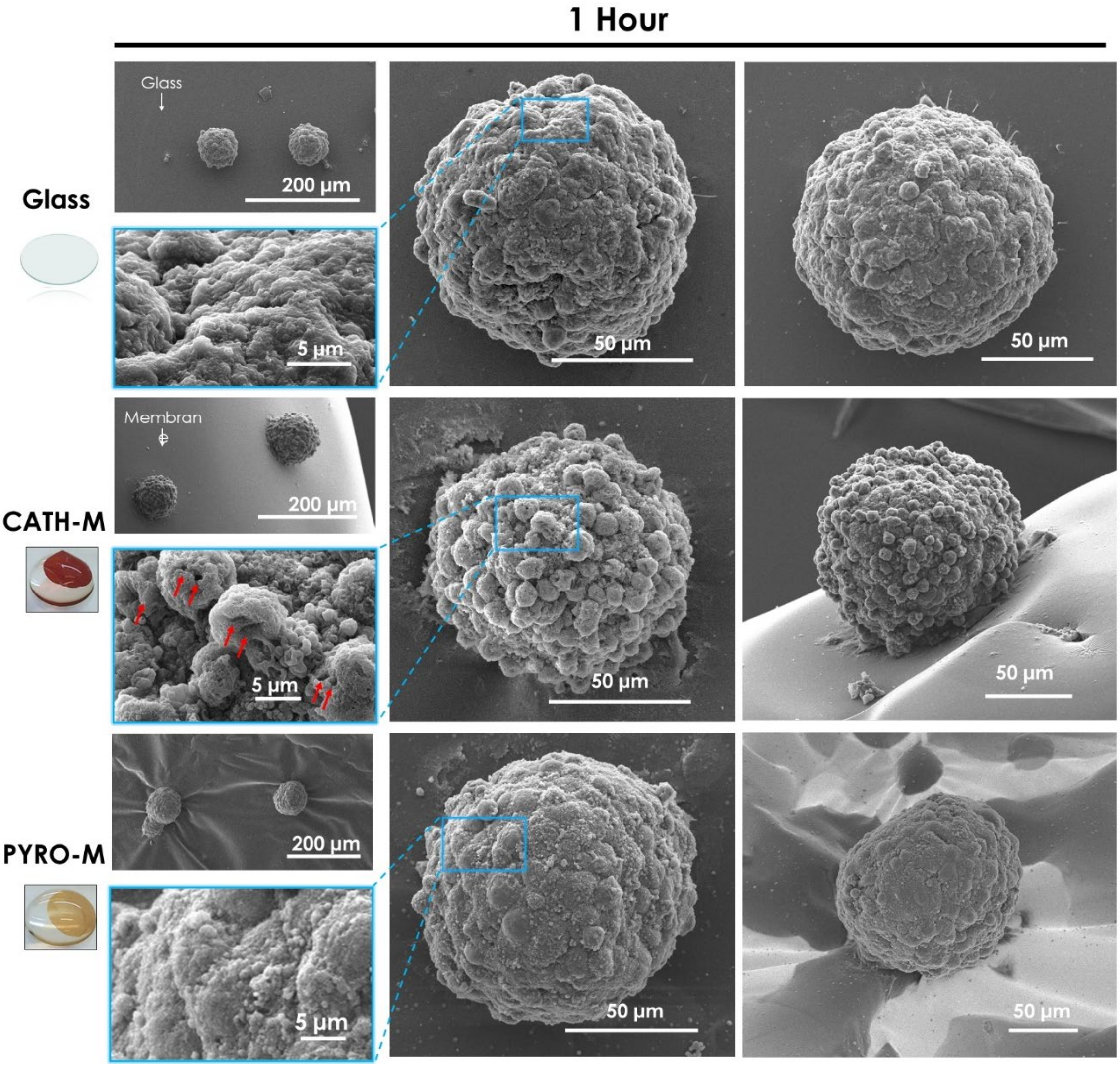

Figure 4.45. Spheroids early culture. Representative SEM images of LN229 spheroids cultured on glass (control), **CATH-M** for **PYRO-M** membrane for 1 hour. A clear difference can be observed in the outlayer cells of the spheroids seeded on **CATH-M** (irregular morphology, sphericity, and cell damage) and the seeded on glass or **PYRO-M** (homogeneous, even, and without cell damage)**.** Red arrows highlight invaginations/pores/damage in the cell membrane.

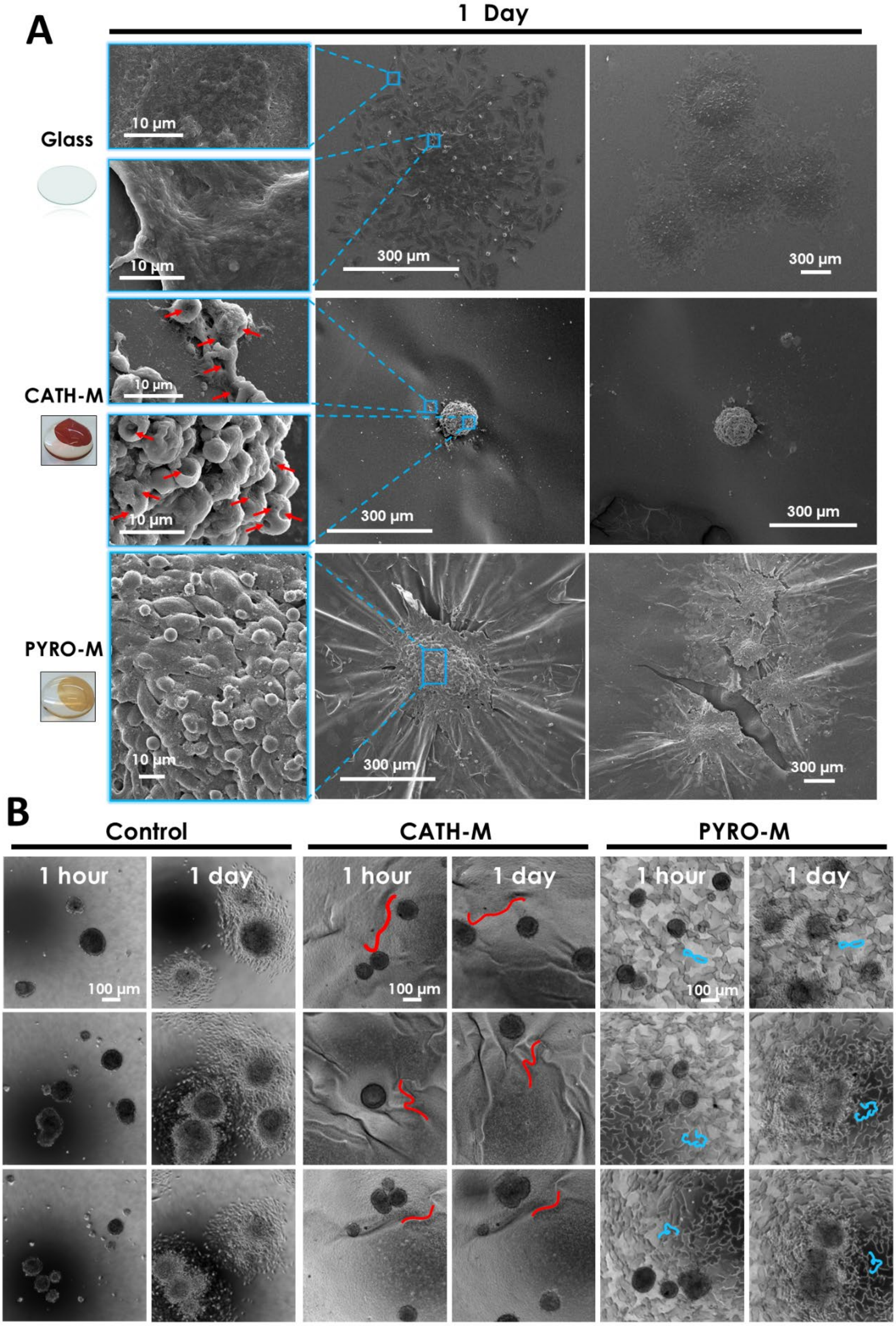

Figure 4.46. Spheroids 1 day culture. A) Representative SEM images of LN229 spheroids cultured on glass (control), **CATH-M** for **PYRO-M** membrane for 1 day. Whereas the spheroids seeded on **CATH-M** shown marginal signs of expansion and a noticeable cell damage, those on glass and **PYRO-M** achieved a substantial expansion. Red arrows highlight invaginations/pores/damage in the cell membrane. **B)** Bright field images of the spheroids and their evolution after 24 h. Since the membranes can rotate in the media, a specific membrane shape has been colored (red for the **CATH-M** and blue for the **PYRO-M**) for better comparison between incubation times. Pictures are compared from 1 hour to 1 day (left to right), showing 3 examples for each condition (up to down).

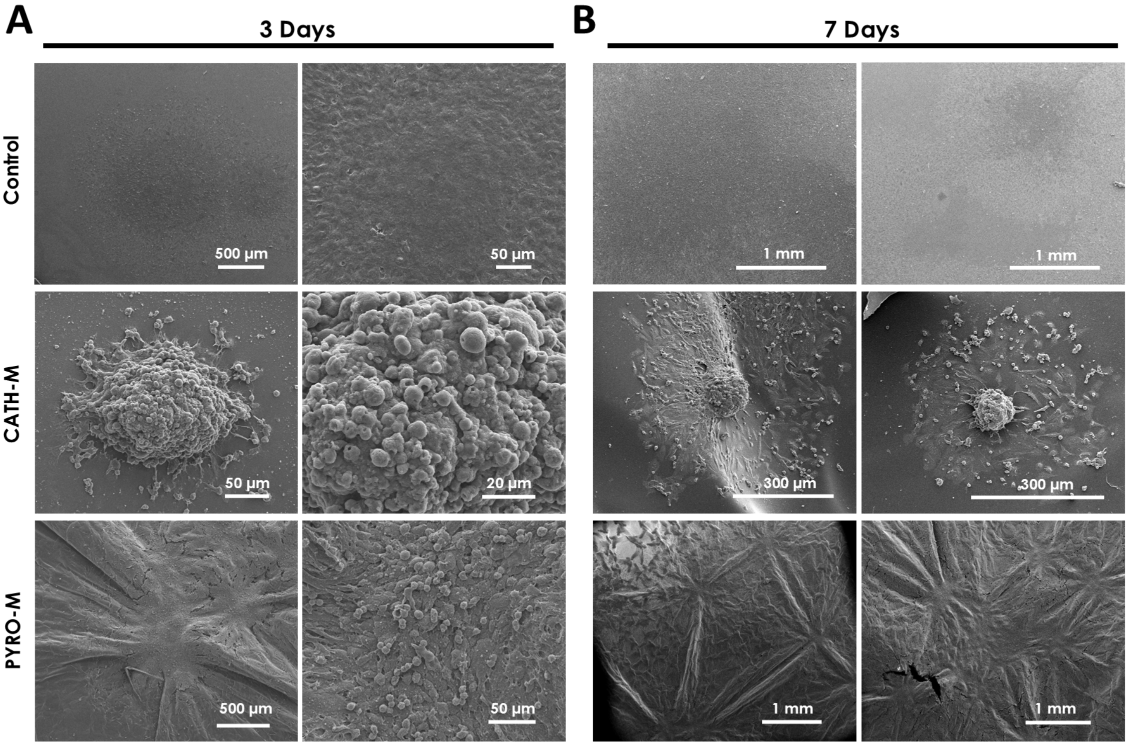

Figure 4.47. Spheroids progression. Representative SEM images of LN229 spheroids cultured on glass (control), **CATH-M** or **PYRO-M** membrane for **A)** 3 days and **B)** 7 days. In both cases, the differences between the growth of the control and **PYRO-M** compared to **CATH-M** are considerably large, as the catechin membrane was able to contain the expansion of the LN229 cells.

4.2.4.2 Cell migration

Cell migration is a critical mechanism for tumor progression. To quantitatively assess the effect of **CATH-M** on cell migration, cell culture inserts were used. These inserts consist of a portable well with a permeable membrane at the bottom, featuring a fixed pore size (**Figure 4.48A**). This design facilitates the exchange of molecules and nutrients through small pores between an upper chamber (insert content) and a lower chamber (recipient or multiplate-well content where the insert is placed) (**Figure 4.48B**). If these pores are big enough, cells can migrate between chambers through them. For this study, 8 µm pores were selected to enable this free movement of cells towards a chemotactic stimulus, allowing migration from the upper side to the lower side of the insert (**Figure 4.48C**). Specifically, 4 × 10^4 LN229 cells were seeded in the upper chamber (attached to the upper side of the insert's membrane), whereas varying amounts of **CATH-M** or **PYRO-M** (five discs of 1, 2, 4, or 6 mm diameter) were introduced into the lower chamber as potential chemotactic stimuli (**Figure 4.48D**).

The selected migration time was 16 h of incubation, which was empirically optimized to achieve a similar ratio of migrated to non-migrated cells in the control (depending on cell type and number). Regarding this, it was observed that a shorter time might not reveal sufficient migration, whereas a longer period could hide the chemotactic effect when compared to a control, as most cells would have already migrated. Interestingly, after 16 h, it was observed that increasing the amount of **CATH-M** resulted in a decreased migration, whereas lower

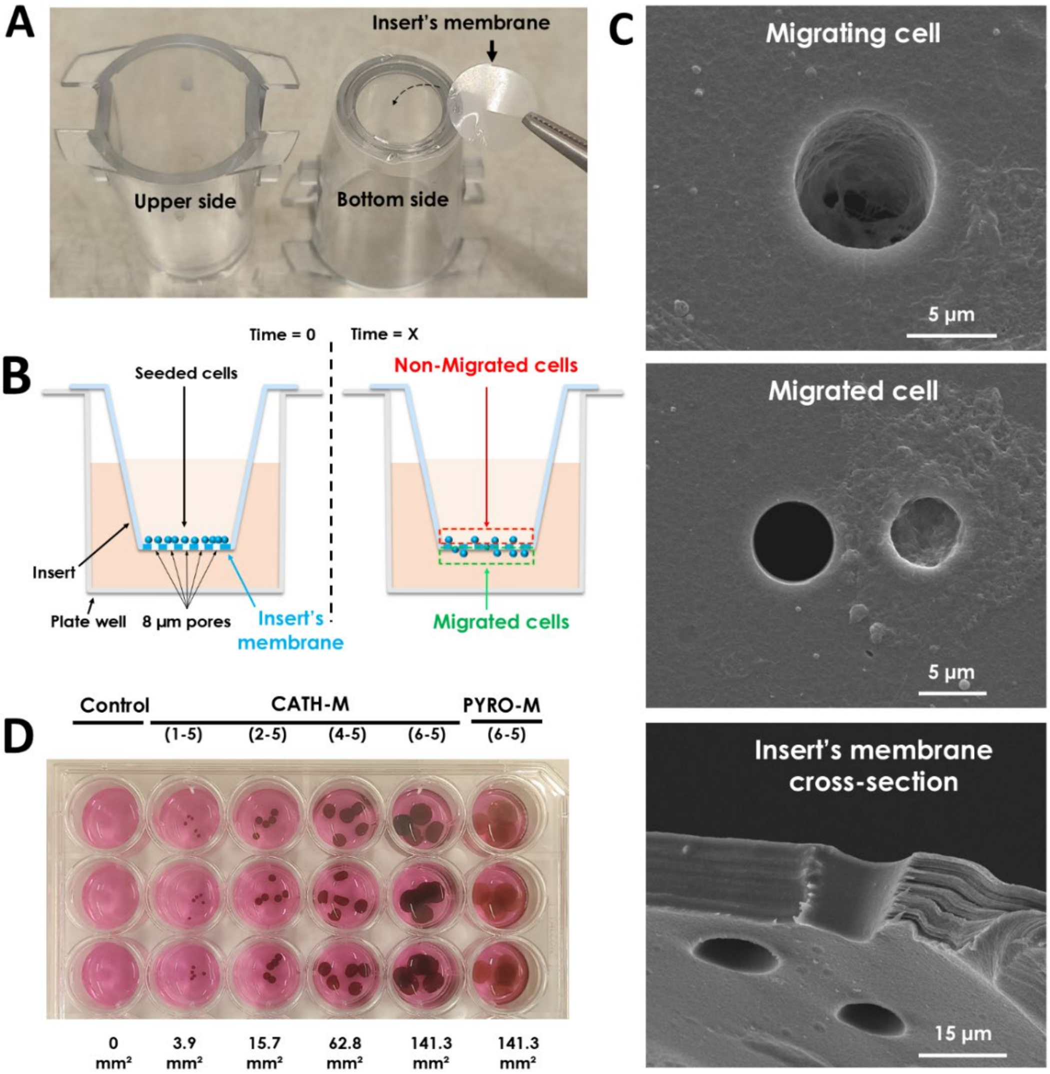

Figure 4.48. Inserts test scheme. A) Image of the selected inserts, as well as the membrane (cut) that contains the pores through the cells migrate. **B)** Schematic representation of how the inserts work, allowing the cell migration between chambers. **C)** Examples of migrating and already migrated cells in the inserts (bottom side is shown), as well as the structure of their pores. **D)** Amount of material of each membrane used in the migration test, which is represented as "(disc diameter in mm - number of discs)" and the equivalent total area in mm^2.

concentrations enhanced migration by up to 10% (five discs of 1 mm) compared to the control, which suggests a chemoattractant effect (**Figure 4.49A** and **4.50A**). This effect could play an essential role in trapping cells. Given the hypothesis that **CATH-M** might induce ROS production, and considering the role of H_2O_2 in tumoral cell migration,[58] H_2O_2levels in the media of the lower chamber were measured after 16 h of incubation with **CATH-H**. Surprisingly, a linear relationship between H_2O_2generation and **CATH-M** concentration was observed, which was inversely correlated with migration, suggesting a potential link between both (**Figure 4.49B**). Finally, the cell death in LN229 cells within the inserts (both migrated and non-migrated) after 16 h of incubation was quantified. It was observed that **PYRO-M** did not induce cell death. Conversely, **CATH-M**, particularly at higher concentrations, considerably increased cell death, with a nearly 90% mortality rate at the highest membrane concentration (**Figure 4.49C** and **4.50B**). SEM analysis revealed that most LN229 cells exposed to high amounts of **CATH-M**

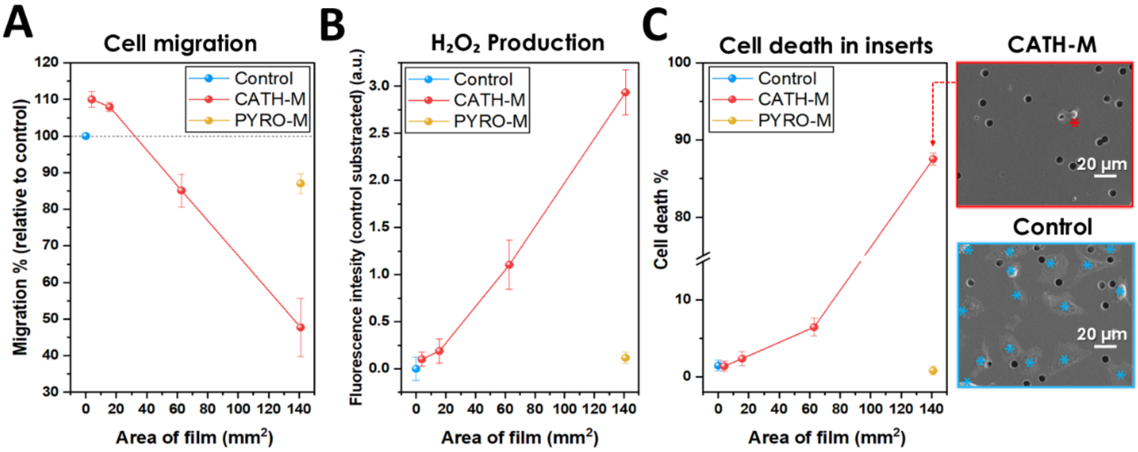

Figure 4.49. CATH-M influence in cell migration. A) CATH-M was capable to influence the LN229 cell migration in function of its amount (mm²) in the media, increasing it until a 110% or decreasing it below 50%. **B)** This decrease has shown to be inversely proportional to the H_2O_2 generated for the same amount of material, and to be related with **C)** the cell death % in the insert. The SEM micrographs show the remaining cells in the bottom face of the inserts for the control and the highest amount of **CATH-M** (each cell was marked with a blue or red asterisk, respectively).

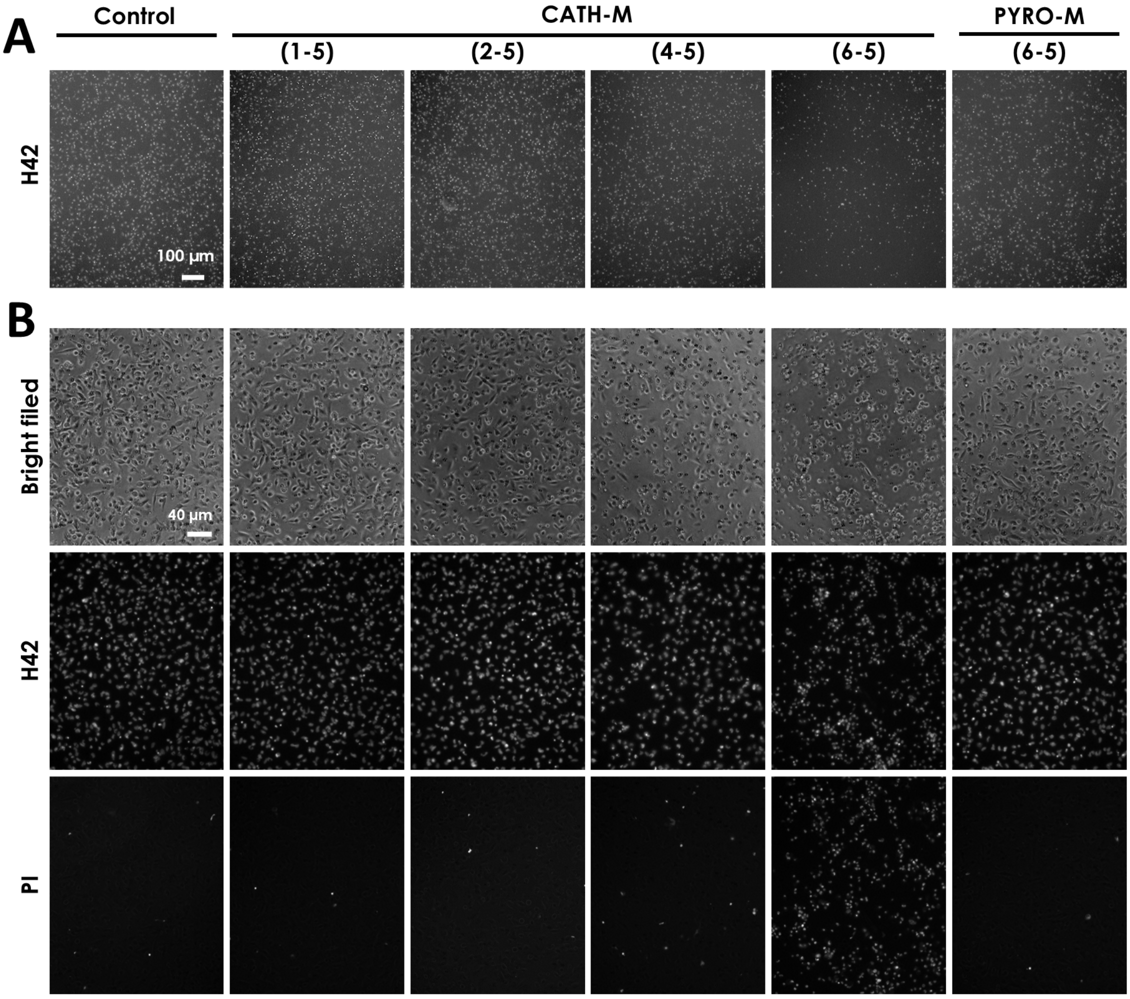

Figure 4.50. Observation of the LN229 migrated cells. A) Representative H42 images of the LN229 cells that migrated to the lower face of the insert after being 16 h with increasing amounts of **CATH-M** membrane and a fixed one of **PYRO-M**. It can be clearly observed that the **CATH-M** is inhibiting the migration. **B)** Representative bright field, H42 and PI images of a similar experiment, where the cell death of the migrated and non-migrated cell (simultaneously) has been assessed, which indicates a substantial cytotoxicity in the case **CATH-M** (6-5). Amount of material of **CATH-M** used in the migration test is represented as "(disc diameter in mm - number of discs)".

exhibited a damaged spherical morphology; also, that they were predominantly located in the upper chamber of the insert, which supported the migration and viability results (**Figure 4.51**).

Overall, these observations suggest that, whereas **CATH-M** can enhance LN229 cell migration under specific conditions, the observed decrease in migration at higher concentrations is likely due to the increased cell death, where the generation of H_2O_2 seems to potentially contribute. The relationship between **CATH-M** concentration and H_2O_2 production, coupled with cell migration, underscores the complex interplay between chemotactic stimuli and cellular responses. These findings highlight the dual role of **CATH-M** in modulating cell behavior, functioning as a chemoattractant at lower concentrations but inducing cytotoxicity at higher levels, demonstrating its potential use as a tumoral cell trap. Understanding this duality is crucial for elucidating the mechanisms underlying cell migration and developing therapeutic strategies targeting tumor cell movement.

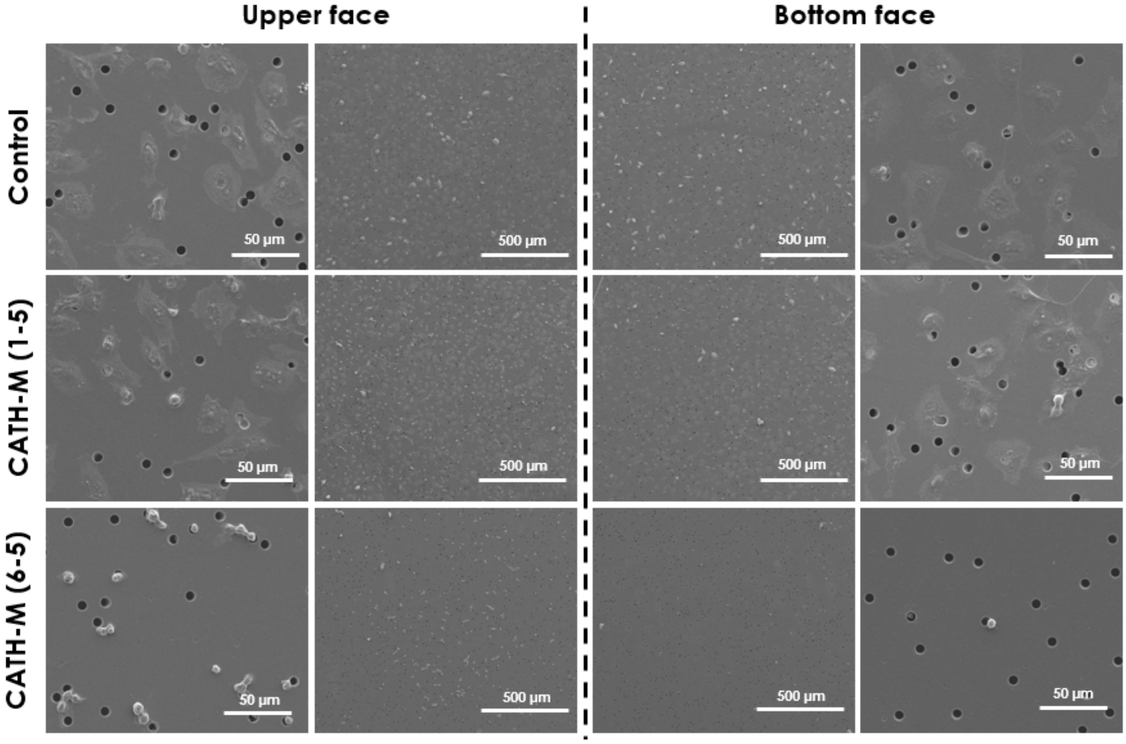

Figure 4.51. Migrated and non-migrated cells visualization. Representative SEM images of the cells that cells remaining on each side of the membrane of the insert. The results are showing for the control and **CATH-M** with the lowest and highest amount of material. Amount of material of **CATH-M** used in the migration test is represented as "(disc diameter in mm - number of discs)."

4.2.4.3 Cell adhesion

Given the potential influence of the adhesion on the cytotoxic effect of **CATH-M**, a study was performed where LN229 cells were cultured on different surfaces and exposed to the membrane. Cells were seeded onto both cell culture plates and non-cell culture plates, while maintaining all other test conditions identically. As expected, no significant differences were observed between the two surfaces, except for slower cell growth on the non-cell culture plates (**Figure 4.52A**). The adhesion strength of LN229 cells to the cell culture plate (control) was compared with their adhesion to both **CATH-M** and **PYRO-M**. For this experiment, 4 x 10^4 cells were seeded and subsequently incubated for 3 h on the cell culture plate or the membranes. This duration was sufficient for the cells to attach onto the plate or membrane surface, yet short enough to prevent any cytotoxic effects from **CATH-M** that could potentially alter the results. The cells were then trypsinized for 30 min, and the number of detached cells was quantified for each condition. Notably, the number of cells detached from the membranes was at least seven-fold lower than that of the control, which demonstrates strong cell-membrane adhesion (**Figure 4.52B** and **C**). This was further confirmed by the observation of cells remaining attached and homogeneously distributed across the surface of both membranes (**Figure 4.52D**).

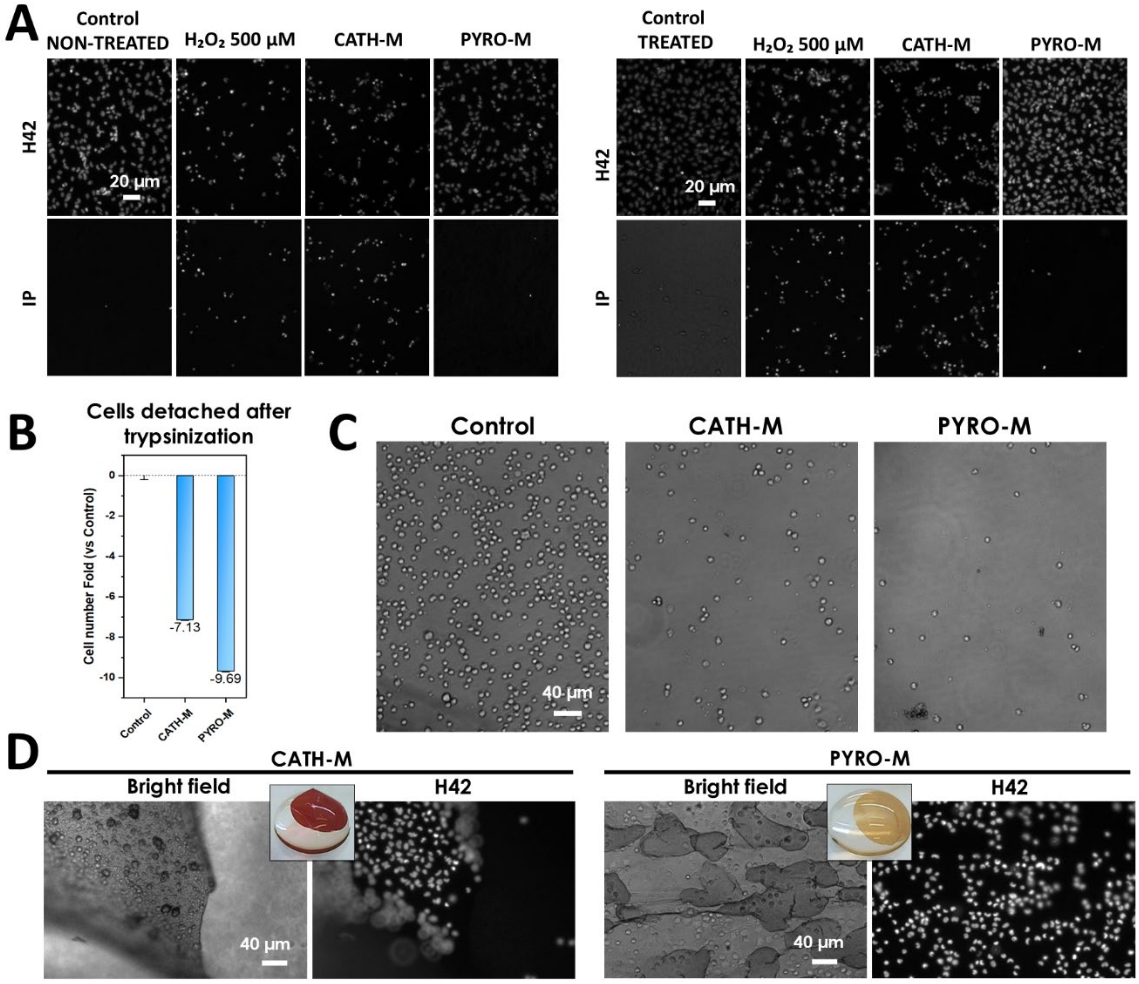

Figure 4.52. Glioblastoma cells adhesion on catechol-based membranes. A) H42 and PI images where it can be observed that **CATH-M** shows the same cytotoxic activity when LN229 cells are seeded in treated and non-treated plates (more and less adhered, respectively). **B)** The trypsinization of adhered LN229 cells to **CATH-M** or **PYRO-M**, compared to the bottom of a surface treated 96-well plate (control), was considerably less efficient (approximately 7 and 9 times less, respectively). **C)** Representative bright field images of the LN229 cells that were detached, suggesting that the cell adhesion on the membranes should be much stronger than the control. **D)** It was observed that cells were able to remain homogeneously attached to the membranes after the trypsinization. Cells Error bars represent the standard deviation of a data set relative to the mean.

4.2.5 Cell energetic metabolism alterations

These results highlight that both **CATH-M** and **PYRO-M** significantly enhance cell adhesion compared to the cell culture plate. This strong adhesion likely explains why LN229 cells seeded on **CATH-M**, despite being severely damaged (exhibiting holes/invaginations in their cell membrane), remain attached to the membrane. This strong adhesion is suggested to result from the broad range of interactions of polyphenols and their exposed functional groups with the surrounding environment, which makes them highly effective in promoting cell-membrane interactions.

Mitochondrial damage is a critical factor in this scenario, as it contributes to the generation of ROS, such as H_2O_2. This oxidative stress can significantly impact cell migration and viability. Understanding mitochondrial damage is essential for elucidating the mechanisms underlying these cellular responses.

4.2.5.1 Ultrastructural analysis

Transmission electron microscopy (TEM) analysis of LN229 cells treated with **CATH-M** demonstrated severe mitochondrial damage. This damage was characterized by a complete loss of cristae and decreased electron density, which was also observable in the nucleus and the cytoplasm, an indication of the compromised integrity of the mitochondrial matrix and intermembrane space (**Figure 4.53**). Additionally, a reduction in mitochondrial number, loss of cytoplasmic material (resulting in a more rounded cell shape with mainly the nucleus visible) and cell membrane permeabilization (presence of pores) were observed, especially in the later stages (**Figure 4.54**). Whereas **PYRO-M** treatment induced only minor mitochondrial damage, both **CATH-M** and **PYRO-M** treatments significantly upregulated autophagocytosis, as evidenced by increased formation of vacuoles and autophagosomes.

4.2.5.2 Mitochondrial function

To evaluate potential mitochondrial damage, a Seahorse assay was conducted to analyze the oxygen consumption rate (OCR) and extracellular acidification rate (ECAR) profiles of LN229 cells following exposure to **CATH-M** for 2 and 8 h (**Figure 4.55A**). Whereas the control group exhibited an overall increase in OCR and ECAR from 2 to 8 h, indicative of cell growth, **CATH-M** exposure resulted in a more linear profile, suggesting mitochondrial dysfunction. To accurately compare both conditions, individual respiration parameters derived from the OCR profiles were obtained (**Figure 4.55B** and **C**).

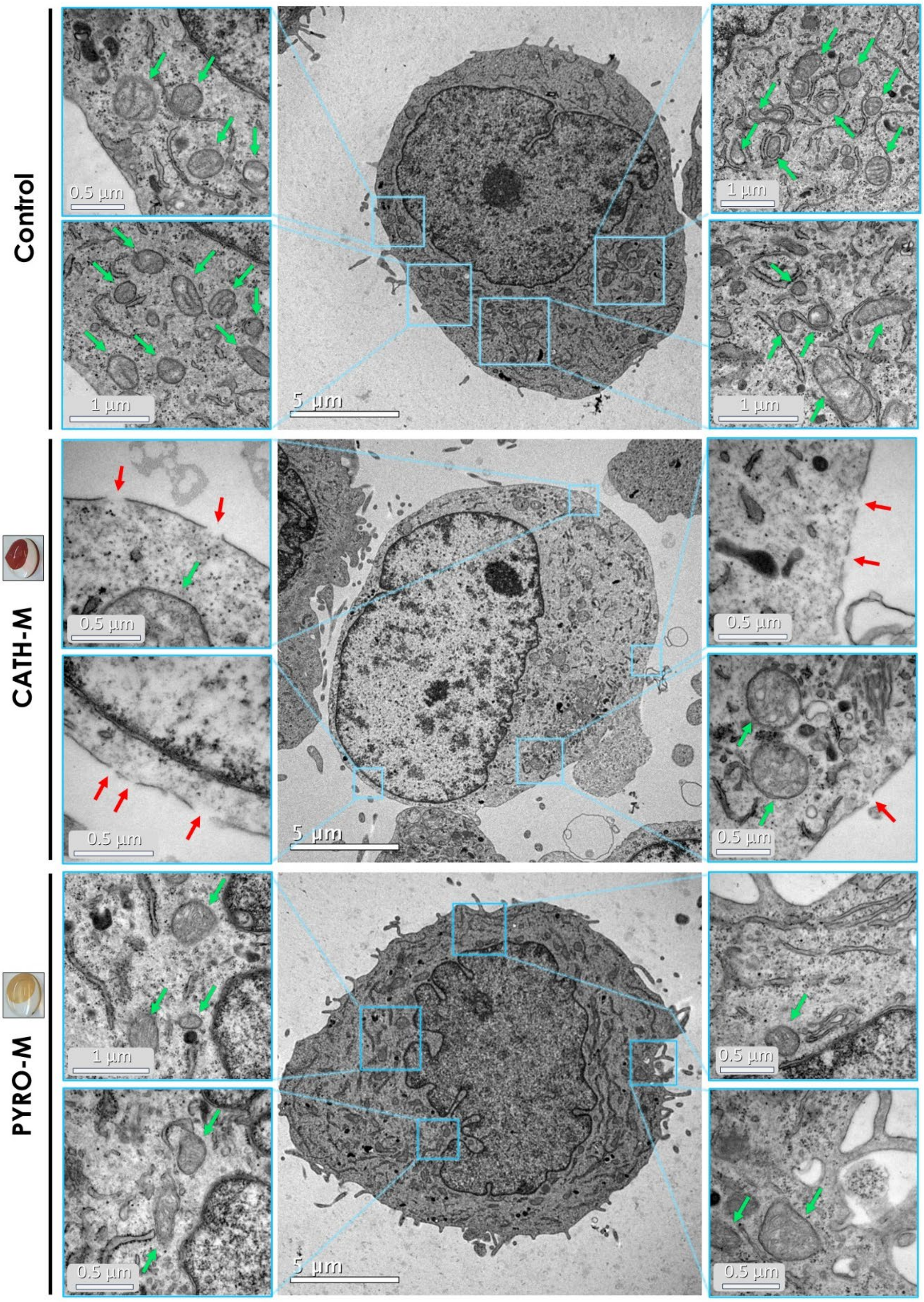

Figure 4.53. CATH-M damage the cell internal structures. Representative transmission electron microscopy (TEM) images of LN229 cells exposed to **CATH-M** and **PYRO-M** membrane. Green and red arrows indicate mitochondria and damage in the cell membrane (pores), respectively.

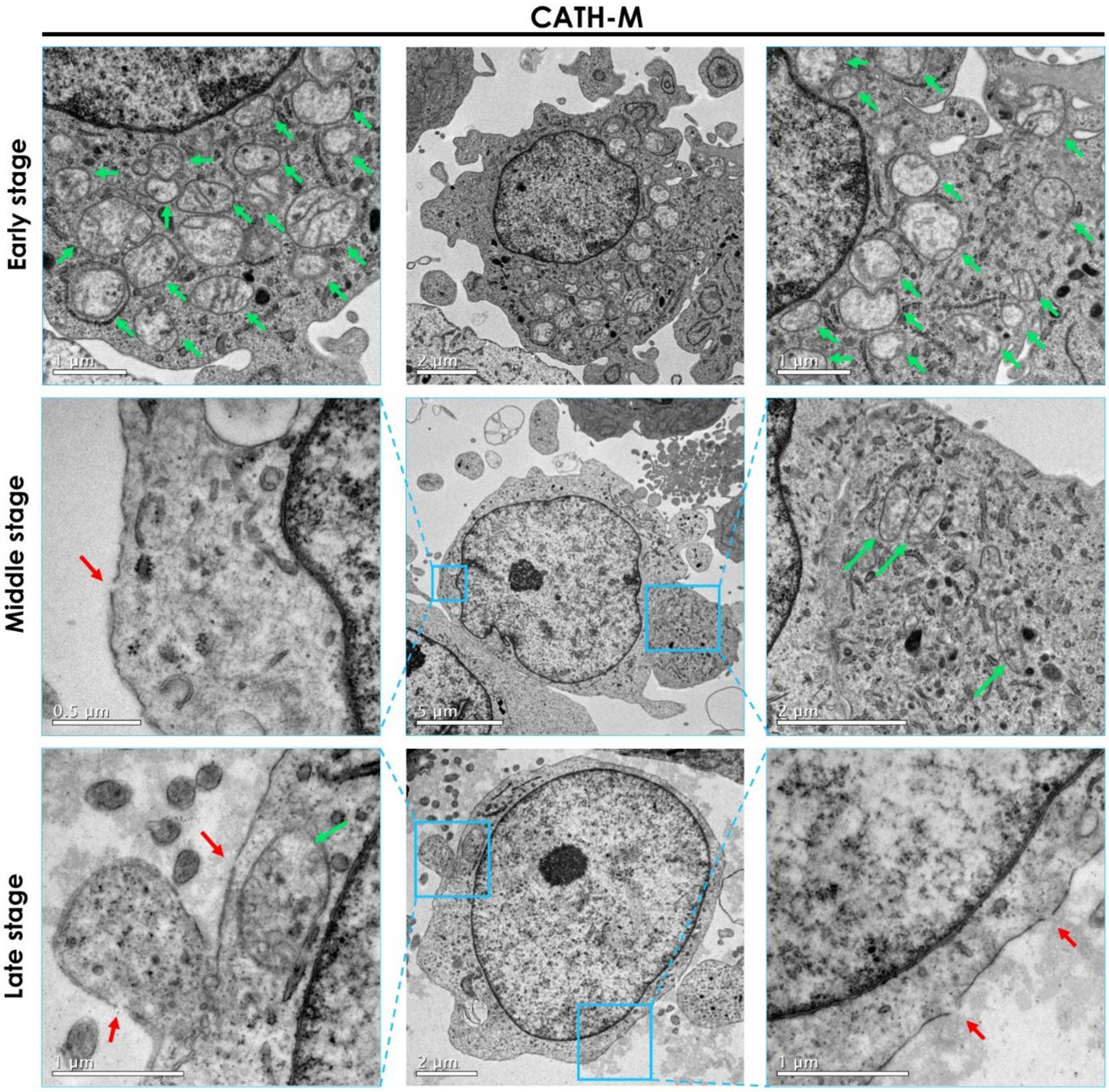

Figure 4.54. Alterations in the LN229 internal structures at different stages. Representative transmission electron microscopy (TEM) micrographs of the LN229 after being exposed to **CATH-M**. Each image row shows a different cell, ordered in function of their damage stage, from early (up) to late (down). Green and red arrows indicate mitochondria and damage in the plasmatic membrane, respectively.

One crucial parameter related to mitochondrial activity is ATP-linked respiration. This parameter increased in the control group but decreased in **CATH-M**-exposed cells, particularly after 8 h, thus indicating mitochondrial dysfunction and impaired oxidative phosphorylation. Proton leak also moderately increased with **CATH-M** exposure, reaching its higher value at 8 h, possibly due to mitochondrial membrane damage or as a protective mechanism against elevated ROS levels. Notably, in **CATH-M**-exposed cells, inhibition with oligomycin followed by carbonyl cyanide 4-(trifluoromethoxy)phenylhydrazone (FCCP) failed to restore the OCR level of basal respiration (whereas the control group reached their maximum peaks), resulting in negative values of spare respiration, which suggested damage in the mitochondrial machinery.

The increase in non-mitochondrial respiration in **CATH-M**-exposed cells could be attributed to energy compensation mechanisms or non-energetic processes such as stress-related metabolism, inflammatory responses, or ROS-mitigating enzyme activities like peroxidase. Furthermore, ECAR analysis revealed a substantial decrease in **CATH-M**-exposed cells, indicating reduced glycolytic activity (**Figure 4.55D**). Additionally, the lower ECAR increase in

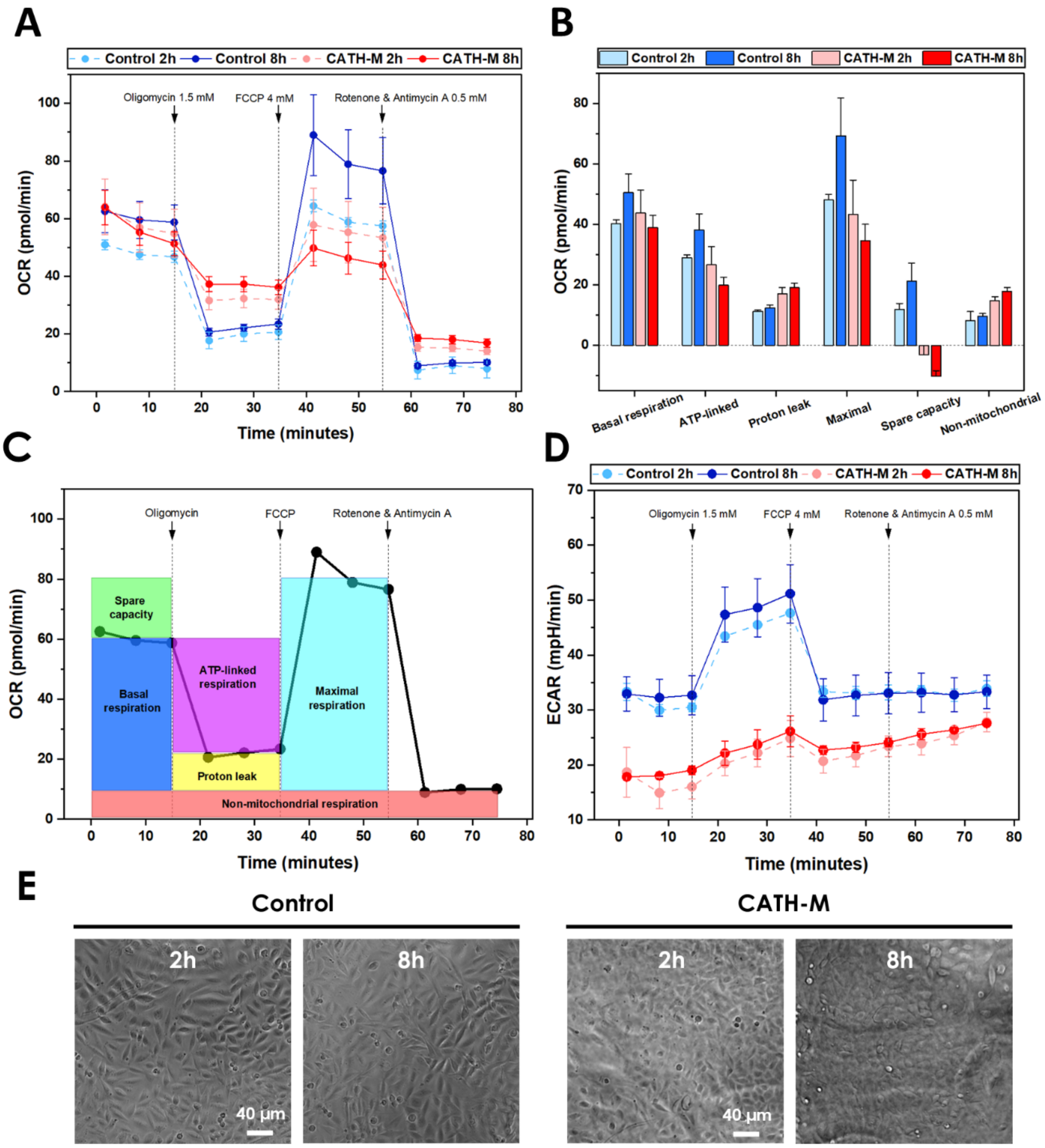

Figure 4.55. CATH-M decreases the metabolic capacity. A) Oxygen consumption rate (OCR) profile of LN229 after being exposed to **CATH-M** membrane for 2 and 8 h. **B)** Individual respiration parameters obtained from the OCR profiles, where a decrease of the ATP-linked respiration can be observed, suggesting a severe damage in the mitochondrial function. **C)** Visual scheme of the individual parameters obtained in function of the Oxygen Consumption Rate (OCR) profile, using as example the control at 8 h. **D)** Extracellular Acidification Rate (ECAR) profile obtained simultaneously as the OCR, showing a clear decrease in the acidification of the **CATH-M** treated cells, which could be related with a lower glycolytic activity. **E)** Representative bright field LN229 cells images right before reading their metabolic profile. Error bars represent the standard deviation of a data set relative to the mean.

CATH-M-exposed cells after oligomycin addition compared to the control suggests that the cells cannot compensate for energy deficiencies through enhanced glycolysis.

Despite the absence of significant morphological changes in **CATH-M**-exposed cells after 8 h (**Figure 4.55E**), the observed decreases in OCR and ECAR parameters suggested that the cells may be losing their viability and energy synthesis capacity, potentially leading to eventual cell death when these parameters decline to a critical threshold. This theory could be supported by previous results in the cytotoxic time-course profile (section 4.2.2.), where morphological changes and cell death were primarily observed after the first 9-12 h of incubation.

4.2.6 ROS production and oxidative damage

In view of the redox properties of polyphenols, the presence of hydroxyl groups in the **CATH-M**, and our previous findings (as demonstrated with the catechol-amine coatings from Chapter 3), it was hypothesized that ROS production could play a leading role in **CATH-M** cytotoxicity. To test this hypothesis, a comprehensive study of ROS generation was conducted.

4.2.6.1 Antioxidant protection and ROS modulation

To investigate the relationship between NAC concentration and protection against **CATH-M**-induced cytotoxicity, 2 × 10^4 LN229 cells were treated with increasing concentrations of NAC (1-20 mM) in the presence of **CATH-M**. After 24 h, a slight decrease in cell death was observed with 1 mM NAC, a minimal cell death with 5 mM, and cell viability reached control levels at 10 mM (**Figure 4.56**). Interestingly, concentrations above 20 mM of NAC (data not shown) began to exhibit cytotoxic effects. Nevertheless, in presence of the membrane, the cytotoxic effect of NAC was mitigated, as subtly observed at 20 mM NAC (**Figure 4.56**). These results demonstrated that the cytotoxic effects of **CATH-M** can be modulated by the antioxidant NAC (**Figure 4.56B**).

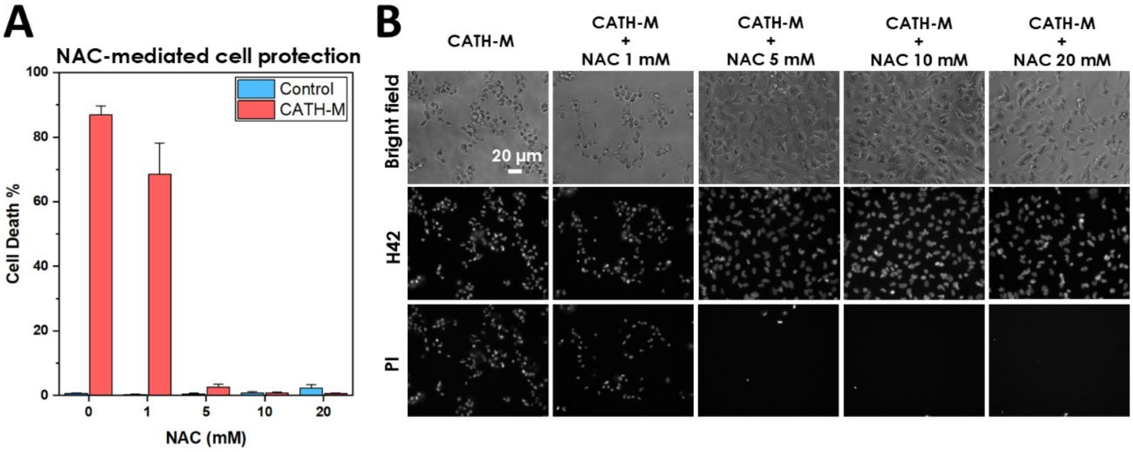

Figure 4.56. NAC modulation of the LN229 cell death. A) The antioxidant N-acetylcysteine shows a clear protective effect against **CATH-M**, being capable to decrease completely the cell death induced by the membrane. **B)** Representative bright field, H42 and PI images of the test.

Based on these results, ROS production by the **CATH-M** and **PYRO-M** was tested, both in the presence and absence of LN229 cells after 24 h of incubation. Whereas **PYRO-M** did not produce detectable ROS, **CATH-M** generated a strong signal, supporting the theory of oxidative cell damage (**Figure 4.57A**). The generation of ROS in culture media was then measured every 20 min for 24 h, while simultaneously adding NAC at concentrations ranging from 1 to 20 mM. The ROS-induced signal profile showed that **CATH-M** acted as a consistent and steady generator of these species, rather than an abrupt burst (**Figure 4.57B**). Additionally, increasing NAC concentrations led to a proportional decrease in ROS levels and cell death, reinforcing the correlation between these parameters.

To compare the cytotoxic effects of **CATH-M** and H_2O_2, LN229 cells were treated with increasing concentrations of H_2O_2, ranging from 0.1 to 2 mM. After 24 h of incubation, it was found that cell death induced by 2 mM H_2O_2 was comparable to that induced by **CATH-M**. This observation could suggest that, whereas the concentration of H_2O_2 and the amount of membrane may not directly correlate, their cytotoxic potential was similar (**Figure 4.57C** and **D**).

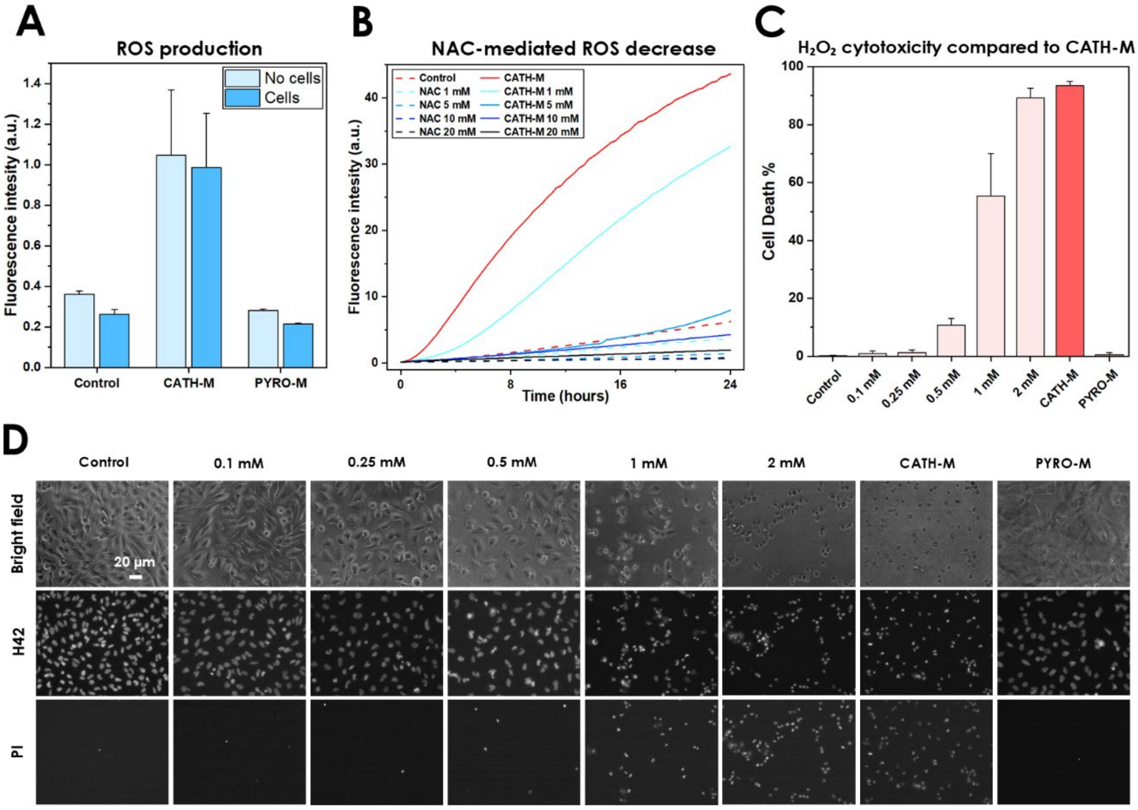

Figure 4.57. CATH-M induces oxidative stress due to reactive oxygen species (ROS) production. A) ROS production of **CATH-M** after 24 h, in presence or not of LN229 cells. **B)** The **CATH-M** ROS generation in the media can be also modulated in base of the concentration of the antioxidant NAC. **C)** Cell death percentage of the LN229 treated with **CATH-M**, **PYRO-M**, and increasing concentrations of hydrogen peroxide. **D)** Representative bright field, H42 and PI images of the experiment. Error bars represent the standard deviation of a data set relative to the mean.

4.2.6.2 ROS capacity and identification

To ascertain the effects of different environments on ROS generation by **CATH-M**, the membrane was incubated in PBS, Dulbecco's modified Eagle's medium (DMEM), and culture media for 1 h in the absence (**Figure 4.58A**) or presence of 2 × 10^4 LN229 cells (**Figure 4.58B**). In both cases, higher ROS production was observed in culture medium, followed by DMEM and

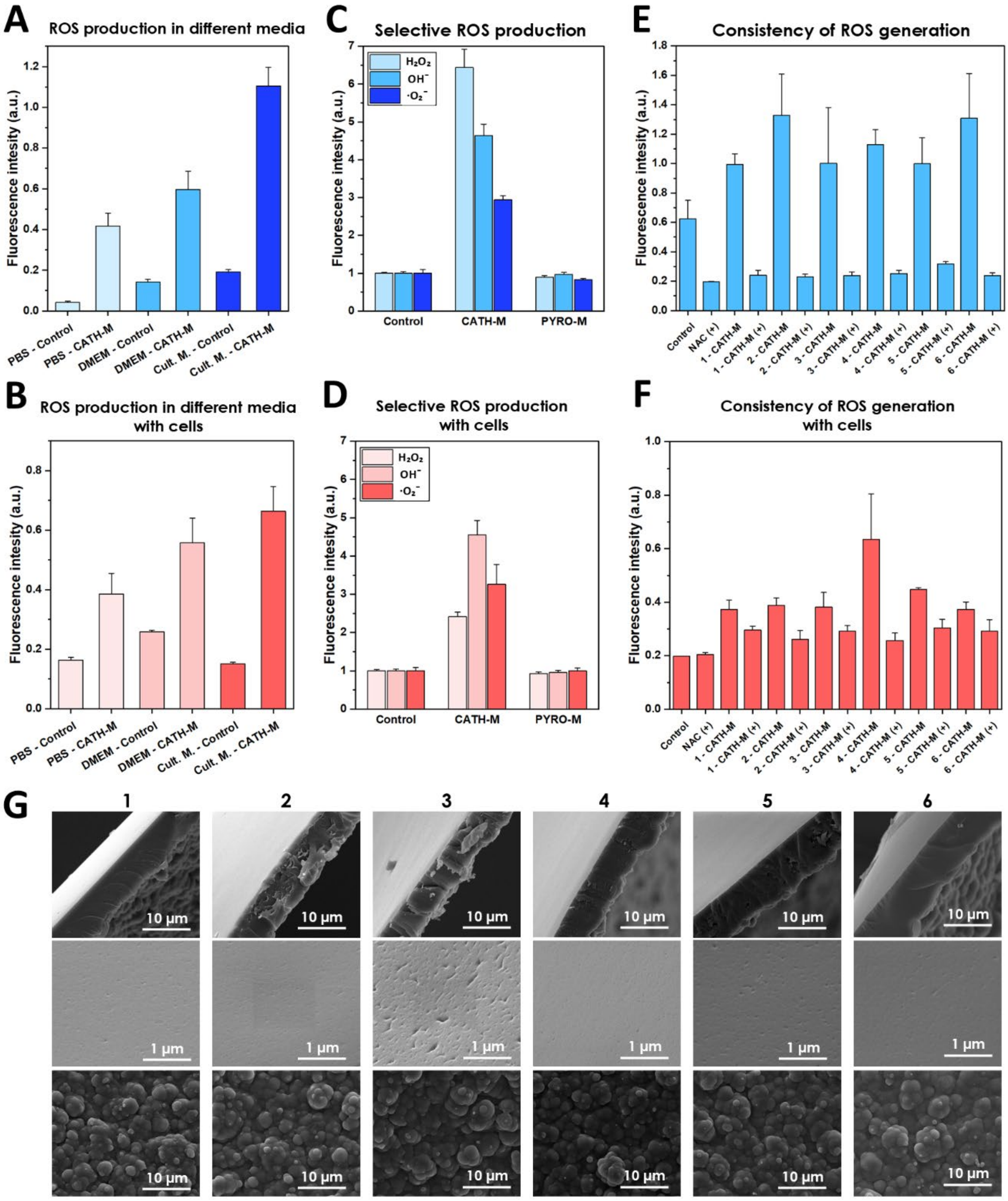

Figure 4.58. CATH-M reactive oxygen species (ROS) production properties. Changes in the ROS production of **CATH-M** between PBS, DMEM, and culture media in **A)** the absence or **B)** the presence of LN229 cells. Selective reactive oxygen species induced by **CATH-M** and **PYRO-M** membrane in **C)** the absence or **D)** the presence of LN229 cells. **E)** Consistency in **CATH-M** ROS generation and NAC inactivation, represented as "(+)" between different synthesis in **E)** the absence or **F)** the presence of LN229 cells, and **G)** the comparison by SEM of the 6 membranes used.

PBS. The signal observed in the absence of cells was slightly higher, which was attributed to be due to the buffering effect of the cells, as they can internalize ROS (particularly H_2O_2) and metabolically counteract its effects.

To identify and quantify the specific ROS species generated by **CATH-M**, three selective kits were used to detect hydrogen peroxide, hydroxyl radicals, and superoxide radicals. After 1 h of incubation with **CATH-M** or **PYRO-M**, both in the absence (**Figure 4.58C**) or presence (**Figure 4.58D**) of 2 × 10^4 LN229 cells, it was found that only **CATH-M** generated significantly higher signals for all three ROS species compared to the control. Interestingly, the presence of cells considerably decreased only the hydrogen peroxide signal (remaining unchanged for the hydroxyl and superoxide radicals), thus indicating that this specie (H_2O_2), which is permeable to the cell membrane, might play a key role in the cytotoxic effect of **CATH-M.**

To assess the robustness and reproducibility of **CATH-M** properties, six different **CATH-M** membranes were studied simultaneously in the absence or presence of 2 × 10^4 LN299 cells, with or without NAC (5 mM). It was observed that the signals achieved by the different membranes, as well as their shifts after NAC-induced inactivation, were strongly homogeneous and consistent, both without (**Figure 4.58E**) and with cells (**Figure 4.58F**). Moreover, SEM analysis revealed that slight topographic differences in these membranes did not affect their ROS generation capacity (**Figure 4.58G**).

Finally, a comparison of the ROS generation was assessed in the seven media used in the previous degradation assay, along with DMEM and fetal bovine serum (FBS). After 1 h of incubation, elevated ROS levels were observed in PBS, DMEM, FBS, pH10 solution, and ethanol (**Figure 4.59A**). However, after 24 h, only pH 10 solution and trypsin (the only media in which **CATH-M** showed signs of degradation) maintained high ROS levels (**Figure 4.59B**).

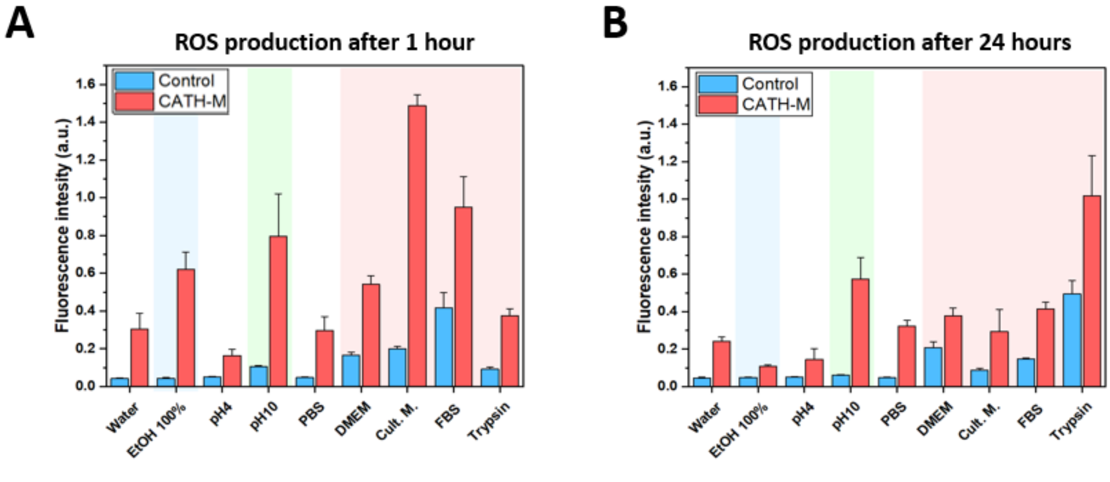

Figure 4.59. Changes in the CATH-M ROS in base of the media. CATH-M ROS production in 9 different media after **A)** 1 h and **B)** 24 h of incubation. Conditions with high signals are represented with a colored background in blue (ethanol), green (ph10 buffer) and red (medias used in cell culture). Error bars represent the standard deviation of a data set relative to the mean.

4.2.6.3 Lipid peroxidation

To shed more light on the oxidative stress and damage mechanism of the plasma membrane, LN229 cells were incubated with **CATH-M** or **PYRO-M** and their lipid peroxidation was monitored by staining it with a dye that changes color from red (reduced state) to green (oxidized state). Control and **PYRO-M** showed a minimal color change, remaining predominantly red. Conversely, **CATH-M**-exposed cells exhibited a clear shift to green, almost completely losing the red color in the plasma membrane (**Figure 4.60**). This data further supports the previously observed ROS production. Moreover, since the ferroptosis-mediated cell death is strictly related with the lipid peroxidation,[27] these results also support the protection previously observed with the ferrostatin-1 and the deferoxamine (strong ferroptosis inhibitors) against the effects of **CATH-M**.

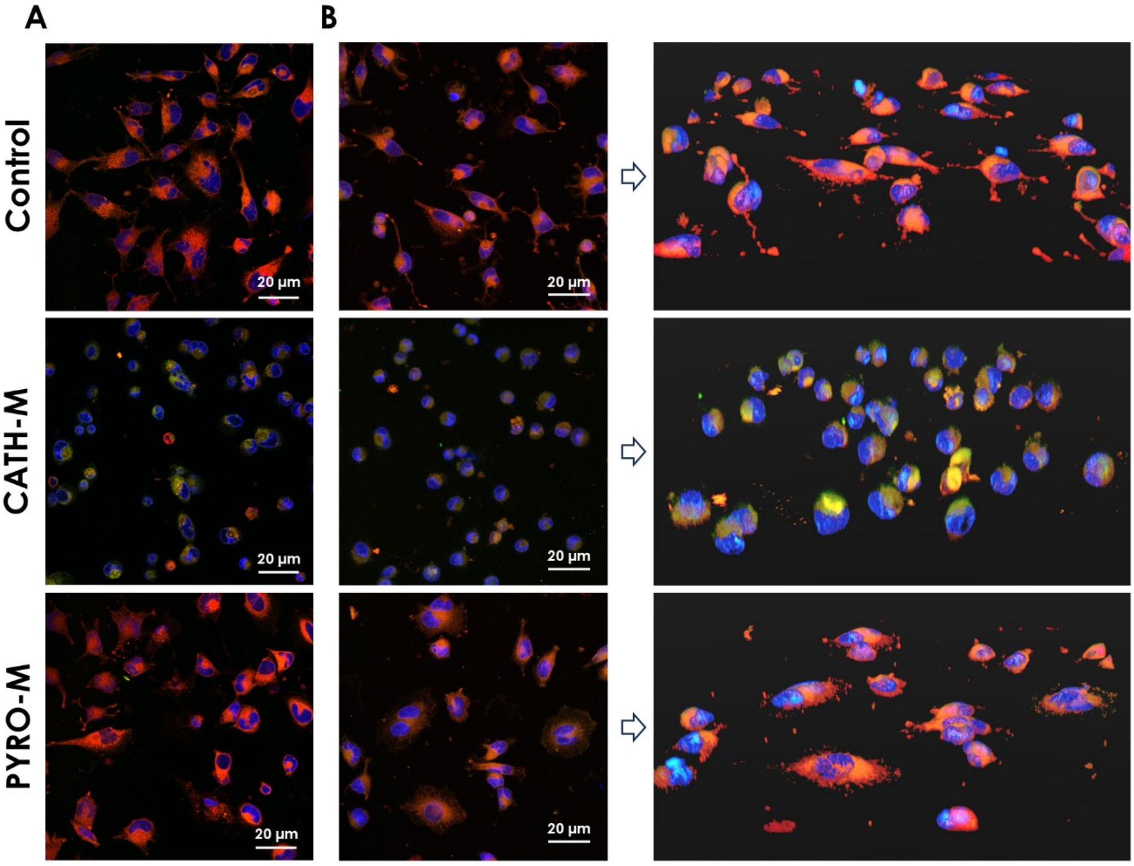

Figure 4.60. Lipid peroxidation. **A**) Confocal images (in a specific plane) showing the lipid peroxidation of the plasmatic membrane induced by **CATH-M** exposure. **B**) Z-stacking the signal obtained in the whole cell. Images in the left and right column are the same but in 2D and 3D view, respectively. The specific plane method is slightly more precise due to the color-shift (oxidation) induced by the long laser exposure of the Z-stacking. Blue = nuclei, RED = dye reduced-state, Green= dye oxidized-state.

4.2.7 Storage and stability of the CATH-M activity

Although **CATH-M** has demonstrated great potential as an effective treatment, preserving its properties over time is essential to ensure its long-term stability, facilitate its practical implementation, and maximize its therapeutic efficacy.

4.2.7.1 Presence of water

Since water is present in all the stages of the me membrane production (synthesis, cleaning and manipulation), the initial storage and transport method selected was under humid conditions. Membranes were transferred to a new container immediately after cleaning, removing the excess water while ensuring a full hydration (standard conditions). In order to determine how these conditions could affect their therapeutic function against tumor cells, two different **CATH-M** membranes were tested against LN229 cells under the standard conditions right after the synthesis. The membranes were then tested again with LN229 cells under the same conditions after being stored for 1, 7 and 30 days. The results indicated that no significant differences were observed between the day of synthesis and one day of storage (**Figure 4.61A**). However, a substantial decrease in the percentage of cell death was detected after 7 days, been even more pronounced after 30 days (**Figure 4.61A**). Despite the abrupt decrease in cytotoxicity observed in both membranes, SEM analysis revealed no noticeable changes in their morphology between the day of synthesis and 30 days after of humid storage (**Figure 4.61B**). These results suggested

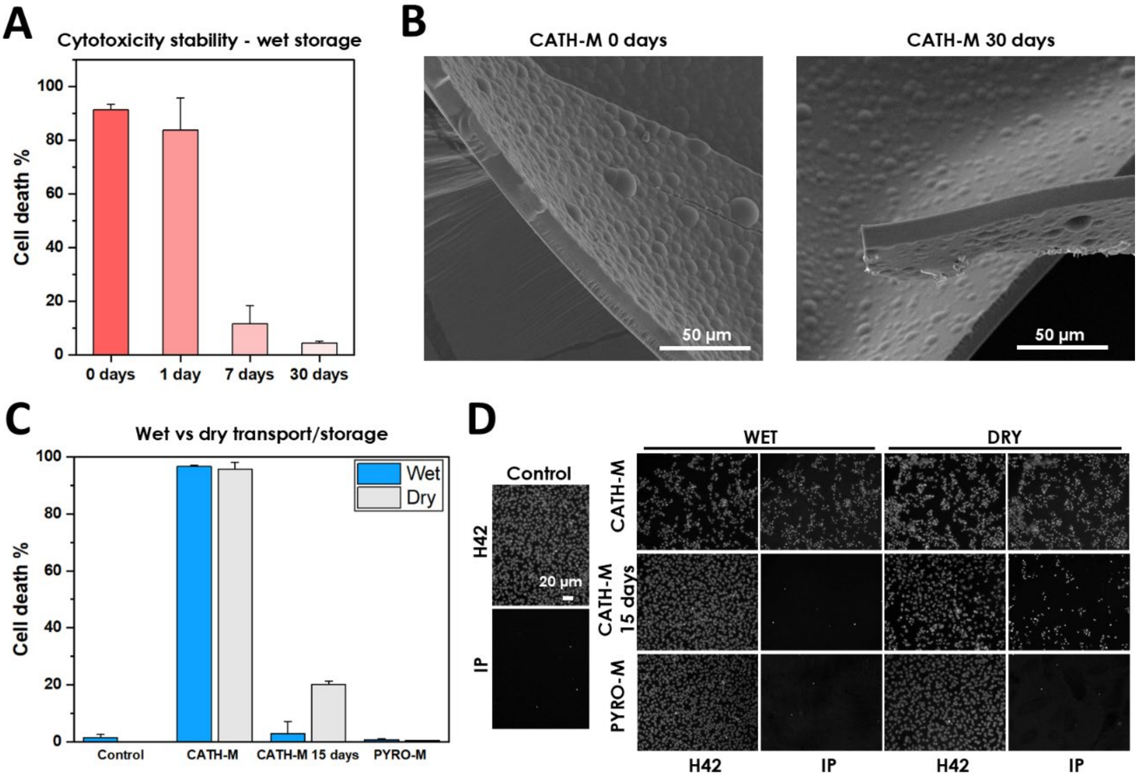

Figure 4.59. Water influence in the CATH-M properties. A) Cell death percentage of the LN229 cells treated with **CATH-M** membranes that were previously divided and stored in humid conditions for 0, 1, 7 and 30 days. **B)** SEM pictures of one of the membranes before and after 30 days of storage, where no apparent change in the structure of the membrane can be observed. **C)** Comparison on the cell death percentage of the LN229 cells when treated with **PYRO-M** and **CATH-M** membranes, which were divided and stored in both humid and dry conditions for 1 hour (transport) and for days (storage). **D)** Representative bright field, H42 and PI images of the experiment. Error bars represent the standard deviation of a data set relative to the mean.

that, since no apparent physical degradation was observed in the membranes after 30 days, the decrease in cytotoxicity could be attributed to the interaction between the material and its surrounding medium (water). Therefore, the membrane may remain in a "reactive state" immediately after synthesis, evolving with time at varying rates, which depend on environmental conditions (ageing process). Based on previous findings, it was proposed that this reactive state primarily affects the exposed functional groups of the polymer, which could play a key role in ROS induction under suitable conditions, such as the presence of water.

To determine whether humidity played a key role in the loss of cytotoxicity, a similar procedure was conducted, but this time with the membranes stored either completely dry or wet for 15 days. As expected, it was observed that the dry membranes exhibited a much slower decrease in cytotoxic potential compared to those stored wet. This suggested that, although the absence of water may not fully preserve the cytotoxic properties of the membrane, it considerably improves its activity lifespan (**Figure 4.61C** and **D**).

4.2.7.2 Presence of light and inert atmosphere

Based on the previous observations, the effects of environmental light and an inert atmosphere were studied. Dry **CATH-M** pieces were stored under both light and dark conditions, as well as in the presence of air (atmospheric composition) or argon (inert gas) for 30 days. Afterwards, the membranes were tested against the LN229 cells. Interestingly, it was observed that membranes stored in darkness or under argon conditions exhibited higher cell death, especially when both conditions were present simultaneously (**Figure 4.62A** and **B**). The ROS generation of these membranes was also measured. The results obtained mirrored the cell death profile, exhibiting higher signal in the cases of darkness and argon storage (**Figure 4.62C**). These results suggested that whereas **CATH-M** may be photosensitive, the presence of oxygen could also trigger reactions in the material, resulting in a reduced ROS induction capacity (which is closely linked to the cytotoxicity of the membrane). Photosensitivity and self-oxidation observed in the presence of oxygen align with the natural properties of catechols and polyphenols, as mentioned in Chapter 1.

Although more studies are necessary to understand how to extend and preserve the properties of the **CATH-M** membrane, these findings lay the groundwork for future studies.

4.2.8 Evaluation of protein profile alteration induced by CATH-M

After performing a thorough physicochemical and biological characterization, the alteration in the protein profile induced by **CATH-M** was assessed. The evaluating of shifts in protein production is crucial to understand how cells respond to the presence of a new material intended for medical applications. This helps to ensure biocompatibility, minimize immune responses, and identify potential interactions with a biological system. Therefore, by understanding these interaction patterns, it is possible to predict the material's behavior in the body. and further validate the previously obtained information.

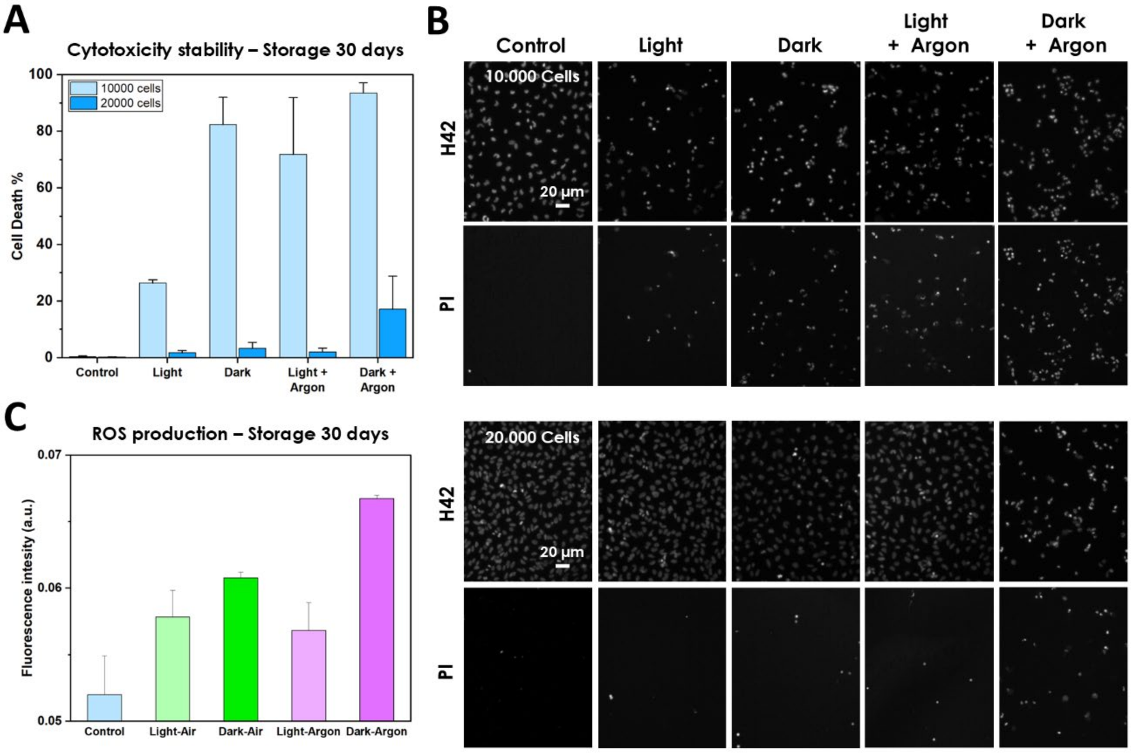

Figure 4.62. Light and oxygen exposure effects in the CATH-M properties. A) Cell death percentage of the LN229 cells treated with a **CATH-M** membrane that was divided and stored for 30 days in dry conditions, with/without light exposure and with/without an inert atmosphere (argon). **B)** Representative bright field, H42 and PI images of the experiment. **C)** ROS production of the **CATH-M** pieces stored in each condition. Error bars represent the standard deviation of a data set relative to the mean.

4.2.8.1 Protein arrays

To investigate the impact of **CATH-M**-induced cell death on human protein expression, a comprehensive proteomic analysis was conducted in both the supernatant (proteins excreted into the media) and the cell lysate (proteins inside the cell). The analysis of the supernatant revealed that cells exposed to **CATH-M** did not express proteins that were absent under healthy conditions. However, **CATH-M** exposure led to a reduction in the expression of several proteins involved in angiogenesis, including osteopontin, PDGF-AA, and serpin E1 (**Figure 4.63A-D**). Conversely, proteins associated with cell survival under normal conditions were upregulated. The analysis of intracellular lysates from **CATH-M**-exposed cells mirrored the general pattern observed in the supernatants, thus indicating that the membrane did not induce the expression of new proteins not previously expressed in healthy cells. Overall, **CATH-M**-treated cells displayed a lower protein expression, with an upregulation in some cases pre-existing proteins involved in survival. This was demonstrated by the protein arrays for cytokines (**Figure 4.63A-D**), proteases (**Figure 4.63E-H**), chemokines (**Figure 4.64A-D**), ubiquitin-involved proteins, and phospho-immunoreceptors.

Notably, protein expression in the ubiquitin array was the most prominent (**Figure 4.64E** and **F**), whereas no signals were detected in the phospho-immunoreceptor array for either the control or **CATH-M** groups. (**Figure 4.64G**).

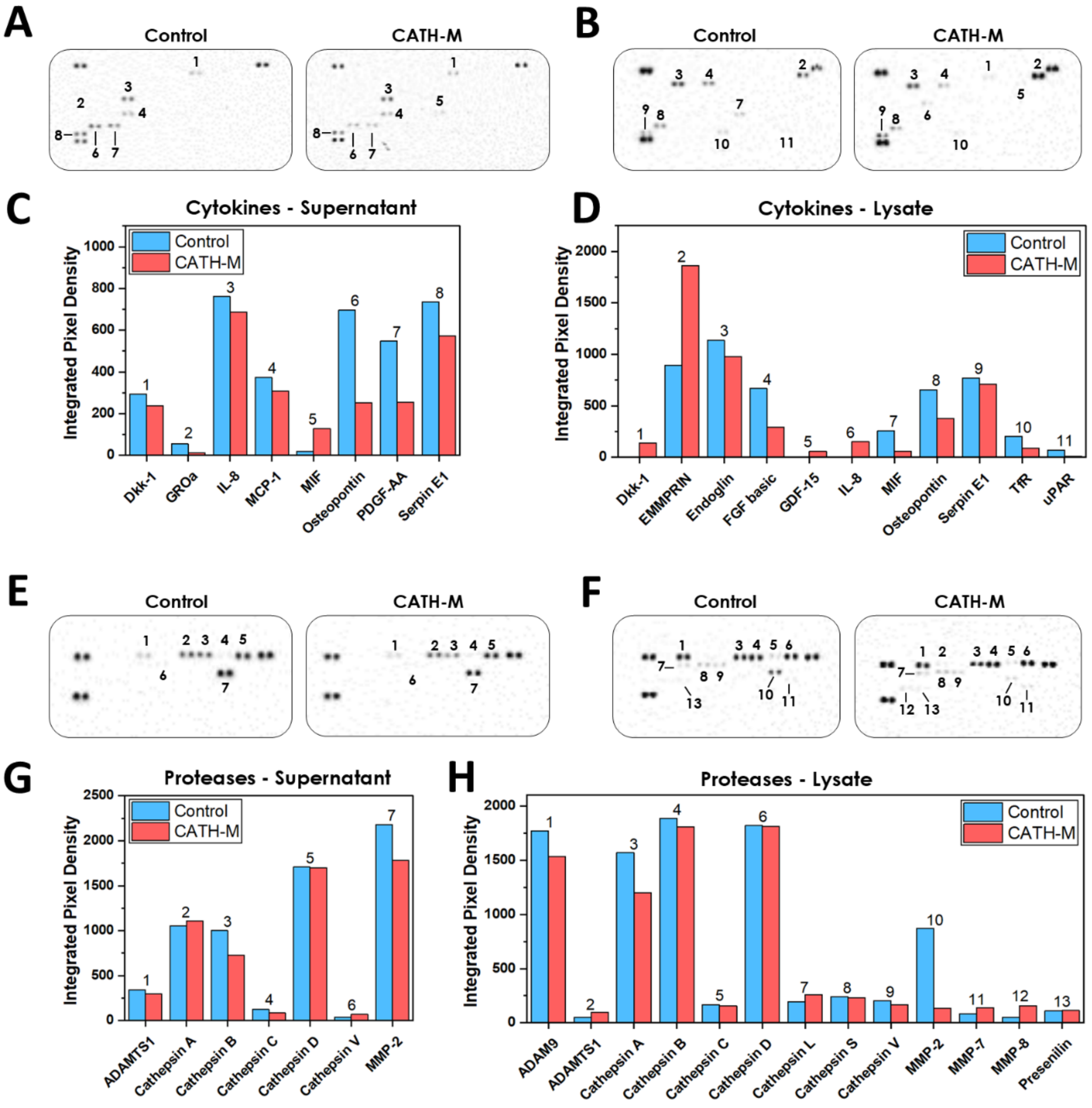

Figure 4.63. LN229 cytokines and proteases protein microarrays. A) Comparison of the cytokine signals from the LN229 supernatant and **B)** lysate arrays in both control and **CATH-M**-treated conditions. **C)** Quantification of each spot pair for the cytokines supernatant and the **D)** lysate. **E)** Similarly in the case of the protease signals from the LN229 supernatant and **F)** lysate arrays. **G)** Quantification of each spot pair for the protease supernatant and the **H)** lysate. Numbers above the columns represents the mean signal obtained in each spot pair of the array for both conditions.

4.2.8.2 Proteomic analysis

Exposure of LN229 cells to the **CATH-M** membrane induced a series of responses compared to their respective controls, leading to a down/upregulation of different genes (**Figure 4.65A**). These differentially expressed genes are involved in different biological processes, as categorized by Gene Ontology (GO) analysis (**Figure 4.65B**). Notably, a downregulation of proteins involved in folding (GO:0006457), stress response (GO:1990120), and quality control mechanisms

(GO:1901564) was observed. Additionally, a reduction in the cellular capacity to respond to oxidative stress (GO:0034599, GO:1901564) was noticed, along with a diminished protection against metabolic byproducts such as methylglyoxal (GO:0009438). Proteins encoded by genes essential for mitochondrial energy production and metabolic processes were also downregulated (GO:0006091, GO:1901564). Among all these findings, the downregulation of the protein encoded by the Frataxin (FXN) gene was particularly notable (**Figure 4.65B**). This gene participates in the regulation of iron levels in the mitochondria, preventing iron overload. Frataxin is also essential for the biosynthesis of iron-sulphur clusters, which are important cofactors for various mitochondrial enzymes involved in metabolism and respiration. By regulating iron levels and contributing to iron-sulphur cluster assembly, Frataxin helps to protect cells from oxidative damage.

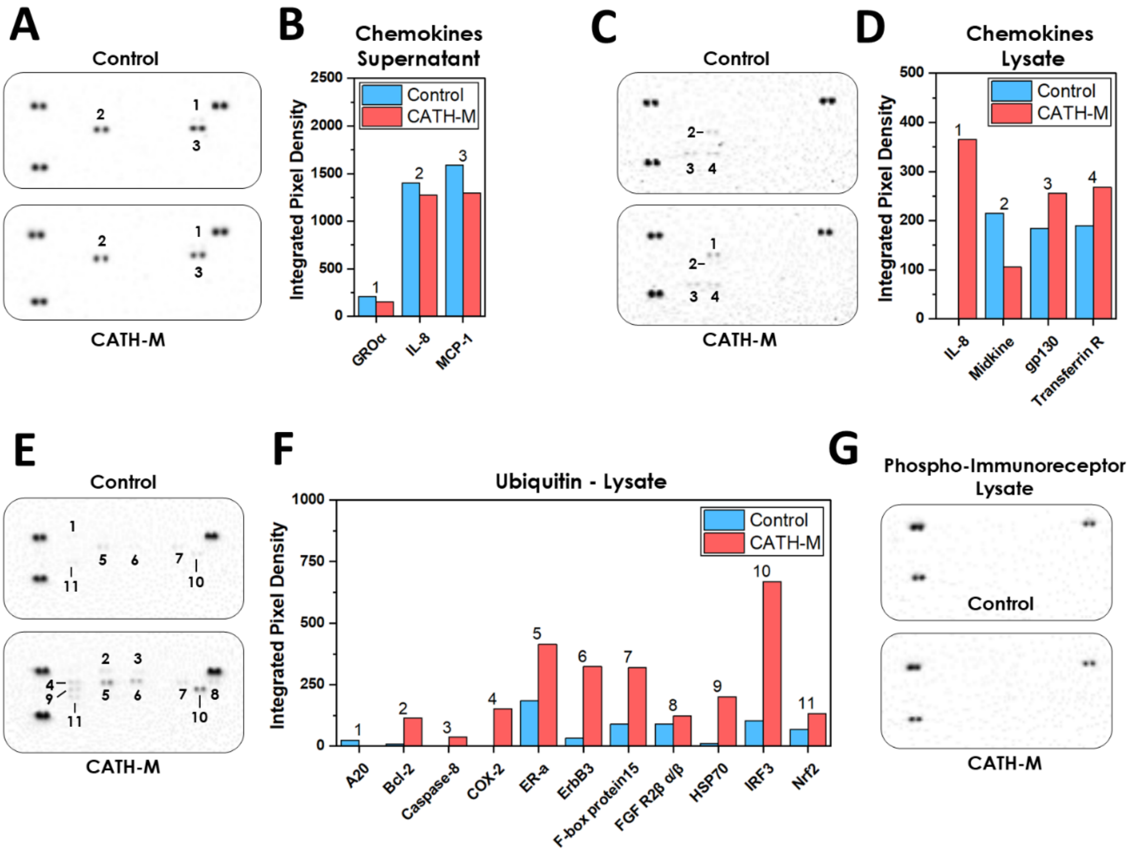

Figure 4.64. LN229 chemokines, ubiquitin, and phospho-immunoreceptor protein microarrays. A) Comparison of the chemokine signals from the LN229 supernatant and **B)** quantification of each spot pair. **C)** Signal obtained in the case of the chemokines lysate and **D)** its quantification. **E)** Singal achieved in the ubiquitin lysate array and **F)** its quantification. **G)** No signal, besides the controls, were obtained in the phospho-immunoreceptor array. Numbers above the columns represents the mean signal obtained in every spot pair in the array for both conditions.

On the other hand, an upregulation of the proteins involved in cytoskeleton regulation, lamellipodia formation, cell adhesion, migration and extracellular matrix formation, and remodeling was observed (GO:1902905, GO:0099159, GO:0034330, GO:0030155, GO:0110020, respectively). An increase of the proteins related to changes in cellular state in response to the presence of oxygen-containing compounds was also identified (GO:1901700). Additionally, proteins related with the glutamine process (GO: 0006541) were found to be upregulated. Nevertheless, their role as energy or intermediate metabolites providers for the tricarboxylic acid cycle, nucleotide, and amino acid biosynthesis, or contributing to redox homeostasis cannot be elucidated from this analysis. Finally, other upregulated proteins involved in membrane and vesicle trafficking, nuclear transport, protein sorting, and endocytosis, categorized under the intracellular transport (GO:0046907), were also identified. Among the upregulated proteins, the one encoded by ROCK2 was prominent (**Figure 4.65A**). ROCK2 regulates actin cytoskeleton dynamics, promoting actin filament stabilization and cell contractility, thereby affecting cell shape, migration, and morphology.

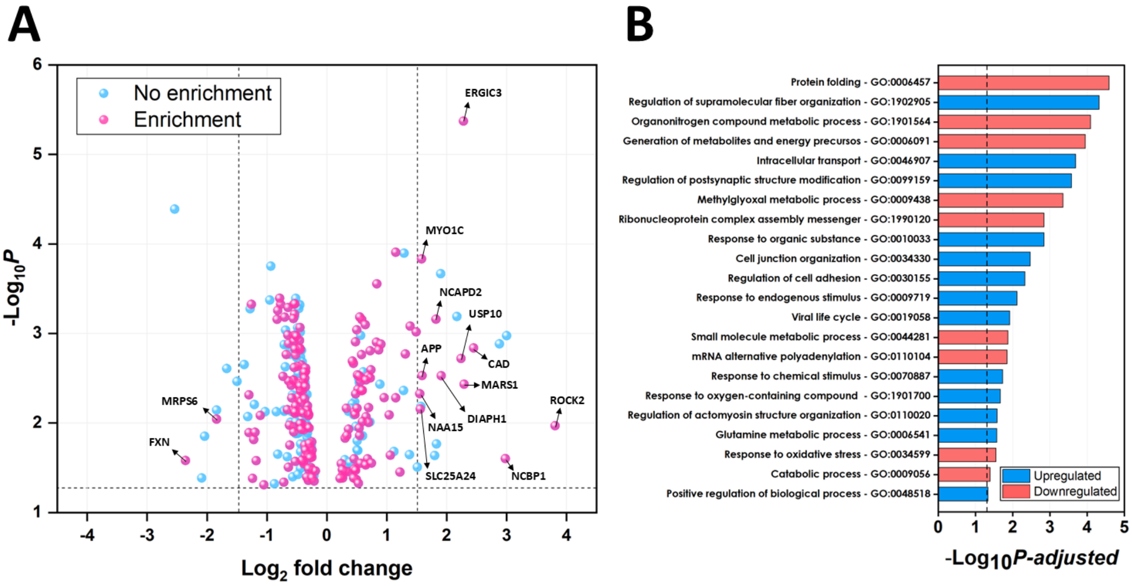

Figure 4.65. Alterations in the protein profile after CATH-M exposure. A) Volcano representation of the proteomic analysis results, showing the downregulated and upregulated genes after LN229 exposure to **CATH-M**. Horizontal dashed lines represent a *P* value = 0.05. Blue and pink dots represent the genes observed before and after performing and enrichment analysis. **B)** The different upregulated (blue) and downregulated (red) Biological Processes of the LN229 cells after being exposed to **CATH-M**, showing their gen-ontology (GO) number and their *P-adjusted* value. Horizontal and vertical dashed lines represent a *P-adjusted* value = 0.05 and fold change = 1.5, respectively.

4.3 Conclusions

i. A series of catechol-amine membranes were synthesized and optimized to ensure mechanical manipulability. The HMDA-based membranes were identified as the most robust, with **PYRO-M** and **CATH-M** being the best performing.

ii. The developed membranes follow a simple one-step and scalable synthesis under mild conditions, using affordable materials and green chemistry-based methodologies.

iii. **CATH-M** was the only HMDA-based membrane exhibiting cytotoxic properties against various Glioblastoma and organ-derived cancer cell lines. Additionally, it demonstrated remarkable antibacterial activity.

iv. This membrane was found to enhance the *in vitro* standard-of-care treatments for Glioblastoma, which consisted in temozolomide and radiation.

v. The cell death mechanism induced by **CATH-M** was determined to be oxidative stress-mediated necrosis, driven by a sustained ROS production, with hydrogen peroxide playing a key role.

vi. Cells exposed to **CATH-M** exhibited severe morphological damage, including disruption of the cell membrane and mitochondria, as well as cytoplasmic loss.

vii. The membranes demonstrated exceptional cell adhesion properties. Furthermore, **CATH-M**, in particular, was capable of modulating cell migration.

viii. Proteomic analysis supported the characteristics observed in **CATH-M** during individual experiments conducted in this Chapter, further validating its biological effects.

4.4 Future work

After an in-depth biological and physicochemical characterization, the promising obtained results support advancing to the *in vivo* stage. To ensure the relevance and applicability of these results, a new model is being developed in collaboration with Hospital de Bellvitge. This model, based on Patient-Derived Orthotopic Xenografts, will be designed to accurately reflect the real process of tumor resection. Additionally, it will allow for the establishment of clinical protocols for the first implementation of therapeutic catechol-based membranes. The model's specificity for this methodology (tumor extraction and local treatment) ensures that the findings will be relevant and directly applicable to real-world scenarios. By bridging the gap between experimental studies and clinical applications, this collaboration aims to pave the way for innovative treatments that could revolutionize medical practices and significantly improve patient outcomes.

Regarding the potential degradability of the **CATH-M**, further experiments should be conducted under conditions that mimic physiological parameters. In particular, investigating the role of macrophages and microglia, along with proteases, may provide valuable insights into the biodegradability of these membranes. Additionally, the selected amines not only influence the mechanical properties of the membranes, but also affects their potential degradability. For instance, the incorporation of cystamine (CYS), which contains a disulfide bridge commonly found in proteins, may facilitate the degradation process by enhancing the susceptibility of the membranes to proteolytic activity and phagocytic cell interactions.

Regarding chirality-related cytotoxicity, although the obtained results indicated no observable differences in cytotoxicity between stereoisomers, the possibility of specific recognition between a receptor and a chiral center within the membrane should not be ruled out.

After the extensive biological characterization conducted in this chapter, the results obtained represent a foundation for a deeper understanding of the effects of **CATH-M** on metabolism. In this sense, incorporating a more biochemical approach and methodologies will be essential to further elucidate its underlying mechanisms.

4.5 Experimental section

All reagents, solvents, and kits were purchased and used without further purification from Sigma-Aldrich (Merck, Madrid, Spain) unless otherwise specified. Type 1 ultrapure water from in-house Milli-Q® filtration systems (Millipore, Burlington, MA) was used in all experiments, unless otherwise specified.

Synthesis of the optimized HMDA-based membranes. The synthesis of the membranes was performed after combining hexamethylenediamine (HMDA or -M) with different catechol derivatives: pyrocatechol (PYRO), caffeic acid (CAFF), pyrogallol (GALL), dopamine (DOPI), 4-methylcatechol (4MET), or catechin (CATH), following the proportions (mM): **PYRO-M** (50–75), **CAFF-M** (75–150), **GALL-M** (100-200), **DOPI-M** (50-125), **4MET-M** (100-150) and **CATH-M** (50-125). The selected catechol derivative and its corresponding amount of HMDA were weighted separately and dissolved in a final volume of 50 ml of water. Both reagents were mixed and poured in a sterile 15 cm diameter polypropylene Petri dish. In the case of **CATH-M** film, CATH was dissolved in 45 ml of sterile water, sonicated, and heated. An autoclave-sterilized 15 cm glass dish was used for the membrane synthesis. The oxygenation of the reaction was regulated by opening holes in the corresponding lids: parafilm sealing and 1 hole in the plastic lid (**PYRO-M**, **CAFF-M**, **GALL-M** and **4MET-M**), parafilm sealing and 4 holes in the plastic lid (**DOPI-M**), or no parafilm with a hole in the lid (**CATH-M**). The synthesis was performed for 48 h at 25 ºC. The membranes were obtained at the air/water interface. Afterwards, the membranes were removed from their plates, washed three times with 15 ml of sterile water (until water was clean), and stored in 10 cm sterile Petri dish until use. In each case, membranes were washed and cut to the final size inside 15 ml phosphate buffered saline (PBS) or saline solution (NaCl 0.9%)

right before exposing them to cells or bacteria, respectively. All procedures were performed under biosafety level 2 laminar flow cabins to ensure sterile conditions.

Fourier transformed Infrared (FTIR). Surface FTIR experiments have been performed with the Hyperion 2000 FTIR microspectrometer (Bruker Optik GmbH, Ettlingen, Germany) in reflection mode, equipped with a nitrogen-cooled mercury cadmium telluride (MCT) detector (InfraRed Associates, Inc., Stuart, FL, USA), using a 15 × reflection objective, a gold mirror as a reference and scanning for 30 min with a resolution of 4 cm^{-1}. The membranes were attached on a gold substrate. All the data was treated with OPUS version 7.0 (Bruker) and OriginPro (version 8.0988, OriginLab Corporation, Northampton, MA, USA) software.

X-ray photoelectron spectroscopy (XPS). XPS measurements were performed with a Phoibos 150 analyzer (SPECS EAS10P GmbH, Berlin, Germany) in ultra-high vacuum conditions (based pressure 10^{-10} mbar, residual pressure around 10^{-7} mbar). Monochromatic Al Kα line was used as X-ray source (1486.6 eV and 300 W). The electron energy analyzer was operated with pass energy of 50 eV. The hemispherical analyzer was located perpendicular to the sample surface. The data was collected every eV with a dwell time of 0.5 s. A flood gun of electrons, with energy lower than 20 eV, was used to compensate the charge. The reference was set for C-C at 284.8 eV All the data was treated with CasaXPS version 2.3.17PR1.1 (Casa Software LTD, Teignmouth, UK)[59] and OriginPro software.

Elemental analysis. The membrane composition was determined through elemental analysis conducted by the services at the Parque Científico Tecnológico of the Universidad de Burgos, using an EA Flash 2000 with a TCD detector and a Mettler Toledo XP6 microbalance. Carbon, hydrogen, oxygen and nitrogen molar percentages were acquired for each HMDA-based membrane. Results were expressed as the mean ± standard deviation from 3 different membranes (N=3).

Vibrational Circular Dichroism (VCD). The chirality measurements were performed out using a PMA50 module coupled to a Tensor 27 FTIR spectrometer (both from Bruker), equipped with a PEM-100 Controller photoelastic modulator (HINDS Instruments), an SR830 DSP lock-in amplifier (Stanford Research Systems) and a nitrogen cooled MCT detector. The spectra were obtained with a resolution of 4 cm^{-1} and a spectral accumulation time of 1 hour. The signal in the analyzed range (800-1800 cm^{-1}) was optimized using a cut-off filter at 1800 cm^{-1}. The obtained interferograms were converted into spectra using a macro implemented in the measurement software itself, OPUS 7.0.

Degradation test. The stability of the **CATH-M** and **PYRO-M** membranes was evaluated in water, ethanol 100%, pH 4 solution (HCl/sodium acetate), pH 10 solution (Na_2CO_3/$NaHCO_3$), PBS, cell culture media (see next section) or trypsin (Gibco 25200072). Five ml of each solution were added to sterile 20 ml glass vials containing 2 discs of **CATH-M** or **PYRO-M** membranes. The degradation tests were performed at 37ºC for 1, 2, 3, 4 and 8 months. After each time point, the membranes were removed, washed in water and further characterized by SEM.

Scanning electron microscopy (SEM). The morphology and thickness of the membranes was determined by scanning electron microscopy (SEM, FEI Quanta 650 FEG, Thermo Fisher Scientific, Eindhoven, The Netherlands) in secondary electron mode with a beam voltage of 10 kV. Samples were coated with a 5 nm layer of gold/palladium 60/40 layer (Emitech K550X Sputter Coater) before the observation. In the case of membranes and substrates containing cells, after fixation with 2% paraformaldehyde (PFA) in PBS for 1 h, samples were dehydrated through ethanol serial dilution series until 100 %. Afterwards, samples were dried under cabin airflow and coated with a 5 nm layer of gold/palladium.

Sample preparation for TEM. Initially 3 x 10^6 LN229 cells were homogenously seeded in a 100 mm Petri dish in a final volume of 10 ml of culture media. After 24 h incubation at 37ºC, media was changed for 12 ml of fresh culture media and an 8 cm diameter disc of **CATH-M**, **PYRO-M** was introduced in the Petri dish, or not (control). After 8-10 h incubation, membranes were carefully removed and media removed. After following the trypsinization protocol, a cell pellet was obtained and fixed with glutaraldehyde 2.5% and PFA 2% in PBS for 1 hour, after what the solution was changed for a fresh one to ensure the fixation. Then, Sample Preparation Service of *Universitat Autònoma de Barcelona* Microscopy Unit obtained microtomes for each condition. Finally, samples were observed by TEM (Hitachi H-7000 with CCD GATAN ES500W Camera).

Cell culture. Glioblastoma cell lines were routinely cultured and maintained in 100 mm cell culture dishes (Falcon™ 353003, Fisher Scientific), using 10 ml of Dulbecco's modified Eagle's medium (DMEM), supplemented with 100 µg/ml streptomycin, 100 U/ml penicillin, and 10 % heat-inactivated fetal bovine serum (FBS) (Invitrogen), from now on culture media. Cells were incubated at 37 ºC in a saturating humidity atmosphere composed of 95% air and 5% CO_2 (Fisherbrand™ CO_2 Incubator Isotemp™). After achieving 85–90% of confluence, cells were rinsed with PBS (100 mM, pH 7.4) and incubated at 37 ºC for 3 min with 0.05% trypsin-EDTA (Trypsin) until dissociated. Afterwards, culture media was added to neutralize trypsin and the resulting suspension was centrifuged at 200 g for 5 min. Finally, the pellet was resuspended in CM and, unless otherwise indicated, the cell density was adequately adjusted to conduct each experiment. The LN229 huma Glioblastoma-derived cells (ATCC CRL-2611, 2010) were tested during entire study. Besides, four commercial cell lines (LN18 (ATCC CRL-2610, 2010)), A172 (ATCC CRL-1620, 2010), U87-MG (ATCC HTB-14, 2010) and U251-MG (ECACC 09063001, 2013)), two primary cultures (MSO4 and MSO7) and rat primary cortical astrocytes and neurons were used during specific tests, as representative tumoral and healthy nervous system cells. In the case of the neurons, 24 hours before seeding them, plates were treated with 25 µM/ml polylysine Moreover, A549 (ATCC CCL-185, 2015), PANC-1 (ATCC CRL-1469, 2015), CACO-2 (ATCC HTB-37, 2024), SAOS-2 (ATCC HTB-85, 2007) and HELA (ATCC CCL-2, 2012), were selected as representative tumoral cell lines for lungs, pancreas, colorectal, bone and cervical cancer, respectively. All procedures were performed in a biosafety level 2 laminar flow cabins in sterile conditions. These procedures adhered strictly to the specific approved protocols established by the Ethical and Biosafety Committee of the *Universitat Autònoma de Barcelona*, as well as governmental authorities (protocol numbers: A/ES/20/I-40 and A/ES/20/86).

Cell viability. A double staining was used to evaluate the cytotoxic effect of the treatments performed in a 96-well plate (Falcon™ 353072, Fisher Scientific). Initially, a specific cell density was seeded in a 96-well plate, followed by a 24 hours incubation. Then, media was changed for 100 µl of fresh culture media and followed by the introduction in each well of a 6 mm diameter disc of the desired membrane, not taking into consideration the disposition of the faces of the membranes (Janus property) unless it was the case of the **CATH-M**, which water-face was always set pointing to the cells. This was performed due the nature of the membrane, which is prone to bend itself towards the water face, achieving a better reproducibility of the test and decreasing observation problems (cell/membrane planes superposition) when this methodology was followed (being irrelevant in the case of the other five membranes). After the materials were set, 50 µl of media were removed in order to decrease their distance and the cells. Following to the desired incubation time of the cells and the membranes, 50 µl more of culture media with Propidium Iodide (PI, 1µg/ml) and Hoechst 33342 (H42, 2 µg/ml) were added to each well without removing the membranes (unless otherwise specified). Then, plates were incubated at room temperature protected from light for 30 min. H42 can pass through intact cell membranes, but PI can only enter cells that have suffered membrane damage. Finally, samples were examined under a Nikon ECLIPSE TE2000-E microscope, equipped with epifluorescence optics for visualizing fluorescent signals and a Hamamatsu ORCA-ER photographic camera for capturing high-quality images. Images were collected for each dye and bright field at various locations for each experimental condition. Cell death percentage was quantified as the percentage of cells with damaged membranes (PI-positive) relative to the total number of cells (H42-positive). In the case of the cytotoxic effect of the reagents, the cells were treated for 24 hours with an increasing concentration of each of the six catechol derivates or HMDA in 50 µl of PBS (from 0.025 to 10 mM). The tolerance was determined as the concentration in which the cells shown no morphological differences when compared with the control (N=2).

Clonogenic assay. LN-229 cells were seeded at an initial density of 2.5×10^5 cells/well in 9 of 12 wells within a 12-well plate (Falcon 353003™, Fisher Scientific) using a total volume of 1 mL of culture media. After a 24-hour incubation period at 37°C, the media was replaced with 0.75 ml of fresh culture media, and 21 mm diameter discs cut from either the **CATH-M** or **PYRO-M** membrane were carefully introduced into each well, with control wells receiving no membrane (Treatment control). Additionally, 1.0 x 10^3 LN229 cells were seeded in the remaining three empty wells to serve as a long-period growth control. Membranes and cells were incubated for an additional 24 h. Subsequently, the membranes were removed, each well was washed with PBS, and crystal violet staining was performed in one plate to represent day 0 (T0). In the remaining four plates, after membrane removal and media removal, 1 ml of filtered conditioned medium (50% fresh medium and 50% medium from a confluent LN229 plate) was added to each well. The culture medium was refreshed weekly with fresh medium, and cell growth was monitored until day 20 (T20). At the end of the experiment, all four plates were stained with crystal violet. A total of three replicates were performed for each condition at T0, while twelve replicates were performed for each condition at T20. To perform the crystal violet staining, culture media was removed from the well, followed by a washing step with PBS. Then, 100% methanol at -20ºC was added to each well, and the plate was incubated at -20ºC for 10 min. Afterwards, the methanol was removed, and crystal violet solution (0.5 g in 100 ml of 25% methanol) was added to the wells, where it remained for 10 min. Finally, the dye was removed, washing the plate generously with distillate water to eliminate the unattached colorant. The plate was then allowed to dry completely before imaging the results. To quantify the amount of dye retained in each well (T20), 1 mL of 15% acetic acid in PBS was added to dissolve the dye, and the absorbance of the 10^{-1} dilution was measured at 595 nm using a Varioskan™ LUX microplate reader (Thermo Scientific™).

Isolation and culture of cortical astrocytes form rat. Primary cultures of cortical astrocytes were prepared from 1-day-old Sprague–Dawley rats following the protocol described previously.[60] Cells were plated into 10 mm dishes containing a coverslip at a density of 0.3 × 10^6 viable cells/ml in DMEM supplemented with 10% FBS, 50 units/ml penicillin and 50 µg/ml streptomycin. The cultures were incubated at 37 °C in a humidified atmosphere of 5% CO_2/95% air and used at 21 days *in vitro*.

Isolation and culture of cortical neurons form rat. Primary cultures of cortical astrocytes were obtained from the Laboratori de Cultius Neuronals Inc-UAB. Poly-ᴅ-Lysine at 50 µg/ml in distillated water was added in the plates 24 h before seeding the cell. Cortical neurons were seeded at a density of 0.3 × 10^6 viable cells/ml in DMEM supplemented with 10% FBS, 50 units/ml penicillin and 50 µg/ml streptomycin in a 96-well plate. The cultures were incubated at 37 °C in a humidified atmosphere of 5% CO2/95% air and used at 7 days *in vitro.*

Glioblastoma spheroids. From a LN229 cell suspension, 3 x 10^6 cells were homogenously seeded in a 100 mm non-treated Petri dish in a final volume of 12 ml of culture media, changing it every

5 days. After reaching a desired spheroid size, the plate was gently hit to detach them. Then, the suspension containing the spheroids was carefully recollected, letting them precipitate for 5 min and removing unnecessary supernatant. Previously obtained LN229 spheroids with an approximated size of 80-100 µm were used. In four 12-well plate, 1 ml of culture media was added to each well, as well as **CATH-M** or **PYRO-M** membrane, a circular 21 mm glass coverslip (SEM Control), or nothing (Control), having in each plate N=3 for each condition. Subsequently, 20-40 spheroids/well were seeded and kept incubating for 1 h and 1, 3 and 7 days (each time corresponding to a specific 12-plate). Bright field images were obtained in each incubation time, followed by a PFA 2% fixation for 1 h. **CATH-M** and **PYRO-M** membranes, as well as glass coverslip containing fixed spheroids were observed by SEM.

Cell Migration. To determine the influence of the membranes in the migration of the cells, 8 µm pore diameter inserts were used (Falcon® 353097™, Fisher Scientific). The correlation between migration, H_2O_2 production and survivability was assessed. First, for migration, a 24 well plate (Falcon® 353047™, Fisher Scientific) was filled with 800 µl of culture media, then no discs (control), 5 discs of 1, 2, 4 or 6 mm diameter of **CATH-M**, or 5 discs of 6 mm diameter of **PYRO-M** were added and remained incubating at 37º for 6 h, in order to start the test with an considerable difference of stimulus between both chambers produced due the leaking effect of the membrane. Subsequently, the insert was introduced in the well (containing or not membranes) and seeding 200 µl of culture media with 4 x 10^4 cells over the inserts. After incubating for 16 h at 37ºC (which was empirically determined to be the ideal incubation time to observe differences in migration), the cells that migrated to the lower face of the insert were quantified. To achieve that, cells were fixed with PFA at 4% final for 1 h, followed by the removal of the attached cells in the upper part of the insert (non-migrated cells) with a cotton swab. Afterwards, inserts were generously washed, stained with H42 in PBS and observed by fluorescence microscopy the remaining cells in the lower face of the insert (migrated cells). Three independent tests, with N=3 each one, were performed. The H_2O_2 production in the lower chamber was measured after the 16 h of incubation with the inserts and the membranes using the kit of OxiVision™ Green hydrogen peroxide sensor (see next section). Finally, to determine the survivability, after the 16 h of incubation with the inserts and the membranes, culture media with H42 and PI was added to both sides of the insert, incubated at room temperature for 30 min to then determine the cell death percentage off all the cells in the inserts, migrated plus non-migrated (N=3). Right after, cells were fixed with PFA 2% in PBS for 1 hour. Then, the insert's membranes containing the cells were removed, prepared and observed by SEM both the upper and lower face.

Cell Adhesion. In a 96 well plate, 100 µl/well of culture media were added, inserting a **CATH-M** or **PYRO-M** membrane, or not (control). Subsequently, 100 µl with 4 x 10^4 LN229 cells were seeded in each well. After 3 h incubation at 37ºC, media was carefully aspirated and 200 µl of 1/5 of Trypsin in PBS were added and subsequently incubated for 30 min. Then, the plate was consistently hit to detach the affected cells, moving the supernatant to a new well (detached cells) and the membranes to another one (still attached cells). Besides, 100 µl of culture media with H42 (2 µg/ml final) were added to both cases to neutralize the Trypsin and to visualize the cells by fluorescence (N=4).

Mitochondrial Function. The alteration of the oxygen consumption rate (OCR) after exposing **CATH-M** membrane to LN229 cell line was performed with the Seahorse XF Cell Mito Stress Test Kit (Agilent). Firstly, 1.3 x 10^4 cells were seeded in a final volume of 100 µl of culture media in 6 wells of an 8-well seahorse plate (XF HS miniplate 103725-100), while 100 µl without cells in the remaining 2 wells (blank), followed by overnight incubation at 37ºC. Then, media was changed for 50 µl of fresh culture media and a 4 mm **CATH-M** membrane disc was introduced in each of the wells already containing cells, or not (control). After 2 and 8 h incubation at 37ºC, membranes were removed and media was exchanged for 180 µl of XF DMEM medium (Agilent), enriched with Pyruvate (1 mM), Glutamine (2 mM) and Glucose (10 mM), followed by 45 min incubation at 37ºC in a non-CO_2 incubator. Then, the assay started and oligomycin 1.5 mM, FCCP 4 mM and rotenone/antimycin A 0.5 mM at final concentrations were used for each cycle (Seahorse XF HS Mini Analyzer, Agilent). For each incubation time, N=3 was obtained.

Antioxidant protection assays. The antioxidant NAC was used to demonstrate and regulate the oxidative effect induce by **CATH-M** membrane. Firstly, 2 x 10^4 LN229 cells/well were seeded in a 96 well plate, followed by a 24 h incubation at 37ºC. Then, media was changed for 50 µl of fresh culture media, containing 1, 5, 10 or 20 mM of NAC, or not (control). Besides, a **CATH-M** 6 mm disc membrane was added to each well or not in base of the condition (N=5). Finally, after 24 h incubation at 37ºC, cell death percentage was quantified.

Furthermore, the H_2O_2 tolerance of the LN229 was also tested following a similar procedure. In this case, media was changed for 50 µl of fresh culture media containing 0, 0.1, 0.25, 0.5, 1 or 2 mM H_2O_2, as well as only culture media with a 6 mm disc **CATH-M** or **PYRO-M** membrane (N=5). Therefore, after 24 h incubation at 37ºC, cell death percentage was also quantified.

ROS determination. The reactive oxygen species (ROS) production of the **CATH-M** membrane was assessed with the MAK143 Fluorometric ROS KIT. Initially, 2 x 10^4 LN229 cells/well were seeded in a 96 well plate, followed by a 24 h incubation at 37ºC. Then, media was changed for 50 µl of fresh culture media (unless otherwise specified) and a 6 mm **CATH-M** or **PYRO-M** disc was introduced in the well, or not (control). In case of measuring in absence of cells, membranes were introduced directly in 50 µl the specific solvent. After the desired incubation time at 37ºC, the fluorescence intensity inside the wells was measured after 30 min of incubation with the kit (Varioskan™ LUX, Thermo Scientific™ and $\lambda_{excitation}$ = 490 nm / $\lambda_{emission}$ = 525 nm for excitation and emission wavelength, respectively) in at least 3 repetitions. The selective determination of ROS was performed with three kits, OxiVision™ Green hydrogen peroxide sensor (Kit A), MitoROS™ OH580 (Kit B) and MitoROS™ 580 (Kit C), in order to detect hydrogen peroxide (H_2O_2), hydroxyl radicals ($^{\cdot}OH$) and superoxide anions ($^{\cdot}O_2^-$), respectively (AAT Bioquest, US, California). Kit A: after preparing the working-solution at 20 µM on 20 mM Hepes buffer in PBS, 50 µl were added to each well; Kit B: after obtaining a 2X working-solution of the assay buffer, 50 µl were added to each condition; Kit C: after achieving a 2X working-solution in 20 mM Hepes buffer in PBS, 50 µl were added to each well. All the kits were prepared simultaneously and incubated for 30 min at room temperature and protected from light after adding them. Right after, KIT A was read at $\lambda_{excitation}$ = 490 nm/ $\lambda_{emission}$ = 525 nm, while Kits B and C at $\lambda_{excitation}$ = 510 nm/$\lambda_{emission}$ = 580 nm. For each Kit/condition N=5 was performed.

Lipid peroxidation. To observe the effect of ROS in the plasmatic membrane, the Image-iT™ Lipid Peroxidation Kit (ThermoFisher Scientific) was selected. Upon oxidation in live cells, fluorescence shifts from red (reduced dye $\lambda_{excitation}$ = 581 nm/ $\lambda_{emission}$ = 590 nm) to green (oxidized dye is $\lambda_{excitation}$ = 488 nm/ $\lambda_{emission}$ = 510 nm). Firstly, 200 µl of culture media are added in each well of a u-slide 8 well plate (Ibidi 80807), followed by 300 µl of culture media containing 7 x 10^4 LN229 cells. After being incubated overnight, media was changed for 250 µl of culture media with 15 µM Image-iT™ sensor, followed by additional 30 min incubating at 37ºC. Then, media was removed and changed for 200 µl of fresh one, adding to them two 8 mm discs of **CATH-M** or **PYRO-M** membrane, or not (control). The plate remained incubating for additional 3 h at 37ºC. Finally, three washes with PBS were performed, adding in the last one H42 (nuclei staining), and samples were observed by confocal microscopy (Leica SP5). An important consideration is that the dye fastly gets oxidized when observed with a green filter (creating false positives), therefore, desired planes should be searched with a blue (for H42) or red filter (for reduced dye). Both pictures in a specific plane (more precise due the low green filter exposition) and z-stacking were obtained. Images were 3D rendered with Blender 4.2.

Bacteria growth conditions. *Escherichia coli* (*E. coli*, MG 1655) and Methicillin-resistant *Staphylococcus aureus* (MRSA, CECT 9951) were selected as representative gram-negative and gram-positive bacteria, respectively. The selection of these strains was mainly due to their impact in current human health and relevance in research stated by the WHO and UN and their implication in brain surgery's infection. Initially, an aliquot from the bacteria was streaked on a 100 mm Petri dish containing Miller's Luria-Bertani (LB) with agar and incubated for 24 h at 37 ºC (Forma™ Series II Water-Jacketed CO_2 Incubator) under a saturating humidity atmosphere composed of 95 % air and 5 % CO_2. For each experiment, a single colony was selected and grown in 10 ml of Miller's LB for 24 h at 37 ºC. Bacteria cultures were resuspended in NaCl saline solution at 0.9 % and the optical density (OD_{600}) of the suspension was adjusted (Fisherbrand™

Cell Density Meter Model 40) to 0.2 for *E. coli*, and 0.3 for MRSA. In every case, 100 mm Petri dish plates with Miller's LB with agar were used for bacteria growth and antibacterial tests. All procedures were performed under biosafety level 2 laminar flow cabins and sterile conditions. These procedures adhered strictly to the specific approved protocols established by the Ethical and Biosafety Committee of the *Universitat Autònoma de Barcelona*, as well as governmental authorities (protocol numbers: A/ES/18/I-12 and HR676-21).

Antibacterial properties in suspension. Two methodologies were followed: suspension and close contact. For the suspension approach, after obtaining the respective OD_{600} for each bacteria strain, 50 µl of bacteria suspension was added per well in a 96 well plates (Falcon™ 353072, Fisher Scientific), introducing inside of them a disc of 6 mm of **CATH-M**, **PYRO-M**, or nothing as control, followed by incubation at 37º for 24 h. Subsequently, the plate was sonicated for 1 min (Elmasonic S 30H) and serial dilutions were performed. Plates were seeded following the already described methodology for single plate-serial dilution spotting (SP-SDS)[61] and kept incubating at 37ºC for 24 h. Finally, viable colony-forming units (CFU) were counted afterwards, with a total number of repetitions of N = 12 for each condition. To determine ROS generation in base of bacteria/membrane selected, after the 24 h incubation, 50 µl of MAK143 kit was added to each well and incubated at room temperature for 30 min to finally read the fluorescence intensity (N=6) (Varioskan™ LUX, Thermo Scientific™ and $\lambda_{excitation} = 490$ nm/$\lambda_{emission} = 525$ nm). In the case of the close contact approach, squares of 2.5 cm^2 **CATH-M** or **PYRO-M** membranes were cut and attached by capillarity to coverslips of 2 cm of diameter. After obtaining the respective OD_{600} for *E. coli*, 20 µl of bacteria suspension were added on the top of a 2.5 cm squared glass, which was over a similar glass piece, and this one over the bottom of the well-plate. Then, the coverslip-membrane was put in contact with the drop, spreading it across the whole membrane. To ensure the humidity an avoid the dryness of the bacterial suspension (which was observed to be a kay factor to avoid false positives), 80 µl of saline solution were added to the bottom of the well-plate (not in contact with the bacterial suspension), inter-well space was filled with water and the plate sealed twice with parafilm. After the desired incubation time, same procedure as with the suspension approach was followed to determine the CFU logarithmic reduction (N=2).

Protein arrays. LN229 cells (3 x 10^6) were distributed in a 100 mm Petri dish containing 10 ml of culture media. Following a 24-hour incubation at 37°C, the medium was replaced with 12 ml of fresh culture media, and an 8 cm diameter disc of **CATH-M** was introduced into the dish, or the dish remained as a control. After an additional 8-10 h, the membrane was carefully removed, and the medium was collected. Cells were trypsinized, pelleted, and washed with PBS. Subsequently, lysates or supernatants from each condition were analyzed using five distinct microarrays: the Proteome Profiler Human XL Cytokine, Chemokine, Protease, Ubiquitin, and Phospho-Immunoreceptor Array Kits (R&D Systems).

Proteomic analysis by liquid chromatography with mass spectrometry (LC-MS/MS). LN229 cells (3 x 10^6) were homogenously seeded in a 100 mm Petri dish containing 10 ml of culture media. After 24 h incubation at 37ºC, media was changed for 12 ml of fresh culture media and an 8 cm diameter disc of **CATH-M** or **PYRO-M** was introduced in the Petri dish, except for the control. After an additional 8-10 hours, the membranes were carefully removed, and the medium was discarded. Cells were washed once with PBS and lysed using a lysis buffer (1 % NP-40, 0.1 % Sodium deoxycholate, 150 mM NaCl, 1 mM EDTA, 50 mM Tris pH 7.5) to obtain a protein suspension. Samples were subsequently processed by the CRG/UPF Proteomics Unit (Barcelona, Spain). Post-analysis for protein identification and quantification were performed using MaxQuant software, version 2.6.1.0.[62,63] The LTQ Orbitrap was operated with default parameters, enabling label-free quantification. The UniProt reference proteome (release 2024_02) was used, limited to reviewed entries. Statistical analysis for quantification was conducted using the Differential Enrichment Proteomics (DEP) package from R-Bioconductor.[64,65] A filter was applied to retain proteins identified in at least two out of three replicates for at least one condition. Data normalization was conducted using variance stabilizing transformation (vsn) from the vsn-R package. For missing values deemed 'Missing Not At Random', data imputation was performed by random draws from a Gaussian distribution centered around a minimal value. Principal component analysis (PCA) was conducted on the 500 most variable proteins between groups. Differential expression analysis was performed for three comparisons: '**CATH-M** vs control', '**PYRO-M** vs control', and '**CATH-M** vs **PYRO-M**', based on protein-wise linear models and empirical Bayes statistics using the limma package. False Discovery Rates (FDRs) were estimated using the 'fdrtool' R package. A Gene set enrichment analysis was conducted using the g:GOSt platform, with the g:SCS algorithm as the default method for computing multiple testing correction for p-values gained from GO and pathway enrichment analysis. Only proteins with a p-value lower than 0.05 from the '**CATH-M** vs **PYRO-M**' comparison, previously filtered for the commons expressed in both control comparisons ('**CATH-M** vs control', ' **PYRO-M** vs control'), were included in the enrichment.

Statistical analysis. The SP-SDS logarithmic reduction test analysis was conducted as described in previous studies.[61] Cell viability or death was expressed as the mean ± standard deviation for each condition, relative to the control (percentage), with a minimum of N=5, unless otherwise specified. Cell counting was performed using Fiji software. For crystal violet measurements, each repetition was divided into 6 replicates and read. The obtained signal was adjusted by subtracting the mean blank value and expressed relative to the "Treatment Control" as the mean (of the repetitions) ± standard deviation. Cell migration was expressed as the mean ± standard deviation from 3 independent experiments, each containing 3 replicates, relative to the control. Adhesion strength was indicated as the mean ± standard deviation of detached cells from 4 replicates, expressed as fold change relative to the control. OCR and ECAR signals were presented as the mean ± standard deviation of 3 replicates for each condition, with the blank automatically subtracted. In the ROS generation tests, the obtained signal was represented as the mean ± standard deviation of at least 3 repetitions for each condition. For specific ROS species, the results from each of the 3 kits were analyzed separately. The mean of the blank was subtracted from the mean of the 5 repetitions for each condition, and the data were expressed as fold change relative to the control. Cells were counted using ImageJ 1.54f software, and data were represented using OriginPro software.

4.6. References

[1] Flores-Jiménez, M. S.; Garcia-Gonzalez, A.;Fuentes-Aguilar, R. Q. *ACS Applied Bio Materials* **2023**, *6*, 1-23. https://doi.org/10.1021/acsabm.2c00740

[2] Agocsova, S. V.; Culenova, M.; Birova, I.; Omanikova, L.; Moncmanova, B.; Danisovic, L.; Ziaran, S.; Bakos, D.; Alexy, P. *Materials* **2023**, *16*, 4267. https://doi.org/10.3390/ma16124267

[3] Jia, B.; Huang, H.; Dong, Z.; Ren, X.; Lu, Y.; Wang, W.; Zhou, S.; Zhao, X.; Guo, B. *Chemical Society Reviews* **2024**, *53*, 4086-4153. https://doi.org/10.1039/d3cs00923h

[4] National Cancer Institute. https://www.cancer.gov/about-cancer/understanding/what-is-cancer#definition (accessed: 17 February 2025).

[5] Bray, F.; Ferlay, J.; Soerjomataram, I.; Siegel, R. L.; Torre, L. A.; Jemal, A. *CA A Cancer Journal For Clinicians* **2018**, *68*, 394-424. https://doi.org/10.3322/caac.21492

[6] Sung, H.; Ferlay, J.; Siegel, R. L.; Laversanne, M.; Soerjomataram, I.; Jemal, A.; Bray, F. *CA A Cancer Journal For Clinicians* **2021**, *71*, 209-249. https://doi.org/10.3322/caac.21660

[7] Bray, F.; Laversanne, M.; Sung, H.; Ferlay, J.; Siegel, R. L.; Soerjomataram, I.; Jemal, A. CA A Cancer Journal For Clinicians 2024, 74, 229-263. https://doi.org/10.3322/caac.21834

[8] Siegel, R. L.; Giaquinto, A. N.; Jemal, A. *CA A Cancer Journal For Clinicians* **2024**, *74*, 12-49. https://doi.org/10.3322/caac.21820

[9] National Cancer Institute. https://www.cancer.gov/about-cancer/diagnosis-staging/diagnosis/tumor-grade (accessed: 17 February 2025).

[10] Vaz-Salgado, M. A.; Villamayor, M.; Albarrán, V.; Alía, V.; Sotoca, P.; Chamorro, J.; Rosero, D.; Barrill, A. M.; Martín, M.; Fernandez, E.; Gutierrez, J. A.; Rojas-Medina, L. M.; Ley, L. *Cancers* **2023**, *15*, 4279. https://doi.org/10.3390/cancers15174279

[11] Brown, N. F.; Ottaviani, D.; Tazare, J.; Gregson, J.; Kitchen, N.; Brandner, S.; Fersht, N.; Mulholland, P. *Cancers* **2022**, *14*, 3161. https://doi.org/10.3390/cancers14133161

[12] Pleskacova, Z.; Bartos, M.; Vosmikova, H.; Dolezal, R.; Krupa, P.; Vitovcova, B.; Kasparova, P.; Rudolf, E.; Skarkova, V.; Pohankova, D.; Novotna, V.; Petera, J. *Biomedicines* **2024**, *12*, 1210. https://doi.org/10.3390/biomedicines12061210

[13] Grochans, S.; Cybulska, A. M.; Simińska, D.; Korbecki, J.; Kojder, K.; Chlubek, D.; Baranowska-Bosiacka, I. *Cancers* **2022**, *14*, 2412. https://doi.org/10.3390/cancers14102412

[14] Rong, Y.; Durden, D. L.; Van Meir, E. G.; Brat, D. J. *Journal Of Neuropathology & Experimental Neurology* **2006**, *65*, 529-539. https://doi.org/10.1097/00005072-200606000-00001

[15] Lakomy, R.; Kazda, T.; Selingerova, I.; Poprach, A.; Pospisil, P.; Belanova, R.; Fadrus, P.; Vybihal, V.; Smrcka, M.; Jancalek, R.; Hynkova, L.; Muckova, K.; Hendrych, M.; Sana, J.; Slaby, O.; Slampa, P. *Frontiers In Oncology* **2020**, *10*, 840. https://doi.org/10.3389/fonc.2020.00840

[16] Rodgers, L. T.; Villano, J. L.; Hartz, A. M. S.; Bauer, B. Cancers 2024, 16, 2638. https://doi.org/10.3390/cancers16152638

[17] Tohidinezhad, F.; Zegers, C. M. L.; Vaassen, F.; Dijkstra, J.; Anten, M.; Van Elmpt, W.; De Ruysscher, D.; Dekker, A.; Eekers, D. B. P.; Traverso, A. *Neuro-Oncology* **2024**, *26*, 1467-1478. https://doi.org/10.1093/neuonc/noae035

[18] Jezierzański, M.; Nafalska, N.; Stopyra, M.; Furgoł, T.; Miciak, M.; Kabut, J.; Gisterek-Grocholska, I. *Current Oncology* **2024**, *31*, 3994-4002. https://doi.org/10.3390/curroncol31070296

[19] Razavi, S.; Lee, K. E.; Jin, B. E.; Aujla, P. S.; Gholamin, S.; Li, G. *Frontiers In Surgery* **2016**, *3*, 11. https://doi.org/10.3389/fsurg.2016.00011

[20] Iturrioz-Rodríguez, N.; Sampron, N.; Matheu, A. *Theranostics* **2023**, *13*, 2734-2756. https://doi.org/10.7150/thno.82005

[21] Bausart, M.; Préat, V.; Malfanti, A. *Journal Of Experimental & Clinical Cancer Research* **2022**, *41*,35. https://doi.org/10.1186/s13046-022-02251-2

[22] Da Silva, E. C.; Mercier, M.; Etienne-Selloum, N.; Dontenwill, M.; Choulier, L. *Cancers* **2021**, *13*, 1795. https://doi.org/10.3390/cancers13081795

[23] Vaz-Salgado, M. A.; Villamayor, M.; Albarrán, V.; Alía, V.; Sotoca, P.; Chamorro, J.; Rosero, D.; Barrill, A. M.; Martín, M.; Fernandez, E.; Gutierrez, J. A.; Rojas-Medina, L. M.; Ley, L. *Cancers* **2023**, *15*, 4279. https://doi.org/10.3390/cancers15174279

[24] Alifieris, C.; Trafalis, D. T. *Pharmacology & Therapeutics* **2015**, *152*, 63-82. https://doi.org/10.1016/j.pharmthera.2015.05.005

[25] Chang, C.; Chavarro, V. S.; Gerstl, J. V. E.; Blitz, S. E.; Spanehl, L.; Dubinski, D.; Valdes, P. A.; Tran, L. N.; Gupta, S.; Esposito, L.; Mazzetti, D.; Gessler, F. A.; Arnaout, O.; Smith, T. R.; Friedman, G. K.; Peruzzi, P.; Bernstock, J. D. *International Journal Of Molecular Sciences* **2024**, *25*, 6733. https://doi.org/10.3390/ijms25126733

[26] Chamberlain, M. C. *Journal Of Neuro-Oncology* **2010**, *101*, 319-323. https://doi.org/10.1007/s11060-010-0251-4

[27] Ju, S.; Singh, M. K.; Han, S.; Ranbhise, J.; Ha, J.; Choe, W.; Yoon, K.; Yeo, S. G.; Kim, S. S.; Kang, I. *International Journal Of Molecular Sciences* **2024**, *25*, 12387. https://doi.org/10.3390/ijms252212387

[28] Olivier, C.; Oliver, L.; Lalier, L.; Vallette, F. M. *Frontiers In Molecular Biosciences* **2021**, *7*, 620677. https://doi.org/10.3389/fmolb.2020.620677

[29] Saurty-Seerunghen, M. S.; Daubon, T.; Bellenger, L.; Delaunay, V.; Castro, G.; Guyon, J.; Rezk, A.; Fabrega, S.; Idbaih, A.; Almairac, F.; Burel-Vandenbos, F.; Turchi, L.; Duplus, E.; Virolle, T.; Peyrin, J.; Antoniewski, C.; Chneiweiss, H.; El-Habr, E. A.; Junier, M. *Cell Death And Disease* **2022**, *13*, 913. https://doi.org/10.1038/s41419-022-05358-8

[30] Cheung, E. C.; Vousden, K. H. *Nature Reviews Cancer* **2022**, *22*, 280-297. https://doi.org/10.1038/s41568-021-00435-0

[31] Sies, H.; Belousov, V. V.; Chandel, N. S.; Davies, M. J.; Jones, D. P.; Mann, G. E.; Murphy, M. P.; Yamamoto, M.; Winterbourn, C. *Nature Reviews Molecular Cell Biology* **2022**, *23*, 499-515. https://doi.org/10.1038/s41580-022-00456-z

[32] Harris, I. S.; DeNicola, G. M. *Trends In Cell Biology* **2020**, *30*, 440-451. https://doi.org/10.1016/j.tcb.2020.03.002

[33] Liberti, M. V.; Locasale, J. W. *Trends In Biochemical Sciences* **2016**, *41*, 211-218. https://doi.org/10.1016/j.tibs.2015.12.001

[34] Wu, S.; Lu, H.; Bai, Y. *Cancer Medicine* **2019**, *8*, 2252-2267. https://doi.org/10.1002/cam4.2101

[35] Cesca, B. A.; Caverzan, M. D.; Lamberti, M. J.; Ibarra, L. E. *International Journal Of Molecular Sciences* **2024**, *25*, 7525. https://doi.org/10.3390/ijms25147525

[36] Huang, H.; Zhang, S.; Li, Y.; Liu, Z.; Mi, L.; Cai, Y.; Wang, X.; Chen, L.; Ran, H.; Xiao, D.; Li, F.; Wu, J.; Li, T.; Han, Q.; Chen, L.; Pan, X.; Li, H.; Li, T.; He, K.; et. al. *Nature Communications* **2021**, *12*, 3720. https://doi.org/10.1038/s41467-021-24108-6

[37] Buccarelli, M.; D'Alessandris, Q. G.; Matarrese, P.; Mollinari, C.; Signore, M.; Cappannini, A.; Martini, M.; D'Aliberti, P.; De Luca, G.; Pedini, F.; Boe, A.; Biffoni, M.; Pallini, R.; Ricci-Vitiani, L. *Journal Of Experimental & Clinical Cancer Research* **2021**, *40*, 228. https://doi.org/10.1186/s13046-021-02031-4

[38] Yan, G.; Elbadawi, M.; Efferth, T. *World Academy Of Sciences Journal* **2020***, 2*, 39-48. https://doi.org/10.3892/wasj.2020.40

[39] An, X.; Yu, W.; Liu, J.; Tang, D.; Yang, L.; Chen, X. *Cell Death And Disease* **2024**, *15*, 556. https://doi.org/10.1038/s41419-024-06939-5

[40] Lee, J.; Cho, H. R.; Cha, G. D.; Seo, H.; Lee, S.; Park, C.; Kim, J. W.; Qiao, S.; Wang, L.; Kang, D.; Kang T.; Ichikawa, T.; Kim, J.; Lee, H.; Lee, W.; Kim, S.; Lee, S.; Lu, N.; Hyeon, T., et. al. *Nature Communications* **2019**, *10,* 5205. https://doi.org/10.1038/s41467-019-13198-y

[41] Lang, Y.; Gao, N.; Zang, Z.; Meng, X.; Lin, Y.; Yang, S.; Yang, Y.; Jin, Z.; Li, B. *Journal Of Future Foods* **2023**, *4*, 193-204. https://doi.org/10.1016/j.jfutfo.2023.07.002

[42] Andrés, C. M. C.; De la Lastra, J. M. P.; Juan, C. A.; Plou, F. J.; Pérez-Lebeña, E. *Processes* **2023**, *11*, 2771. https://doi.org/10.3390/pr11092771

[43] Saiz-Poseu, J.; Mancebo-Aracil, J.; Nador, F.; Busqué, F.; Ruiz-Molina, D. *Angewandte Chemie International Edition* **2018**, *58*, 696-714. https://doi.org/10.1002/anie.201801063

[44] Zhang, X.; Li, Z.; Yang, P.; Duan, G.; Liu, X.; Gu, Z.; Li, Y. *Materials Horizons* **2020**, *8*, 145-167. https://doi.org/10.1039/d0mh01317j

[45] Almajidi, Y. Q.; Ponnusankar, S.; Chaitanya, M.; Marisetti, A. L.; Hsu, C.; Dhiaa, A. M.; Saadh, M. J.; Pal, Y.; Thabit, R.; Adhab, A. H.; Alsaikhan, F.; Narmani, A.; Farhood, B. *International Journal Of Biological Macromolecules* **2024**, *264*, 130683. https://doi.org/10.1016/j.ijbiomac.2024.130683

[46] Naghavi, M.; Vollset, S. E.; Ikuta, K. S.; Swetschinski, L. R.; Gray, A. P.; Wool, E. E.; Aguilar, G. R.; Mestrovic, T.; Smith, G.; Han, C.; Hsu, R. L.; Chalek, J.; Araki, D. T.; Chung, E.; Raggi, C.; Hayoon, A.

G.; Weaver, N. D.; Lindstedt, P. A.; Smith, A. E.; et. al. *The Lancet* **2024**, *404*, 1199-1226. https://doi.org/10.1016/s0140-6736(24)01867-1

[47] Wu, Y.; Liu, P.; Mehrjou, B.; Chu, P. K. *Advanced Materials* **2023**, *36,* 2305940. https://doi.org/10.1002/adma.202305940

[48] Shi, Z.; Xu, M.; Wang, Y.; Luo, X.; Chen, G.; Wang, X.; Wang, T.; Tang, M.; Zhou, J. *British Journal Of Neurosurgery* **2016**, *31*, 5-9. https://doi.org/10.1080/02688697.2016.1253827

[49] Suárez-García, S.; Saiz-Poseu, J.; Ruiz-Molina, D. *Catecholamine-based Membrane, Process for its Preparation and Uses Thereof* **2021**, EP21382516.

[50] Suárez-García, S.; Sedó, J.; Saiz-Poseu, J.; Ruiz-Molina, D. *Biomimetics* **2017**, *2*, 22. https://doi.org/10.3390/biomimetics2040022

[51] Maroli, G.; Rosati, G.; Suárez-García, S.; Bedmar-Romero, D.; Kobrin, R.; González-Laredo, Á.; Urban, M.; Alvárez-Diduk, R.; Ruiz-Molina, D.; Merkoçi, A. *Biosensors And Bioelectronics* **2024**, *260*, 116421. https://doi.org/10.1016/j.bios.2024.116421

[52] López-Moral, A.; Bolaños-Cardet, J.; Alibés, R.; Busqué, F.; Yuste, V. J.; Ruiz-Molina, D.; Suárez-García, S. *Journal Of Colloid And Interface Science* **2024**, *680*, 987-996. https://doi.org/10.1016/j.jcis.2024.11.042

[53] López-Moral, A. *Synthesis of Phenolic Functional Interfaces* **2024** (PhD Thesis, Autonomous University of Barcelona) http://hdl.handle.net/10803/692875

[54] Salle, H.; Deluche, E.; Couvé-Deacon, E.; Beaujeux, A.; Pallud, J.; Roux, A.; Dagain, A.; De Barros, A.; Voirin, J.; Seizeur, R.; Belmabrouk, H.; Lemnos, L.; Emery, E.; Fotso, M.; Engelhardt, J.; Jecko, V.; Zemmoura, I.; Van, T. L.; Berhouma, M.; et. al. *Infection* **2020**, *49*, 267-275. https://doi.org/10.1007/s15010-020-01534-0

[55] Shi, Z.; Xu, M.; Wang, Y.; Luo, X.; Chen, G.; Wang, X.; Wang, T.; Tang, M.; Zhou, J. *British Journal Of Neurosurgery* **2017**, *31*, 5-9. https://doi.org/10.1080/02688697.2016.1253827

[56] Kim, J. H.; Scialli, A. R. *Toxicological Sciences* **2011**, *122*, 1-6. https://doi.org/10.1093/toxsci/kfr088

[57] Belmokhtar, C. A.; Hillion, J.; Ségal-Bendirdjian, E. *Oncogene* **2001**, *20*, 3354-3362. https://doi.org/10.1038/sj.onc.1204436

[58] Aggarwal, V.; Tuli, H.; Varol, A.; Thakral, F.; Yerer, M.; Sak, K.; Varol, M.; Jain, A.; Khan, M.; Sethi, G. *Biomolecules* **2019**, *9*, 735. https://doi.org/10.3390/biom9110735

[59] Fairley, N.; Fernandez, V.; Richard-Plouet, M.; Guillot-Deudon, C.; Walton, J.; Smith, E.; Flahaut, D.; Greiner, M.; Biesinger, M.; Tougaard, S.; Morgan, D.; Baltrusaitis, J. *Applied Surface Science Advances* **2021**, *5*, 100112. https://doi.org/10.1016/j.apsadv.2021.100112

[60] Servitja, J.; Masgrau, R.; Sarri, E.; Picatoste, F. *British Journal Of Pharmacology* **1998***, 124*, 1728-1734. https://doi.org/10.1038/sj.bjp.0701997

[61] Thomas, P.; Sekhar, A. C.; Upreti, R.; Mujawar, M. M.; Pasha, S. S. *Biotechnology Reports* **2015**, *8*, 45-55. https://doi.org/10.1016/j.btre.2015.08.003

[62] Tyanova, S.; Temu, T.; Cox, J. *Nature Protocols* **2016**, *11*, 2301-2319. https://doi.org/10.1038/nprot.2016.136

[63] Sinitcyn, P.; Tiwary, S.; Rudolph, J.; Gutenbrunner, P.; Wichmann, C.; Yılmaz, Ş.; Hamzeiy, H.; Salinas, F.; Cox, J. *Nature Methods* **2018**, *15*, 401. https://doi.org/10.1038/s41592-018-0018-y

[64] Reimers, M.; Carey, V. J. *Methods In Enzymology* **2006**, *411*, 119-134. https://doi.org/10.1016/s0076-6879(06)11008-3

[65] Zhang, X.; Smits, A. H.; Van Tilburg, G. B.; Ovaa, H.; Huber, W.; Vermeulen, M. *Nature Protocols* **2018**, *13*, 530-550. https://doi.org/10.1038/nprot.2017.147

Chapter 5

General Conclusions

In this Thesis, catechol-amine-based coatings and membranes have been successfully developed for antimicrobial and cancer treatment applications, respectively. Both materials were thoroughly characterized from a physicochemical and, most notably, a biological perspective. The main conclusions are as follows:

1. The synthesis methodology used to obtain both materials is a one-step, simple, and cost-effective process. It is designed to be user-friendly, carried out under mild conditions, and does not require harmful solvents, drugs, metals, or additional polymers.

2. This synthesis approach allows for the tuning of material properties through the selection of specific catechol derivatives and amines. These variations influence attributes such as coloration, selectivity toward certain bacterial or fungal strains (e.g., **PYRO-H** vs. **CAFF-H**), and ROS production (e.g., **CATH-M** vs. **PYRO-M**).

3. The selected coatings demonstrated broad-spectrum antimicrobial activity, effectively neutralizing six bacterial strains within 3 h and two fungal species within 24 h. In general, pathogen reduction exceeded 99%.

4. As proof-of-concept, commercially available band-aids coated with the developed coatings exhibited strong antimicrobial activity *in vitro* and showed promising outcomes in *ex vivo* models, highlighting their potential for real-world biomedical applications.

5. For the first time, catechol-amine membranes have been synthesized without the incorporation of pre-existing polymers, while also demonstrating remarkable mechanical manipulability. In particular, the **CATH-M** membrane showed enhanced ROS production, further supporting its potential biomedical uses.

6. From and *in vitro* point of view, the **CATH-M** membrane significantly improved the standard-of-care for Glioblastoma treatment. This, coupled with its proven ability to eliminate various organ-derived cancer cell lines and its successful application and adhesion in *ex vivo* models, strongly suggests its potential as a targeted, post-surgical therapy for Glioblastoma.

7. The membranes showed excellent cell adhesion properties. Depending on their composition, they behaved either as a trap for sustained cytotoxic ROS generation (**CATH-M**) or as a promising scaffold for tissue regeneration (**PYRO-M**).

8. In both coatings and membranes, the antimicrobial and cytotoxic effects were attributed to i) direct contact with the material, causing electrostatic interactions or membrane disruption, and ii) sustained ROS production, which damages pathogen structures and DNA, ultimately inducing oxidative stress-mediated cell death.

9. In both cases, the impact of the coatings and **CATH-M** on the morphology of the different bacteria and the LN229 cell line exhibited similarities, showing perforations in their cellular membrane, which indicates a severe cellular damage.

10. The ROS activity in both materials was sustained for longer periods when protected from light. This property was more effectively preserved when stored in dry conditions and under argon atmosphere.

11. This Thesis is based on two research articles: one already published (Chapter 3 - *Chemical Engineering Journal* **2024**, 481, 148674. https://doi.org/10.1016/j.cej.2024.148674) and the other currently under revision (Chapter 4). Additionally, a European patent related to Chapter 4 (*Catecholamine-based membrane for use in the treatment of cancer*, EP25382323, 01/04/25) has been presented.

The versatility of the developed coatings and membranes in addressing key challenges within their respective fields, combined with their straightforward synthesis and the potential to generate novel materials using similar formulations, points toward a promising future for further innovations. Overall, this Thesis underscores the transformative potential of catechol-based materials in biomedical applications, offering new avenues of hope in the fight against some of the most pressing medical challenges of our time. Bridging chemistry, materials science, and biomedicine, this multidisciplinary work exemplifies how academic research can move beyond the lab bench, driving real impact, empowering healthcare innovation, and turning scientific progress into tangible change for society.